Karlsruher Institut für Technologie

ETP-KA/2021-14

INVESTIGATION OF RADIATION DAMAGE IN SILICON SENSORS FOR THE PHASE-2 UPGRADE OF THE CMS OUTER TRACKER

Zur Erlangung des akademischen Grades eines
DOKTORS DER NATURWISSENSCHAFTEN (Dr. rer. nat.)
von der KIT-Fakultät für Physik des
Karlsruher Instituts für Technologie (KIT)

genehmigte

DISSERTATION

von

M. Sc. Jan-Ole Müller-Gosewisch
aus Hannover

Tag der mündlichen Prüfung: 29.10.2021

Referent:	Prof. Dr. Thomas Müller	Institut für Experimentelle Teilchenphysik
Korreferent:	Prof. Dr. Ulrich Husemann	Institut für Experimentelle Teilchenphysik

Jan-Ole Müller-Gosewisch:
Investigation of Radiation Damage in Silicon Sensors for the Phase-2 Upgrade of the CMS Outer Tracker
October 2021

Contents

I. Introduction and Basics 1

1. Introduction 3

2. The LHC and the CMS Phase-2 Upgrade 5
- 2.1. The LHC at CERN . . . 5
- 2.2. The Compact Muon Solenoid (CMS) Experiment . . . 7
- 2.3. The Integrated Luminosity . . . 8
- 2.4. The High-Luminosity Upgrade of the LHC . . . 9
- 2.5. The Phase-2 Upgrade of the CMS Outer Tracker . . . 10
  - 2.5.1. Requirements for the High Luminosity Phase . . . 10
  - 2.5.2. Tracker Design and Outer Tracker Module Concept . . . 11
  - 2.5.3. Radiation Environment and Outer Tracker Sensors . . . 12

3. Basic Properties of Silicon Sensors 17
- 3.1. The Band Model . . . 17
- 3.2. Doping of Silicon . . . 18
- 3.3. Manufacturing of Silicon Structures . . . 19
- 3.4. The pn-Junction . . . 20
  - 3.4.1. Electrical Properties of a pn-Junction . . . 23
- 3.5. Interaction of Particles in Matter . . . 24
  - 3.5.1. Realistic Energy Loss in a Thin Layer . . . 26
- 3.6. Sensor Principles and Design . . . 26
  - 3.6.1. Design of Silicon Strip Sensors in Phase-2 of CMS . . . 27
  - 3.6.2. Shockley-Ramo Theorem and Weighting Field . . . 28
  - 3.6.3. Noise Contributions . . . 30

4. Radiation Damage 31
- 4.1. Microscopic Bulk Damage . . . 31
  - 4.1.1. NIEL Hypothesis . . . 31
  - 4.1.2. Defects in the Band Scheme . . . 33
- 4.2. Impact of Bulk Damage on Sensor Properties . . . 35
  - 4.2.1. Leakage Current . . . 37
  - 4.2.2. Depletion Voltage . . . 37
  - 4.2.3. Charge Collection . . . 38
  - 4.2.4. Annealing . . . 40
- 4.3. Surface Damage . . . 41
  - 4.3.1. Interface Traps . . . 42
  - 4.3.2. Fixed Oxide Charge . . . 43
  - 4.3.3. Other Defects . . . 43
  - 4.3.4. Impact of Silicon Nitride . . . 44
- 4.4. Defect Generation due to Ionising Radiation . . . 45

II. Test Devices and Procedures 47

5. Working Principle of Test Structures 49
- 5.1. Diode Structure 49
- 5.2. MOS Capacitor 51
  - 5.2.1. States of a MOS 51
  - 5.2.2. Flat-band Voltage Extraction from a Capacitance Measurement 51
- 5.3. GCD Structure 53

6. Experimental Basics and Procedures 57
- 6.1. Probe Stations 57
  - 6.1.1. Improvements of the Probe Station Chuck 57
- 6.2. Signal Measurements with an ALiBaVa Setup 59
  - 6.2.1. Noise and Calibration 60
  - 6.2.2. Signal Analysis 61
- 6.3. Irradiation Facilities 64
  - 6.3.1. Proton Irradiation at ZAG 64
  - 6.3.2. Neutron Irradiation in Ljubljana 65
  - 6.3.3. X-Ray Irradiation at ETP 65
- 6.4. TCAD Simulation with Synopsys Sentaurus 66

III. Investigation of Radiation Damage 71

7. Irradiation Tests for the CMS Phase-2 Outer Tracker Sensor Production 73
- 7.1. Introduction to Irradiation Tests 76
- 7.2. Irradiation Tests with Hadron Irradiation 78
  - 7.2.1. Electrical Characterisation pre Irradiation 79
  - 7.2.2. Electrical Characterisation of Diodes after Irradiation 81
  - 7.2.3. Electrical Characterisation of Strip Sensors after Irradiation 86
  - 7.2.4. Signal Measurements on Strip Sensors after Irradiation 87
  - 7.2.5. Electrical Characterisation after Annealing and Signal Measurements . . 92
- 7.3. Irradiation Tests with X-Ray Irradiation 93
  - 7.3.1. Characterisation pre Irradiation 94
  - 7.3.2. First Investigations after Irradiation 99
  - 7.3.3. Pre-production Results after Irradiation 103
- 7.4. Escalation Strategy 107

8. Interstrip Isolation of p-type Strip Sensors 109
- 8.1. Measurement Procedure 111
- 8.2. Simulated Device 111
- 8.3. Situation pre Irradiation 113
  - 8.3.1. Experimental Results 113
  - 8.3.2. Destruction of the Electron Layer 114
  - 8.3.3. Impact of the Doping Concentration 115
- 8.4. Pure Surface Damage 117
  - 8.4.1. Experimental Results 117
  - 8.4.2. Surface Defect Simulations 118
  - 8.4.3. Impact of Interface Traps on the Interstrip Resistance 120
  - 8.4.4. Replication of Measurements 121

8.5. Hadron Irradiation 122
8.5.1. Experimental Results 123
8.5.2. Simulation of Bulk Defects 124
8.5.3. Impact of Bulk Defects on the Interstrip Resistance 125
8.5.4. Comparison of Simulations to Measurements 128

IV. Summary and Outlook **131**

9. Summary and Outlook **133**

V. Appendix **137**

A. Appendix to Chapter 5 **139**

B. Appendix to Chapter 6 **141**

C. Appendix to Chapter 7 **143**

D. Appendix to Chapter 8 **145**
D.1. Example Sentaurus Device File 145
D.2. Optimisation GUI 150
D.3. Follow-Up Studies to Chapter 8 151
D.3.1. Biased X-Ray Irradiation 151
D.3.2. Simulated Impact of Bulk Defects during X-Ray Irradiation 154
D.3.3. Different Oxide Variants for the CMS HGCAL 155
D.3.4. Impact of Charge Multiplication on the Interstrip Resistance 157
D.3.5. Sufficient Interstrip Resistance in Terms of Charge Collection 159

List of Figures **161**

List of Tables **165**

Bibliography **167**

Part I.

Introduction and Basics

1

Introduction

Our natural urge to understand the world around us leads us again and again to the question how nature is structured and why it behaves the way it does. Our view of the world has changed several times in the past, but the fundamental idea that it is composed of small elementary particles always stayed the same. In the past centuries humankind has developed several atomic models, slightly improved and adapted from time to time. Scattering experiments have been conducted, like for example by Rutherford, Geiger and Marsden, resulting in the observation that atoms consist of atomic nuclei and shell electrons [Rut11]. Further experiments showed that the nucleus is composed of protons and neutrons. Going to even higher energies in scattering experiments revealed that also protons and neutrons are composed of smaller particles – the quarks. Whether these are finally elementary is not concluded yet. The current self-consistent theory explaining the properties of the smallest particles is called the *Standard Model of particle physics*.

The last building block that was missing for the Standard Model, the Higgs boson, has been predicted a long time ago, in the 1960s, and discovered more recently, in 2012, at CERN [ATL12][CMS12]. This was the greatest milestone achieved by the particle collider LHC and the detector experiments ATLAS and CMS so far. Despite this success, there are still a lot of questions, which cannot be answered by the Standard Model. Instead, new, so far unknown, physical mechanisms need to be developed to explain certain phenomena, who are therefore referred to as beyond Standard Model physics.

In order to perform high-precision measurements of Standard Model physics but also to investigate new processes, the LHC will be upgraded to a high-luminosity phase (HL-LHC). The full upgrade is currently foreseen to be conducted in the time period from 2025 to 2027. This upgrade will result in an increased instantaneous luminosity, which is by a factor of five to seven higher compared to the nominal luminosity of the LHC. In addition, the integrated luminosity of the HL-LHC per year will reach the value of the full runtime of the LHC. With a foreseen runtime of at least ten years, the integrated luminosity will be increased accordingly, by a factor of greater than ten.

The HL-LHC implies new challenges for the existing detector systems. Therefore, they will be upgraded in the upcoming years and in the course of these upgrades the CMS Outer Tracker will be replaced entirely. A crucial aspect of this new Outer Tracker is the required radiation hardness of the silicon sensors. The increase of integrated luminosity leads to proportionally increased radiation damage. If the sensors are not able to cope with the harsh radiation environment of the HL-LHC, the detector will not be efficiently operable anymore. The production of new sensors has recently started. Irradiation tests complement the quality assurance procedures which are continuously performed during the sensor production. This thesis is dedicated to the investigation of radiation damage in silicon sensors for the new CMS Outer Tracker.

The first part of this work deals with the development of reliable irradiation testing procedures that will be performed during the next years of sensor production. The expected radiation environment of the new tracker is composed of several particle types. Therefore, irradiation with protons and neutrons on diodes and miniature strip sensors and X-ray irradiation on MOS and GCD structures are planned on a regular basis. The current-related damage rate due to damage of the silicon substrate by non-ionising radiation is extracted from a leakage current measurement on the diodes after irradiation to monitor the behaviour of the silicon substrate. Strip measurements are conducted on a miniature sensor with similar properties to the full-sized sensors. In addition, charge collection measurements on the same device indicate whether the signal strength allows for efficient particle detection over the full runtime. The proneness to surface damage is evaluated with the help of MOS and GCD structures, from which the flat-band voltage and the surface generation velocity are extracted. This work yields first tightly bounded benchmark values of the various parameters. By monitoring these parameters during the production of the subsequent wafer batches in the following years it is possible to identify potential issues concerning the radiation hardness.

The second part of this thesis is dedicated to the strip isolation mechanism of silicon strip sensors. In general, it is expected that there is no strip isolation of an n-on-p sensor as long as it does not feature a specific strip isolation implant. However, in preceding studies, isolated strips were observed after such sensors had been irradiated with protons. The hypothesis is therefore that the substrate defects are beneficial in terms of strip isolation. This is investigated in detail by considering sensors without any strip isolation feature. Hence, disguising effects from usual strip isolation implants are excluded. These sensors stem from the CMS Outer Tracker prototyping wafers. Thus, the difference to the new Outer Tracker strip sensors is solely these sensors not featuring a specific strip isolation measure. The sensors are irradiated with protons, neutrons and X-rays, resulting in different fractions of substrate and surface damage. This allows to disentangle the impact of the two damage types on the strip isolation. The strip isolation is characterised by interstrip resistance measurements in dependence of the reverse bias potential. These measurements are complemented by finite-element TCAD models to get deeper insight into the underlying mechanism. A composite TCAD model is developed to describe the complex interplay of surface and substrate damage and their impact on the strip isolation. Finally, it is shown that the substrate defects are indeed crucial and therefore the mechanism how they contribute to the strip isolation of silicon strip sensors is explained.

This work starts with an introduction to the LHC and the upgrades of the CMS detector in chapter 2. An overview on the basic structure of a silicon sensor is given in chapter 3. In chapter 4 a stronger focus is set on the radiation damage in the substrate and the surface of these sensors. The working principle of specific test devices and their characterisation are introduced in chapter 5. Test systems, irradiation facilities and the simulation framework used to conduct the investigations are described in chapter 6. Then, the irradiation tests in the course of the CMS Outer Tracker upgrade are discussed in detail in chapter 7. The investigation of the strip isolation of silicon strip sensors follows in chapter 8. Finally, the results are summarised and an outlook is given in chapter 9.

2

The LHC and the CMS Phase-2 Upgrade

2.1. The LHC at CERN

The Large Hadron Collider (LHC) at CERN (European Organisation for Nuclear Research) in Geneva is the largest scientific facility for particle physics worldwide. A lot of scientists are doing research directly at CERN or in association with CERN facilities. In total, approximately 11 000 scientists from 85 different nations are working on research for CERN laboratories. The overall goal is to gain a better understanding of nature and its fundamental building blocks. This does not only include the discovery of new elementary particles but also the interaction properties at high-precision level. At the LHC, beams of protons or heavier ions are accelerated to velocities close to the speed of light and are then brought to collisions.

The CERN accelerator complex is displayed in fig. 2.1. Particles are accelerated in several pre-accelerators before they are fed to the LHC and reach the highest energies. An overview of the stations that protons pass through on the way to the LHC is given in the following. First of all, hydrogen ions (H^-) are produced. These ions are then fed to a linear accelerator, the LINAC4, which accelerates them to an energy of 160 MeV. Afterwards the electrons are stripped off and the bare protons are injected into the BOOSTER, in which they are boosted to an energy of 2 GeV. The last two steps before the LHC are the PS (Proton Synchrotron) and the SPS (Super Proton Synchrotron), where energies of 26 GeV and 450 GeV are reached, respectively. Finally, the protons are injected into the LHC, where they are accelerated to the nominal energy of 6.5 TeV. Afterwards, the particles can be stored inside the LHC for several hours with the respective energy.

These high-energetic protons are brought to collisions at specific locations. In each bunch crossing, approximately 1000 secondary particles are generated every 25 ns. Large detector complexes like ATLAS (A Toroidal LHC ApparatuS) and CMS (Compact Muon Solenoid) are built hermetically around these interaction points, in order to collect as much information as possible about the particles' properties like energy, momentum, charge and mass. The working principle of such a detector is explained for the CMS experiment in the next section.

One of the most important milestones that has been achieved at CERN is the discovery of the Higgs boson in July 2012. The Higgs boson as an indicator for the Higgs mechanism was the last required building block of the *Standard Model of particle physics* and had already been predicted 50 years earlier. A sketch of a possible Higgs-like event within the CMS detector is illustrated in fig. 2.2. The Higgs boson decayed into two Z bosons. One of these two decayed into a pair of electrons, indicated with the green lines. The other one decayed into a pair of muons which are coloured in red. Although all elementary particles that have been predicted by the Standard Model of particle physics have been detected in experiments, there are still questions left open that can only be answered with physics beyond the Standard Model.

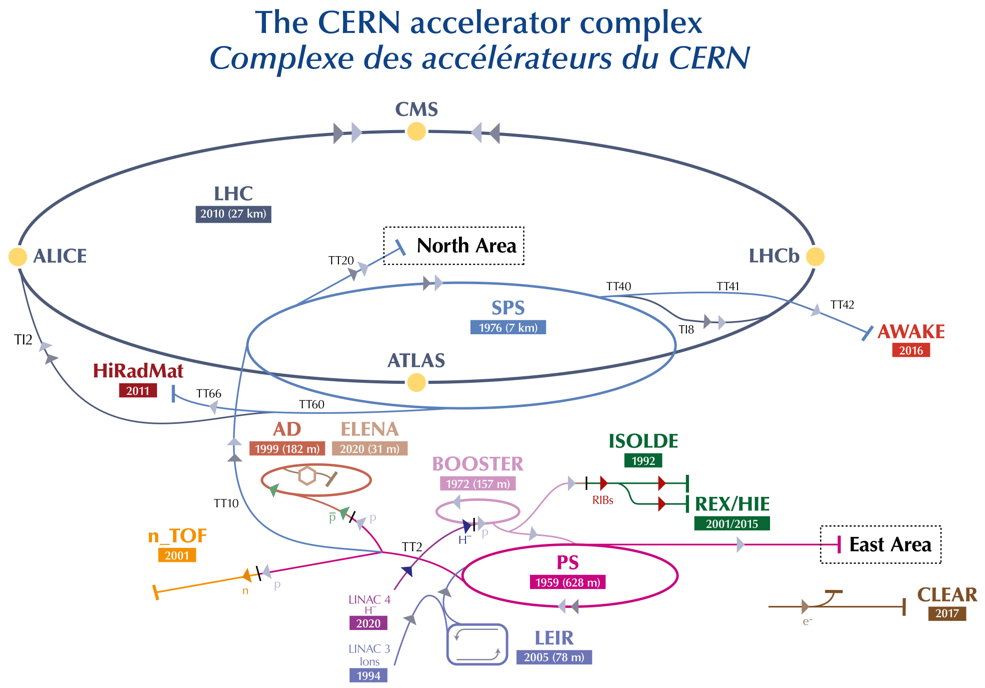
The CERN accelerator complex
Complexe des accélérateurs du CERN
CMS
LHC
2010 (27 km)
ALICE
North Area
LHCb
TT20
TT40
TT41
TT42
AWAKE
2016
SPS
1976 (7 km)
TI8
TI2
ATLAS
HiRadMat
2011
TT66
TT60
AD
1999 (182 m)
ELENA
2020 (31 m)
ISOLDE
1992
BOOSTER
1972 (157 m)
RIBs
REX/HIE
2001/2015
TT10
p̄
p
H⁻
East Area
n_TOF
2001
TT2
PS
1959 (628 m)
n
p
CLEAR
2017
e⁻
LINAC 4
H⁻
2020
LINAC 3
Ions
1994
LEIR
2005 (78 m)

Figure 2.1.: The CERN accelerator complex. Detector experiments are indicated with yellow circles on the LHC ring [Mob19].

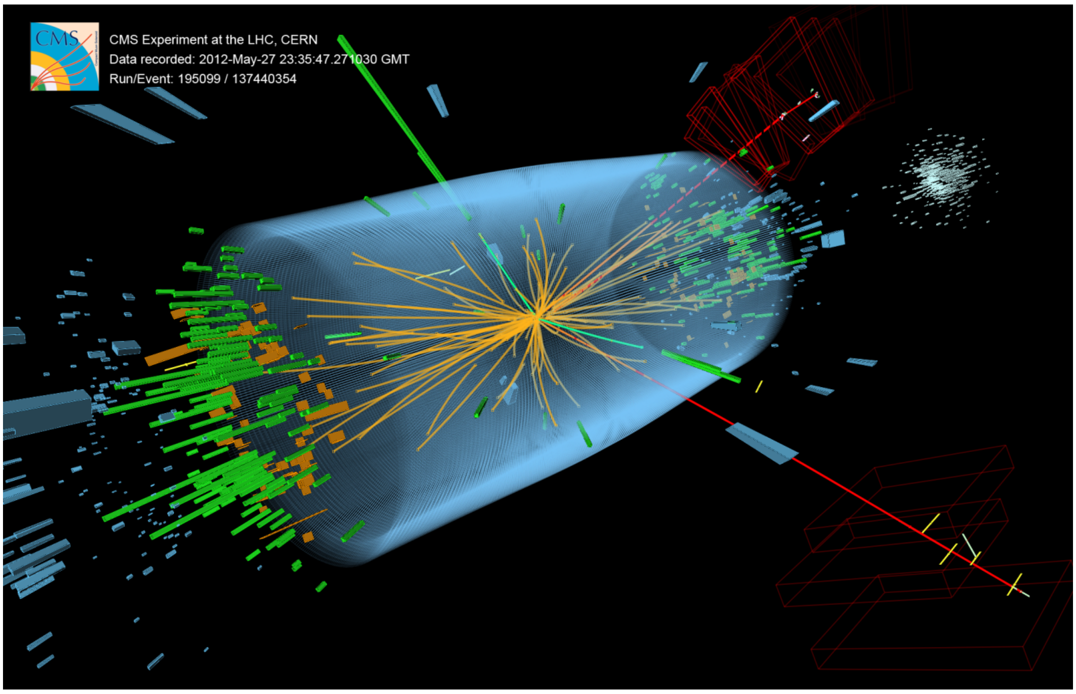
CMS
CMS Experiment at the LHC, CERN
Data recorded: 2012-May-27 23:35:47.271030 GMT
Run/Event: 195099 / 137440354

Figure 2.2.: Visualisation of a Higgs-like event in CMS. The Higgs boson decayed to two Z bosons and further in an electron (green lines) and a muon pair (red lines) [MT12].

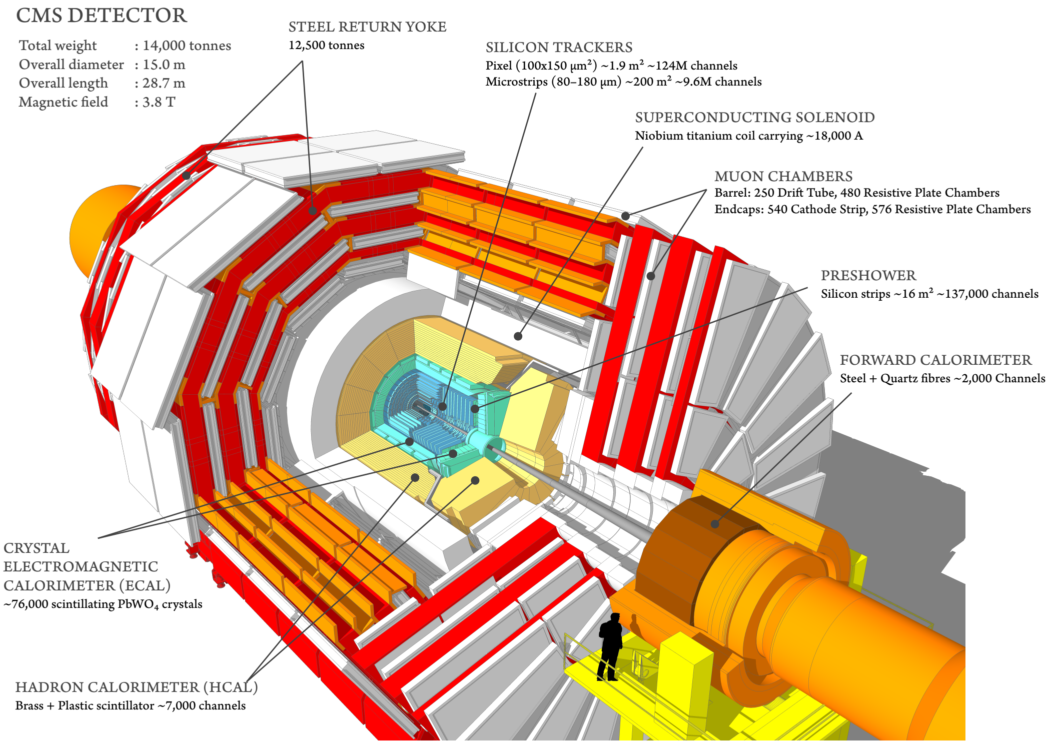
CMS DETECTOR
Total weight : 14,000 tonnes
Overall diameter : 15.0 m
Overall length : 28.7 m
Magnetic field : 3.8 T
STEEL RETURN YOKE
12,500 tonnes
SILICON TRACKERS
Pixel (100x150 μm²) ~1.9 m² ~124M channels
Microstrips (80–180 μm) ~200 m² ~9.6M channels
SUPERCONDUCTING SOLENOID
Niobium titanium coil carrying ~18,000 A
MUON CHAMBERS
Barrel: 250 Drift Tube, 480 Resistive Plate Chambers
Endcaps: 540 Cathode Strip, 576 Resistive Plate Chambers
PRESHOWER
Silicon strips ~16 m² ~137,000 channels
FORWARD CALORIMETER
Steel + Quartz fibres ~2,000 Channels
CRYSTAL ELECTROMAGNETIC CALORIMETER (ECAL)
~76,000 scintillating PbWO₄ crystals
HADRON CALORIMETER (HCAL)
Brass + Plastic scintillator ~7,000 channels

Figure 2.3.: Illustration of the Compact Muon Solenoid (CMS) detector. From inside to outside: Tracker (blue), ECAL crystals (light blue), HCAL (yellow), Solenoid (white barrel), Muon chambers (white) with iron yoke plates (red) [Sak19].

2.2. The Compact Muon Solenoid (CMS) Experiment

The CMS detector complex is one of the main experiments at the LHC. A schematic view of the detector with its various components is illustrated in fig. 2.3. The main detector components are - from inside to outside - a silicon tracker, an electromagnetic calorimeter, a hadronic calorimeter, solenoid and the muon chambers. With the combination of these sub-detectors it is possible to identify particles originating from the collisions.

The particle identification with the detector systems in the CMS detector is illustrated in fig. 2.4. Different particle types are discriminated by their signature in the detector systems. First, a tracking system indicates the trajectories of charged particles. The CMS detector houses a powerful superconducting magnet that delivers a magnetic field of up to 3.8 T. With the knowledge of the bending of the trajectories inside the magnetic field the charge sign and momentum can be determined. Next, in the electromagnetic calorimeter, an electromagnetic shower builds up if the incoming particle is an electron or a photon. In order to detect hadrons more stopping mass is required, which is achieved by a specific hadronic calorimeter. Similar to the electromagnetic calorimeter, a shower builds up. It is possible to determine the energy of the incident particles by summing up the deposited energy of the secondary particles inside the calorimeter. A muon chamber system is installed in the outermost layers, since muons in the relevant momentum range are MIPs (minimal ionising particles) which can cross all detectors with minimum energy loss. Outside of the magnet, the magnetic field is held in shape by a massive iron yoke. Some more technical details concerning the sub-detector systems are given in the following:

- **Tracker:** The tracker is placed inside the solenoid whose magnetic field sufficiently bends the particles even with high transverse momentum. It consists of thin silicon strip and pixel detectors which have a position resolution of 10 µm. In addition, these sensors are lightweight in order to cause as little scattering as possible, so that the energy measurement in the outer regions stays reliable. Since it is the innermost detector layer of CMS, the sensors and also the electronics have to cope with the highest particle densities and also harshest radiation environment [CERf].

- **ECAL:** The electromagnetic calorimeter (ECAL) consists of lead tungstate crystals. These crystals are massive enough to absorb the energy of leptons and at the same time serve as scintillators. Hence, the energy can be determined by measuring the emerged light with photon detectors, glued onto the crystal layers [CERb].

- **HCAL:** The hadronic calorimeter (HCAL) is a sandwich structure of an absorber material, which consists of brass or steel, and plastic scintillator plates. Traversing hadrons interact with some of the first layers leading to a hadronic shower. In order to induce such a hadronic shower, a massive absorber material is required, which stops incident particles. When secondary particles traverse the scintillator layers, light pulses are emitted and detected similar to the ECAL. These are then used to determine the energy of the incident hadron [CERc].

- **Muon chambers:** Since muons are MIPs they are able to traverse the superconducting solenoid and the other detector subsystems. Therefore, it is possible to determine the muons' momenta also outside of the solenoid. In the case of CMS, there are in total nearly 2000 muon chambers arranged alternately with iron plates as indicated in red in fig. 2.4. This iron return yoke leads to a magnetic field of 2 T, roughly. A muon generates a track in the tracker that is matched with the trajectory from the muon chambers. Hence, it is possible to determine the momentum of muons by the trajectory bending in both sub-detector systems [CERa].

2.3. The Integrated Luminosity

The main goal of accelerator experiments in fundamental particle physics is to discover new particles and to provide high-precision information about their interaction properties. In order to produce heavy particles, a high collision energy is required. However, a statistical relevance is of equal importance. Since the particle interactions are probabilistic processes, the statistical significance increases with a large collision number. The *luminosity* $\mathcal{L}$ is determined by the number of collisions per time $\frac{\mathrm{d}N}{\mathrm{d}t}$ and the interaction cross section σ_p:

$$\frac{\mathrm{d}N}{\mathrm{d}t} = \mathcal{L} \cdot \sigma_p. \tag{2.1}$$

For two colliding beams with a density that equally is Gaussian distributed in space, it holds

$$\mathcal{L} = \frac{N_1 N_2 f N_b}{4\pi\sigma_x\sigma_y}, \tag{2.2}$$

where the number of particles per bunch is represented by N_1 and N_2, the circulation frequency by f, the number of bunches by N_b and the cross sections of the beam in x and y-direction perpendicular to the beam axis by σ_x and σ_y. In order to describe the potential of discoveries for a certain experiment, the *time integrated luminosity* is used. It is a measure of the amount of data and directly related to the number of events, thus to statistical significance:

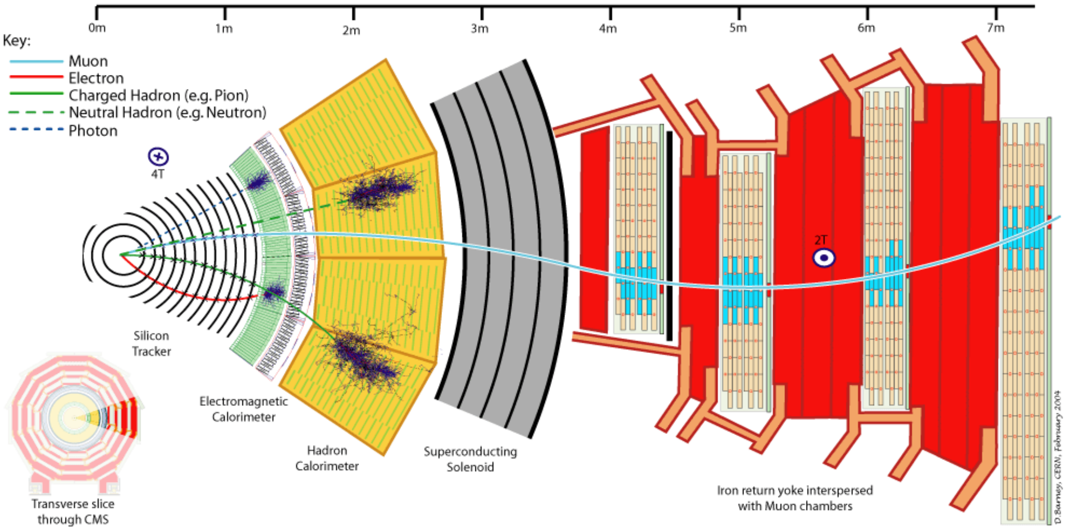
0m
1m
2m
3m
4m
5m
6m
7m
Key:
Muon
Electron
Charged Hadron (e.g. Pion)
Neutral Hadron (e.g. Neutron)
Photon
4T
2T
Silicon Tracker
Electromagnetic Calorimeter
Hadron Calorimeter
Superconducting Solenoid
Iron return yoke interspersed with Muon chambers
Transverse slice through CMS
D.Barney, CERN, February 2004

Figure 2.4.: Slice of the CMS detector with exemplary particle trajectories. A tracking system provides information about charged particles trajectories. Outwards, the energy is measured in the electromagnetic and hadronic calorimeter. Muons are usually measured in the outermost region since they are MIPs traversing most of the material with negligible energy loss [Dav16].

$$\mathcal{L}_{\text{int}} = \int_0^T \mathcal{L}(t')dt' \tag{2.3}$$

$$N = \mathcal{L}_{\text{int}} \cdot \sigma_p \tag{2.4}$$

where T represents the runtime of the experiment. The integrated luminosity is usually expressed in units of inverse femtobarns (fb^{-1} with $1\,\text{b} = 10^{-28}\,\text{m}^2$) because of the small cross section and high interaction rates.

2.4. The High-Luminosity Upgrade of the LHC

The LHC has been improved continuously after the start of its operation in 2009. During the first running period from 2010 to 2012, called Run 1, the centre-of-mass energy $\sqrt{s}$ has been increased from 7 TeV to 8 TeV. At the same time, the instantaneous luminosity has been ramped up from $2.1 \times 10^{32}\,\text{cm}^{-2}\,\text{s}^{-1}$ to $7.7 \times 10^{33}\,\text{cm}^{-2}\,\text{s}^{-1}$. Run 1 was followed by a so-called Long Shutdown 1 (LS1) of two years where several upgrades of the accelerator but also of the detectors have been performed. The next Run 2 started in 2015 with an increased centre-of-mass energy of 13 TeV and instantaneous luminosity of $1.5 \times 10^{34}\,\text{cm}^{-2}\,\text{s}^{-1}$, which actually exceeded the design value of $1.0 \times 10^{34}\,\text{cm}^{-2}\,\text{s}^{-1}$. Since 2018 the LHC is in the second Long Shutdown (LS 2). The integrated luminosity[1] up to now from the beginning is $189\,\text{fb}^{-1}$, which exceeds the targeted luminosity of $160\,\text{fb}^{-1}$ by 10%. Before the next run will be started, specific upgrades of the LHC injector complex are performed. After the following Run 3 the expected collected integrated luminosity is $300\,\text{fb}^{-1}$. It is planned that after this run a more intense long shutdown will take place in which the LHC will be upgraded significantly, entering a phase which is referred to as high-luminosity phase. Here, the instantaneous luminosity will be increased to $5 \times 10^{34}\,\mathrm{cm^{-2}\,s^{-1}}$ with the possibility to go to $7.5 \times 10^{34}\,\mathrm{cm^{-2}\,s^{-1}}$ in an ultimate scenario. This is five to seven times higher than the design luminosity. Because of this significant improvement the name LHC is augmented to HL-LHC (High Luminosity LHC). To ensure an optimal performance of the detectors but also to protect the near-interaction magnets, the instantaneous luminosity should be constant in time. Without any measures, the luminosity will decay rapidly after a fill. Therefore, in the beginning, a high interaction rate leads to a large pile-up in the detector but also high energy deposit in the magnets close to the interaction point. Hence, the magnets' ageing would be accelerated. To prevent this, luminosity levelling mechanisms will be implemented that lead to constant instantaneous luminosities. The integrated luminosity will increase to $300\,\mathrm{fb^{-1}}$ per year which is similar to the integrated luminosity of the LHC during its whole runtime including the next run after LS2. With a foreseen runtime of at least ten years the HL-LHC will collect an integrated luminosity of $3000\,\mathrm{fb^{-1}}$ or even $4000\,\mathrm{fb^{-1}}$ with the ultimate performance [CMS18][CERd]. This will enable a significantly higher discovery potential for new physics. Further information regarding the upgrade measures of the HL-LHC can be found in [CERe].

---

[1] regarding the ATLAS and CMS proton run

2.5. The Phase-2 Upgrade of the CMS Outer Tracker

2.5.1. Requirements for the High Luminosity Phase

In order to cope with the new requirements of the HL-LHC the detector systems will be upgraded. The upgrade of the CMS detector is referred to as CMS Phase-2 Upgrade. Besides several improvements, the silicon tracker of the CMS experiment will be replaced entirely. The new tracker will consist of an inner part and and outer part referred to as Inner Tracker (IT) and Outer Tracker (OT). The requirements of the new tracker are briefly covered in the following.

- **Radiation damage**: The increased luminosity results in the fact that the detectors have to withstand a significantly higher level of radiation. In particular the Outer Tracker has to be efficiently operable up to the full total integrated luminosity of $3000\,\mathrm{fb^{-1}}$. This has to be achieved without accessing the detector over the foreseen runtime of 10 years because no hardware maintenance will be possible. The Inner Tracker has to withstand even harsher radiation environments because it is closer to the beampipe. However, similar to the current situation of the CMS detector it will be possible to exchange parts or even the full Inner Tracker.

- **Increased granularity:** Since the increased instantaneous luminosity of the HL-LHC is partially achieved by a stronger focus of the beam, the *pile-up*, which is the number of collisions per bunch crossing, will be increased to 140 or even 200 in the ultimate performance scenario. Hence, the granularity of the detectors has to be enhanced to distinguish the tracks inside the detector. In order to cope with the increased bandwidth and to speed up the data acquisition the readout of the signal will be changed from analogue to binary information in Phase-2. Therefore, the information about the signal height does not need to be processed anymore but just the information of a particle hit in a particular readout channel.

- **Contribution to the Level-1 Trigger:** The CMS trigger is composed of a first level hardware trigger (L1) and a high-level trigger (HLT) with an approximately 100 times slower trigger rate. Because of the increased event rate, the trigger rate would increase as well. In order to keep the trigger rate at a feasible level, less interesting physics events have to be discriminated at a very early stage. Hence, the CMS community has decided

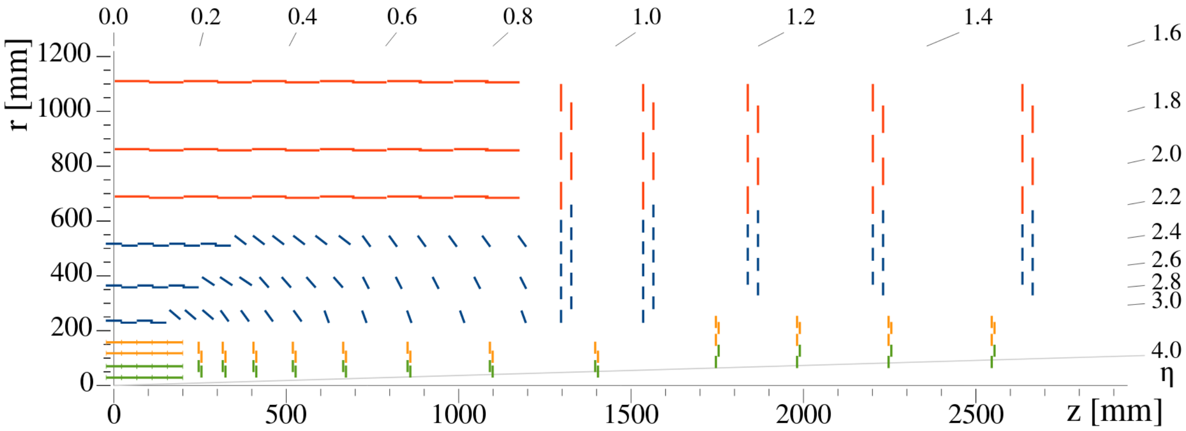

Figure 2.5.: Schematic design of a quarter of the new CMS tracker in Phase-2. Inner Tracker pixel modules close to the beam pipe ($r = 0\,\mathrm{mm}$) are indicated in orange and green. Outer Tracker modules incorporating a macro pixel and a strip sensor (PS) are indicated in blue and modules housing two strip sensors in red (2S) [CMS18].

to add information about tracks with high transverse momentum to the L1 trigger. This is achieved by a new module concept, referred to as p_T-modules. The concept of the modules is explained in more detail in section 2.5.2.

2.5.2. Tracker Design and Outer Tracker Module Concept

A sketch of the new Outer Tracker design is shown in fig. 2.5. It can be seen that the tracker is divided in Inner Tracker (green and orange lines) and Outer Tracker (blue and red lines) regions. Each line represents a detector module, which incorporates silicon sensors, read-out chips and mechanical and electrical support. One new feature is that the Outer Tracker PS modules in the barrel region with $\eta > 0.4$ will be tilted so that they are facing towards the interaction point (at $r = 0$ and $z = 0$). This results in a similar angular coverage with less material. As shown on the right y-axis, the pseudorapidity η coverage is increased to $|\eta| = 4.0$ (from $|\eta < 2.5|$ of the old tracker).

For the Outer Tracker there are two different types of detector modules, the 2S modules (red in fig. 2.5) incorporating two strip sensors back-to-back with 5 cm long strips and the PS modules (blue in fig. 2.5) housing a macro-pixel and a strip sensor back-to-back (blue). The module design of the 2S modules is shown on the left side of fig. 2.6 as an exploded view and assembled (with dimensions) in the frame. Similarly the PS module design can be seen on the right side of fig. 2.6.

A main design feature of the 2S and PS module is the possibility to discriminate low transverse momentum (p_T) particles on the module level. This is the reason why they are also referred to as the p_T-modules. How the low transverse momenta can effectively be filtered out is illustrated in fig. 2.7. The figure shows the two back-to-back sensors inside a module where the strips are aligned in parallel. Here, every bin represents a strip perpendicular to the paper level with a pitch of 90 µm (2S) or 100 µm (PS). The spacing is between 1.6 or 4 mm dependent on the position in the tracker and module type. Since the magnetic field lines are pointing out of the paper level, the trajectory of a positively charged particle, for example a pion, is bent to the right due to the Lorentz force. The radius R of the trajectory depends on the transverse

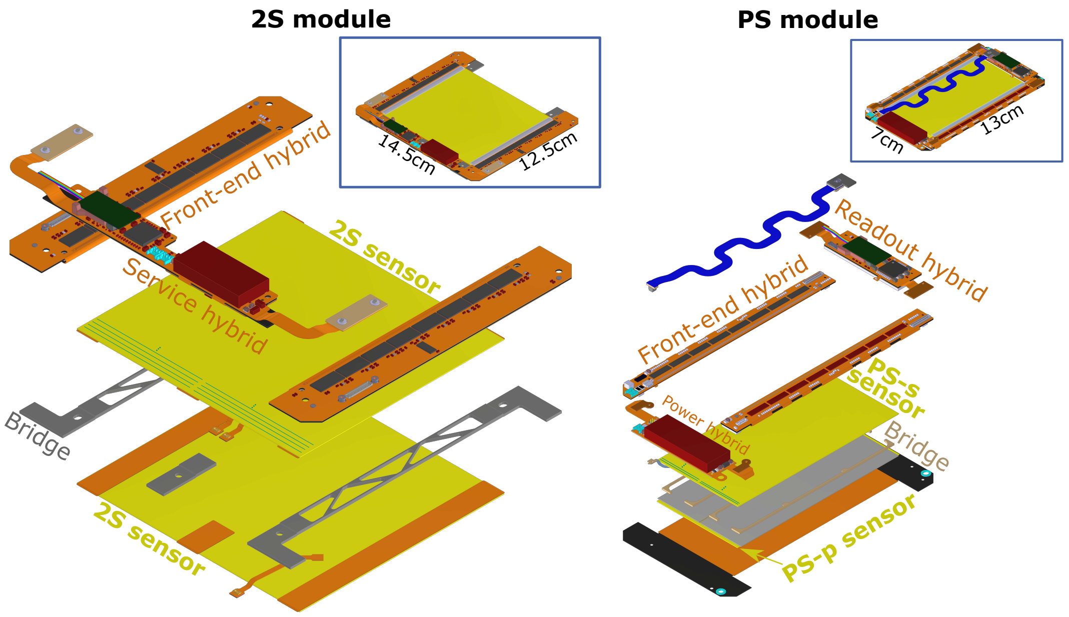

Figure 2.6.: Outer Tracker module design as an exploded view on the bottom and assembled module in the frame. The 2S module housing two strip sensors is shown on the left side and the PS module with a strip and a macro-pixel sensor on the right side. The figure is modified from [CMS18].

momentum p_T of the particle

$$p_T \left[\frac{\text{GeV}}{\text{c}}\right] = 0.3 \cdot B[\text{T}] \cdot R[\text{m}] \tag{2.5}$$

with the magnetic flux B. With a detected hit (yellow) in the lower detector layer it is possible to define a programmable search window of, for example, three strips. If a second hit can be identified within this search window, a so-called *stub* is read out as indicated in blue on the left side in fig. 2.7. In case the transverse momentum of the incident particle is low, the trajectory will be bent stronger, resulting in a hit in the second layer which is outside of the search window. Hence, it is possible to discriminate low p_T particles on the module level by defining the width of the search window. For the CMS detector it is planned to accept stubs that have a $p_T > 2\,\text{GeV}\,\text{c}^{-1}$. The hint to a high-energetic particle from the module level is used in a fast track finder system to identify the particle trajectories in the tracker. These tracks are then used for the L1 trigger.

2.5.3. Radiation Environment and Outer Tracker Sensors

After an intensive development phase and review process the approved sensor types are now in production and the module production will start in 2022. During the sensor production a continuous quality assurance takes place besides the quality control of the vendor. It is divided into three main tasks. The process quality control (PQC) validates the process quality of the wafer processing with dedicated test structures. The sensor quality control (SQC) features an optical and electrical inspection of the full-sized sensors and ensures the expected electrical performance. Additional irradiation tests (ITs) are performed in order to ensure the reliability of the sensors' performance evolution in the radiation environment. These tests are one of the main topics of this thesis and discussed in detail in chapter 7.

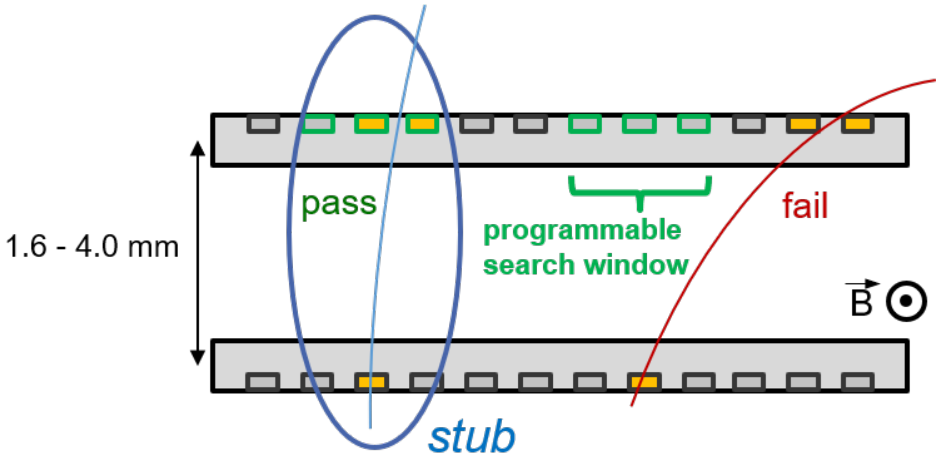

Figure 2.7.: Schematic illustration of the p_T-module concept. The sensors are located back-to-back in the module such that strips align with each other. If a hit is detected in the lower and the upper layer, a high p_T particle can be identified if the upper hit is located in a previously defined search window. Otherwise, if the incident particle has low p_T, the curve will be bent stronger and therefore it will generate a hit outside of the search window in the second layer [Ada+20].

The expected radiation environment in Phase-2 can be estimated with the FLUKA simulation tool [Fer+05][Böh+14]. In the simulation, single events are generated by a primary event of, for example, two colliding particles as it is the case for proton-proton collisions at the LHC. It uses the Monte Carlo method to generate secondary particles from the collision. Then, these particles are transported through the detector material where they react further. The physics models like interaction cross sections are based on parametrisations or entries in tables to keep a reasonable simulation time. When all particles are destroyed or their energy falls below pre-defined thresholds, the simulated event is finished. The process of generating primary events with secondary particles and transportation through the materials is performed several times. The output is then an averaged value over all these events.

The FLUKA simulation tool incorporates the opportunity to directly extract the NIEL in silicon (non-ionising energy loss; compare section 4.1.1) that is caused by nuclear interactions and the TID (total ionising dose). This feature has been used to estimate the total fluence that the detector systems of CMS have to cope with for the expected integrated luminosities. A map of the expected fluence distribution in the tracker is illustrated in fig. 2.8 considering a total integrated luminosity of $3000\,\mathrm{fb}^{-1}$ in Phase-2. The fluences are in a range from $1 \times 10^{14}\,\mathrm{n_{eq}/cm^2}$ to $1 \times 10^{15}\,\mathrm{n_{eq}/cm^2}$ for the Outer Tracker region. This results in severe bulk damage that leads to increased leakage currents and decreased signal strength. Detailed information about the radiation damage in silicon sensors is given in chapter 4.

The corresponding expected TID is visualised in fig. 2.9 and reaches values of 1 MGy in the innermost Outer Tracker region. These TID estimations are relevant for surface properties of the sensor and functionality of the readout electronics. There can be single event failures when an ionising particles switches an electronic state in the readout chip, but also irreversible damage by charge built-up in isolator regions of the readout chip or sensor surface.

The charged particle fraction of the fluence is mainly varying with the radius of the detector, as illustrated in fig. 2.10. These particle fractions are again gained from simulations with FLUKA. Since pions are the particles which are most likely produced in proton-proton collision, their fraction dominates in the region close to the beam pipe (small radii). On the other

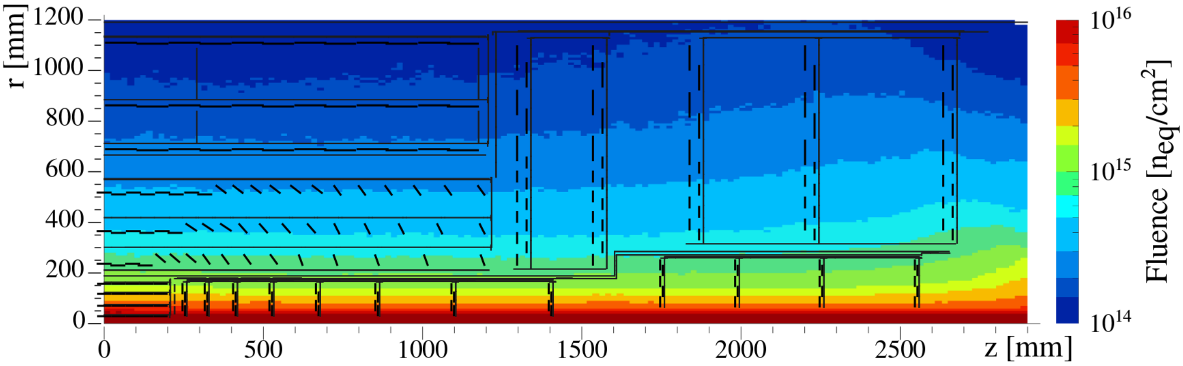

Figure 2.8.: Expected fluence distribution of the CMS tracker in Phase-2 after the expected runtime of 10 years according to FLUKA simulations [CMS18].

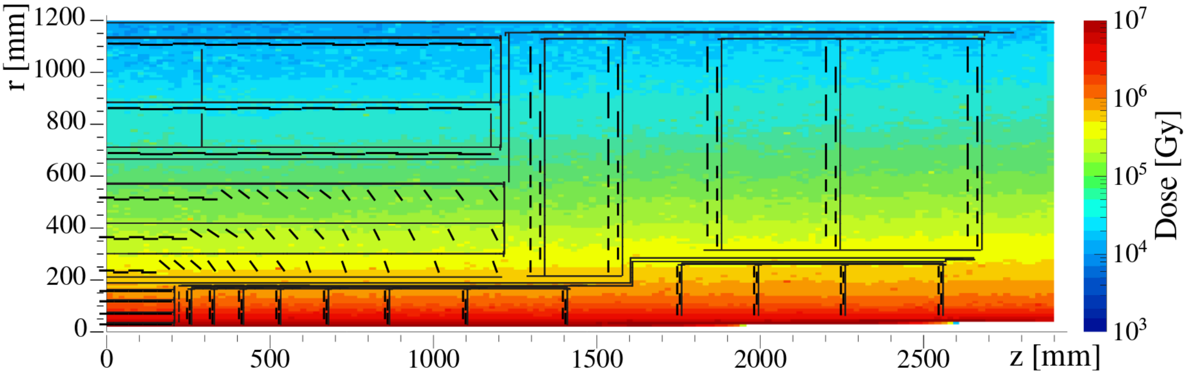

Figure 2.9.: Deposited ionising dose after the expected runtime of 10 years according to FLUKA simulations [CMS18].

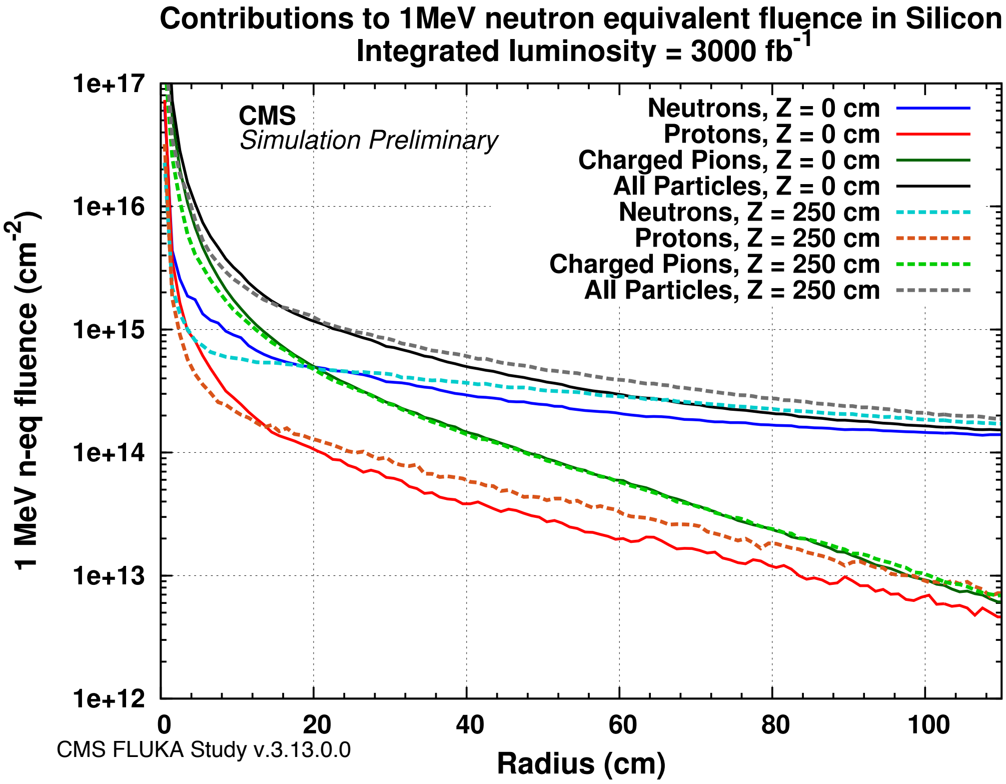

Figure 2.10.: Expected particle fraction in the CMS tracker in Phase-2 dependent on the radius. The charged particle fraction is dominant for low radii but decreases towards the outer regions where neutrons are the most significant fraction of particles [Gut15] .

hand, they decay or interact rapidly while traversing the detectors and the neutron fraction becomes dominant at higher radii. This effect is amplified by backscattered neutrons from the calorimeters, which increases the neutron fraction further.

3

Basic Properties of Silicon Sensors

The essence of silicon sensors as charged particle detectors are the properties of the base material. Silicon is a semiconducting material that can be found in abundance. Hence, it is rather cheap and widely used in industry, from which high energy particle physics can benefit. Because of the availability of experienced manufactures all over the world, it is possible to manufacture silicon sensors in mass productions. The fundamentals of the material silicon and of silicon as a sensor are explained in the following.

3.1. The Band Model

The electrical conductivity of solids can be understood with the *band model*. The following explanations and derivations follow [Kit13]. The wave function $\Psi_{\vec{k}}(\vec{r})$ of an electron inside a periodic crystal lattice can be described by

$$\Psi_{\vec{k}}(\vec{r}) = \exp(i\vec{k} \cdot \vec{r}) \cdot u_{\mathrm{n}}(\vec{r}), \tag{3.1}$$

with the wave vector $\vec{k}$ and a modulation $u_{\mathrm{n}}(\vec{r})$ that incorporates the periodicity of the lattice. Such a *Bloch function* is only unique up to a constant reciprocal lattice vector $\vec{G}$. Hence, in solid state physics, it is sufficient to describe the physics in the first *Brillouin zone*. The Brillouin zone is the equivalent of the Wigner-Seitz cell, which is the primitive cell of the crystal, but in reciprocal space. The Bragg condition for scattering at the crystal lattice holds

$$(\vec{k} + \vec{G})^2 = k^2. \tag{3.2}$$

This can be simplified in a 1-dimensional space to

$$k = \pm\frac{1}{2}G = \pm n\pi/a, \tag{3.3}$$

with $G = 2\pi n/a$ and an integer n. The region between $k = \pm\pi/a$ is the first Brillouin zone. Since the Bragg condition of $k = \pm\pi/a$ is fulfilled at the borders of the Brillouin zone, the electron waves are back-scattered there. Hence, a standing wave builds up with the solutions

$$\Psi(+) = \exp(i\pi x/a) + \exp(-i\pi x/a) = 2\cos(\pi x/a) \tag{3.4}$$

$$\Psi(-) = \exp(i\pi x/a) - \exp(-i\pi x/a) = 2i\sin(\pi x/a). \tag{3.5}$$

The sign $(+)$ or $(-)$ indicates whether the wave function changes its sign under sign inversion of x to $-x$. The probability density of a wave function is defined as the absolute value squared $\rho = \Psi^*\Psi = |\Psi|^2$. Calculating the probability density functions of electrons, developing standing waves yields

$$\rho(+) \propto \cos^2(\pi x/a) \tag{3.6}$$

$$\rho(-) \propto \sin^2(\pi x/a). \tag{3.7}$$

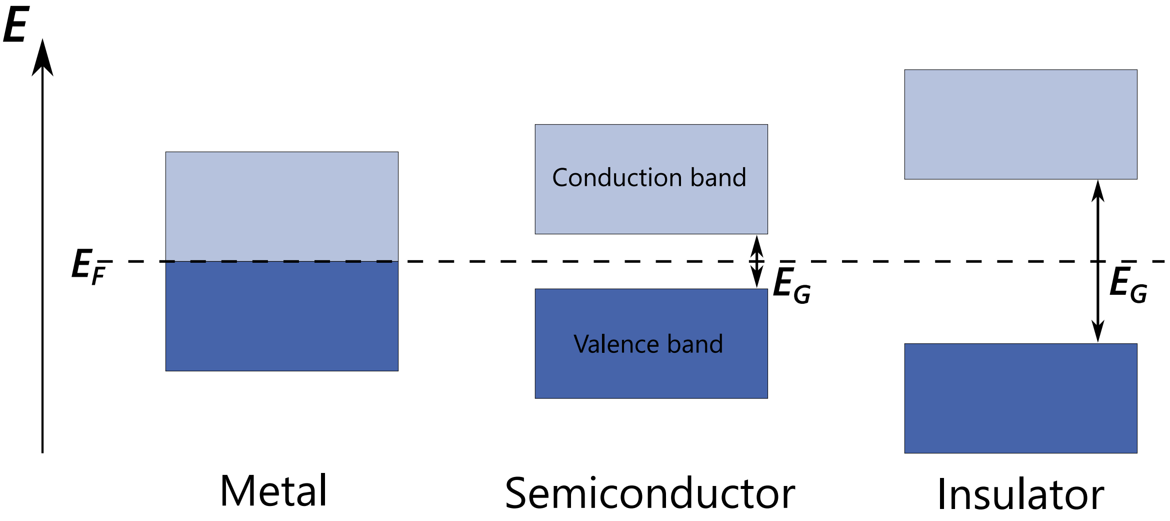

Figure 3.1.: The band scheme of different materials. For metals, the valence and conduction band overlap. In case of semiconductors, a small band gap arises, separating valence and conduction band. If the band gap is even wider, the material is classified as an insulator.

Hence, the formation of standing waves results in a charge accumulation in specific places. The $\Psi(+)$ wave function accumulates electrons at $x = 0, a, 2a, ...$, thus at the positive remnant ions of the lattice. On the other hand, $\Psi(-)$ accumulates electrons exactly between the atomic bodies. Because of the attractive potential due to the positive ions, the energy of $\rho(+)$ is smaller than the energy of free electrons and also than $\rho(-)$. Since $\rho(-)$ accumulates electrons far from the ions, the potential energy is higher than for free electrons and $\rho(+)$. The difference in the energy of $\rho(+)$ and $\rho(-)$ is labelled as E_G, the energy gap or *band gap*. This motivates the occurrence of distinct energy bands and the band gap. However, the band structure of a real crystal is much more complex and its derivation is beyond the scope of this thesis.

With the band model scheme and the knowledge of occuring energy band gaps, a classification of crystal materials can be performed. These three material classes are illustrated in fig. 3.1. The valence band is the band with the highest energy that is fully occupied by electrons. The conduction band is the band that is energetically above the valence band. In case of metals, both bands overlap or the band gap is smaller than 1 eV so that electrons can occupy the conduction band. The Fermi energy E_F denotes the energy level at which the occupation probability is $1/2$ with a temperature at absolute zero $T = 0\,\mathrm{K}$. It is usually located in the middle of the band gap. At a finite temperature, some electrons can access the conduction band, where they are mobile, leading to a high electric conductivity. For semiconductors the band gap is between 1 eV and 4 eV. However, borders are not sharply defined. The energy gap is big enough that the semiconductor is not conductive at low temperatures, but becomes conductive at higher temperatures. Its properties can be altered by doping as explained in the next section. In case of insulators, the energy gap is so wide that the conduction band is empty. Hence, due to the lack of free charge carriers, the material cannot contribute to any electric current flow.

3.2. Doping of Silicon

In general, impurities in a material are not desired, especially for pure high precision devices. They can lead to significant changes in the crystal structure and therefore change the behaviour

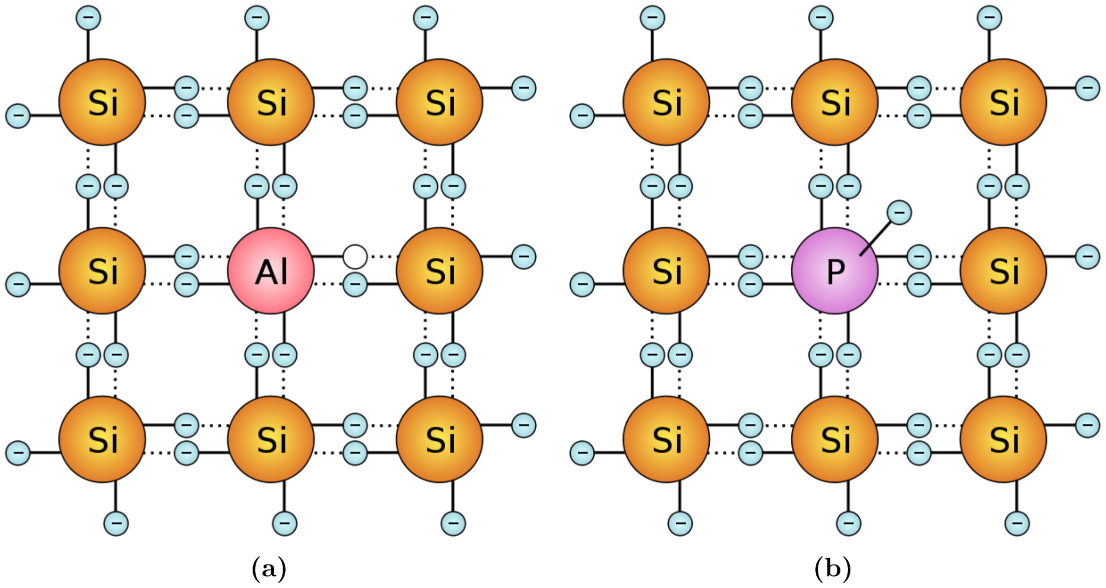

Figure 3.2.: Schematic visualisation of dopants in a silicon crystal lattice. Doping with aluminium (left) results in a vacant electron position, also referred to as hole. If phosphorus is present in the crystal (right), an additional weakly bound electron is introduced into the lattice. Both charge carriers, electrons and holes are contributing to the conductivity of the material [Hen06a][Hen06b].

of the silicon device. On the other hand, if impurities are inserted in a controlled way, the change of the macroscopic behaviour might be desirable. Introducing foreign atoms on purpose inside the silicon is referred to as *doping*. The two doping types are illustrated in fig. 3.2. Introducing an element of the third main group is called *p-doping*. This is illustrated in fig. 3.2a for aluminium. Due to the lack of an electron, a crystal bond is missing. This is referred to as a hole. Contrary, for *n-doping* an element of the fifth main group, thus an additional electron is introduced as visualised in fig. 3.2b for phosphorus. This is weakly bound since it is not contributing to the required crystal bonds of the silicon main lattice. Both free charge carrier types, holes and electrons, contribute to the conductivity of the material. Thus, doping can be used to alter the electrical properties of silicon. How dopants can be described by states inside the band gap of silicon is described further together with radiation induced states in chapter 4.

3.3. Manufacturing of Silicon Structures

This section briefly introduces the manufacturing and processing of silicon wafers. Silicon as base material is rather cheap, since it is present in abundance as SiO_2 in quartz sand. Especially, if the cost of the following processing steps are taken into account, the price of the raw material can be neglected.

First of all, the silicon oxide needs to be reduced to elemental silicon. That is usually done with carbon, which reacts in a strongly endothermic reaction with silicon oxide to carbon monoxide and silicon at a temperature of 2100 °C.

$$\mathrm{SiO_2\ (s) + 2\ C\ (s) \rightarrow Si\ (s) + 2\ CO\ (g)}. \tag{3.8}$$

However, the yielded raw material is contaminated with roughly 2% of other elements like iron, aluminium, calcium or magnesium. For detector grade silicon, the material needs to be purified significantly to 1/100 ppba[1]. This purification is done with the help of hydrogen chloride gas that reacts with silicon at 600°C to trichlorosilane

$$\mathrm{Si\ (s) + 3\ HCl\ (g) \rightarrow H_2\ (g) + HSiCl_3\ (g)}. \tag{3.9}$$

The crucial point of the purification is the boiling temperature of trichlorosilane. Because it is only 31°C, trichlorosilane can be very efficiently separated via destillation from impurities. The distilled trichlorosilane is then brought into contact to hydrogen so that the reaction eq. (3.9) is reversed. This reaction takes place at 1100°C hot silicon rods so that the elemental silicon deposition leads to an enlargement of the rods. Hence, pure high grade polycrystalline silicon rods are the outcome of this chemical purification process.

The next step is to produce a silicon ingot that is a large $(1-2\,\mathrm{m})$ single crystal. Two of the main techniques are illustrated in fig. 3.3. On the left side, the *float zone* (FZ) method is visualised. The initial material is the polycrystalline silicon rod which is in contact with a single crystal seed. The rod is locally heated up with an RF[2] heater, which leads to a locally bounded melting. Since impurities tend to stay inside the liquid due to the different diffusion constant, they can be effectively pulled out by slightly moving the RF heater up. When the melted silicon crystallises a pure single crystal ingot is produced. The material doping can be achieved by gas diffusion. Additionally, since it turned out that oxygen enriched material is more radiation hard in some scenarios, materials are sometimes oxygenated via diffusion. This material is then referred to as *Diffusion Oxygenated Float Zone* (DOFZ).

The *Czochralski* (Cz) technique is another possibility to produce a high grade doped single crystal. The method is indicated on the right side in fig. 3.3. First, silicon is melted and dopants are added into the melt. These could be for example phosphorus or aluminium for n-type or p-type doping of the base material, respectively. Afterwards, the single crystal is grown by pulling a seed slowly out of the melt while rotating. If the inert gas contains oxygen, it is diffusing into the silicon in the meantime, leading to an oxygen enriched material. An advanced Czochralski method is to grow the crystal within a magnetic field. Therefore, it is also referred to as *magnetic Czochralski* (mCz) method. This procedure leads to a more homogeneous distribution of the dopants inside the ingot.

After a purely doped single crystal is achieved, the ingot is diced into small slices, called wafers. The next step is to process this silicon substrate further with *photolithography* to apply a structuring. The method is illustrated in fig. 3.4. First of all, a masking film, which is usually silicon oxide or nitride, is applied on the whole wafer and covered with a layer of photoresist. Afterwards, the structure is illuminated with light (for example ultraviolet light) through a mask. The masks have to be very precise and are therefore the limiting factor and usually very expensive. After some additional steps like baking and development, the uncovered part is etched. Removing the photoresist finally results in a defined layer of the firstly applied material.

3.4. The pn-Junction

If two differently doped (p- and n-type) materials are in electrical contact, a *pn-junction* is obtained. The resulting space charge region is of crucial importance for common semiconductor devices. The mechanism is sketched in fig. 3.5. A p-doped (on the left) and an n-doped material (on the right) are connected to each other. Because the n-doped side has an excess and the p-doped side a lack of electrons, the free electrons start to diffuse into the p-doped region. Vice versa, holes diffuse into the n-doped region. The electrons and holes recombine at the border

---

[1] ppba: parts per billion atomic (impurity atoms per billion silicon atoms)

[2] RF: Radio Frequency

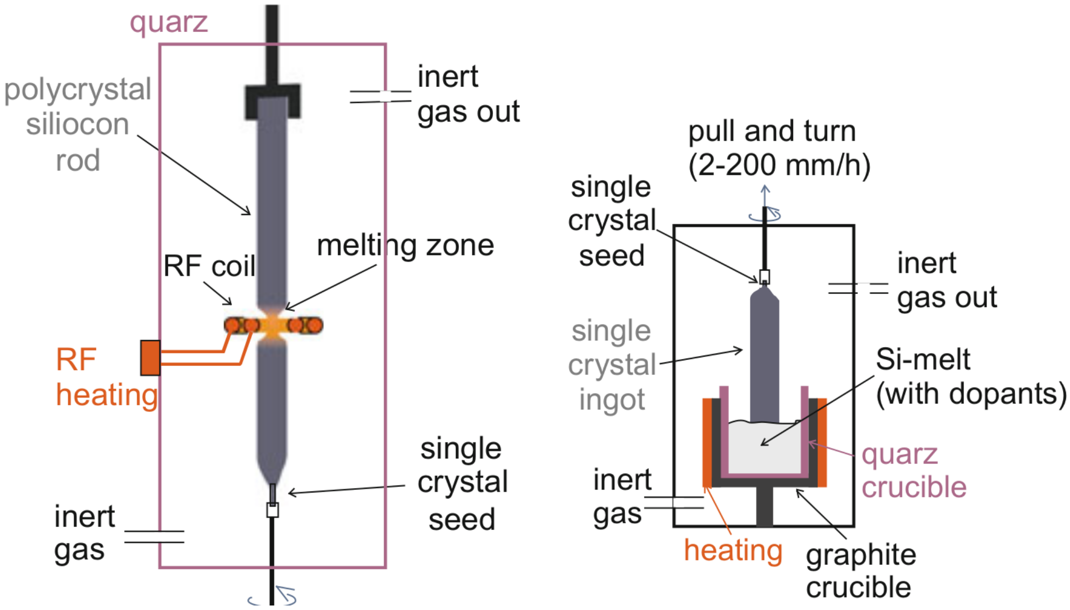
quarz
polycrystal siliocon rod
inert gas out
RF coil
melting zone
RF heating
single crystal seed
inert gas
pull and turn (2-200 mm/h)
single crystal seed
single crystal ingot
inert gas out
Si-melt (with dopants)
quarz crucible
inert gas
heating
graphite crucible

Figure 3.3.: The float zone growth method (left) uses the fact that impurities tend to diffuse into liquid silicon. A polycrystal silicon rod is melted locally while rotating and pulling up the heater. With the connection to a single crystal seed, this results in a pure silicon single crystal. The single crystal is grown directly out of silicon melt with the Czochralski method (right). Here, a single crystal seed is pulled out of the melt while rotating [Har17].

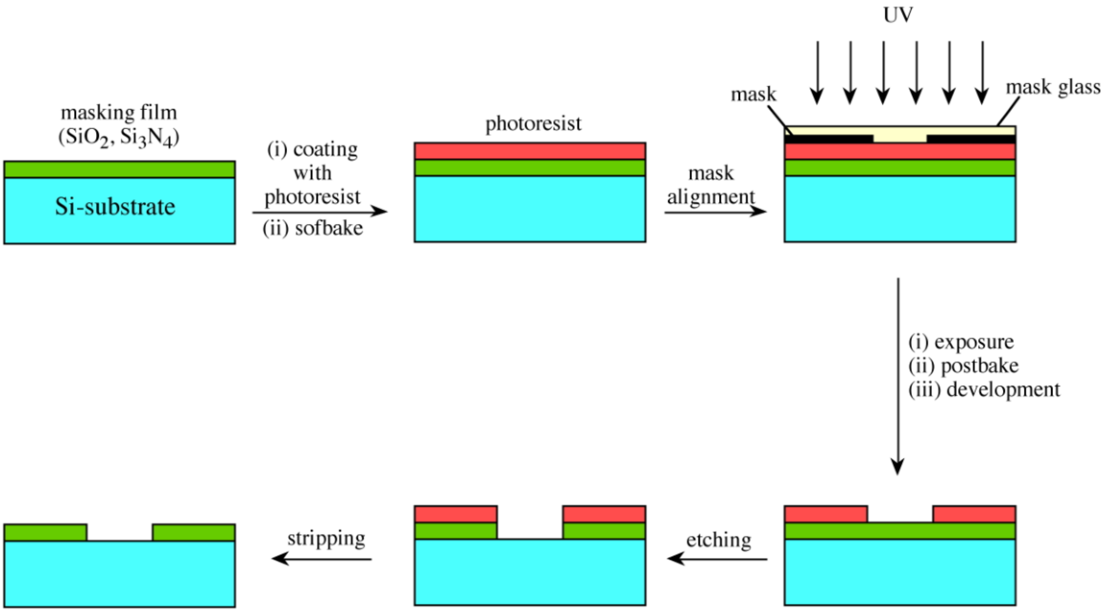
masking film
(SiO$_2$, Si$_3$N$_4$)
Si-substrate
(i) coating with photoresist
(ii) sofbake
photoresist
mask alignment
UV
mask
mask glass
(i) exposure
(ii) postbake
(iii) development
etching
stripping

Figure 3.4.: Schematic illustration of photolithography where a structured layer of a masking film is applied. The masking film is first covered with photoresist, which is removed by the exposure to light. Therefore, a mask can be used to define where it is removed by UV illumination. Afterwards, the opened structure is etched, which results in the desired geometry. Finally, the photoresist is stripped off again [Bar09].

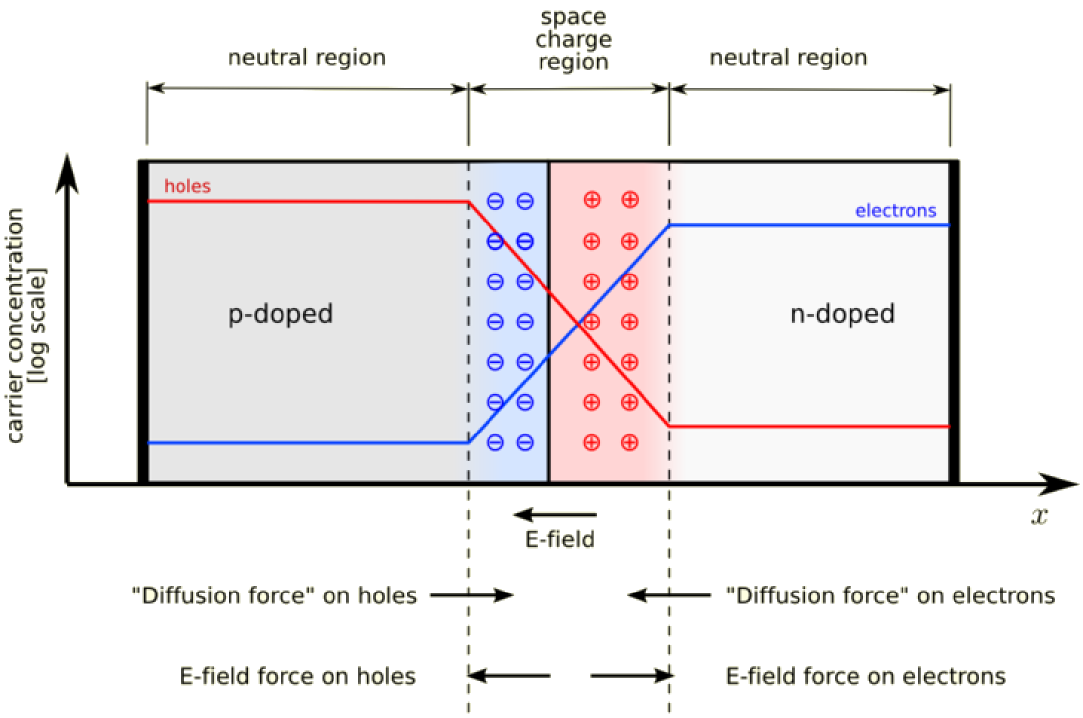
neutral region
space charge region
neutral region
carrier concentration [log scale]
holes
electrons
p-doped
n-doped
x
E-field
"Diffusion force" on holes
"Diffusion force" on electrons
E-field force on holes
E-field force on electrons

Figure 3.5.: The pn-junction in equilibrium. Electrons of the n-doped side and holes of the p-doped side recombine. The net charge of the ionised dopants results in a space charge region. This diffusion stops when the diffusion force is equal to the force of the emerging electric field [The07].

region. Since they were initially compensating the charge of the dopants, the left-over dopant atoms are now globally ionised, which leads to a local fixed charge in this border region. Thus, a *space charge region* is built up between the two layers as indicated in the picture. Since the free charge carriers are recombined inside the space charge region, it is also referred to as *depletion region* (depleted of free charge carriers). This space charge on the other hand generates an electric field counteracting the diffusion force. Therefore, the device is in equilibrium when these two forces are equally strong. The electrostatic potential difference that emerges is called *built-in voltage*.

Applying an external voltage to this pn-junction results in an increase or decrease of the space charge region depending on the polarity. If a positive potential is applied at the p-doped side and a negative potential at the n-doped side, the junction is operated in *forward bias*. The ionised dopants in the space charge region are refilled with charge, thus the space charge region is destroyed and the current can flow through the device. Switching the polarity, with a negative potential applied on the p-doped side and positive potential on the n-doped side, leads to an increase of the depletion layer. Even more electrons recombine with holes and vice versa in the depletion region, thus its width increases. A fully depleted pn-junction is the basis for the functionality of a silicon particle detector.

3.4.1. Electrical Properties of a pn-Junction

In general, the electrostatic properties of the pn-junction can be calculated by solving Poisson's equation

$$\Delta\varphi(\vec{r}) = -\nabla\vec{E}(\vec{r}) = -\frac{1}{\epsilon_0\epsilon_{\mathrm{Si}}}\rho(\vec{r}), \tag{3.10}$$

with the electrostatic potential $\varphi(\vec{r})$, the electric field $\vec{E}(\vec{r})$, the permittivities ϵ_0 and ϵ_{Si} and the charge density $\rho(\vec{r})$. Since, the charge distributions are constant in the respective regions, integrating in x-direction leads to a linear electric field and a parabolic electrostatic potential.

However, since the full calculation is very involved, only the most important results are given here. A more detailed description can be found in [Spi05] and [Har17]. The pn-junction's electrostatic potential difference in the space charge region is given by the doping concentrations. This built-in voltage V_{bi} is given by

$$V_{\mathrm{bi}} = \frac{k_{\mathrm{B}}T}{e}\ln\left(\frac{n_{\mathrm{A}}\cdot n_{\mathrm{D}}}{n_i^2}\right) \tag{3.11}$$

with the Boltzmann constant k_{B}, temperature T, elementary charge e, intrinsic charge carrier density n_i and the ionised acceptor and donor concentrations n_A and n_D. Provided that all acceptor and donor states are ionised, these concentrations translate to the doping concentrations. In case of strip sensors and diodes used within this thesis $n_A \approx 5\times10^{12}\,\mathrm{cm}^{-3}$ and $n_D \approx 1\times10^{19}\,\mathrm{cm}^{-3}$, which yields $V_{\mathrm{bi}} \approx 0.7\,\mathrm{V}$. The width of the space charge region w is given by

$$w = \sqrt{\frac{2\epsilon_0\epsilon_{\mathrm{Si}}}{e}\frac{n_A+n_D}{n_A\cdot n_D}V_{\mathrm{bi}}} = \sqrt{\frac{2\epsilon_0\epsilon_{\mathrm{Si}}}{e}\frac{1}{N_{\mathrm{eff}}}V_{\mathrm{bi}}}. \tag{3.12}$$

If the acceptor and donor concentration are of vastly different magnitude, the effective doping concentration N_{eff} can be replaced by the lower concentration. Since the doping concentrations of the strip implants is six to seven orders of magnitudes higher than the the bulk doping, the middle term is dominated by the bulk doping $N_{\mathrm{eff}} \approx n_A$.

If an external bias voltage is applied, it adds up on top of the built-in voltage. The so-called Schottky approximation of sharp transitions from the undepleted materials to the space charge region is valid if $V_{\mathrm{bi}} - V_{\mathrm{bias}} \gg k_{\mathrm{B}}T$ so that eq. (3.12) simply extends to

$$w = \sqrt{\frac{2\epsilon_0\epsilon_{\mathrm{Si}}}{e}\frac{1}{N_{\mathrm{eff}}}|V_{\mathrm{bi}} - V_{\mathrm{bias}}|}. \tag{3.13}$$

Since the sensors are always biased in reverse bias, the sign of the external voltage is negative so that the left side of the Schottky condition is greater than $k_{\mathrm{B}}T$. Thus, the condition is always true and eq. (3.13) is valid in the scope of this work. The external bias voltage during operation is typically above 300 V so that the built-in voltage can be neglected. From the equation it can be seen that the width of the pn-junction is increasing with the square root of the external voltage. However, w is limited by the thickness of the device. In case of full depletion, where the whole pn-junction with a thickness D is depleted, the equation eq. (3.13) can be transposed to

$$V_{\mathrm{fd}} = \frac{e}{2\epsilon_0\epsilon_{\mathrm{Si}}}N_{\mathrm{eff}}\,D^2 \tag{3.14}$$

yielding the voltage that is required in order to fully deplete the pn-junction dependent on the bulk doping concentration and thickness.

The current flow through a pn-junction with reverse bias can be described by

$$I = I_R \times (\mathrm{e}^{eV_{\mathrm{bias}}/k_{\mathrm{B}}T} - 1) \tag{3.15}$$

with the reverse current $I_R = D + G$, elementary charge e, Boltzmann constant k_{B} and temperature T. The term D describes the diffusion current and depends on the diffusion constants and doping concentrations which are independent of the applied bias voltage. The other term $G \propto w$ depends on the width w of the pn-junction and represents the generation current. Often for pn-junction in industrial use, the device is fully depleted at millivolts already so that the current is dominated by the exponential term. However, sensors that are used for particle detection have a depletion region of hundreds of micrometers and are biased with voltages of hundreds of volts. Both are required in order to achieve a sufficiently large volume with high electric fields. In eq. (3.15) the exponential term decreases significantly by applying a small voltage in the (negative sign) single volt region already, compared to the $k_{\mathrm{B}}T$ term that is 26 meV at room temperature. Hence, the exponential characteristic can be neglected and the current is fully driven by the size of the depletion zone w. This leads to the proportionality between current and applied bias of

$$I \propto -\sqrt{|V_{\mathrm{bias}}|}. \tag{3.16}$$

By using the parallel plate capacitor equation with the area A of two plates, the capacitance can be calculated via

$$C = \epsilon_0 \epsilon_{\mathrm{Si}} \frac{A}{d}. \tag{3.17}$$

A pn-junction can be approximated as a parallel plate capacitor with a silicon medium. The thickness of the pn-junction is the distance between the plates $d = w$ which following eq. (3.13) leads to

$$C = A \sqrt{\frac{\epsilon_0 \epsilon_{\mathrm{Si}}\, e\, N_{\mathrm{eff}}}{2V_{\mathrm{bias}}}} \tag{3.18}$$

with the area A of the device. This equation is valid until full depletion is reached. The capacitance in full depletion can be calculated by inserting the depletion voltage from eq. (3.14)

$$C = A \frac{\epsilon_0 \epsilon_{\mathrm{Si}}}{D} \tag{3.19}$$

It stays constant when the total volume is depleted. The capacitance measurement of a diode or strip sensor can be used to extract the full depletion voltage and the effective doping concentration. This will be discussed further in chapter 5.1.

3.5. Interaction of Particles in Matter

Before the concrete implementation of a silicon detector is discussed, a deeper understanding of the interactions of incident particles in matter is required. Silicon sensors are used to detect charged particles and photons by ionisation of the detector material. The mean energy loss of heavy charged particles due to ionisation can be described by the *Bethe equation*. It holds

$$-\left\langle \frac{\mathrm{d}E}{\mathrm{d}x} \right\rangle = 4\pi N_A r_e^2 m_e c^2 z^2 \frac{Z}{A} \frac{1}{\beta^2} \left[\frac{1}{2} \ln \left(\frac{2 m_e c^2 \beta^2 \gamma^2 T_{\mathrm{max}}}{I^2} \right) - \beta^2 - \frac{\delta(\beta\gamma)}{2} \right] \tag{3.20}$$

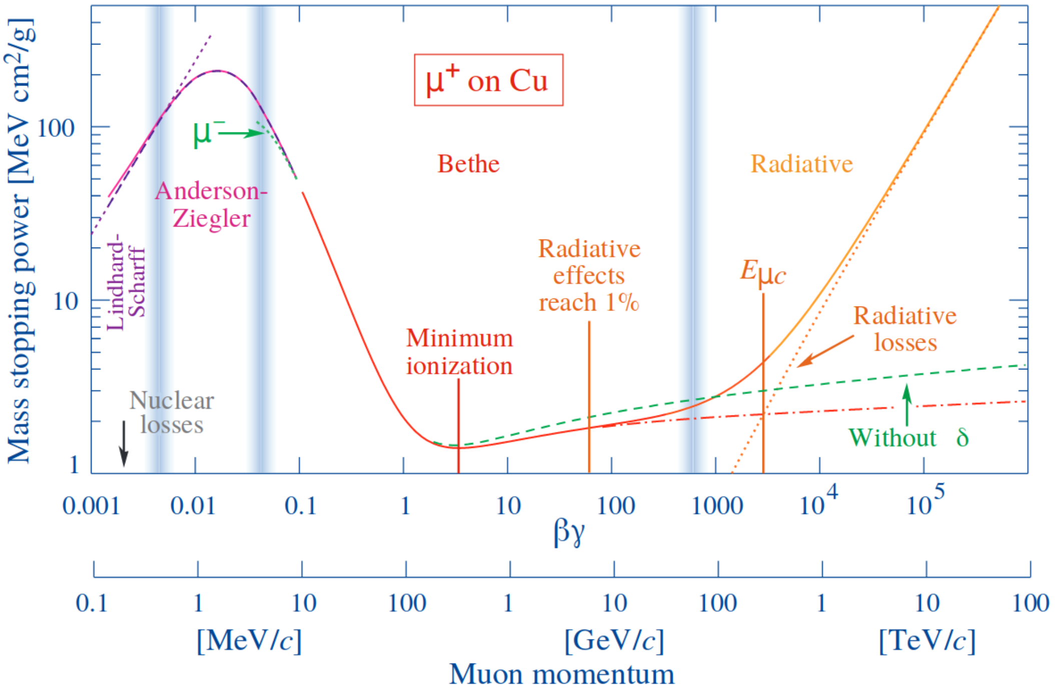

Figure 3.6.: Stopping power of muons in copper. The curve, which follows the Bethe equation (red), shows a minimum at $\beta\gamma \approx 3 - 4$ [Tan+18].

with the Avogadro number N_A, electron radius r_e, electron mass m_e, speed of light c, charge of incident particle z, atomic number Z, velocity β, Lorentz factor γ, mean excitation energy I, a density correction $\delta(\beta\gamma)$ and maximum transferred kinetic energy T_{max}. The Bethe equation is valid within a few percentage for charged particles which fulfil $0.1 \leq \beta\gamma \leq 1000$ [Tan+18].

The stopping power of a muon inside a copper block dependent on $\beta\gamma$ is illustrated in fig. 3.6. For low energies, the dominant energy loss is nuclear loss, which occurs due to interactions with the atomic body. In the range of $0.1 \leq \beta\gamma \leq 1000$ the graph is calculated with the Bethe equation and indicated by the red line. It can be seen that the function has a minimum at $\beta\gamma = 3 - 4$, approximately. Since the ionisation is minimal, such particles are called *minimal ionising particles* (MIPs). If the energy and therefore momentum of the muon is higher, radiative losses become relevant and even dominate at some point.

Since $\beta\gamma$ is higher for smaller masses (at the same energy), radiative losses are even more important to describe the energy loss of electrons. However, the Bethe equation is not valid for electrons, because it does not take the Pauli-Fermi exclusion principle into account. The most frequent interactions in the crystal lattice occur with the shell electrons which makes the Pauli-Fermi exclusion principle relevant. An illustration of the energy loss of electrons traversing lead can be found in fig. 3.7. It can be seen that bremsstrahlung becomes dominant already at 10 MeV due to the relatively low mass.

When a photon traverses a medium, it mainly scatters at the shell electrons as well. Hence, the main mechanism of energy loss is ionisation due to the photo-effect or Compton scattering at energies below 1 MeV. Above 1 MeV pair production might take place and for even higher energies emerging electromagnetic showers come into play.

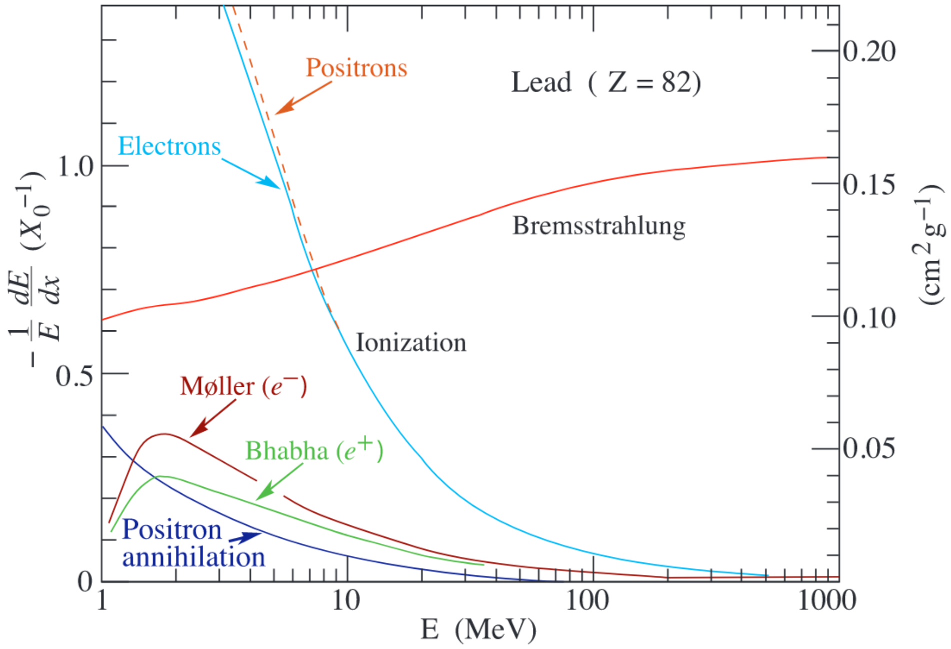

Figure 3.7.: Energy loss of electrons (light blue) and positrons (orange dashed) in lead. For low energies, ionisation is the main interaction type. With increasing energy, the ionisation fraction drops rapidly until bremsstrahlung eventually becomes predominant above 10 MeV [Oli+14].

3.5.1. Realistic Energy Loss in a Thin Layer

The energy loss of a particle traversing a medium has been discussed so far for charged particles and photons. The average energy deposition can be estimated with the Bethe equation. However, the probability distribution $f(\Delta/x)$, where Δ is the energy loss and x the thickness, follows a Landau distribution. There are tails, which reach very high energies, due to the possibility of transferring a large amount of energy to a shell electron. The energy of the excited electron might be high enough to ionise the material further. Such electrons are referred to as δ-electrons. Some examples of probability functions $f(\Delta/x)$ for different thicknesses are illustrated in fig. 3.8. It can be seen that the *most probable value* (MPV) of energy loss is roughly 30% smaller than the average value. This is because the high energy tails distort the mean value, while in fact 90% of energy losses are smaller than on average [Har17].

3.6. Sensor Principles and Design

The working principle of a silicon strip sensor is schematically illustrated in fig. 3.9. Strips of n-doped material are implanted into a p-doped bulk, leading to various parallel pn-junctions. The bulk thickness is in the order of some hundreds of micrometer. In the case of the Outer Tracker in Phase-2 it is 320 µm with an active thickness of 290 µm. The sensor is biased in reverse mode so that the depletion zone is growing from the top to the bottom. The operation voltage should exceed the voltage at which the whole bulk is fully depleted. For similar doping concentrations the full depletion voltage depends only on the thickness, following eq. (3.14) The depleted region is necessary because the number of free charge carriers in the silicon without bias would be of the order of 10^9 while the generated signal of a traversing MIP is of the order of 10^4. electron-hole pairs [Har17] for a typical sensor. The emerging electrons and holes due

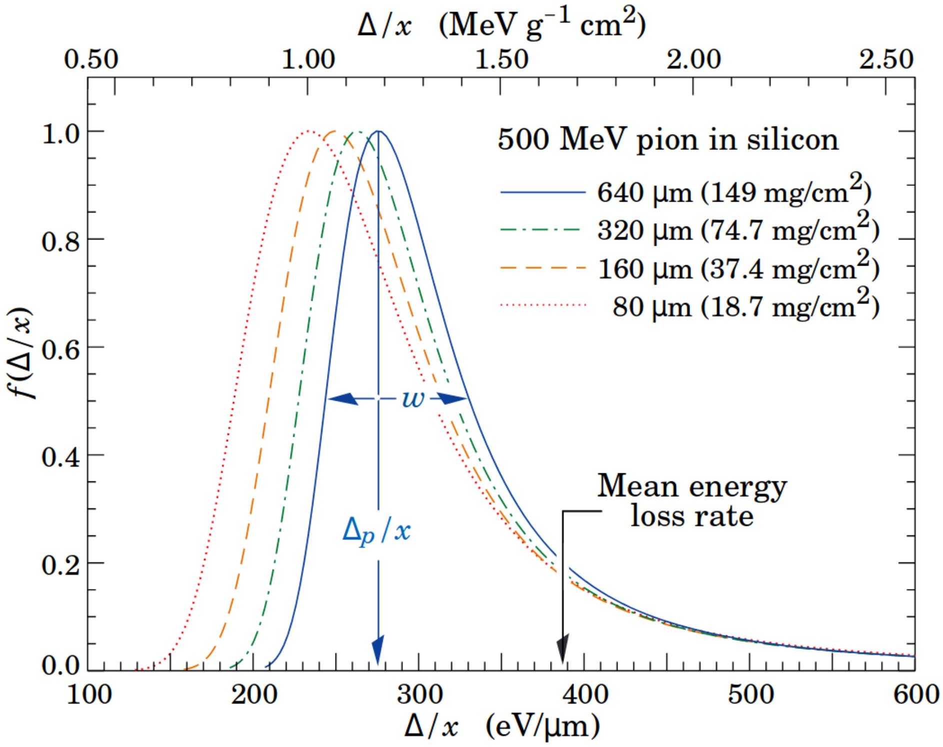

Figure 3.8.: Energy deposit in thin silicon layers of different thicknesses. The most probable value is approximately 1/3 less than the mean energy loss due to the tails towards high energies [Tan+18].

to an incident ionising particle drift to the appropriate electrodes following the electric field. A signal is generated in the aluminium strips that are connected to a readout chip via induction during the drifting process. Details about the sensor design of the CMS Phase-2 Outer Tracker and the signal formation are given in the following.

3.6.1. Design of Silicon Strip Sensors in Phase-2 of CMS

The design of silicon strip sensors for the CMS Outer Tracker in Phase-2 is sketched in fig. 3.10. A corner of a sensor is illustrated with various structures that are required besides the basic functionality. From the bottom up, the sensor consists of an aluminium backplane which enables contacting the whole backside. For testing, the sensor is placed on an aluminium chuck which is biased to the desired high voltage. Above the backplane, a highly doped p-type implant is required in order to avoid a Schottky barrier, which is a result of the metal-semiconductor junction. Then, the p-doped (boron) bulk is the sensitive substrate of the sensor where signal is generated. The electrons are accelerated towards the n-doped (phosphorus) strip implants which are connected by a via to the DC[3] pad. This pad is connected via a polysilicon resistor to the bias ring, which is grounded with a bond during operation or a bias needle during electrical tests. All strip implants are connected to the bias ring in the same way so that not every single implant has to be contacted separately. The use of an DC aluminium pad on the surface is that it can be used to directly contact the n^+-implant enabling electrical tests. A p-stop structure is implemented between the strip implants in order to keep a sufficient interstrip isolation. The functionality of a p-stop and the behaviour of the strip isolation is a central topic of this thesis

---

[3] DC: Direct Coupling

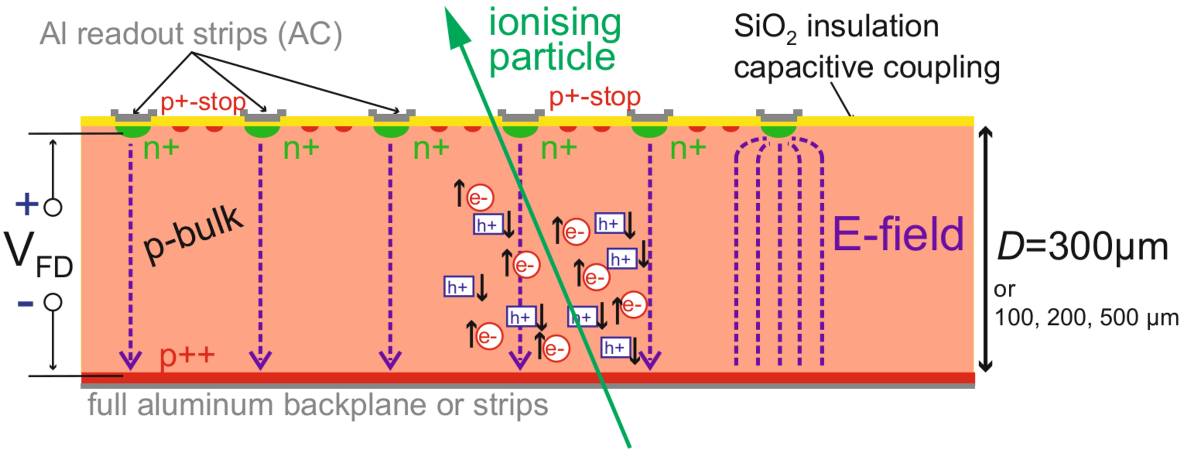

Figure 3.9.: Cross section of a silicon strip sensor. An ionising particle creates electron-hole pairs inside the silicon bulk. The sensor is fully depleted due to a reverse bias voltage V_{fd} which enables the readout of the charge inside the strips [Har17].

and comprehensively investigated in chapter 8. Aluminium AC[4] strips are located above the n$^+$ implants and a thin oxide layer for capacitative coupling. The electric field is laterally shaped by the bias ring implant and an additional guard ring structure next to it. This prevents a connection between the substrate and the less well defined crystal structure of the edge.

3.6.2. Shockley-Ramo Theorem and Weighting Field

When electron-hole pairs are generated inside the sensor substrate by an incident ionising particle, the charge is accelerated towards the electrodes. The acceleration is due to the electric field inside the sensor. Because of the movement of the charge, a current I is induced in the electrodes until the charge is finally collected. Hence, the term *charge collection* might be misleading, but refers to the process of collecting the charge. Especially for AC coupled sensors, no charge is flowing from the bulk directly into the readout chip but the signal is induced. This induction mechanism was first described by Shockley and Ramo [Sho38] [Ram39], hence referred to as Shockley-Ramo theorem. The induced current I_k in an electrode k can be calculated by a weighting field $\vec{E}_w$

$$I_k = -q\vec{v} \cdot \vec{E}_w \tag{3.21}$$

with the charge q, the drift velocity $\vec{v}$ and the weighting field $\vec{E}_w$ which describes the coupling of a charge to a specific electrode on the basis of the geometry. The weighting field can be determined by setting the potential of the electrode to 1 V (unit potential) and the other electrodes to 0 V [Spi05]. An example of the weighting field and weighting potential is illustrated in fig. 3.11. The figure shows a cross section of a strip sensor with the backplane on the bottom and several strip implants on the top. To calculate the weighting field of the middle strip its potential is set to 1 V while the others are set to 0 V. The drift field E_{drift} can be assumed to be uniform in the bulk, thus accelerates the charge perpendicular to the strips.

Most of the signal in a strip sensor is induced from charge drifting close to the strips where the weighting potential lines are more dense. The generated charge of a moving charge from an arbitrary point 1 to 2 is given by

---

[4] AC: Alternating Coupling

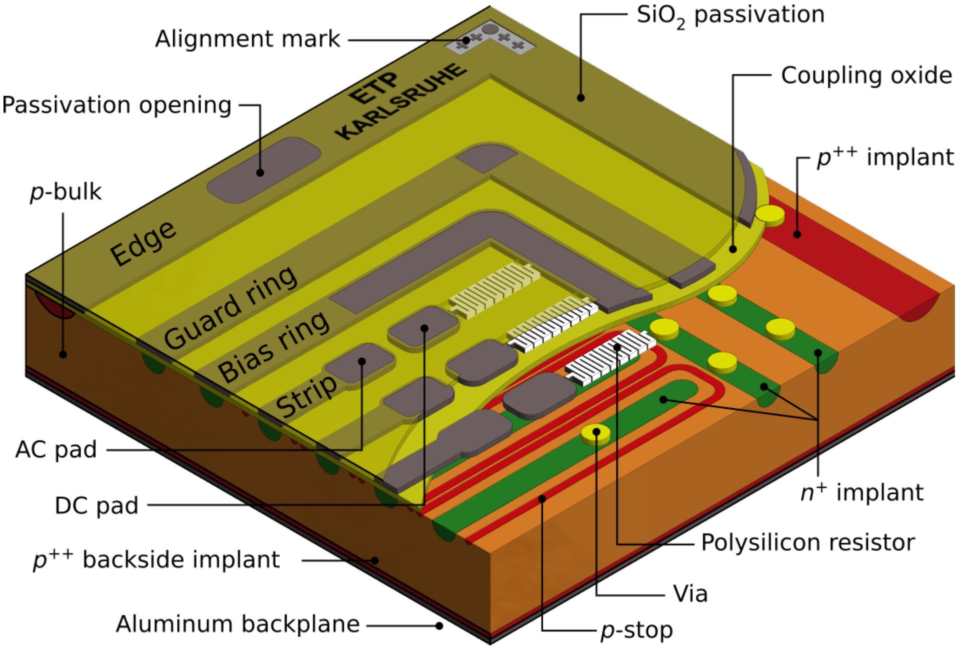
Alignment mark
SiO$_2$ passivation
Coupling oxide
Passivation opening
ETP
KARLSRUHE
p^{++} implant
p-bulk
Edge
Guard ring
Bias ring
Strip
AC pad
DC pad
n^{+} implant
Polysilicon resistor
p^{++} backside implant
Via
Aluminum backplane
p-stop

Figure 3.10.: Silicon strip sensor design for the CMS Outer Tracker in Phase-2. Implants with p-doping are indicated in red, n-doping in green. Grey coloured structures are made from aluminium. Figure reproduced from [Har17].

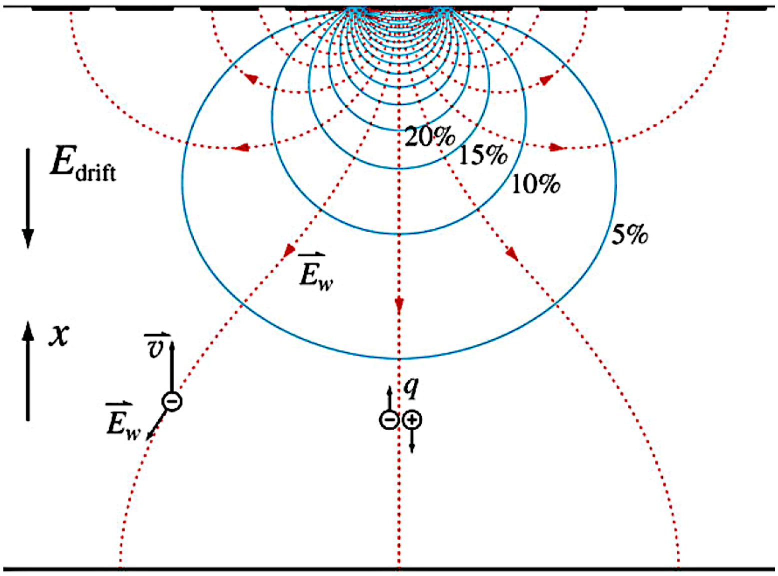
E_{drift}
20%
15%
10%
5%
$\vec{E}_w$
x
$\vec{v}$
$\vec{E}_w$
q

Figure 3.11.: Sketch of the weighting field and potential of a strip sensor. The weighting field $\vec{E}_w$ is indicated with the red dashed lines and the blue equipotential lines indicate the weighting potential. Figure adapted from [Rad20].

$$\Delta Q_k = q(\Phi_k(2) - \Phi_k(1)) \tag{3.22}$$

with the weighting potential Φ. If a charge q moves inside a plate capacitor to one of the electrodes, the total induced charge is simply $Q = I \cdot t_{\mathrm{drift}} = q$ as expected intuitively. Hence, the induced charge during the charge collection procedure equals the total charge that has been generated by an incident particle. However, this is only valid under the assumption that the charges live long enough to reach the electrodes. As will be explained in chapter 4, this is not true anymore after irradiation.

3.6.3. Noise Contributions

Besides the signal that a sensor is able to deliver, the noise is another crucial parameter. In the end, the signal-to-noise ratio determines how efficient a sensor is able to detect particles. Several effects contribute to the noise of a sensor and its readout chip. The main electronic noise which is occurring independent of the generated signal is expressed as equivalent noise charge (ENC) following [Har17]. It consist of four different noise portions, originated by the load capacitance C_d, the leakage current I_L, the parallel R_P and the series resistance R_S that sum up quadratically

$$ENC = \sqrt{ENC_C^2 + ENC_{I_L}^2 + ENC_{R_P}^2 + ENC_{R_S}^2}. \tag{3.23}$$

The predominant term for CMS Outer Tracker sensors is the load capacitance C_d

$$ENC_C = a + b \cdot C_d \tag{3.24}$$

where a and b are readout chip specific parameters. All other parameters increase the noise proportional or inversely proportional to their square root. The shot noise is determined by the leakage current I_L

$$ENC_{I_L} = \frac{e}{2}\sqrt{\frac{I_L \cdot t_p}{q_e}} \tag{3.25}$$

with the Euler number e, the electron charge q_e and the peaking or integration time of the readout chip t_p. Parallel thermal noise is generated by the bias resistance R_P

$$ENC_{R_P} = \frac{e}{q_e}\sqrt{\frac{k_{\mathrm{B}}T \cdot t_p}{2R_P}} \tag{3.26}$$

with the Boltzmann constant k_{B}, temperature T and the serial thermal noise due to the series resistance, mainly the aluminium strip resistance R_S

$$ENC_{R_S} = C_d\frac{e}{q_e}\sqrt{\frac{k_{\mathrm{B}}T \cdot R_S}{6t_p}}. \tag{3.27}$$

The typical noise of sensors and readout chips that will be used for the new Outer Tracker is around some hundreds of electrons whereas the signal strength is in the order of $10^4\,\mathrm{e}^-$.

4
Radiation Damage

Crucial properties of silicon devices change after irradiation. The radiation damage is usually divided into two parts, bulk and surface damage. However, as will be shown in chapter 8, the interplay is of major importance and cannot be neglected. The radiation defects and their influence on the sensor properties are explained in the following.

4.1. Microscopic Bulk Damage

Bulk damage is mainly created by hadrons. When a particle with high momentum traverses the sensor, it can interact with the nucleus of a crystal atom. This might displace the crystal atom, dependent on the transferred momentum. The displaced atom is called primary knock on atom (PKA) and moves through the crystal. It will leave a vacancy behind and stops as an interstitial somewhere in the lattice. If the displaced atom stops close by, the combination is called *Frenkel pair* as illustrated in fig. 4.1 on the top right. The figure gives an overview of the *point defects* which can be generated in a silicon sensor substrate. If the PKA gets a very high momentum transferred from the incident particle, it may interact with another nucleus of the lattice or even a number of other nuclei. Hence, a *cluster* of defects is created. Defect clusters are the main damage introduced by neutrons since they are uncharged and only interact with nuclei via nucleus-nucleus scattering. Therefore, usually most of a neutron's energy is transferred. Charged particles like pions and protons mainly interact via the Coulomb force, thus creating point defects. However, dependent on their energy they can also generate defect clusters.

The simulated distribution of vacancies for three different incident particles is illustrated in fig. 4.2. On the left side, low energetic protons (10 MeV) create a significant amount of point defects via Coulomb interactions. The picture in the middle shows the damage of proton irradiation as well, but with an energy that is three orders of magnitude higher. This leads to more defect clusters, since the probability of a high momentum transfer is increased. In the third case on the right side, the impact of neutrons with 1 MeV is indicated. Since they are not able to interact via Coulomb force, mainly defect clusters are introduced.

4.1.1. NIEL Hypothesis

A quantity is desirable to make radiation damage of different particles and energies comparable. The energy loss of a particle traversing silicon that is not caused by ionisation of the substrate is the cause of bulk damage. Hence, the *non ionising energy loss* (NIEL) is a measure that quantifies the bulk damage with the assumption that the damage scales proportionally with the deposited energy. The *displacement cross section* $D(E)$ is a function of the energy and can be normalised to 95 MeV mb for 1 MeV neutrons. This normalisation is illustrated in fig. 4.3 dependent on the energy and particle type. The inserted plot shows the relevant region for high energy physics applications. A comparable quantity which is called *fluence* can be defined by introducing a hardness factor κ that scales the damage of different particle types to the

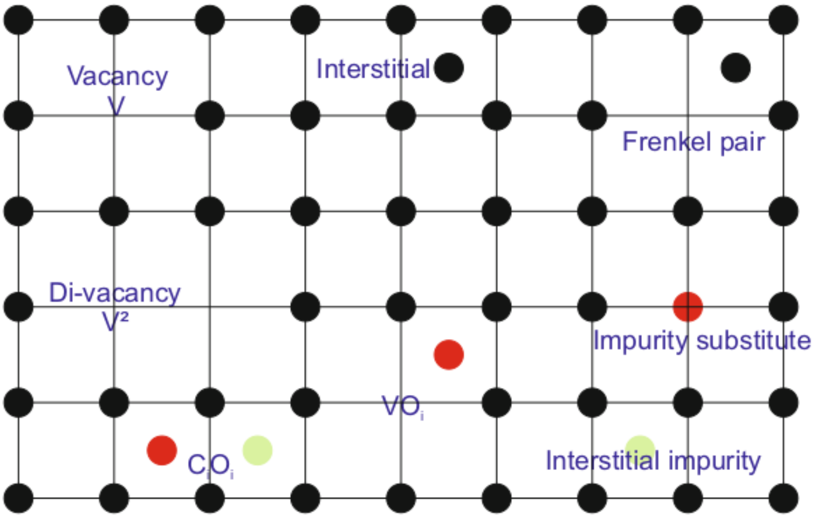
Vacancy
V
Interstitial
Frenkel pair
Di-vacancy
V²
Impurity substitute
VO_i
C_iO_i
Interstitial impurity

Figure 4.1.: Illustration of the various defects which can occur in a silicon crystal lattice. The most prominent one is the Frenkel pair which consists of a vacancy and an interstitial atom. It is generated by knocking off an atom from its place in the lattice [Har17].

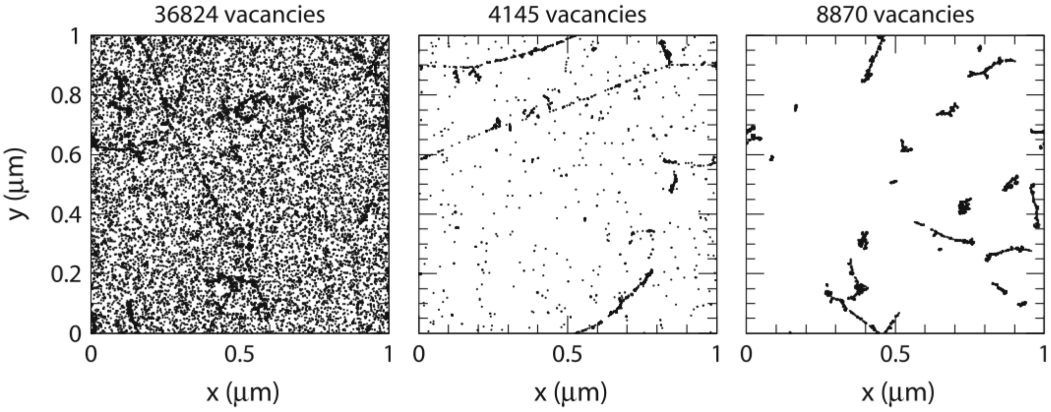

Figure 4.2.: Simulated vacancy distribution in a silicon volume of 1 µm^3 for 10 MeV protons (left), 24 GeV protons (middle) and 1 MeV neutrons (right). Protons create both, point and cluster defects, since they are charged particles and interact via Coulomb and nucleus-nucleus interaction. Neutrons on the other hand are only able to scatter directly at the nucleus, thus transferring most of their energy, which results in defect clusters [Huh02].

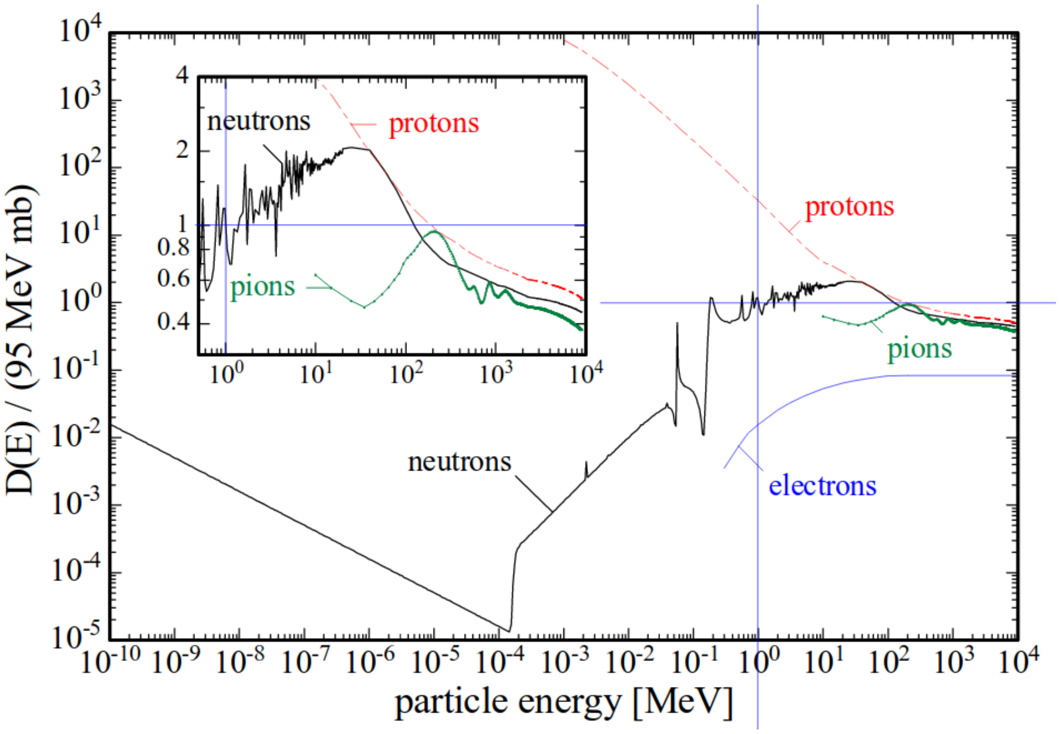

Figure 4.3.: Displacement damage cross section dependence on the particle energy for different particles, following the NIEL hypothesis [Fre+02].

equivalent damage of a neutron with 1 MeV. The hardness factor is given by

$$\kappa = \frac{\int D(E)\Phi(E)\mathrm{d}E}{D_{\text{neutron}}(1\,\text{MeV}) \cdot \int \Phi(E)\mathrm{d}E} \ . \tag{4.1}$$

The 1 MeV *neutron equivalent fluence* can then be calculated by

$$\Phi_{\text{eq}} = \kappa\Phi = \kappa \int \Phi(E)\mathrm{d}E \tag{4.2}$$

and is always given in the following in order to quantify the radiation damage because it is a particle and energy independent parameter. However, the NIEL hypothesis is not always a good approximation, especially if the sensor substrate is oxygen enriched. The oxygen atoms react with otherwise electrical active defects, which leads to a mitigation of the effective damage [Lin+01]. Still, it is the best way to quantitatively compare different irradiation scenarios to each other.

4.1.2. Defects in the Band Scheme

Since the understanding of the effect of defects inside the band gap is of major importance for this thesis, it is discussed in more detail. Any kind of defect in the crystal lattice can result in an additional state inside the band gap of silicon. The defect states are referred to as donor and acceptor states and are sometimes desired, for example in case of dopants. A donor is a state, which can donate an electron to the crystal lattice. Hence, when a donor is filled by an electron it is in the state where it would be outside of the crystal lattice (e.g. in case of dopants, complex defect states can be less intuitive) and therefore neutral. This is sometimes called occupied because it cannot further accept an electron, although it has not captured anything yet. In general, the term *filled* or *occupied* refers to an electron state, although in some cases it would be more intuitive to refer to a hole. If the donor defect donates its electron to the crystal lattice, it becomes positively charged due to the charge of the remnant. This state is then referred to as empty, which should not be confused with the intuitive neutral state (where it is filled by an electron). The definition of a donor state in short is that it is neutral if filled (by an electron) and positively charged if empty.

In the case of an acceptor, the defect can accept an electron. The state is neutral in its natural state (e.g. outside of the lattice) which is referred to as empty because of the lack of an electron. Note the difference to a donor state which is filled in its natural state which might lead to confusion. If the acceptor state gets occupied by an electron it is denoted as filled. Due to the additional electron the defect's charge gets negative. The definition of an acceptor in short is that it is negatively charged when filled by an electron and neutral if empty.

Whether a donor or acceptor state is occupied or not is determined by the Fermi level which is usually located in the middle of the band gap. This is not necessarily true under all conditions but a good approximation at room temperature and helps to understand the general situation. A scheme of the band gap with various defects is illustrated in fig. 4.4. The notation of the charge states is indicated with a "$-$" for negative charge, "$+$" for positive charge and "0" for neutral. The charge levels in the band scheme are indicated by the horizontal line. The state below the line is the charge when the defect is unoccupied and above during occupation (of an electron).

If an acceptor state is located close to the valence band or in general below the Fermi level, it is occupied by an electron. States below the Fermi level are in general likely to be occupied by an electron and states above the Fermi level are unlikely to be filled. Hence, the acceptor state is occupied and negatively charged. The usual charge of a defect at room temperature is marked in green in the figure. Doping atoms of the third main group (e.g. B in the picture) are acceptor states close to the valence band, thus negatively charged so that they can contribute to the effective doping concentration. On the other hand, if an acceptor level is introduced in the upper half of the band gap, it is not occupied at room temperature. Therefore, it is not charged and does not change the effective doping concentration. Such states are usually introduced by radiation damage. Since they are unoccupied at around room temperature (relevant temperatures for this thesis), they can trap an electron for a short period of time. This results in a local negative charge and also degrades the signal strength. The probability to trap charge carriers depends on temperature and charge carrier concentration. The impact of the defects on the macroscopic sensor properties will be discussed in the next section.

For dopants of the fifth main group, which are donor levels close to the conduction band, the state is labeled as unoccupied at room temperature. This is because it is located above the Fermi level so that electrons are unlikely to reach it and it donates its electron to the lattice. However, the term unoccupied should not be confused with uncharged, since donors are positively charged when they lack an electron. Therefore, the donor state close to the conduction band contributes to the effective doping concentration which is what dopants are supposed to do. On the other hand, if a donor state is introduced close to the valence band or in general below the Fermi level, the state is likely to be occupied by an electron. This means that the donor state is neutral since the occupation by an electron is the natural state which the corresponding atoms or molecules would be in outside of the crystal lattice. Such defect states are introduced by radiation and can trap holes, resulting in a local positive charge.

A different terminology is sometimes used to avoid confusion, especially when referring to traps which are generated by radiation. Then, the term *occupied* does not refer to occupation of an electron only. Instead, both trap types, acceptor and donor states are uncharged when unoccupied and negatively or positively charged, respectively, when occupied. The way of thinking is that donors are trapping a hole instead of donating an electron. In fact, both

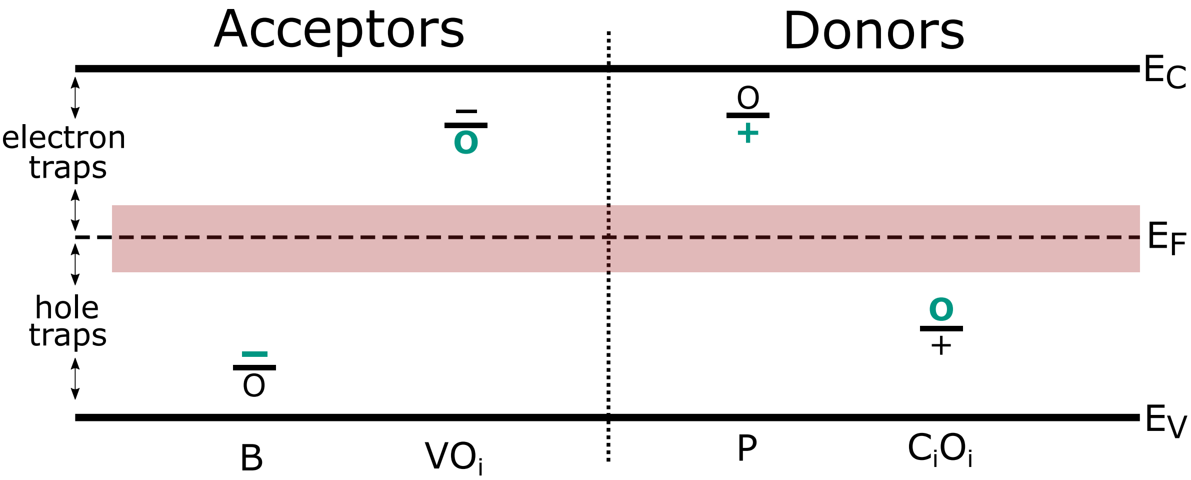

Figure 4.4.: Defect locations inside the band scheme. Dopants are usually states close to the valence band for acceptors and close to the conduction band in the case of donors. However, for defects which are generated by radiation, the situation is often reversed. Hence, they are able to trap an electron or hole as explained in the text. The figure is reproduced from [Mol99].

definitions are equivalent. However, this definition might be more intuitive to describe traps, because both trap types are usually uncharged. This is because radiation induced acceptors are often located above and donors below the Fermi level. Hence, they carry a negative or positive charge when trapping an electron or hole, respectively. The definition is used in the simulation framework Synopsys Sentaurus T-CAD ([Syn21]) to describe traps. In the end, it does not matter which definition is preferred, but it has to be taken care that they are not mixed up which would lead to inconsistencies.

4.2. Impact of Bulk Damage on Sensor Properties

Defects in the silicon lattice can be represented by states in the band gap, as discussed in the previous section. The impact on important sensor properties is summarised in fig. 4.5. Case (a) describes the generation of leakage current due to states which are located close to the middle of the band gap. These states act like stepping stones for charge carriers, so that they are excited to the defect state first and then further to the valence or conduction band. Donor or acceptor states can be charged (b) at room temperature if they are located close to the conduction or valence band, respectively. These defects affect the effective doping concentration N_{eff} due to their charge, thus affecting the electric field and full depletion voltage. If trap states are located elsewhere in the band gap (c) they are effectively trapping electrons and holes. The collected signal or CCE (charge collection efficiency) decreases due to the trapping of generated charge carriers. The trapped charge is released after a finite time but usually after the readout of the sensor is finished, hence the charge is lost in terms of signal formation. The trapping and emission rates and probabilities can be described by Shockley-Read-Hall statistics [SR52]. The classification in leakage current generating or trapping defects is sometimes ambiguous and can overlap. Especially when several defects are condensed in a defect cluster, the interplay of these defects (d) differs from their impact when they are isolated. In the following, the change of the leakage current, depletion voltage and charge collection after irradiation is discussed further.

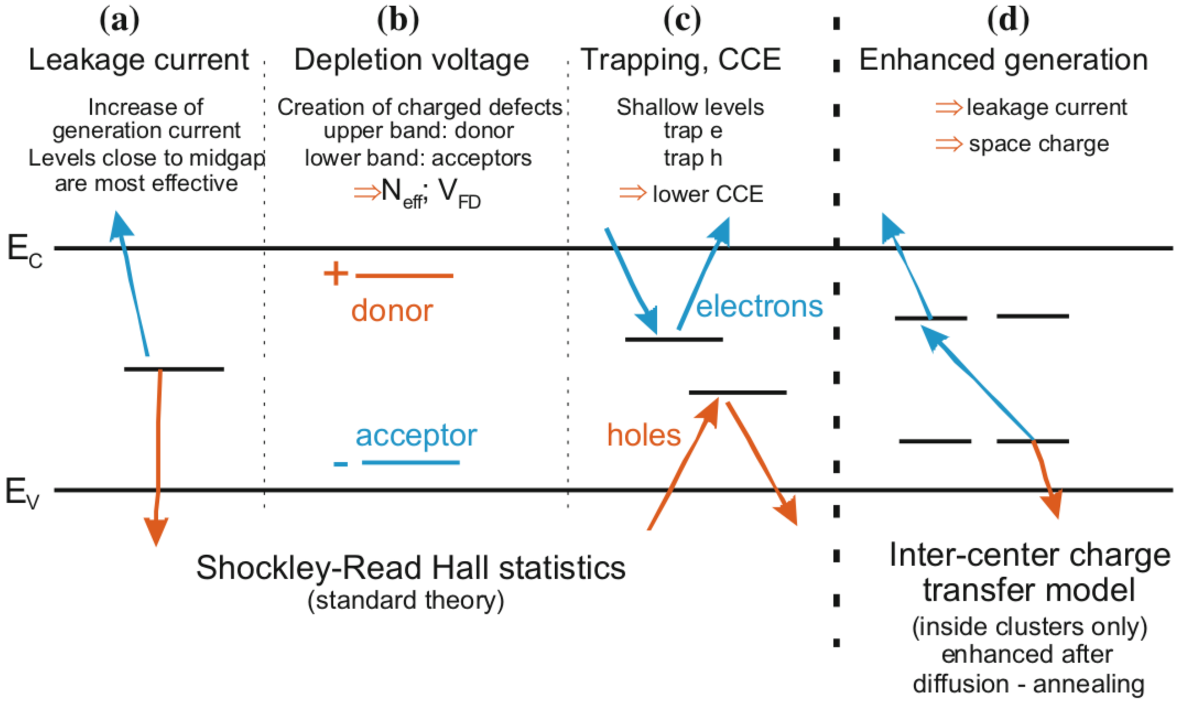
(a)
Leakage current
Increase of generation current
Levels close to midgap are most effective
(b)
Depletion voltage
Creation of charged defects
upper band: donor
lower band: acceptors
⇒N_{eff}, V_{FD}
(c)
Trapping, CCE
Shallow levels
trap e
trap h
⇒ lower CCE
(d)
Enhanced generation
⇒leakage current
⇒ space charge
E_C
E_V
+
donor
acceptor
-
electrons
holes
Shockley-Read Hall statistics
(standard theory)
Inter-center charge transfer model
(inside clusters only)
enhanced after
diffusion - annealing

Figure 4.5.: Influence of microscopic defects on macroscopic properties of silicon sensors. Defect states in the middle of the band gap are able to generate leakage current effectively (a). If a donor state is located close to the conduction band, it will donate its electron, thus it is positively charged. Acceptors are negatively charged when they are located close to the valence band. The charged defects contribute to the effective doping concentration and increase the full depletion voltage (b). States elsewhere in the band gap capture electron or holes and therefore decrease the collected charge (c). Combining different states leads to enhanced generation of leakage current or space charge, mainly in defect clusters (d) [Har17].

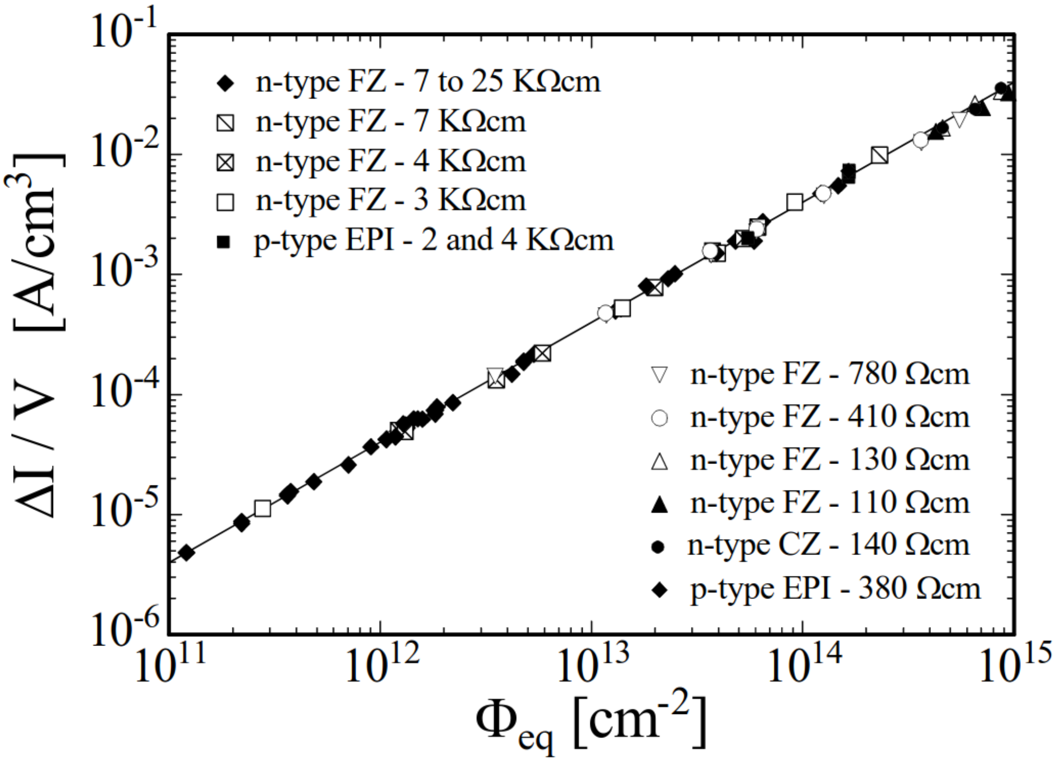

Figure 4.6.: Increase of leakage current per volume after radiation. The linear increase is independent of the bulk doping type and bulk resistivity before irradiation [Mol99].

4.2.1. Leakage Current

The leakage current of a silicon sensor is increasing proportional to the applied fluence, following the NIEL hypothesis. This is illustrated in fig. 4.6 where many samples of different base materials were irradiated to fluences ranging from 1×10^{11} to 1×10^{15} $\mathrm{n_{eq}/cm^2}$ and the current increase has been measured [Mol99]. The leakage current increase ΔI normalised by the volume V can be expressed by

$$\frac{\Delta I}{V} = \alpha \cdot \Phi_{\mathrm{eq}} \tag{4.3}$$

where the proportionality factor α to the neutron equivalent fluence Φ_{eq} is denoted by *current-related damage rate*. The damage rate is a substrate type independent quantity which can be used to compare and validate different irradiations by measuring the current. However, if measurements at different temperatures are compared the temperature dependence of the leakage current has to be taken into account, since the leakage current increases with temperature, following

$$I(T) \propto T^2 \exp(-1.21\mathrm{eV}/2k_{\mathrm{B}}T) \tag{4.4}$$

with the Boltzmann constant k_{B} [Chi13].

4.2.2. Depletion Voltage

When acceptor or donor states are introduced into the sensor substrate, they can be charged dependent on their relative location in the band gap to the Fermi level. Defect states affect the

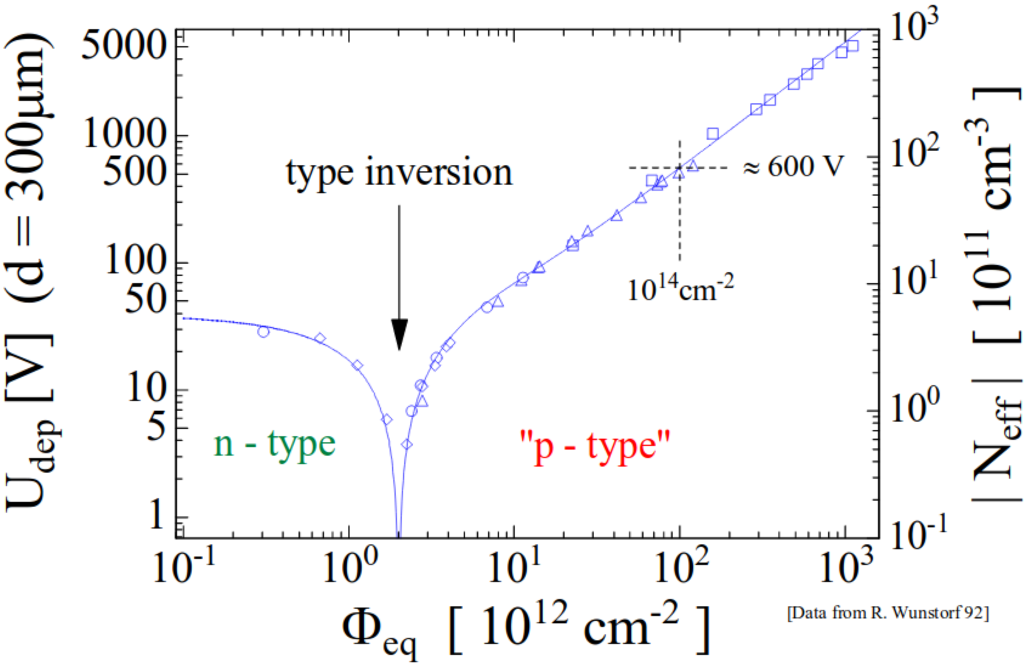

Figure 4.7.: Type inversion of sensor with an n-doped bulk. Mainly acceptor states are introduced by radiation, which decrease the effective doping concentration for lower fluences. As the fluence gets higher, the acceptor states become predominant and the effective doping concentration and depletion voltage increases [Fre+02].

effective doping concentration N_{eff} dependent on their charge. By irradiation mainly acceptors are induced into the bulk and donors are removed. Hence, the sensor can be understood as getting effectively more p-doped. The depletion voltage of sensors with a p-type bulk increases with applied fluence because of the increasing effective doping concentration.

A different picture arises for sensors with an n-type bulk. The effective doping concentration decreases when bulk defects are generated by radiation as illustrated in fig. 4.7. Therefore, the depletion voltage also decreases, which is indicated on the left y-axis and proportional to the effective doping concentration that is indicated on the right y-axis. However, at a certain fluence the induced acceptor states become predominant over the donors and the primary doping concentration. Hence, the absolute value of the effective doping concentration and depletion voltage rises again. This mechanism is referred to as as *type inversion* since the n-doped bulk is now effectively p-doped. After the type inversion, the sensor is still operable with the same bias polarity, because the doping concentration of the strip implant is usually several orders of magnitude higher than the bulk doping. However, in this case it is even more important that the sensor is fully depleted because the depletion zone is now growing from the backside[1]. This implies that charge might be lost in the undepleted region beneath the strips if the full depletion voltage exceeds the reasonably applicable bias voltage.

4.2.3. Charge Collection

The collected charge due to the induced signal decreases after irradiation. Besides the potential issue that the sensor cannot be fully depleted anymore, charge carriers are lost by trapping, where acceptor or donor states within the band gap get occupied with an electron or hole.

---

[1] pn-junction: p-type bulk and n^{++} backplane

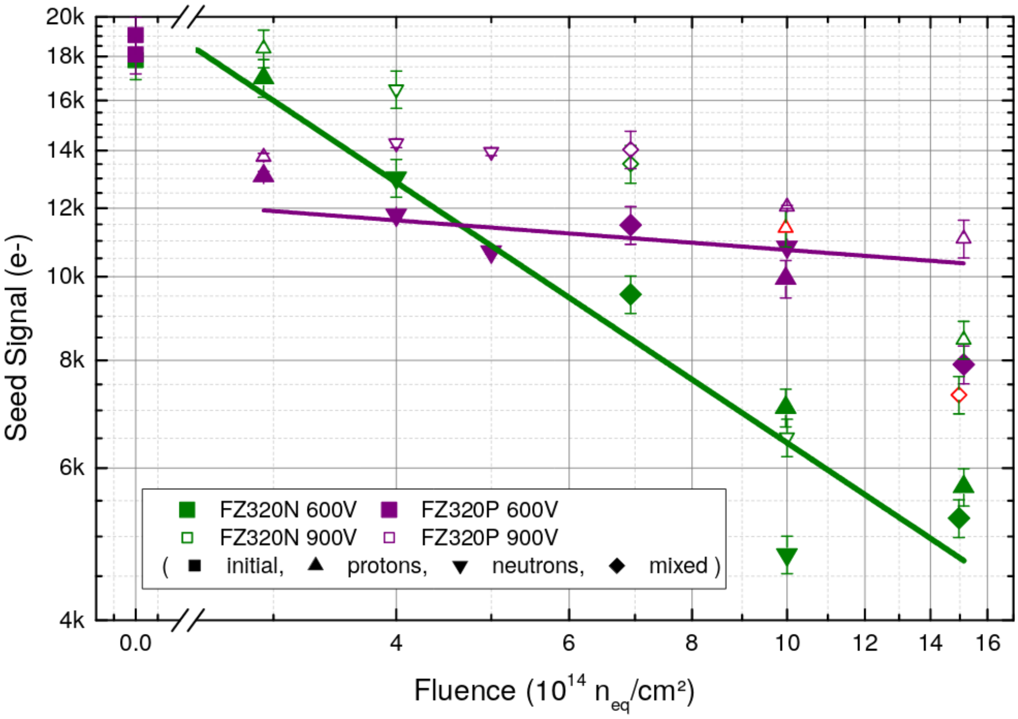

Figure 4.8.: Signal of n-type (green) and p-type (purple) substrate after irradiation with fluences expected for Phase-2 of the CMS tracker. The signal of n-type sensors is rapidly decreasing with applied fluence due to trapping and increasing depletion voltage. Sensors with a p-type bulk also suffer from higher fluences but less than sensors with an n-type substrate [Die13].

The charge is later released, but after the main signal formation is over. Therefore, it does not contribute to the initial signal anymore and lost in noise. The mechanism is similar for sensors with an n-type or p-type bulk. However, for n-type sensors the collected charge at the electrodes is dominated by drifting holes and in p-type sensors by electrons. In general, since in silicon the mobility of holes is lower than the mobility of electrons, holes are collected slower and trapped more likely. Initially, for low fluences the n-type sensors benefit from the decrease of N_{eff} and consequently reduced full depletion voltage. Regarding fluences expected for the operation in the tracker of the CMS Phase-2 detector, this effect can be neglected because the final fluence is at least two orders of magnitude above the type inversion fluence. For these fluences, it is not possible to fully deplete the sensor anymore, thus an undepleted region arises. In case of n-type sensors, this region is just below the strips which means that charge is lost before the strips can be reached. This is problematic since the signal in the readout strip is induced via induction where the strongest contribution comes from the regions close to the strip. As discussed in section 3.6.2 the weighting field decreases rapidly oppositely directed from the strips. These effects explain the measured signals of n-type and p-type samples at high fluences in the region of 1×10^{14} and $1.5 \times 10^{15}\,\text{n}_{\text{eq}}/\text{cm}^2$ shown in fig. 4.8. The signal in units of electron charge is decreasing towards higher fluences for both types, n-type in green and p-type in purple. For low fluences, the n-type substrate yields more signal but the difference vanishes rapidly as the fluence rises. This is why all silicon sensor substrates of the new CMS tracker will be p-doped [Ada+17].

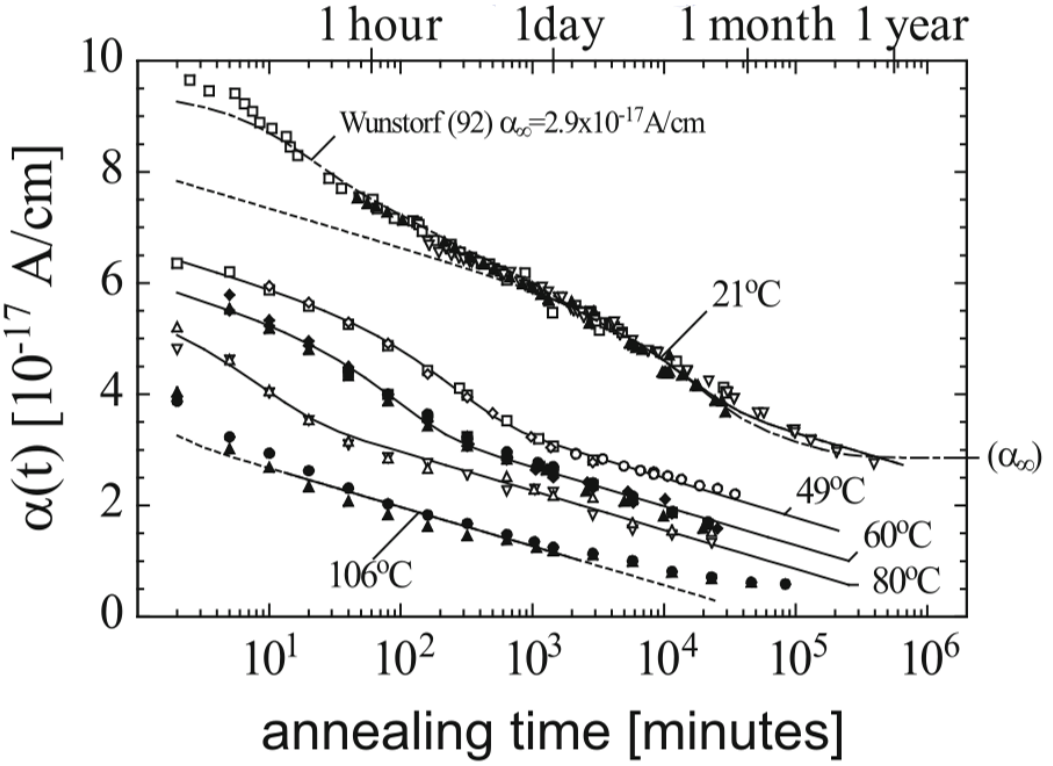

Figure 4.9.: Dependence of the current-related damage rate α on the annealing time. Measurements have been performed after annealing at temperatures up to 106°C. Annealing is always beneficial regarding the leakage current [Mol99].

4.2.4. Annealing

Changes of the defects in the crystal lattice over time at a finite temperature are referred to as *annealing*. The induced defects can be mobile at room temperature and for example a Frenkel pair might recombine. Since this recombination is beneficial for the macroscopic properties, the process is denoted by *beneficial annealing*. On the other hand it is also possible that defects combine with each other forming lager defects. This *reverse annealing* happens usually on a larger time scale, which makes it possible to benefit from beneficial annealing and avoid reverse annealing. In general, below 0°C annealing effects are suppressed to an extend where they become negligible [Har17].

The effect of annealing on the leakage current of several irradiated diodes is illustrated in fig. 4.9. In short, the current-related damage rate α respectively the leakage current always decreases and reverse annealing does not appear, which would manifest as increase of leakage current. The damage rate can be parametrised by an exponential and a logarithmic term according to [Mol99], which is referred to as the Hamburg model. Hence, it is possible to calculate the equivalent time at room temperature for an annealing time at a higher temperature. This will also be used in this thesis in order to reach an effective annealing time at room temperature longer than a year, which would not be feasible without accelerated annealing at a higher temperature (usually 60°C or 80°C).

The change of the effective doping concentration due to annealing has also been parametrised within the Hamburg model. It consist of three parts, a stable term $\propto N_\mathrm{C}$ which is independent

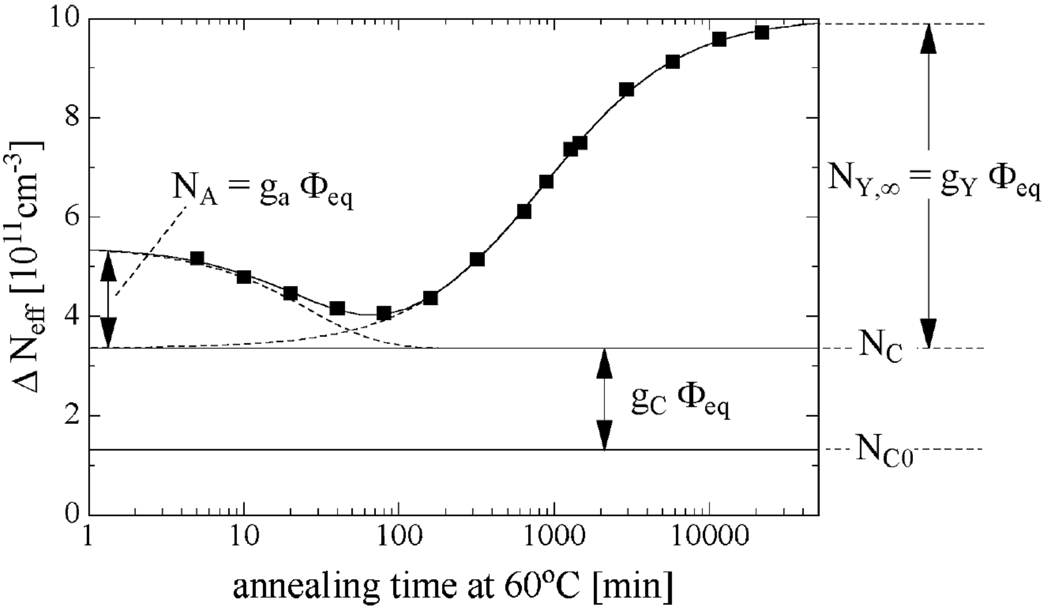

Figure 4.10.: Annealing impact on the effective doping concentration. The dependence on the annealing time can be parametrised with three terms. A stable term N_C leads to an increase due to the initial irradiation. The short annealing term N_A dominates for small annealing times and leads to a decrease of N_eff which is usually beneficial. On a larger time scale, N_Y becomes predominant and increases the effective doping concentration to even higher values [Mol99].

of annealing, a short annealing term $\propto N_\mathrm{A}$ and a long (reverse) annealing term $\propto N_\mathrm{Y}$. The effect on N_eff is illustrated in fig. 4.10 where ΔN_eff denotes the change of N_eff due to irradiation. The constant term N_C just increases the effective doping concentration proportionally to the applied fluence. As soon as annealing starts N_eff decreases with time $\propto N_\mathrm{A}$ due to the decay of acceptor defects. On the other hand if the annealing time gets orders of magnitude longer, a second order effect $\propto N_\mathrm{Y}$ comes into play which leads to the formation of acceptor states. Hence, the space charge increases (becomes even more negative) and the effective doping concentration increases as well. This leads to a higher full depletion voltage and decreases the collected charge if the full depletion voltage cannot be reached anymore. Consequently, it should be avoided to reach the reverse annealing regime during operation. A short annealing time should always be applied since it is beneficial in terms of signal and depletion voltage but it is also always beneficial regarding the leakage current, thus power consumption and noise.

4.3. Surface Damage

The term *surface damage* refers to changes of the properties of the SiO_2 surface as well as to the Si-SiO_2 interface by irradiation. Additionally, the small bulk region below the interface affects interface traps, thus plays an important role as well. Damage on the surface can be expressed similarly to bulk damage by point-like defects which are represented by states in the band gap. The band gap of SiO_2 is 8.8 eV, thus larger than the 1.12 eV band gap of silicon. Radiation-induced defects can generated leakage current similar to the bulk defects at the Si-SiO_2 interface. However, in an operating environment like the HL-LHC, the current generated by bulk defects will be predominant. What is more important is that surface defects affect the electric field distribution and the interstrip isolation (which are correlated). In short, the

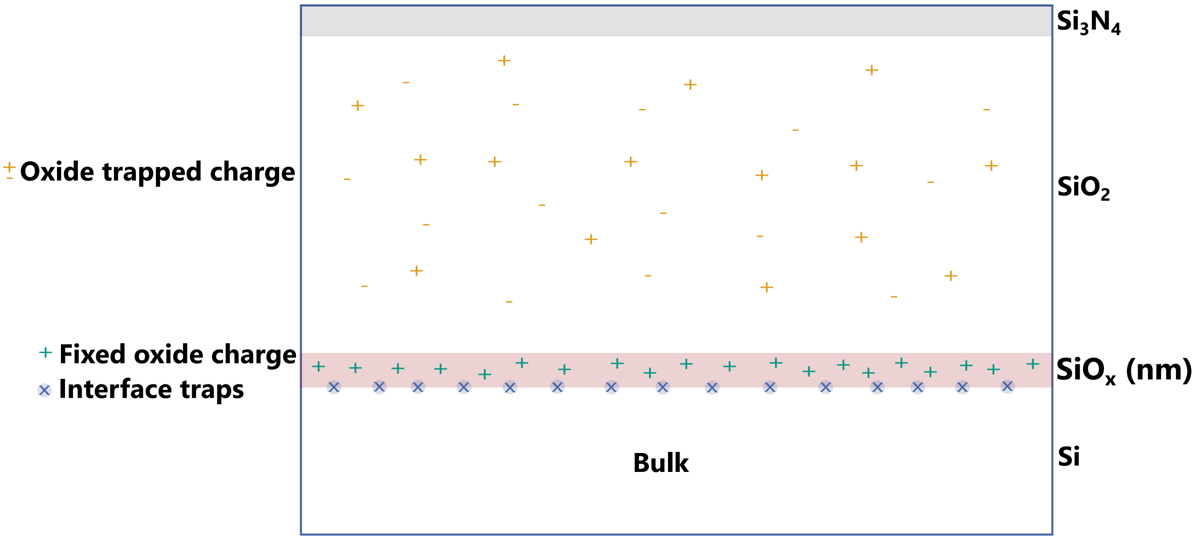

Figure 4.11.: Schematic illustration of the surface defects. Between the SiO_2 and the Si, a small interface region of SiO_x builds up. Here, mainly interface traps and positive fixed charge is located. Additionally, traps in the SiO_2 can be negatively or positively charged.

interstrip (or interpixel) isolation can be insufficient already before irradiation but is expected to be lost certainly after irradiation, if no precautions were taken. This is because the surface is usually slightly positively charged, which attracts electrons from the bulk that establish a conductive channel between the strips. Since the investigation of the interstrip isolation is one of the main topics of this thesis, it will be discussed in more detail in chapter 8. Another difference to bulk defects is that surface damage is induced in most radiation environments, since it is generated by ionising particles. Silicon sensors are designed to detect ionising particles with the help of a depleted bulk, hence naturally the surface will also be ionised during operation. The main parts of the surface with respective defects are presented in fig. 4.11. Between the silicon bulk region on the bottom and the SiO_2, there is a small interface region with a severely distorted crystal lattice. It is highly distorted due to the naturally appearing dangling bonds when different crystal structures are fused together. Traps located directly at the interface are denoted as *interface traps* and a specific trap is the cause of positive *fixed oxide charge*, which is always present. Additional traps elsewhere in the SiO_2 surface can induce positive or negative charge, which is referred to as *oxide trapped charge*. Sometimes, a silicon nitride layer (Si_3N_4) is applied on top of the SiO_2, which can improve radiation hardness. The illustrated defects from downside to upside will be explained in the following paragraphs in more detail.

4.3.1. Interface Traps

Interface traps are traps that are located at the Si-SiO_2 interface where the crystal lattice is highly distorted. A fusion of two different crystal types leads to dangling bonds in the interface region. Details of the interface traps were figured out with the help of electron paramagnetic resonance (EPR) experiments, like in [Poi+81] and [Poi+84]. Dependent on the silicon substrate crystal orientation the interface traps are identified to be mainly P_b[2] centres for $\langle 111 \rangle$ (Miller indices) substrate and P_{b0} and P_{b1} centres for $\langle 100 \rangle$ substrate. The two defects for $\langle 100 \rangle$ substrates are schematically illustrated in fig. 4.12 since the silicon substrate used within this thesis is $\langle 100 \rangle$ oriented. Both defects consists of a trivalent bond of silicon atoms with a missing

---

[2] The historical name P_b centre is because it is the second (b) kind of paramagnetic (P) defects [Nis71]

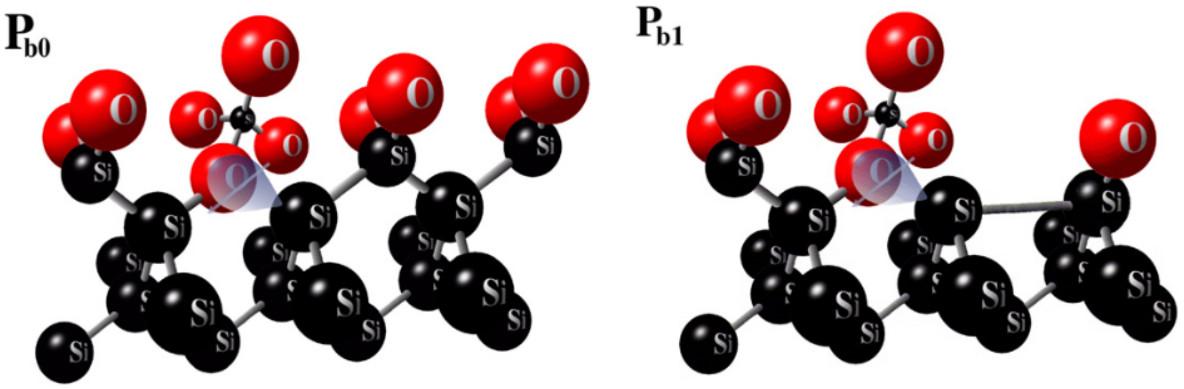

Figure 4.12.: The two major defects at the interface of Si-SiO_2 with $\langle 100 \rangle$ substrate. Both can be represented with by the sum formular $Si_3{\equiv}Si\bullet$. The main difference is the bonding symmetry and the state distribution in the energy band [Len07].

bond $Si_3{\equiv}Si\bullet$. The main difference between the P_{b0} and P_{b1} centre is the symmetry of the dangling bond axis [Rya+10]. Both types are amphoteric due to their energy distribution inside the band gap. That means that both can act as a donor or acceptor, thus positively or negatively charged, respectively, as discussed in section 4.1.2. As will be shown in chapter 8, interface traps are of major importance regarding the interstrip isolation of strip sensors. The interface trap concentration is denoted by N_{it} (unit: cm^{-2}) or interface trap state density D_{it} (unit: $eV^{-1}\,cm^{-2}$) following the standard nomenclature [Dea80]. A general overview of the defects in the interface region can be found in [HP94] and corresponding determination techniques in [LC98].

4.3.2. Fixed Oxide Charge

Positive charge is fixed in a small region above the interface, mainly due to E' centres. An example of an E' centre is illustrated in fig. 4.13. In the SiO_2 crystal every silicon atom is connected to the next silicon atom via an oxygen atom. If one oxygen atom is missing, the silicon atom is weakly bound to its neighbouring silicon atom. This bond can be replaced by a trapped hole, which results in a fixed positive charge. Due to the missing oxygen, the defect is also referred to as oxygen vacancy and the charge is denoted by *fixed oxide charge*. Hence, because of several E' defects in the silicon dioxide close to the interface, a positive fixed charge is built up. The positive charge attracts bulk electrons which might form a layer that is short-circuiting the strip implants and deteriorates the strip isolation. This is also relevant before any irradiation, since the E' centres are already present as impurities in the material. Details concerning oxygen vacancies can be found in [Nic+02]. Although it has been suggested in [Dea80] that the fixed oxide charge concentration should be written as N_{f}, it will be denoted by N_{ox} in this thesis in order to stay consistent with other more recent publications. Additionally, within this thesis the term N_{ox} incorporates not only the pure fixed charge but also the net charge of the oxide trapped charge elsewhere. Hence, N_{ox} can be seen as the number of net fixed charge inside the SiO_2 surface of the device per area.

4.3.3. Other Defects

Additional to the interface traps and the fixed oxide charge, there are other charged defects present in the oxide. However, they are not relevant for this thesis and therefore only briefly mention for the sake of completeness:

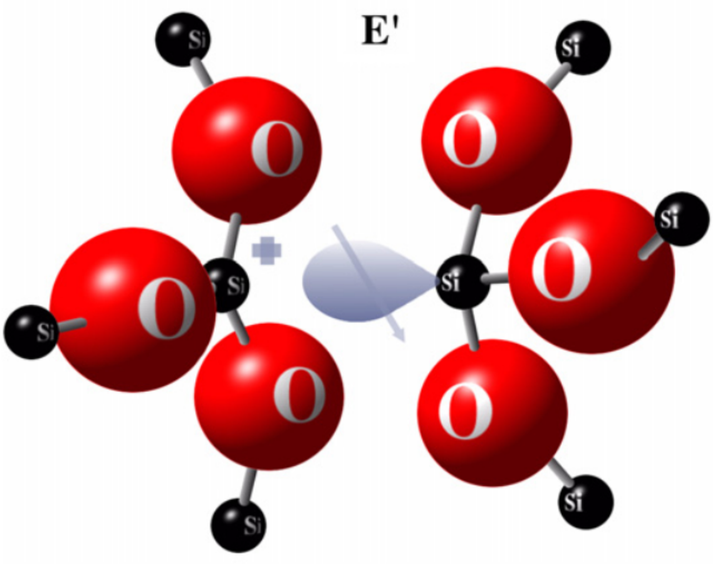

Figure 4.13.: Illustration of an oxygen vacancy also referred to as E' centre. Because of the lack of oxygen, two silicon atoms are weakly bound together. After the trapping of a hole the positive E' centre is formed [Len07].

- **Oxide trapped charge**: Traps can be formed in the silicon oxide, trapping electrons or holes. If an electron is trapped, the charge of the defect becomes negative. If a hole is trapped it is positive. As visualised in figure 4.11, this charge built-up is spread all over the SiO_2 region. The sum of the oxide trapped charge is effectively included in the oxide charge N_{ox} for this thesis, because the net charge in the oxide is the relevant parameter.

- **Border traps**: The term *border traps* has been suggested by [Fle92]. It is used to describe traps which are located at the border of the silicon and the oxide ($\approx 3\,\mathrm{nm}$ above the interface). These defects are able to communicate with the silicon substrate due to tunneling. The term border traps is not sharply distinct from interface traps.

4.3.4. Impact of Silicon Nitride

A silicon nitride layer (Si_3N_4) is sometimes applied above the silicon dioxide, which helps to improve the radiation hardness of the surface. The band gap of SiO_2 and Si_3N_4 is 8.8 eV and 5.1 eV, respectively. Since the band gap of Si_3N_4 is smaller and situated within the band gap of the oxide, electrons or holes created by radiation cannot cross the interface from Si_3Ni_4 to SiO_2, but the other way round. Both, valence and conduction band, are inside the band gap of SiO_2. Therefore, the energy states of electrons or holes inside the nitride are forbidden in the oxide. The result of this barrier is that, dependent on the electric field, charges produced in the nitride are trapped at the nitride-oxide interface and do not drift to the bulk-surface interface. In case of an electric field pointing away from the Si-SiO_2 interface or in absence of an electric field, electrons are trapped at the nitride-oxide interface, which reduces the net positive oxide charge. Additionally, holes which are generated inside the oxide are able to drift through the nitride into the top electrode.

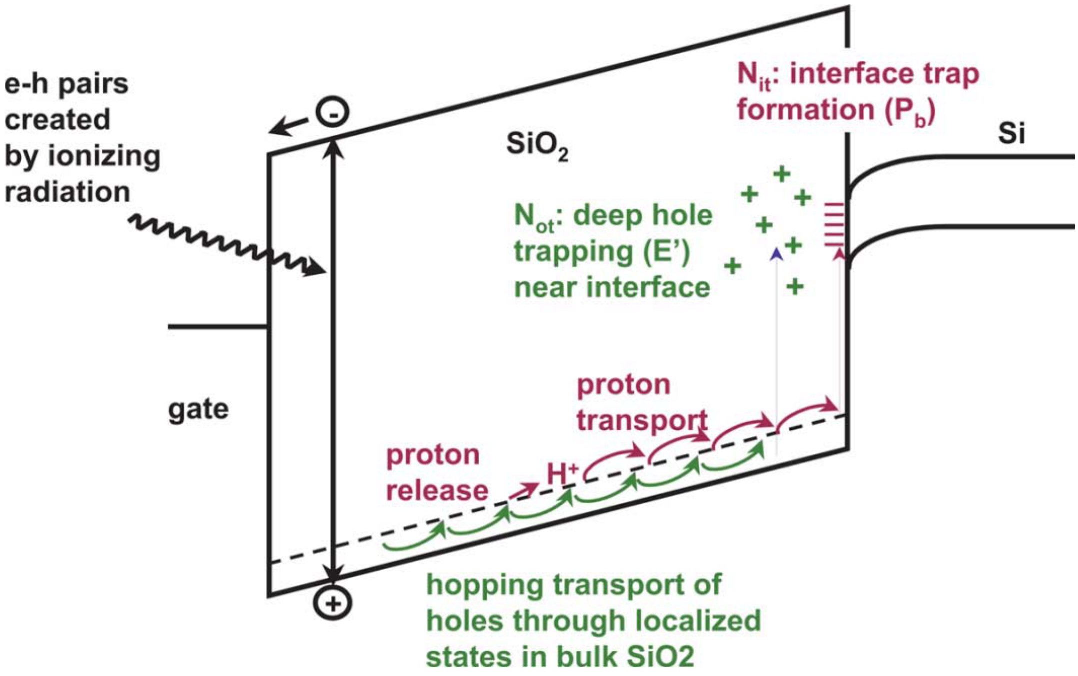
e-h pairs created by ionizing radiation
⊖
⊕
gate
SiO$_2$
Si
N_{it}: interface trap formation (P_b)
N_{ot}: deep hole trapping (E') near interface
proton transport
proton release
H$^+$
hopping transport of holes through localized states in bulk SiO2

Figure 4.14.: Mechanism of fixed oxide charge and interface trap formation by ionising radiation. The incident particle creates an electron-hole pair and the electron is accelerated towards the top electrode (gate). Diffusing holes can be trapped in E' centres close to the interface or release a proton, which forms an interface trap at the Si-SiO$_2$ interface [Sch+08].

4.4. Defect Generation due to Ionising Radiation

In general, irradiation with charged particles or photons can produce electron-hole pairs inside the crystal. A scheme of the damage mechanism for a metal oxide semiconductor structure (more details in section 5.2) is illustrated in fig. 4.14. The excited electron in the conduction band drifts into the gate when a positive voltage is applied. Even if no additional voltage is applied on the gate, the work function of the gate material (usually aluminium) leads to a Fermi level below the Fermi level of silicon. The resulting band bending accelerates electrons towards the gate. Vice versa, the hole is accelerated towards the interface. In the interface region they are trapped by oxygen vacancies (E' centre) and create a fixed positive charge. However, since the hole mobility is orders of magnitude smaller in SiO$_2$ than the mobility of electrons, some holes will react before reaching the interface. The holes (h^+) can react with a hydrogenated oxygen vacancy and release protons (H^+) through

$$\mathrm{V_{ox}H_2 + h^+ \rightarrow V_{ox}H_2^+ \rightarrow V_{ox}H + H^+}. \tag{4.5}$$

The proton drifts further to the interface where it can react with a passivated (hydrogenated) silicon and produce an interface trap

$$\mathrm{H^+ + SiH \rightarrow Si\bullet + H_2}, \tag{4.6}$$

which can be a P_{b0} or P_{b1} defect as discussed in 4.3.1.

The mechanism described above is based on the creation of electron-hole pairs in the crystal. However, some of the generated pairs recombine directly after the creation. The fraction of unrecombined holes is indicated in fig. 4.15 dependent on the electric field strength. A biasing

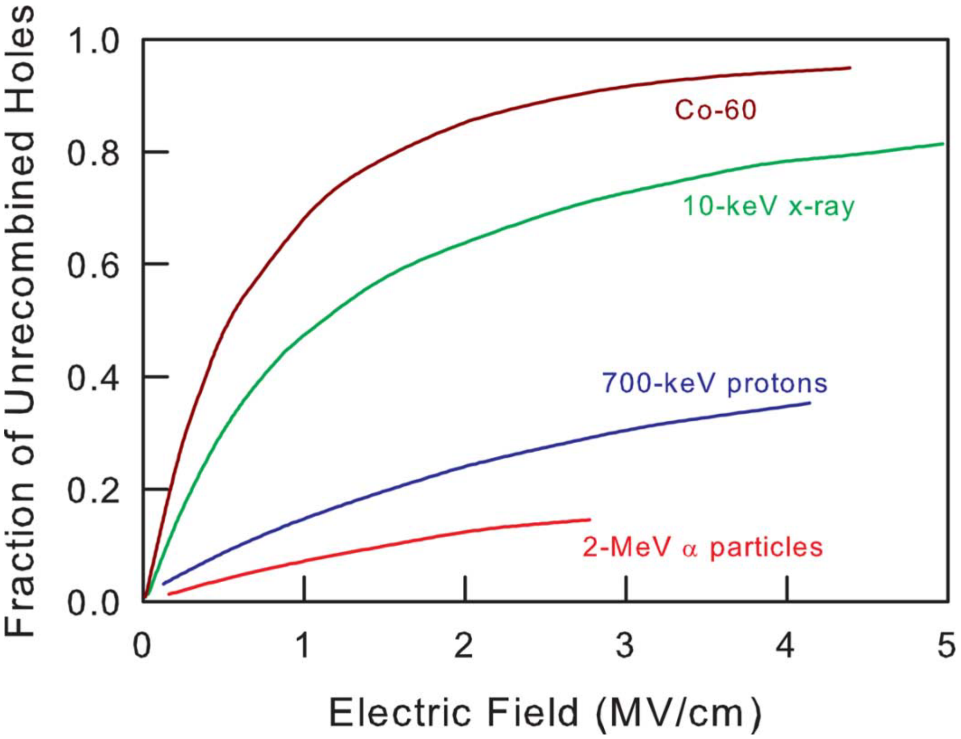

Figure 4.15.: Fraction of unrecombined holes due to irradiation with different particles depending on the electric field strength [Sch+08].

voltage on the gate leads to an electric field inside the SiO_2 layer. The charge is separated faster in a stronger electric field, thus the fraction of unrecombined holes (and electrons) increases. Besides the effect of an electric field, the incident particle type plays an important role as well. Heavier particles create a lot of electron-hole pairs along a straight line where the pair concentration is high. Therefore, the recombination rate is also higher than for the point like creation of electron-hole pairs of photons as incident particles. In case of 700 keV protons this result in 50% fewer unrecombined holes than for 10 keV x-rays, approximately.

Part II.

Test Devices and Procedures

5

Working Principle of Test Structures

There are several parameters that influence the performance of a silicon sensor. Some of them can be extracted from measurements of the full-sized device. However, often the processing parameters are not easily accessible. In any case, it is much more convenient to extract parameters of interest from dedicated test structures. These structures are usually placed on the same wafer around the main sensor and therefore reflect the quality of the same processing procedure. Since this work deals with the irradiation tests in the course of the CMS Phase-2 Outer Tracker sensor production, the respective test devices are introduced here in more detail.

5.1. Diode Structure

A diode is the least complex silicon device incorporating a pn-junction. It can be used to extract the leakage current and depletion voltage of the silicon substrate. In general, for thicknesses and doping concentrations used within this work the leakage current I scales with the applied bias potential V_{bias} following

$$I \propto \sqrt{V_{\text{bias}}} \tag{5.1}$$

because of the growth of the depletion zone (as explained in section 3.4.1). An example of a leakage current measurement over applied reverse bias potential, abbreviated by $I(V)$ curve, on a real diode is presented in figure 5.1a. The curve deviates from an ideal square root shape because the current is so small (sub-nA) that even the smallest parasitic currents from the edge regions get visible and affect the shape significantly.

The capacitance of a diode scales inversely proportional with the square root of the bias voltage for $V_{\text{bias}} < V_{\text{fd}}$ following

$$C = A\sqrt{\frac{\epsilon_0 \epsilon_{\text{Si}}\, e\, N_{\text{eff}}}{2V_{\text{bias}}}}, \tag{5.2}$$

with the area of the device A, the permittivities ϵ_0 and ϵ_{Si}, elementary charge e and effective doping concentration N_{eff}. If a capacitance measurement dependent on the applied bias voltage is performed, it is useful to plot $1/C^2$ instead of the bare capacitance value. This results in a linear graphical representation of the regime below the full depletion voltage. Such a $C(V)$ measurement is shown in fig. 5.1b with a linear fit represented by the orange line. As soon as the depletion zone reaches the backside of the diode, the capacitance stays constant. Consequently, $1/C^2$ is constant as well. This results in a very abrupt kink in the plot that marks the full depletion voltage V_{fd}. Fitting this constant region with another linear function enables the extraction of the depletion voltage defined as the intersection point of the two fits.

Another parameter that can be extracted of the linear functions is the effective doping concentration. It depends on the slope of the linear fit in the region below the depletion voltage with

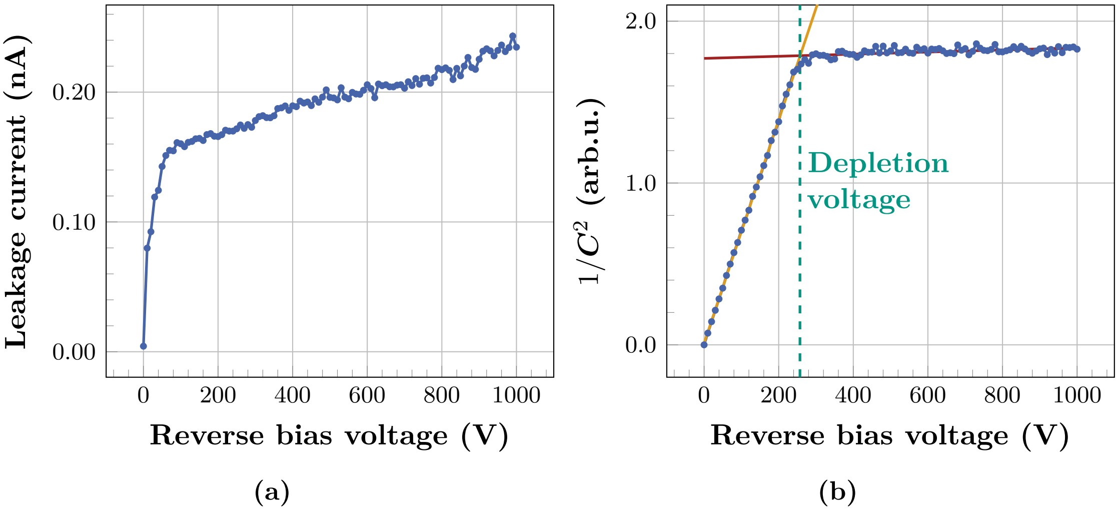

Figure 5.1.: Typical $I(V)$ (left) and $C(V)$ characteristics (right) converted to $1/C^2$ of an n-on-p diode. The depletion voltage can be determined via the intersection point of two linear fits and is indicated with the vertical green line.

$$|N_{\text{eff}}| = \frac{2}{A^2 \epsilon_0 \epsilon_{\text{Si}} e \frac{d(1/C^2)}{dV}}. \tag{5.3}$$

In principle, the depletion voltage and the effective doping concentration could also be determined from $C(V)$ measurements of strip sensors. However, the full depletion voltage of segmented sensors is higher than for planar diodes because of the segmentation. The electric field distribution in a segmented strip sensor is not as homogeneous as in a planar diode. High field regions build up around the strips with lower fields in between the strips. A semi-analytical investigation of the topic that is based on pure geometrical considerations has been performed and presented in [Bar+94; Bra+00]. The full depletion voltage of a strip sensor $V_{\text{dep, strips}}$ is higher than the diode's depletion voltage $V_{\text{dep, diode}}$ following

$$\frac{V_{\text{dep, strips}}}{V_{\text{dep, diode}}} = 1 + \frac{2p}{d} f(w/p) \tag{5.4}$$

with the strip pitch p (middle to middle distance of two adjacent strips), the substrate thickness d and a numerically approximated function $f(w/p)$ that depends on the width-to-pitch ratio w/p. This function $f(x)$ is given by

$$f(x) = -0.00111x^{-2} + 0.0586x^{-1} + 0.24 - 0.651x + 0.355x^2. \tag{5.5}$$

For strip sensors that are used in the course of this work, $d \approx 290\,\mu\text{m}$ and $w/p = 1/4$. Therefore, in case of 2S type strip sensors with a pitch of $p_{2S} = 90\,\mu\text{m}$ and PS type strip sensors with a pitch of $p_{PS} = 100\,\mu\text{m}$ the depletion voltage of the strip sensors is 19.62% and 21.8% higher compared to the diode, respectively. Because of the influence of the surface segmentation and factors that might additionally come with it, for example because of irradiation effects, it is more convenient to investigate diodes when the depletion voltage or the effective doping concentration are determined.

5.2. MOS Capacitor

The sandwich of a metal, oxide and semiconductor (MOS) is a common substructure that exists in most silicon devices. For example such a sandwich is usually part of transistors. With a MOS capacitor it is possible to characterise the oxide and especially the substrate-oxide interface. In case of strip sensors the silicon bulk is covered by oxide everywhere. Hence, the Si-SiO_2 interface is of importance for silicon detectors as well. For the CMS Phase-2 Outer Tracker sensor production, MOS capacitors are used to monitor the oxide quality. The functionality and extractions of useful parameters is explained in the following.

5.2.1. States of a MOS

The different states of a MOS structure with a p-doped bulk are illustrated in fig. 5.2 from (a) to (d). A representation of the band model is shown on the left side and the charge carrier distribution in the device is sketched on the right side. The first case (a) is called the *flat-band* condition since the bands are flat. It is achieved without any external bias when no charge is present in the oxide. However, technically it is impossible to produce such a perfect oxide and positive charge is always present, especially at the interface, where the transition of one crystal to another occurs (as described in section 4.3). Therefore, in practice the flat-band condition is achieved when a negative voltage is applied on the metal, compensating the positive charge. Additionally, the work function of the metal has to be taken into account.

A negative potential on the metal, also referred to as *gate*, results in an upward bending of the bands (b). Therefore, holes, which are the majority charge carriers in p-doped silicon, accumulate at the surface. Hence, the state is referred to as *accumulation*. If the polarity of the applied voltage is inverted (c), bands are bent slightly downwards. This leads to a repulsion of holes, thus depleting the near-surface substrate region of free charge carriers. Hence, this regime is called *depletion*. An increase of the gate voltage to even higher values (d) results in a surface *inversion*. The inversion is reached when the bands are bent so strongly that minority charge carriers (electrons) start to aggregate below the oxide in the substrate.

5.2.2. Flat-band Voltage Extraction from a Capacitance Measurement

Two parameters can be extracted from a high-frequency $C(V)$ measurement on a MOS capacitor: The oxide thickness t_{ox} and the flat-band voltage V_{fb}, which is further connected to the fixed effective positive oxide charge concentration $N_{\mathrm{eff,\,ox}}$. An exemplary $C(V)$ characteristic (measured at 1 kHz) is illustrated in fig. 5.3a for a MOS with a p-type substrate and an aluminium gate. In the scope of this work, the bias potential is always applied on the backside and the gate is grounded with a probe needle. Details of the measurement setup can be found in section 6.1. In some publications the bias is applied on the gate and the backplane is grounded. This leads to a sign inversion of the x-axis compared to results presented within this work. If a positive voltage is applied on the backside, the hole accumulation in the surface region is promoted. Hence, this is the accumulation regime and the capacitance is given by the isolating oxide ($C_{\mathrm{acc}} = C_{\mathrm{ox}}$). It is possible to determine the oxide thickness following the parallel plate capacitor equation

$$t_{\mathrm{ox}} = \epsilon_0 \epsilon_{\mathrm{SiO_2}} \frac{A_{\mathrm{gate}}}{C_{\mathrm{ox}}}, \tag{5.6}$$

with the permittivities ϵ_0 and $\epsilon_{\mathrm{SiO_2}}$ and the gate area A_{gate}. Since the oxide thickness does not change by radiation damage it is not extracted in the scope of this work. However, it is an important parameter that is determined in the course of the process quality control during the CMS Phase-2 Outer Tracker sensor production.

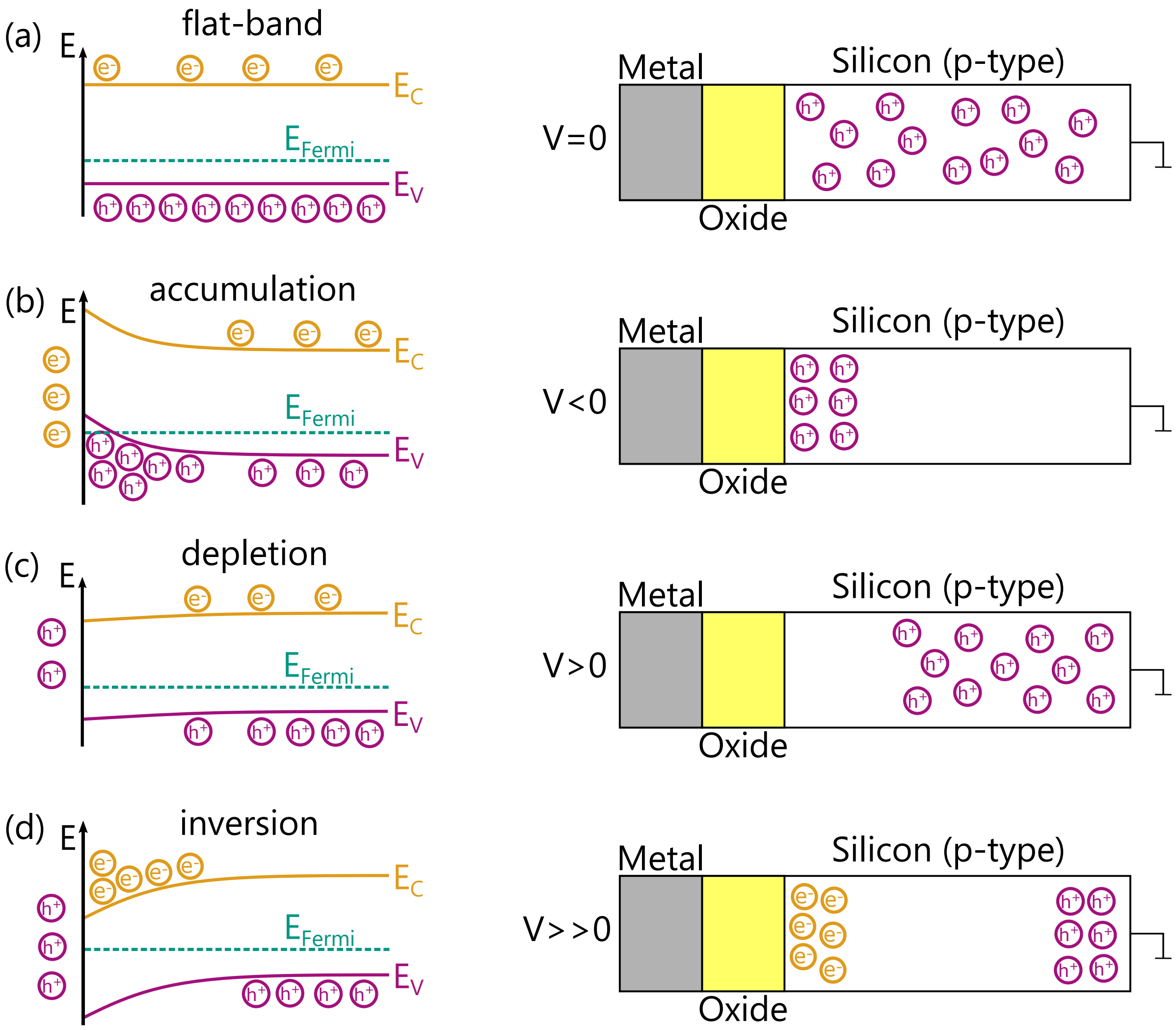
(a)
flat-band
E
e-
E_C
E_{Fermi}
E_V
h+
Metal
Silicon (p-type)
V=0
Oxide
(b)
accumulation
V<0
(c)
depletion
V>0
(d)
inversion
V>>0

Figure 5.2.: Explanation of the different conditions of a MOS capacitor dependent on the applied gate voltage. The band model scheme is shown on the left side and a sketch of the appropriate device on the right side. In a perfect MOS, the flat-band condition would be reached for the flat-band voltage $V_{fb} = 0$. The figure is reproduced from [Har17].

With a decrease of the voltage, the accumulation layer is destructed and the near-surface substrate starts to deplete. The capacitance of the depleted region C_{dep} is now connected to the oxide capacitance in series, thus decreasing the total capacitance following

$$C_{\mathrm{dep}} = \frac{C_{\mathrm{ox}} \cdot C_{\mathrm{dep}}}{C_{\mathrm{ox}} + C_{\mathrm{dep}}}. \tag{5.7}$$

The flat-band voltage is often extracted as the inflection point of the curve. In [PGP14] it has been complained that the inflection point does not match the flat-band condition exactly. However, usually the flat-band voltage is used to compare different oxide qualities to each other, thus an approximated value is sufficient if it is extracted in a similar reliable way. For this work another extraction method is used that is explained and discussed in greater detail in section 7.3.1. Since the flat-band voltage shift from 0 V is a result of the positive oxide charge, it can be used to determine the effective oxide charge concentration via

$$N_{\mathrm{eff,\ ox}} = \frac{C_{\mathrm{ox}}}{eA_{\mathrm{gate}}}(V_{\mathrm{fb}} - \phi_{\mathrm{ms}}), \tag{5.8}$$

with the elementary charge e and the work function difference of the metal and the semiconductor ϕ_{ms}. Radiation with ionising particles increases the effective oxide charge concentration, which can be characterised by the measurement of the flat-band voltage shift.

If the bias voltage is decreased further to the inversion regime, electrons start to aggregate below the surface/substrate interface. For a quasi-static measurement, the capacitance would increase to the full oxide capacitance, since the surface is not depleted. However, in a high-frequency measurement the minority charge carriers are not visible. Consequently, the total capacitance in this regime is given by the oxide and bulk capacitance connected in series

$$C_{\mathrm{inv}} = \frac{C_{\mathrm{ox}} \cdot C_{\mathrm{bulk}}}{C_{\mathrm{ox}} + C_{\mathrm{bulk}}}. \tag{5.9}$$

The $C(V)$ characteristics of a MOS capacitor with an n-doped bulk is illustrated in fig. 5.3b. In principle, the situation is similar to the p-type MOS because the measurement depends on the surface quality, which is independent of the doping of the bulk. Consequently, the flat-band voltage is similar in both cases. The main difference between p-type and n-type bulk is that the accumulation and inversion regimes are inverted. Electrons are the majority charge carriers in n-type silicon and holes in p-type silicon. Thus, the electron aggregation for negative voltages is now the accumulation regime and the measured capacitance is equivalent to the oxide capacitance. The inversion occurs for bias voltages above the flat-band voltage, where holes are aggregated at the surface. In this state, the capacitance measurement yields the oxide capacitance in series with the bulk capacitance, similarly to the inversion condition for p-type base material. The equivalent of the band scheme in fig. 5.2 for a MOS capacitor with an n-type bulk can be found in fig. A.1.

5.3. GCD Structure

A gate-controlled diode (GCD) is a combination of a diode and a MOS sandwich. In the frame of this work it is used to determine surface currents that are mainly generated by interface (Si-SiO$_2$) traps. Similarly to the MOS structure, the oxide quality is determined but in terms of traps at the interface instead of an effective charge, thus flat-band voltage shift. The functionality of a GCD with a p-type substrate is illustrated in fig. 5.4. Again, there are the three states accumulation, depletion and inversion. First of all, a constant bias potential V_{bias} is applied to the diode part (pn-junction on the left) of the structure. Consequently, a

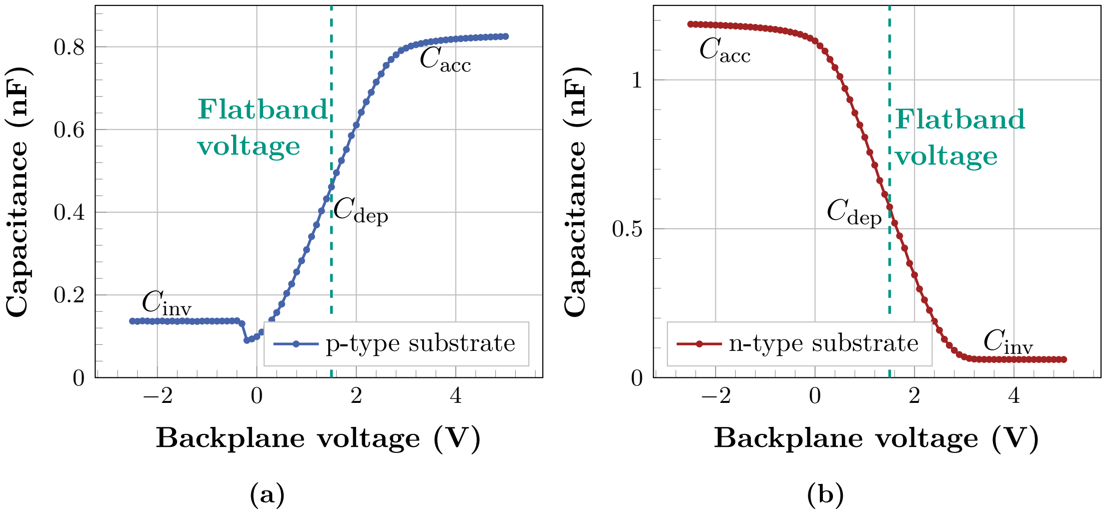

Figure 5.3.: $C(V)$ characteristics (at 1 kHz) of a MOS structure with p-type (left) and n-type (right) bulk. The accumulation and inversion regions are inverted because of the different majority charge carrier type. Flat-band condition is reached in both cases at 1.5 V, approximately.

small depletion zone emerges around the junction. Then, the gate voltage V_{gate} is varied. With a gate potential smaller than the flat-band condition of the MOS part, the hole accumulation layer below the surface is established (left picture). If $V_{\mathrm{gate}} > V_{\mathrm{fb}} + V_{\mathrm{diode}}$, a depletion zone under the oxide growths and connects to the depleted region around the diode part (middle). Applying an even higher gate potential results in the inversion layer of electrons close to the surface (right).

The impact on the current can be seen in a real measurement in fig. 5.5. In this case, a diode current over applied gate voltage characteristic is shown for a GCD with a p-type substrate. The constant diode bias is −5 V on the backplane. Around 0 V the inversion layer is built up on the right of the plot. The current in inversion is nearly constant and can be extract by the mean value of the current in that plateau region. If the absolute value of the gate voltage is increased further until the flat-band condition is reached, a depletion zone below the oxide is established. This depletion zone grows together with the space charge region of the diode part. Hence, interface defects of the $\mathrm{Si/SiO_2}$ interface are exposed to an electric field that directs the current into the diode so that it adds up to the base current. Therefore, the negative diode current is increased by the current generation of the interface defects. Applying a gate potential that is smaller than the flat-band voltage plus the diode bias results in the accumulation condition where the interface states are disconnected again from the pn-junction. As indicated in the figure, the surface current I_{surf}, which is the parameter of interest, is the difference between the current in depletion and in inversion.

From the surface current the *surface generation velocity* s_0 can be obtained via

$$s_0 = \frac{I_{\mathrm{surf}}}{e n_i A_{\mathrm{gate}}}, \tag{5.10}$$

with the elementary charge e, the intrinsic free charge carrier concentration of silicon n_i and the gate area A_{gate}. Since the surface generation velocity is the surface current normalised with the area of the device and the intrinsic charge carrier concentration, it can be used to compare measurements of GCDs with different geometries. The surface generation velocity depends on

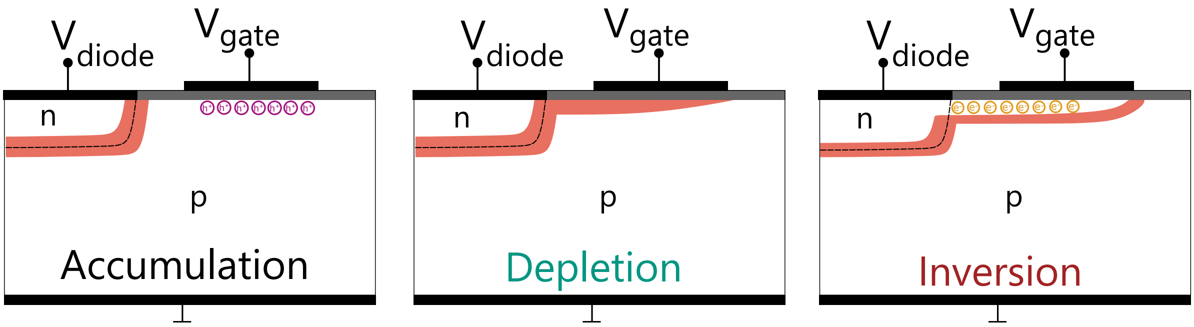

Figure 5.4.: Working principle of a gate-controlled diode (GCD) with a p-type substrate. In accumulation (left) the small depletion zone of the diode is not affected by the area beneath the gate. If a gate voltage smaller than the flat-band voltage is applied, the area depletes and the two depletion zones merge together (middle). Consequently the diode current is increased by surface currents that emerge in the region below the oxide. Applying a higher gate voltage results in the inversion regime with the corresponding electron layer (right). Hence, the depletion zone decreases again as well as the measured current. The figure is reproduced from [Per11].

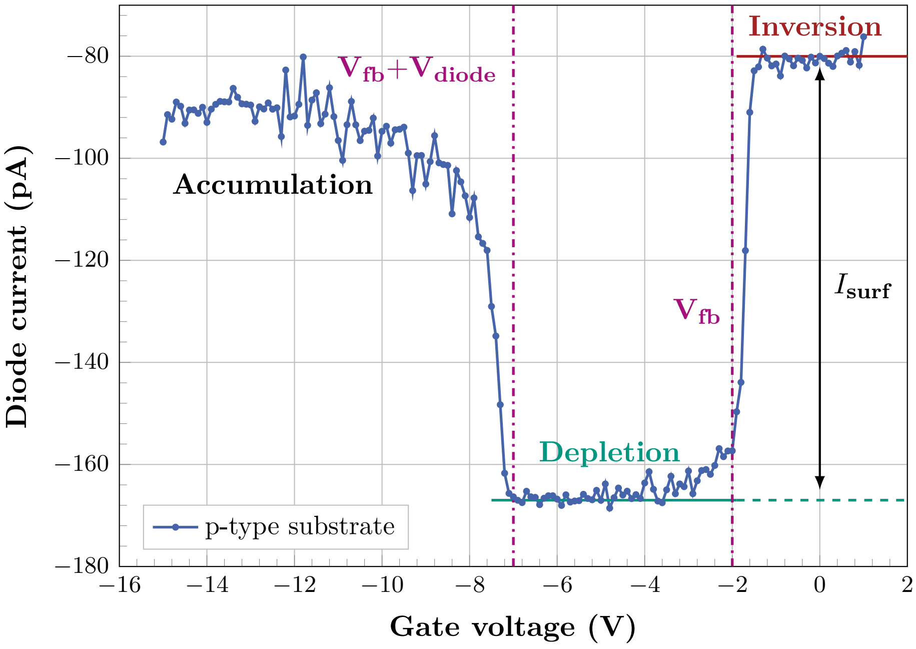

Figure 5.5.: Measurement of the diode current dependent on the gate voltage of a p-type GCD. The accumulation, depletion and inversion regions are indicated as well as the extraction procedure of the surface current I_{surf}.

the interface trap density of states D_{it} and capture cross section σ_{s}

$$s_0 = \frac{\pi}{2} \cdot \sigma_{\mathrm{s}} v_{\mathrm{th}} D_{\mathrm{it}} k_B T, \tag{5.11}$$

with the thermal velocity v_{th}, Boltzmann's constant k_B and temperature T. If further an equal distribution of the states inside the band gap is assumed, D_{it} translates to the interface trap concentration N_{it} with

$$N_{\mathrm{it}} = D_{\mathrm{it}} \cdot \frac{E_{\mathrm{g}}}{2}. \tag{5.12}$$

However, since these calculations depend on assumptions regarding details of the interface traps, within the scope of this work only the surface generation velocity is extracted and compared.

6

Experimental Basics and Procedures

6.1. Probe Stations

There are two custom-made probe stations at the Institute of Experimental Particle Physics (ETP). Both feature similar functionality, which is to measure electrical properties of planar silicon chips. A picture of the setup's exterior can be found in appendix B. The interior of the setup is shown in fig. 6.1. It is surrounded by a lightproof aluminium housing. The sensor under test (here a 2S sensor) is placed on an aluminium chuck. On the edge of the chuck, two temperature sensors are placed that deliver a reference temperature for the whole chuck and consequently for the sensor under test. With the help of four Peltier elements situated below the chuck, the temperature of the sensor can be controlled in a range from $-30\,°\mathrm{C}$ to $40\,°\mathrm{C}$. The waste heat of the Peltier elements is dissipated via a precooling system with a chiller. The housing is constantly flushed with dry air to reduce the humidity. This enables cooling to temperatures below the dew point of the environmental air without any condensation or ice formation on the chuck.

A global bias potential on the device under test is usually applied on the chuck, thus on the backplane of the sensor. Ground potential is applied by the bias probe connected to the bias ring. If strip measurements are performed or more needles are required, for example for the measurement on a gate-controlled diode, two probes with smaller needles are available. The tip radius of these is $2\,\mu\mathrm{m}$, which is considerably smaller than the $7\,\mu\mathrm{m}$ thick bias needle. In order to place the needles, a microscope with a camera is used that projects the microscope picture to a monitor outside the setup. Available devices for electrical characterisation of the silicon chip under test are a high voltage power supply for voltages of up to $1000\,\mathrm{V}$, another low voltage power supply, two current measurement devices and an LCR meter.

The whole setup is controlled with a custom-made software framework based on Python [Pyt]. Temperature monitoring and control is performed by an autonomously working Raspberry Pi[1] that communicates with the main system located on a standard PC. A custom-made switching matrix, based on several relays, sets the desired connections between the measurement devices and the needles. Thus, every measurement type, like global leakage current, global capacitance or specific strip measurement, has a unique switching matrix state.

6.1.1. Improvements of the Probe Station Chuck

Cooling the chuck of the probe station down to a temperature of $-20\,°\mathrm{C}$ reveals new challenges compared to room temperature. Since the environmental air is warmer than the chuck, the temperature of the chuck gets less homogeneous. This is because of the warm dry air stream that circulates around in the interior and warms up the chuck at the edges. Since the temperature sensors are situated on the borders of the chuck, differences of the measured temperature and the real temperature on the position where the sensor under test is placed, can occur. A severe dependence of the sample temperature on dry air flux has been observed prior to

---

[1] Microcontroller with operating system [Ras21]

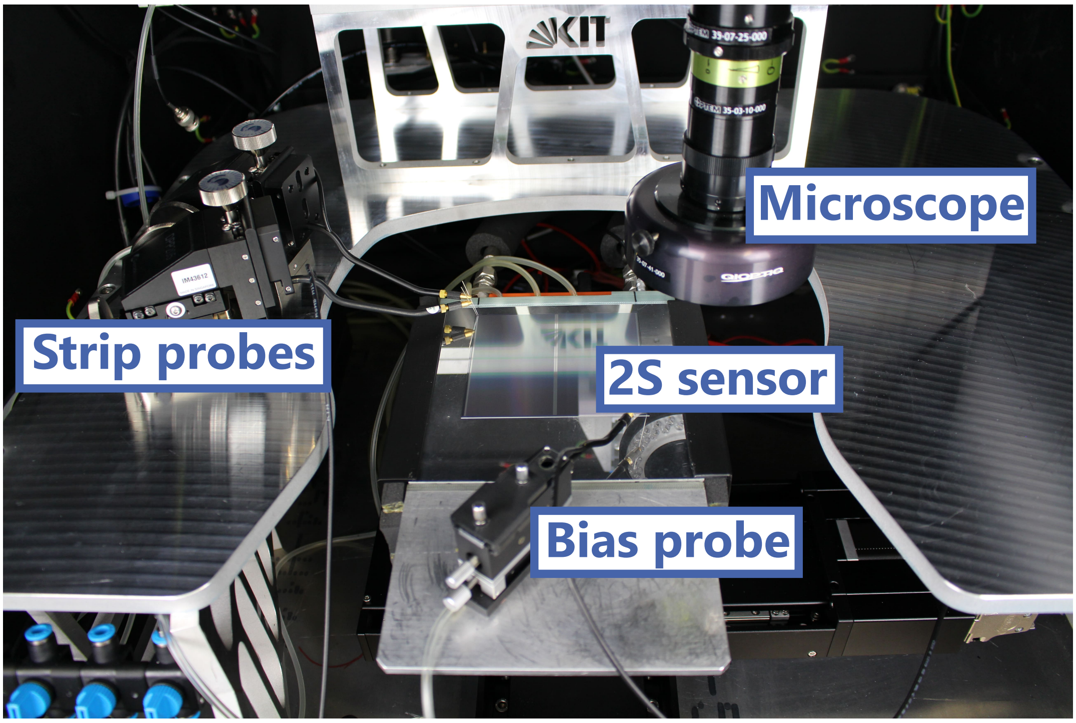

Figure 6.1.: Probing of a sensor inside the probe station. Specific strip or pixel measurements can be performed with the help of two strip probes. A 3D-printed support structure on the edges of the chuck helps to establish a more homogeneous temperature distribution as explained in section 6.1.1.

any precautions during the regular testing of irradiated samples in the frame of chapter 7. To mitigate the impact of the dry air flux, the edges of the chuck have been covered with an insulation material and a 3D-printed support structure that can be seen in fig. 6.1. The temperature sensors are embedded in this structure so that they are insulated from the air flux. This improved the temperature homogeneity of the chuck for low temperatures but still it is not perfect.

The temperature distribution with a set temperature of $-20\,°\mathrm{C}$ is shown in fig. 6.2. This distribution has been measured with an infrared camera. As indicate with the coloured scale on the right, the temperature varies between $-18\,°\mathrm{C}$ on the outer edges and corners and below $-21\,°\mathrm{C}$ inside. This variation is also a result of the positions of the four Peltier elements (each $4 \times 4\,\mathrm{cm}^2$). They are placed centrally with a distance of approximately $2\,\mathrm{cm}$ from the borders and can be identified by the darker regions. The usual placement and measurement location for investigations in this work is indicated with the white dashed rectangle. In this region, the temperature is roughly $1\,°\mathrm{C}$ below the set temperature. With this measurement, a reasonable qualitative overview of the temperature distribution on the chuck is given which shows that the edges and corners are considerably warmer than the central region for a set temperature of $T_{\mathrm{set}} = -20\,°\mathrm{C}$. However, since the concrete temperature depends on the settings of dry air flux, chuck position and precise sample location on the chuck, it is not corrected for it in the following.

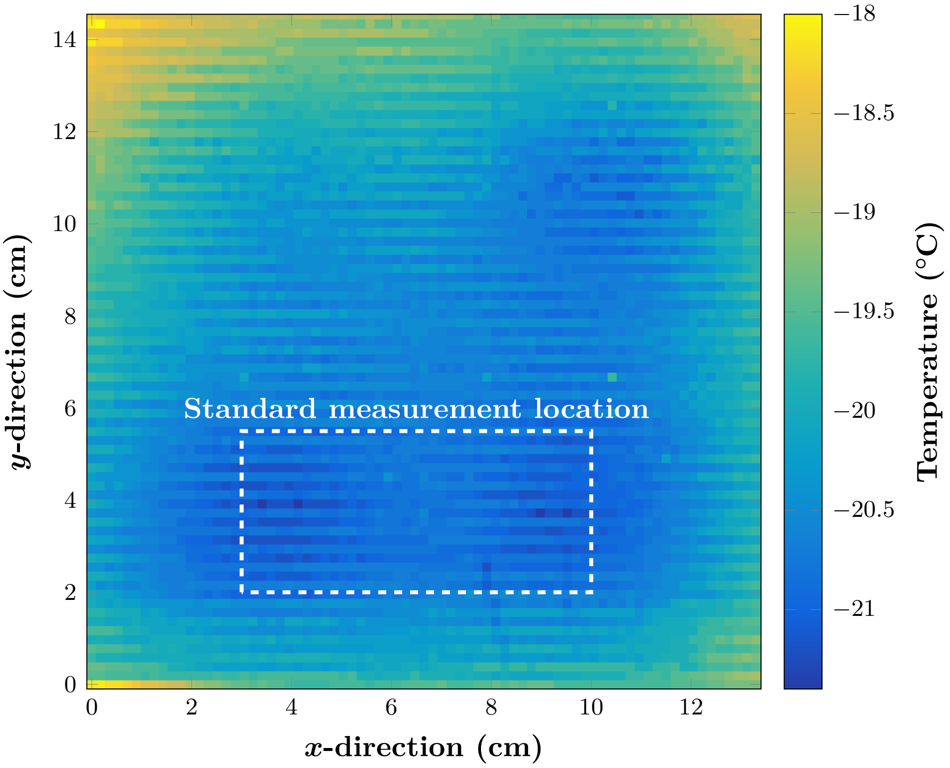

Figure 6.2.: Temperature distribution on the chuck with the usual measurement position for samples tested in the course of this work. The target temperature is $T = -20\,°\mathrm{C}$.

6.2. Signal Measurements with an ALiBaVa Setup

It is essential for the functionality of a sensor that it is able to deliver a certain signal strength. Hence, signal measurements are of great importance in general and in particular for this work and the quality assurance in the course of the Outer Tracker sensor production. To characterise the signal, a custom-designed setup is used that is placed inside an aluminium box. Similar to the probe station setup, the box is required to establish a dry air environment for the cooling and to shield the sensor from light. The heart of this setup is an ALiBaVa[2] system. A motherboard that processes the data is placed outside of the box. The daughterboard that is mounted on a support structure made of GRP[3] is shown in fig. 6.3. The strip sensor under test is placed on the copper plate and wire-bonded to a readout chip, the Beetle[4] chip, over a pitch adapter. Temperature is monitored with a PT1000 sensor on the edge of the copper plate. The achievable temperatures are in a range of −20 °C for measurements and up to 80 °C for accelerated annealing. Similar to the probe stations, Peltier elements, which are located below the copper plate under another copper bridge, are used to control the temperature. The high voltage is applied over the backplane while a bias bond grounds the bias ring. A scintillator is placed below the sensor to trigger the readout when an ionising particle traverses the sensor-scintillator sandwich.

---

[2] ALiBaVa: **A** Liverpool **Ba**rcelona **Va**lencia setup

[3] GRP: **G**lassfibre **R**einforced **P**lastic

[4] Analogue readout chip that has been developed for LHCb [ASI07]

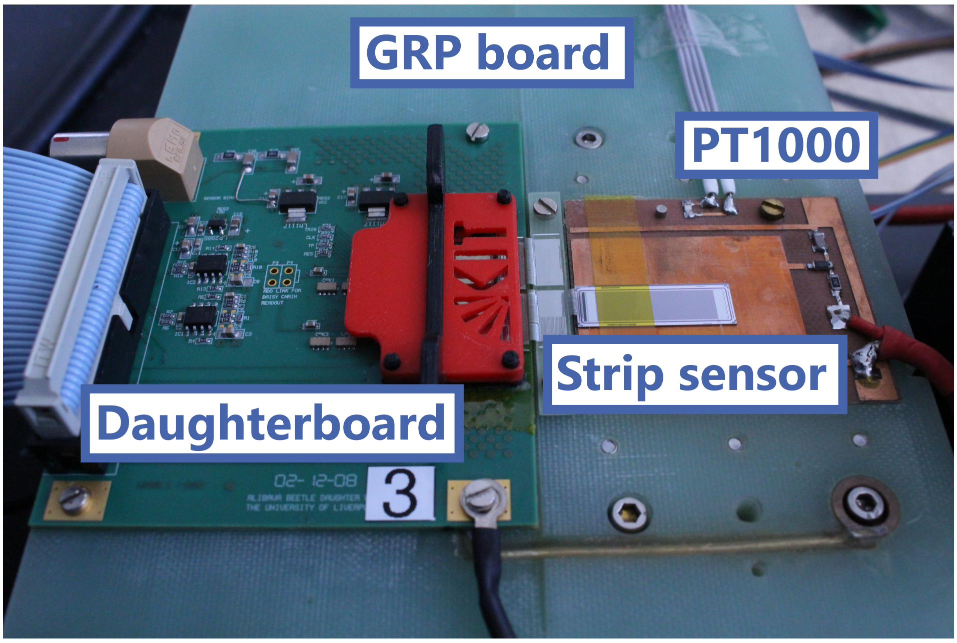

Figure 6.3.: The ALiBaVa setup. The support structure is a GRP board. An ALiBaVa daughterboard and a copper plate are mounted onto it. The strip sensor is placed onto the copper plate and wire-bonded over a pitch adapter to the Beetle chip on the daughterboard. The Beetle chip is secured by the red cover, thus not visible in the picture.

6.2.1. Noise and Calibration

Before the actual signal of the strip sensor can be measured, noise esteminations are performed and the gain is calibrated. The *gain* is the conversion factor from the internal ADC[5] unit of the Beetle chip's channels to the signal in electron equivalent charge. Both, the noise of the sensor and the gain, are extracted before each signal measurement run. To estimate the noise, a so-called *pedestal* run is performed. The readout of all channels is triggered 5000 times randomly. In general, the $ADC(s,e)$ value for every strip s and event e is given by

$$ADC(s,e) = P(s,e) + D(e) + S(s,e) \tag{6.1}$$

with the pedestal $P(s,e)$, common mode $D(e)$ and actual signal $S(s,e)$. However, in a pedestal run where the readout is randomly triggered, the signal term is zero. The common mode is a fluctuation of the electronic signal due to external disturbance that affect all strips in a similar way. Since these fluctuations are Gaussian distributed with a mean value (over events) at zero, the pedestal can be calculated as the mean over all events.

$$P(s) = \frac{1}{N}\sum_{e=1}^{N} ADC(s,e), \tag{6.2}$$

The common mode per event can then be determined by the mean of $ADC(s,e)$ subtracted by the pedestal for every strip with

$$D(e) = \frac{1}{N_s}\sum_{s=1}^{N_s}(ADC(s,e) - P(s)). \tag{6.3}$$

---

[5] ADC: **A**nalog **D**igital **C**ounts

The estimation of the common mode enables a correction for it. However, this method is limited to a reasonable level of external noise. The common mode correction is done by defining a corrected pedestal $P_c(s)$ modifying eq. (6.2) to

$$P_c(s) = \frac{1}{N}\sum_{e=1}^{N} ADC(s,e) - D(e). \tag{6.4}$$

Finally, the noise per strip $N(s)$ can be calculated by the sample standard deviation of this corrected pedestal

$$N(s) = \sqrt{\frac{1}{N-1}\sum_{e=1}^{N}(P_c(s) - \bar{P}_c(s))^2}. \tag{6.5}$$

The noise per strip is an important parameter for the following signal analysis. Additionally, it can be used to identify potential issues with the setup or device under test before full signal runs are conducted.

A typical noise distribution over the channel number is presented in fig. 6.4a. The figure includes only channels that are actually connected to a strip of a test sensor. It can be seen that the strip noise is usually around 4 ADC for all channels.

The next step is to determine the conversion factor in units of ADC into electron equivalent charge e^-. This is done with the help of a *calibration* run. Every channel on the Beetle chip has its own capacitor that can be charged with a configurable number of charges. In the frame of this work, these capacitors are always charged with 15720 electrons. Then, the capacitors are discharged and the respective current flows into the channels. With the extraction of the *ADC* signal of each channel, the gain can be calculated as the quotient

$$\mathrm{gain}(s) = \frac{15\,720\,\mathrm{e}^-}{ADC(s)}. \tag{6.6}$$

In total 5000 events are recorded for a calibration run. The timing between discharge of the capacitors and the recording of the signal of the channels is varied between 0 ns and 100 ns. For every 1 ns step 50 pulses are injected. The resulting signal is averaged over these 50 pulses. Then, the timing which leads to the maximum signal is taken to extract the conversion factor where most of the injected charge has been recorded. The outcome of a typical gain calibration is indicated in fig. 6.4b for the same channels and the same test sensor as in fig. 6.4a. It can be seen that the gain is around $210\,\mathrm{e}^-/\mathrm{ADC}$. Thus, the noise in units of electron charge e is

$$\sigma \approx 4\,\mathrm{ADC} \times \frac{210\,\mathrm{e}^-}{\mathrm{ADC}} \approx 840\,\mathrm{e}^-, \tag{6.7}$$

which is close to the specified value of $1000\,\mathrm{e}^-$ for the CBC and therefore reasonable to emulate the performance during Phase-2.

6.2.2. Signal Analysis

In the measurement setup, a ^{90}Sr radioactive source can be moved right above the sensor with a moveable support structure. Inside the source, strontium decays into ^{90}Yttrium which further decays to ^{90}Zirconium. The second decay with a much shorter lifetime than the first results in electron emission with an energy of $E = 2.282\,\mathrm{MeV}$. These MIP-like electrons traverse the sensor where they generate electron-hole pairs and reach the scintillator beneath. With a high voltage applied to the sensor, the electron-hole pairs drift inside the electric field and generate a signal, as explained in section 3.6.

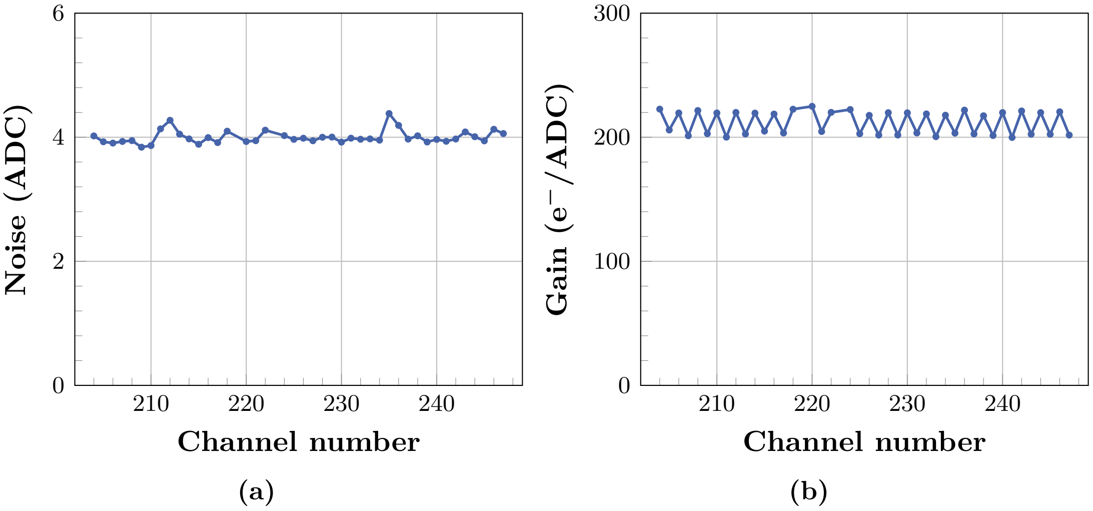

Figure 6.4.: Strip noise and gain estimation. The sensor was irradiatied with an applied fluence of $\Phi = 4.5 \times 10^{14}\,\mathrm{n_{eq}/cm^2}$ and measured with a bias voltage of 600 V at a temperature of $T = -20\,°\mathrm{C}$. The noise is around 4 ADC and the gain is between 200 and 215 e/ADC

During the *radioactive source* run, the scintillator triggers the readout of the sensor 100 000 times. All channels of a chip are read out if the chip is triggered, because there is a priori no information of where the incident particle hit. Thus, most of the acquired data is just noise. To find the actual hit position and the interesting channels, a cluster algorithm is applied. First, the channel with the highest signal, the *seed*, is identified. If the signal-to-noise ratio *SNR* is smaller than a specific limit, the event is discarded. In the frame of this work the required signal-to-noise ration for a channel to be identified as a seed is

$$SNR_{\mathrm{seed}} > 5. \tag{6.8}$$

That means that the signal has to exceed $5 \times \sigma$, with the strip noise $\sigma = N(s)$, to be included. Consequently, following the example from the previous section, this translates to a minimum of 4200 electrons. If the requirement eq. (6.8) is fulfilled for one channel, the recorded signal of neighbouring strips is added up if the signal-to-noise ratio of the neighbour achieves

$$SNR_{\mathrm{neighbour}} > 2. \tag{6.9}$$

The sum of the *seed signal* and the neighbouring strips that together define a cluster is denoted by *cluster signal*.

A 2D histogram of the cluster signal with respect to the timing is shown in fig. 6.5. The pulse shape can indirectly be reconstructed with the help of a system-wide 100 ns clock. If a particle traverses the scintillator, thus triggers the readout at a certain time, the timing can be measured relatively to the end of the clock. Hence, all events can be assigned in a 0 ns to 100 ns wide time window. The y-axis starts at 4200 electrons because the cluster signal cannot be smaller than the seed signal that itself has to be above the 5σ threshold following eq. (6.8). This data representation results in an effective reconstruction of the pulse shape coloured in yellow in the picture. Additional to the requirement of a certain signal strength that discriminates background, a time window is applied. It is chosen such that the maximum of the signal is included as illustrated with the vertical white lines in the plot. Only events that occur in the time window between 35 and 60 ns are accepted. This is to avoid a distortion of the maximum signal by events with bad timing.

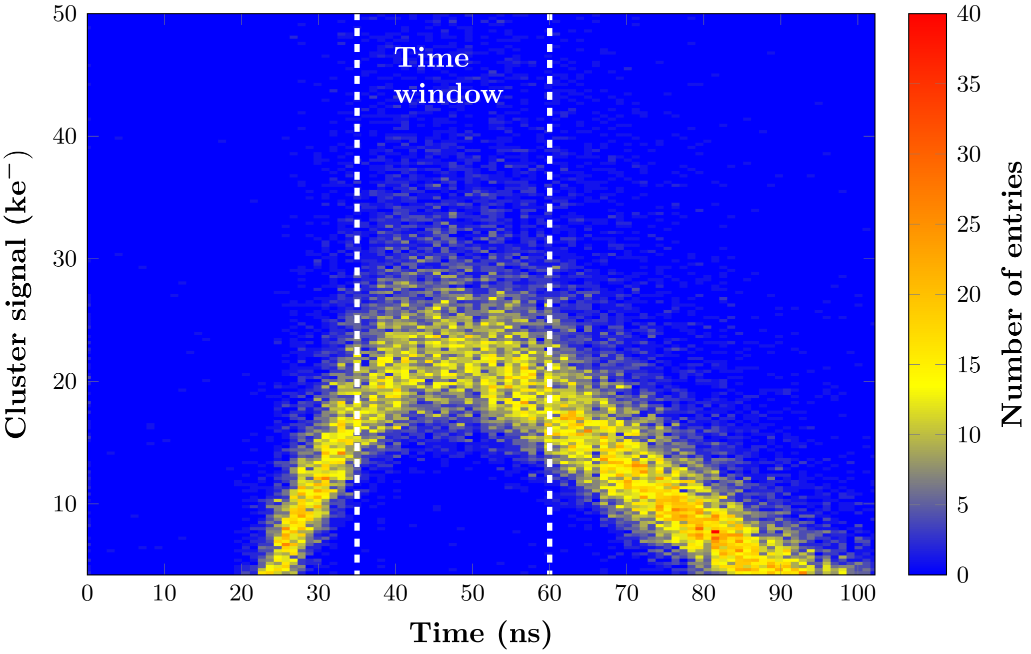

Figure 6.5.: Timing of the cluster signal. Every event consists of a certain time stamp with an associated signal. The 2D histogram effectively reconstructs the pulse shape statistically. Events in a time frame that are outside of the time window from 35 to 60 ns are rejected in the following.

Finally, after the noise estimation, gain calibration, radioactive source run and background discrimination has been performed, the signal distribution can be analysed. The parameter of interest for this work is the most probable value (MPV) of the seed signal. This is because it has to be ensured that the strips are able to exceed a certain threshold that will be applied in the real detector. Since the readout will be binary in Phase-2, a clustering cannot be performed in a similar way based on the absolute value of the signal strength. Instead, a certain threshold is applied beforehand and only strips are counted that exceed this limit with a signal generated by an incident particle.

The seed signal distribution is displayed in fig. 6.6. In general, the deposited energy determining the signal follows a Landau distribution that has to be convoluted with a Gaussian because of electronic noise (compare section 3.5.1). However, since the seed signal lacks the signal of neighbouring strips it does not match a perfect Landau-Gaussian shape. Nevertheless, as can be seen in the figure, the red fit function that is based on [KS84] is acceptable. It yields an MPV for the Landau fraction of the fit of 15 205 e^-. The value is indicated with the vertical red line and the vertical green line marks the cut-off at 5σ. Without this cut a second considerably higher noise peak would rise up on the left side of the line. It can be seen that the right side of the cut includes the whole distribution, thus no signal is lost in noise. Hence, it can be concluded that nearly all incident particles would have been detected in a real use case. Consequently, the sensor is fully functional in this example of an irradiated sensor.

The uncertainty on the signal measurements and analysis procedure is not trivial to estimate. The variance of a Landau distribution is not defined. This makes it difficult to estimate an uncertainty already from a statistical point of view. Additionally, systematic uncertainty have to be taken into account. The channel-to-channel variations are 1.9% but chip-to-chip variations can be as large as 19.1% [Löc06]. In total, an estimation following [Met20] holds an uncertainty on the MPV of 1000 e^-, approximately.

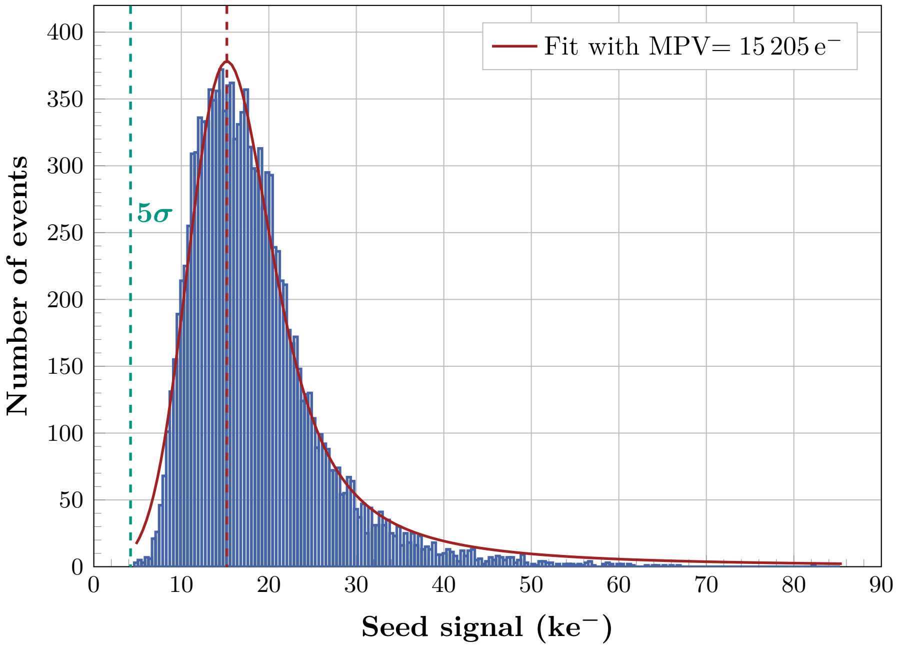

Figure 6.6.: Exemplary seed signal distribution of an irradiated sensor. The vertical dashed green line indicates the cut-off due to the required *SNR* of at least 5. Since the line does not cut into the distribution it can be concluded that nearly all of the incident particles would have been recognised in a real detector. The red curve marks a Landau-Gaussian convoluted fit with an MPV of the Landau fraction of 15205 electrons.

6.3. Irradiation Facilities

In this section all the irradiation facilites that were used in the scope of this work are presented. Every proton irradiation was performed at the proton irradiation facility at KIT and the X-ray irradiations with the in-house X-ray setup at ETP. The neutron irradiation for the investigations of the interstrip isolation in chapter 8 were performed in Ljubljana.

6.3.1. Proton Irradiation at ZAG

Proton irradiation is performed at the ZAG (Zyklotron AG) at KIT [ETPb]. The proton beam from with an average energy at the target of approximately 23 MeV of the compact cyclotron (KAZ) is used. The beam diameter is 4 mm – 8 mm. Because of the small beam spot but also the high beam current of 2 µA, the samples have to be scanned. In order to do so a meander-shaped scanning procedure has been developed. This also makes the fluence deposition more homogeneous. The irradiation setup is shown in fig. 6.7. The samples are fixated with polyimide strips inside the aluminium box in front of the beam pipe. During the irradiation, the box is constantly flushed with cold nitrogen that cools the interior down to −30 °C. After the irradiation, the applied fluence can be extracted from an activity measurement of a Ni-foil. The total uncertainties have been estimated with 15%. In addition to the bulk damage, protons heavily ionise the material. The corresponding estimated dose is 145 kGy per $1 \times 10^{14}\,\mathrm{n_{eq}/cm^2}$ (calculated via Ref. [NIS]). More details about the setup and the procedures can be found in [Fur06].

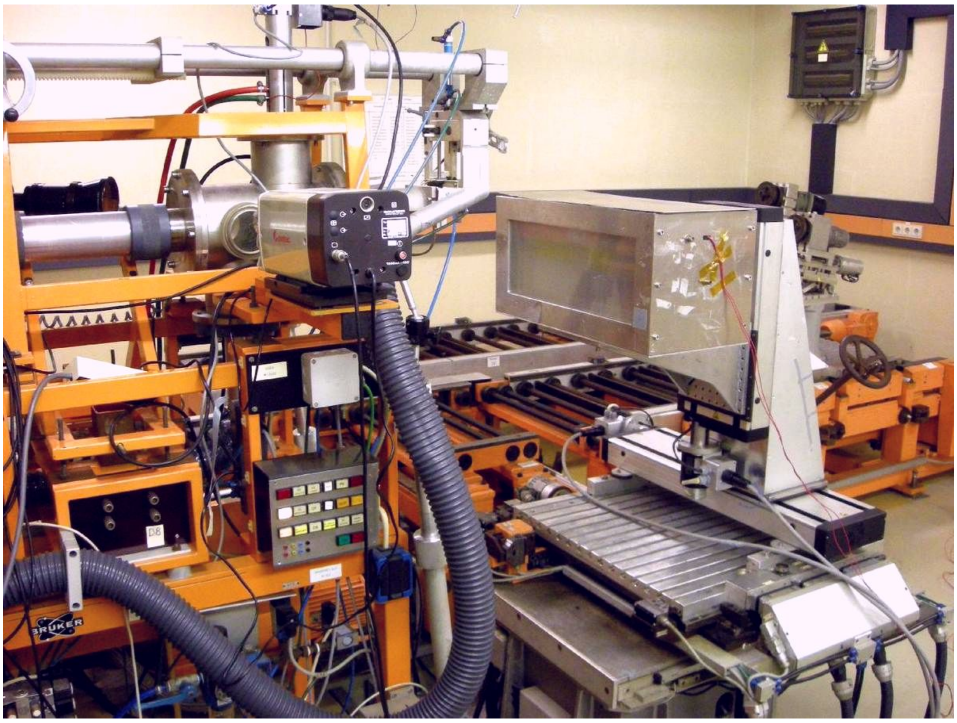

Figure 6.7.: Proton irradiation setup at KAZ. The aluminium box is placed in front of the beam pipe and flushed with cold nitrogen gas. Additionally, it is mounted on a *xy*-stage that moves it around [ETPb].

6.3.2. Neutron Irradiation in Ljubljana

Neutron irradiation is performed at a TRIGA[6] spallation reactor at JSI[7] in Ljubljana, Slovenia [SŽT12]. The fluence uncertainty has been estimated with 10% [Žon+99]. Although neutrons themselves cannot ionise the material, due to photon contamination inside the reactor, the estimated dose is 1 kGy per $1 \times 10^{14}\,\mathrm{n_{eq}/cm^2}$ [Man+04]. During the irradiation, the samples heat up to 40 °C for a few minutes. After the irradiation, the samples' radioactivity has to decay for about 30 min before they can be pulled out. Then, spectroscopy follows at room temperature. All in all, an annealing of around one hour at room temperature is expected. For the shipment back to the institute, ice packs are used to avoid temperatures above 0 °C so that annealing should be effectively frozen out. However, if the shipment takes longer than one day, the temperature rises. All in all, a conservative estimation of 1 day at room temperature equivalent annealing should be taken into account for irradiations at this facility.

6.3.3. X-Ray Irradiation at ETP

The X-ray irradiation in this work is performed with the tungsten X-ray tube of the ETP. It is placed inside a housing made of an aluminium lead sandwich to protect the environment, especially the operator. A typical spectrum of the tube for the maximum operation voltage of $V_{\mathrm{max}} = 60\,\mathrm{kV}$ and a tube current of $I_{\mathrm{tube}} = 33\,\mathrm{mA}$ is indicated in fig. 6.8a. An additional vanadium filter with a thickness of 15 µm is applied to suppress the low-energetic part of the X-ray spectrum. The tube current can be increased to a maximum of $I_{\mathrm{max}} = 50\,\mathrm{mA}$ yielding a power of $P_{\mathrm{max}} = 3\,\mathrm{kW}$. However, to preserve comparability to previous studies, the tube

---

[6] Training, Research, Isotopes, General Atomic

[7] Jožef Stefan Institute

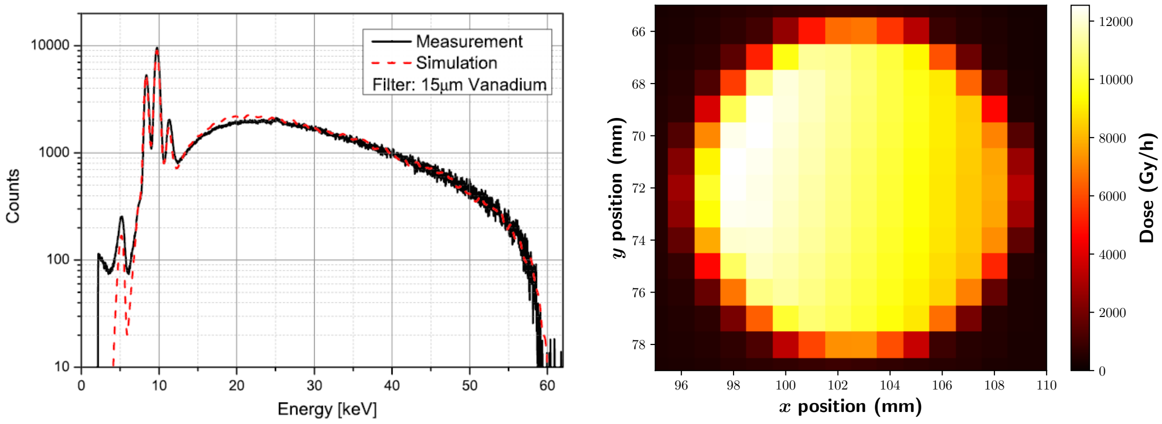

(a)

(b)

Figure 6.8.: Simulated and measured X-ray spectrum for the tube settings of 60 kV, 33 mA at a distance of 155 mm with a 15 µm thick vanadium filter (a) [Gut+12]. Beam spot profile with a tube voltage of 60 kV, current of 30 mA at a distance of 100 mm with the same vanadium filter.

current is fixed to 30 mA in this work and the maximum tube voltage is always used. More details about the tube and the dose rate estimations are given in [Gut+12].

The beam spot profile of the tube has been determined similar to the procedure described in [Gos18]. An example of the beam's profile is given in fig. 6.8b. The profile has been scanned with a small PIN diode under a lead collimator with a diameter of 1 mm, approximately. The diode is driven through the beam in 1 mm steps and the measured current induced by the X-ray beam is translated to a dose rate. It can be seen that the dose rates are considerably higher on the left side in the figure than on the right.

The irradiation setup that is used in this work is shown in fig. 6.9a. The beam of the X-ray tube is entering the irradiation box that incorporates the sample to be irradiated. The box itself is positioned in z direction by height-adjustable tables that are fixated on a xy-stage. Similar to the proton irradiation facility in section 6.3.1, the stage is used to ensure homogeneous irradiation. It is moved in a meander-like pattern during the irradiation, so that inhomogeneities of the beam (that are shown in fig. 6.8b) are cancelled out. The interior of the irradiation box is shown in fig. 6.9b. It mainly consists of an aluminium jig that can be cooled down to avoid annealing during the irradiation procedure. The sample can be fixated on a hole in the middle that is connected to a vacuum pump. Similar to the probe station apparatus, the jig is temperature controlled via a Peltier element whose waste heat is dissipated through a precooling system. Further, the box is flushed with dry air to keep the dew point, monitored with by humidity sensor, low. The setup is closed with a cover that features a thin polyester window which only absorbs a very low fraction of the X-ray photons.

6.4. TCAD Simulation with Synopsys Sentaurus

Simulations of electrical properties of silicon strip sensors are performed with the numerical simulation framework Synopsys Sentaurus TCAD [Syn21]. The simulation is based on the finite element method where the device is divided into several small regions. Inside these regions, terminal currents, voltages and charges are calculated on the basis of equations that describe the carrier distribution and conduction mechanism [Syn18].

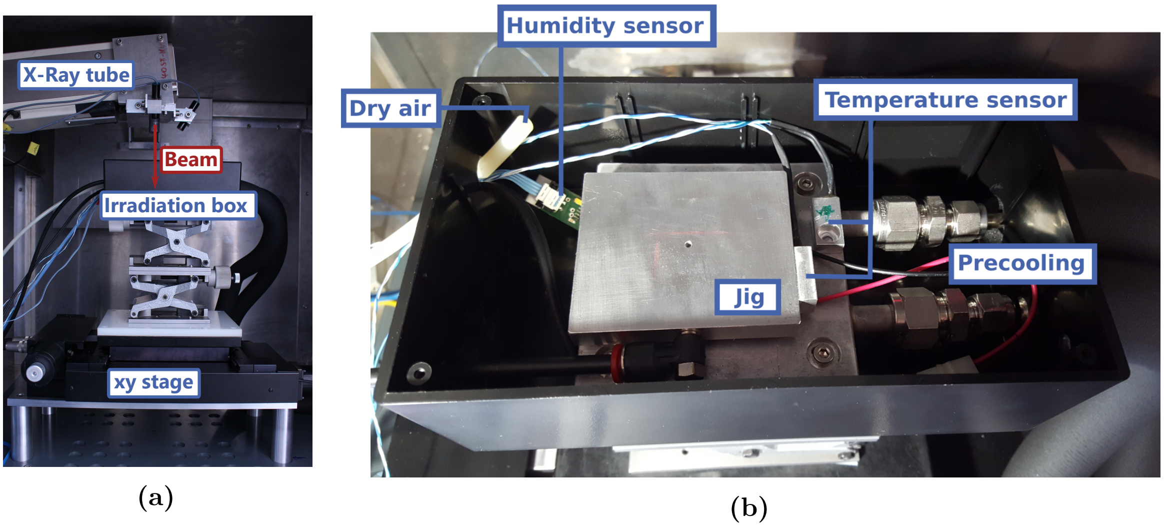

(a) (b)

Figure 6.9.: The X-ray irradiation setup at ETP with the tube, the irradiation box and the xy-stage that is used for a homogeneous irradiation procedure (a). Irradiation box that can be used for permanent cooling during the irradiation procedure (b). The chuck is cooled via Peltier elements. To avoid condensation or even ice formation the box is constantly flushed with dry air.

The general workflow is illustrated in fig. 6.10. First, the geometry of the device is defined in the *Structure Editor*. Additionally, the mesh's size that determines the finite elements is defined here. Its density should be higher in more interesting regions to increase accuracy and smaller in more homogeneous regions to keep the computation time reasonable. Electrical boundary conditions can be applied later for biasing of the sensor. All properties set with the structure editor are saved in a .tdr file. This file is used as an input for the *Sentaurus Device*. Here, the physics is defined. First, parameters for physical models and the models themselves are stated. The system can then be connected to a SPICE[8] framework that handles electric circuits. Further, parameters that should be extracted from the output can be listed, like electric field, electrostatic potential and charge mobilities. Finally, details about the solving strategy can be configured. An example would be that the backplane voltage ramps up to a certain value in small steps and the coupled Poisson equations are solved iteratively. The outcome can then be saved in a .tdr and a .plt file. The exemplary $I(V)$ curve with the V and I data would be saved in the .plt file. The .tdr file incorporates all the other solutions for the device. For example it can be opened with specific visualisation tools of the software that generate a 2D representation of the device. With that it is possible to inspect for example the electric field or electrostatic potential distribution that has been computed.

Defects as a result of radiation damage can be represented by additional states inside the band gap of silicon as explained in chapter 4. Therefore, radiation defects are also represented by states in the band gap in the simulation framework. This distribution is defined in the device file. The general trap definitions in Sentaurus are as follows (extracted from the manual [Syn18]):

- Acceptor traps are uncharged when unoccupied and they carry the charge of one electron when fully occupied.
- Donor traps are uncharged when unoccupied and they carry the charge of one hole when fully occupied

---

[8] SPICE: **S**imulation **P**rogram with **I**ntegrated **C**ircuit **E**mphasis

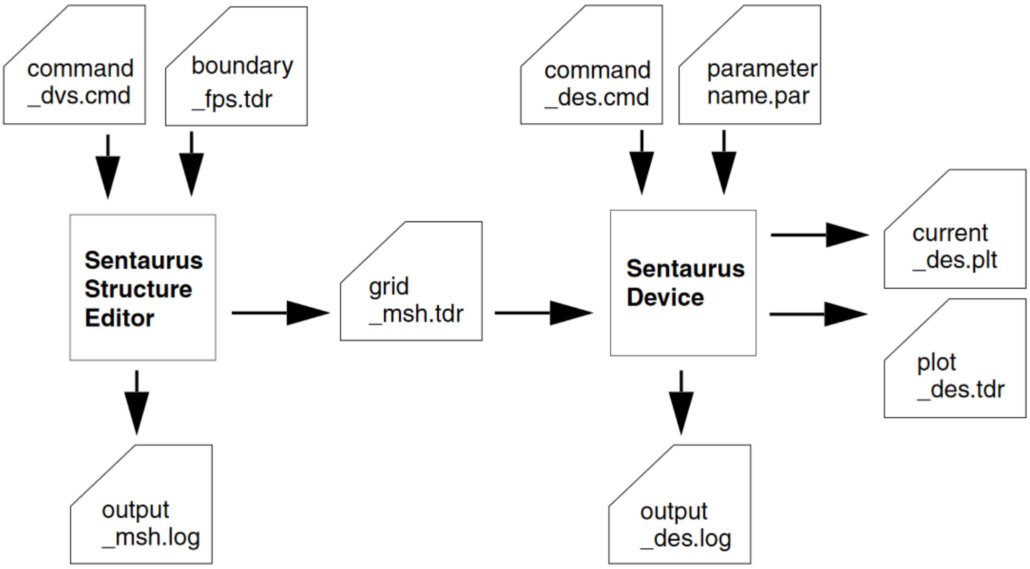

Figure 6.10.: Scheme of Sentaurus workflow. The device's geometry and mesh is configured with the structure editor. It generates a .tdr file that is used as input for the Sentaurus device. This tool takes further input parameters that control the physical models and defines the simulation and calculation procedures. The output that is received when the simulation is done is a file that contains specific measurements and a file that incorporates all the 2D information [Syn18].

Contrary to other definitions where the donor is positively charged when empty (as described in chapter 4), both trap types are simply considered uncharged if empty. In addition to dynamic traps, a fixed charge can be inserted similarly as traps but they are always occupied (thus charged). The possible definitions of the other trap distributions are as illustrated in fig. 6.11:

- One level at an energy level E_0 somewhere in the band gap with a certain concentration N_0 in cm^{-3} or cm^{-2} dependent on the region's definition (volume or interface/surface).
- Uniform distribution of trap states over a specific energy range with the energy width E_s and a certain concentration. For distributions of traps, the concentration is always given in $\mathrm{eV}^{-1}\,\mathrm{cm}^{-3}$ or $\mathrm{eV}^{-1}\,\mathrm{cm}^{-2}$ dependent on the region's definition.
- Exponential distribution with

  $$N_0 \cdot \exp\left(-\left|\frac{E-E_0}{E_s}\right|\right) \tag{6.10}$$

  with the maximum concentration N_0 at the energy E_0 and the spread E_s.
- Gaussian distribution with

  $$N_0 \cdot \exp\left(-\frac{(E-E_0)^2}{2E_s^2}\right) \tag{6.11}$$

  with the maximum concentration N_0 at the energy E_0 and the spread (respective standard deviation) E_s.

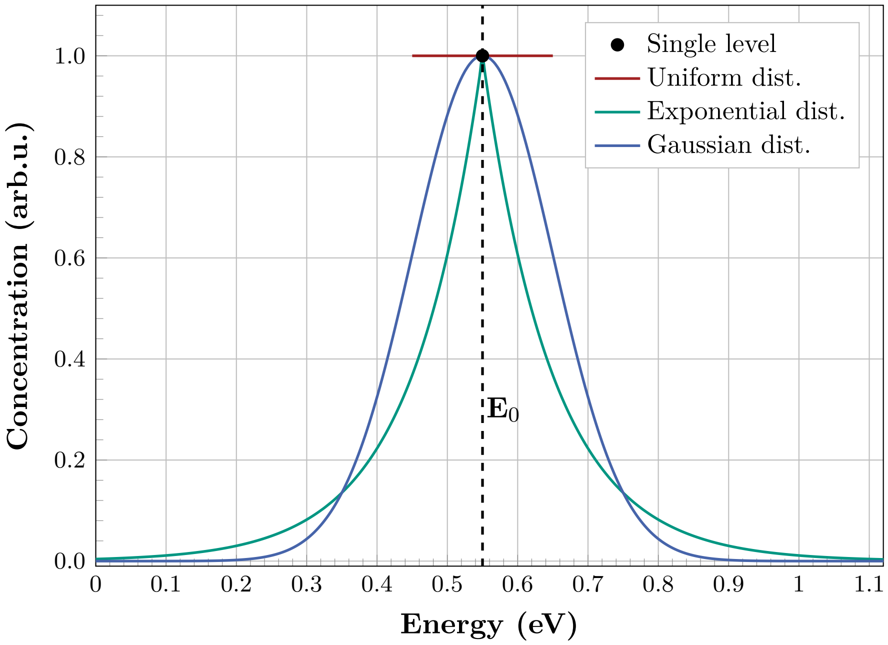

Figure 6.11.: Trap distributions in Sentaurus. Four different options are available: a single level, a uniform energy, an exponentially decreasing and a Gaussian distribution.

Part III.

Investigation of Radiation Damage

7

Irradiation Tests for the CMS Phase-2 Outer Tracker Sensor Production

In the course of the HL-LHC upgrade the luminosity will increase, as explained in section 2.1. This results in various new challenges for the detectors. For the upgrade of the CMS detector, the tracker will be replaced entirely. Its new features and the requirements have been covered in section 2.5. For the new silicon sensors the general design has been shown in section 3.6.1. Radiation hardness is a key feature, since the silicon sensors have to withstand highest fluences. In the context of previous irradiation campaigns, several different design parameters of the sensors have been tailored to an optimum. The latest achieved milestone was the final decision on the active and physical thickness of the sensors. In principle, a smaller thickness is desirable in terms of material budget. The thicker the sensor, the more scattering occurs, which might decrease the accuracy of measurements in the other sub-detector systems that are all located outside of the tracker. On the other hand, the silicon sensors are just a small constitution of the total material budget of the tracker. There are others like electronics, cables, support structures and mechanics. Thinner sensors also means smaller leakage currents, thus less power consumption. On the other hand, a thicker active bulk can in principle deliver more signal, since more energy is deposited by traversing particles. However, this beneficial effect might be fully reset by radiation-induced defects. Because of trapping, the charge collection is considerably decreased for the expected fluences as explained in section 4.2.3. It has been shown in [Gos18] that there is also a complex dependence on the concrete particle mixture. Therefore, a final intense irradiation campaign under conditions that are as close as possible to the expected radiation environment in Phase-2 has been conducted in [Met20]. At that time, two different sensor types were available. One is a thicker sensor with an active thickness of 290 µm that has a thicker backside implant (physical thickness 320 µm) and another one that is thinned down to a thickness of 240 µm. In short the result is that the two substrate types in question both fulfil the requirements. At the highest fluence for the inner part of the Outer Tracker, the PS region, thinner sensors might have a small benefit in terms of signal. However, thinned sensors are more prone to mechanical damage, which is also reflected by the fact that several sensors broke during the campaign independent of the radiation. Additionally, a factor that cannot be neglected on such a mass production is the financial budget. The thinning procedure would have been more expensive than the standard procedure of the vendor HPK (Hamamatsu Photonics K. K.). Hence, considering all these factors lead to the decision pro thicker sensor type.

The sensor production was started in mid 2020 with a first batch to prove one more time that all design parameters are met and the vendor HPK is able to produce the sensors as desired. Then, a pre-production phase has started during which the vendor set up the production line and produced several batches to prove the concept of a mass production with new production lines. The irradiation tests in the course of this pre-production are the topic of this chapter. Several parameters after irradiation are investigated that serve as a baseline for the full mass production that started mid 2021.

There are three types of sensors that will be used for the two module types, 2S and PS, for the Outer Tracker. One is the 2S sensor, which is a strip sensor that features longer strips. Two of these sensors are incorporated in one 2S module. The PS module houses the other two types of sensors which are a smaller (approximately half-sized) strip sensor and a macro-pixel sensor of a similar size. The nomenclature is to append the small letter s or p for *strip* or *pixel* to the PS part to identify the sensor type for a PS module, thus PS-s and PS-p.

An example of the wafer layout is given for the 2S wafer in fig. 7.1. The layouts of the PS-s and PS-p wafer can be found in the appendix in fig. C.1 and fig. C.2, respectively. The basic wafer design for the types 2S, PS-s and PS-p is similar except from small differences. The main sensor is placed in the middle with an area of $A_{2\mathrm{S}} = 9.42 \times 10.2\,\mathrm{cm}^2$ in case of the 2S sensor. Four cuts are applied by the vendor so that the full-sized sensors are extracted. The other structures are therefore separated into four regions, one for every side of the wafer. The surrounding parts are therefore referred to as *cut-offs* or *half-moons*. On the left (west) and right (east) side the specific structures for process quality control are placed. The irradiation test samples are located on the bottom (south). On the top (north) some additional structures like two square strip sensors are located that are not foreseen to be tested on a regular basis during the production.

In case of PS-s and PS-p wafers, two main sensors are placed in the middle, since their area is only the half of the area of the 2S sensor, approximately. The sensors are separated by the vendor by an additional vertical cut through the whole wafer. Because of this dicing line, the test structures are separated from each other by a small gap. Another difference between the layouts is that the PS-p macro-pixel sensor is a DC coupled sensor that does not require a specific coupling oxide. Also, the PS-p sensor in the final detector will be grounded over the readout chip and not over the bias ring. Therefore, a dedicated polysilicon bias structure is not required. However, to be able to test the sensor before it is connected to the readout chip, the bias grid is connected by so-called punch-throughs to the pixel implants (more about the design choice in [Sch19]). This technology requires less space compared to the polysilicon meander-shaped structure. In addition, to be able to test a sensor that is as similar as possible to the main sensor, the right one of the spare sensors on the north half-moon is a macro-pixel sensor instead of a strip sensor for the PS-p wafers.

The general strategy of quality assurance during the production of the Phase-2 Outer Tracker sensors is illustrated in fig. 7.2. The vendor HPK performs a vendor quality control (VQC) on all full-sized sensors and sends conforming sensors and cut-offs to the distribution centre at CERN. The full-sized sensors are then shipped to the sensor quality control (SQC) and cut-offs to the process quality control (PQC) centres. Some of these structures also undergo an irradiation test (IT) procedure. The irradiation tests are the main topic of this chapter and are explained in detail in the subsequent sections.

At the SQC centres, measurements of the global leakage current dependent on the bias voltage ($I(V)$) and of the capacitance over applied bias ($C(V)$) are performed on a fraction of sensors. This ensures the general operability of the main sensors that will be incorporated in the new CMS tracker. In addition, scans are performed in which the DC and AC pads of a single strip are contacted. With this needle position, the bias resistance, strip leakage current, coupling capacitance and pinhole current can be obtained. These parameters are measured for every fourth strip of two sensors per batch. On every 50th strip, the interstrip resistance and interstrip capacitance is measured by contacting two adjacent strips. Bad strips are detected with this procedure so that sensors or full batches can be rejected if the number of bad strips exceeds a certain threshold. More details regarding the SQC can be found in [CMSc].

Besides the sensor quality control, process quality control is performed on test structures that are located on the same wafers as the full-sized sensors. For example, the depletion voltage is extracted from $C(V)$ measurements on diodes, as explained in section 5.1. MOS

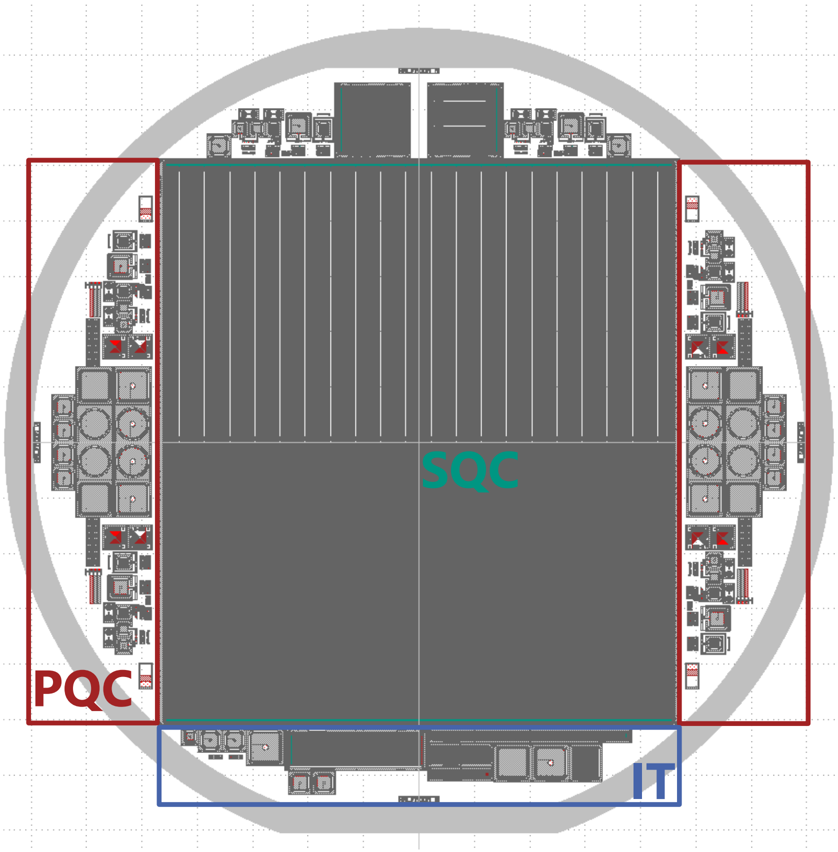

Figure 7.1.: The 2S wafer with the main sensor in the middle and test structures for process quality control on the left and right and irradiation test structures on the bottom.

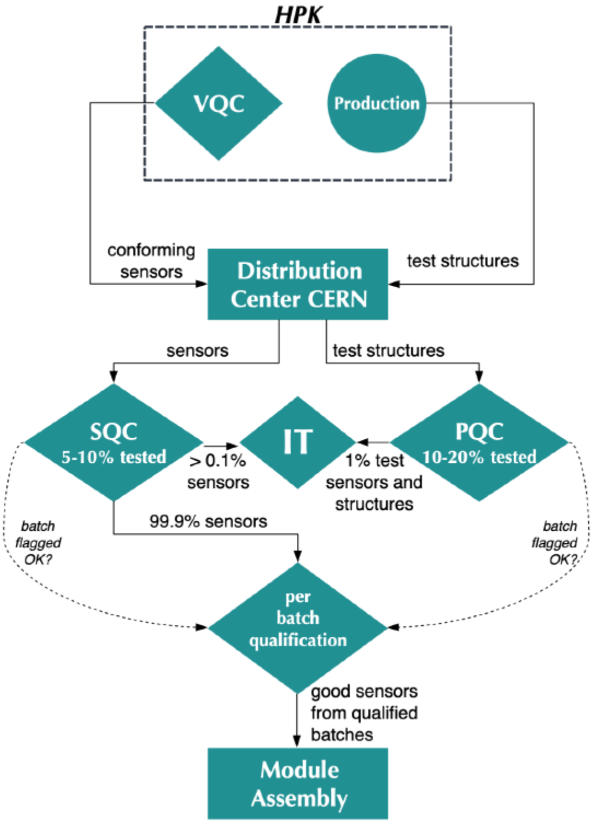
HPK
VQC
Production
conforming sensors
test structures
Distribution Center CERN
sensors
test structures
SQC 5-10% tested
IT
PQC 10-20% tested
> 0.1% sensors
1% test sensors and structures
99.9% sensors
batch flagged OK?
batch flagged OK?
per batch qualification
good sensors from qualified batches
Module Assembly

Figure 7.2.: Scheme of the quality control for the Outer Tracker sensor production [CMSc].

capacitors are used to determine the flat-band voltage and the thickness of the silicon dioxide and measurements on GCD structures yield the surface generation velocity, as explained in section 5.2 and section 5.3. In addition, several Van-der-Pauw structures are used to measure the sheet resistance of different implantation or metallisation layers on the wafers. The various parameters which are extracted and further details can be found in [CMSa]. PQC is performed by several institutes in Europe and one institute at Brown University in the US.

7.1. Introduction to Irradiation Tests

The Outer Tracker sensor community decided on irradiation tests with different particle types. FLUKA simulations yield an estimate of the total fluence silicon sensors receive in the Phase-2 Outer Tracker dependent on the radii and position along the beampipe (compare section 2.5.3). By considering the tracker design with the positions of the modules, it is possible to derive the number of modules that have to withstand a certain fluence. This distribution is illustrated in fig. 7.3. The fluence according to the *nominal scenario* with an operation time of 10 years and $L_{\text{int}} = 3000\,\text{fb}^{-1}$ time integrated luminosity is indicated by the lower x-axis. Fluences with a possible extension to an *ultimate scenario* with $L_{\text{int}} = 4000\,\text{fb}^{-1}$ refer to the upper x-axis. Moreover, the columns represent the total number of modules which have to cope with a specific fluence for the 2S and the PS region. The fraction of modules that accumulate a certain fluence is indicated by the green and red line for 2S and PS modules, respectively. It can be seen that for the 2S modules only 5% have to cope with fluences of $\Phi > 3 \times 10^{14}\,\text{n}_{\text{eq}}/\text{cm}^2$ and 5% of the PS module will accumulate $\Phi > 8.5 \times 10^{14}\,\text{n}_{\text{eq}}/\text{cm}^2$ considering the nominal scenario. If the operation time is extended or the ultimate scenario of the HL-LHC will be reached,

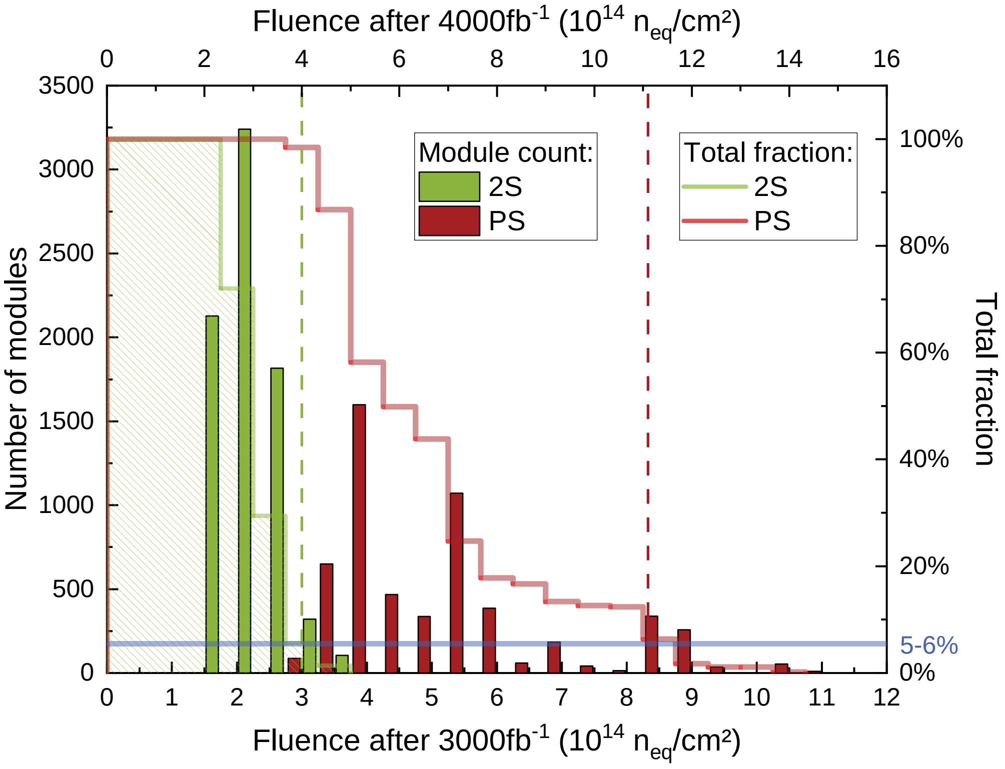

Figure 7.3.: Number of modules over accumulated fluence during Phase-2 for $L_{\text{int}} = 3000\,\text{fb}^{-1}$ (bottom x-axis). Same distribution but for the ultimate scenario with $L_{\text{int}} = 4000\,\text{fb}^{-1}$ (top x-axis) [CMSb]

the time integrated luminosity increases to $4000\,\text{fb}^{-1}$. Therefore, the two fluences increase to $\Phi_{2S} = 4 \times 10^{14}\,\text{n}_{\text{eq}}/\text{cm}^2$ and $\Phi_{PS} = 1.1 \times 10^{15}\,\text{n}_{\text{eq}}/\text{cm}^2$. Hence, the reference fluence for the irradiation tests during the production of the CMS Phase-2 Outer Tracker sensors are set to $4 \times 10^{14}\,\text{n}_{\text{eq}}/\text{cm}^2$ for 2S batches and $1.1 \times 10^{15}\,\text{n}_{\text{eq}}/\text{cm}^2$ for PS-s and PS-p batches in order to obtain a conservative approximation and to monitor changes of the radiation hardness of the sensors.

The test structures that are being used for hadron and X-ray irradiation tests are located on the southern half-moon. A scheme of the design file on the top and a comparison to a photo of the real devices on the bottom is shown in fig. 7.4 for a 2S wafer. The diode set on the outer left side and the *babysensor* are used for hadron irradiation tests. The MOS and GCD devices on the right side are irradiated with X-rays to monitor the surface damage. The concept of the design of the babysensor is that it should match the respective main sensor as much as possible. Therefore, the pitch is $p_{2S} = 90\,\mu\text{m}$ in case of 2S wafers and $p_{PS} = 100\,\mu\text{m}$ for PS wafers similar to the corresponding full-sized sensors. The n$^+$-implant width w to pitch p ratio of $w/p = 0.25$ applies for both. In addition, the results of measurements on the babysensors from different wafer types should still be comparable. Therefore, the strip length is fixed to $l = 2.35\,\text{cm}$ and also for the macro-pixel PS-p wafers the babysensor is a strip sensor although the main sensor features macro-pixels. In addition, the babysensors are biased over a punch-through similar to the full-sized sensor. Since the PS-p has DC coupled pixels that are biased over a punch-through structure, the processes for a specific coupling oxide and polysilicon resistor are omitted. Therefore, the oxide's quality on the PS-p wafers is slightly worse.

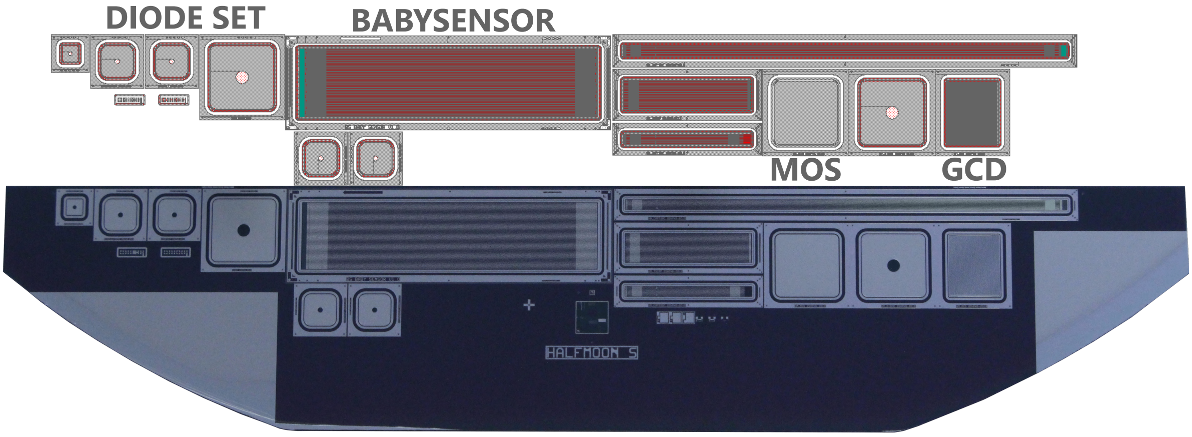

Figure 7.4.: South half-moon of a 2S wafer where test structures for the irradiation tests are placed. The design file with annotations is shown on the top. A photo of the same region on a real wafer is shown with the same structures.

In principle, the diode set and the babysensor could be irradiated together. However, for the ALiBaVa setup (described in section 6.2) the space for the sensor under test is limited. Therefore, a cut between the diode set and the babysensor is applied[1]. It is also more convenient to handle the diodes and the babysensor separately for measurements, storage and annealing. In case of the PS-s and PS-p wafers, there is a small gap between the babysensor and the structures on the right so that no structures are harmed by the default cut that the vendor applies in the middle. The basic placement of the other structures is similar.

In the scope of the irradiation tests many measurements are performed that enable a deeper investigation if potential issues might occur. This is important because most measurements are not repeatable. This is true for measurements prior to irradiation but also after irradiation and pre annealing. Therefore, the strategy is to gain as much information as reasonably possible even if it might never be used. That there are no issues and therefore the information will never be required is actually the desired case.

7.2. Irradiation Tests with Hadron Irradiation

The hadron irradiation tests deal with diodes and strip sensors. The stations that are passed through during irradiation testing are summarised in table 7.1. After the manufacturing, shipments and dicing, first full electrical tests are performed on the strip sensors. In Europe, a small number of half-moon sets, typically five per batch, is selected by the PQC centres on request of the IT centre at KIT. In the US, process quality control and irradiation tests are both performed by Brown University. The electrical characterisation includes global leakage current and capacitance measurements on the strip sensors and diodes with additional strip scans on the small strip sensors. Afterwards, both are irradiated at the proton irradiation facility KAZ at ZAG (details about the facility are given in section 6.3.1) or with neutrons in the US[2]. Any inhomogeneities in terms of annealing due to handling are mitigated by a reception annealing (20 min at 60 °C) after irradiation for the strip sensors. Then, electrical tests are performed again. Afterwards, the strip sensors are bonded onto an ALiBaVa daughterboard so that signal measurements can be performed (as explained in section 6.2). These are done alternating with annealing steps as will be explained in more detail in section 7.2.4. After the full annealing,

---

[1] with blade dicing at the Institute for Data Processing and Electronics (IPE) at KIT

[2] at the RINSC irradiation facility [Rho21]

Table 7.1.: Stations that test structures for hadron irradiation tests pass through in chronological order.

Strip sensors		**Diodes**	
Process	Location	Process	Location
Manufacturing	HPK	Manufacturing	HPK
Shipment	to CERN	Shipment	to CERN
Shipment	to PQC centre	Shipment	to PQC centre
Shipment	to KIT (ETP)	Shipment	to KIT (ETP)
Reception $I(V)$	Probe station		
Dicing	KIT (IPE)	Dicing	KIT (IPE)
Electrical tests	Probe station	Electrical tests	Probe station
Irradiation	KIT (KAZ)	Irradiation	KIT (KAZ)
Reception annealing	Oven	Specific annealing	Oven
Electrical tests	Probe station	Electrical tests	Probe station
Bonding onto ALiBaVa board	Bonding machine		
Signal annealing study	ALiBaVa setup		
Electrical tests	Probe station		
Storage	Freezer	Storage	Freezer

the sensor is detached from the board and strip scans are performed again. The diodes are annealed after irradiation with a specific annealing step of 80 min at 60 °C followed by leakage current and capacitance measurements. Finally, both hadron irradiated test devices are stored in a freezer.

7.2.1. Electrical Characterisation pre Irradiation

First of all, when the structures arrive at the IT centre, a reception measurement on the babysensor is performed. This ensures the general functionality of the sensor. It is not expected that the sensors are broken at this early stage. However, none of these test structures have been tested by the vendor. Also, they have been handled already and dispatched by the PQC centres.

In the usual case of a first successful leakage current measurement, out of the five available wafers, two per batch are selected for the dicing and irradiation procedure. The babysensor and the diode set are separated in case of all wafers and for 2S wafers an additional cut is applied between the sensor and the right side of the half-moon with the MOS and GCD. After the dicing procedure, leakage current measurements are performed again on the sensor and on the biggest diode. The other diodes of the diode set are not further considered but can be used in case the big one breaks or for deeper investigations. The settings for the leakage current and capacitance measurements are given in table 7.2.

Strip scans pre irradiation are necessary in order to assess whether bad strips identified after irradiation emerged due to the irradiation or were present before already. They are performed after dicing to exclude that strips have been damaged during the dicing procedure. The strip scans are performed similarly to the SQC strip scans on full-sized sensors with a constant reverse bias of 600 V. Strip parameters that are to be measured by contacting single strips are:

- **Strip leakage current I_{leak}**: The strip leakage current is the leakage current that flows through one strip. To measure it, the DC pad of one strip is contacted with one needle and the current flow through it is measured while the backplane is biased to 600 V.

Table 7.2.: Settings of the leakage current and capacitance over bias voltage measurements on diodes and sensors prior to irradiation.

Leakage current measurement		**Capacitance measurement**	
Backplane bias	0 V to −1000 V	Backplane bias	0 V to −600 V
Step size	10 V	Step size	10 V
Compliance	30 µA	Compliance	300 µA
		AC amplitude	250 mV
		AC frequency	1 kHz
Temperature	20 °C	Temperature	20 °C

As usual, the bias ring is grounded via the bias needle. The strip current should fulfil $I_\text{leak} < 10\,\text{nA}\,\text{cm}^{-1}$ which translates to $I_\text{leak} < 23.5\,\text{nA}$ for the small test sensors.

- **Polysilicon bias resistance R_poly**: With the same needle configuration of one needle on the DC pad, the bias resistance can be measured. In order to do so, a low voltage ramp is applied on the needle that is connected to the DC pad. This leads to a current flow through the strip's bias resistor into the bias ring and the bias needle. The current adds up to the general leakage current. If a linear fit is applied on the current over DC voltage curve, the bias resistance can be obtained by the inverse slope of this characteristic. According to the specifications, the polysilicon bias resistance should be in the range of $R_\text{poly} = (1.5 \pm 0.5)\,\text{M}\Omega$.

- **AC coupling capacitance C_AC**: The coupling capacitance depends on the quality of the coupling oxide between the n$^+$ implant and the aluminium strip. It is determined by contacting the DC and the AC pad of a single strip with two needles. The capacitance between these two is measured with an LCR meter. It should fulfil $C_\text{ac} > 1.2\,\text{pF}\,\text{cm}^{-1}\,\mu\text{m}^{-1}$ to ensure a sufficient charge collection. This specification results in $C_\text{ac} > 70.5\,\text{pF}$ for the PS-s batches with the strip length of the babysensor of $l = 2.35\,\text{cm}$ and implant width of $w_\text{imp, PS-s} = 25\,\mu\text{m}$. For the 2S batches with the same strip length but an implant width of $w_\text{imp, 2S} = 22\,\mu\text{m}$ it holds $C_\text{ac} > 62\,\text{pF}$.

- **Pinhole test**: A pinhole is a conductive connection between the DC and AC pad. It can occur due to a failure in the coupling oxide but also due to a scratch on the surface that connects the aluminium of both pads. If a pinhole occurs, the noise of the respective channel increases because of the current flow into the readout chip. The pinhole test is performed by applying a low voltage difference of 10 V between the two needles and the expected current is zero when both are isolated. The current through the dielectric should be $I_\text{diel} < 10\,\text{nA}$ otherwise the strip is counted as a pinhole.

In addition to single strip scans, scans with two strips are performed to determine interstrip parameters. The parameters that can be extracted by contacting two adjacent DC pads are:

- **Interstrip resistance R_int**: The interstrip resistance should be high in order to ensure sufficient strip isolation. It is determined by applying a small voltage ramp on one of the two adjacent DC pads while measuring the current flow in the second. The current of the second strip is the sum of the general leakage current and the additional current flow due to the strip potential. Again, a linear fit of the current over applied potential can be performed and the resistance is obtained by the inverse slope of it. The procedure is also explained in considerably more detail in section 8.1. The interstrip resistance pre

Table 7.3.: Results of the strip scans pre irradiation.

	2S batches		**PS-s batches**	
Parameter	Mean	Spread	Mean	Spread
R_{poly}	1.86 MΩ	0.05 MΩ	1.89 MΩ	0.07 MΩ
C_{ac}	74.3 pF	0.99 pF	84.3 pF	0.9 pF
I_{leak}	20 pA	5 pA	22 pA	4.2 pA
R_{int}	990 GΩ	320 GΩ	1400 GΩ	477 GΩ
C_{int}	1.08 pF	0.02 pF	1.08 pF	0.02 pF

irradiation should be $R_{\text{int}} > 10\,\text{G}\Omega\,\text{cm}$ which translates to $R_{\text{int}} > 4.26\,\text{G}\Omega$ for the strip length of the babysensors. Usually, the value pre irradiation is around the resolution of the measurement devices. Hence, a bad contact which would result in a low current and high interstrip resistance might not be spotted immediately but can be identified in the interstrip capacitance measurement.

- **Interstrip Capacitance C_{int}**: With the same needle configuration it is possible to measure the interstrip capacitance with an LCR meter. It is also useful to keep an eye on it during the measurements since it serves as an indicator for a bad needle contact. If one of the needles is not set properly the capacitance is orders of magnitude lower than usual. Therefore, it is possible to spot a bad contact by an extremely low interstrip capacitance value which could not be spotted by the pure interstrip resistance measurements. The specification is $C_{\text{int}} < 0.5\,\text{pF}\,\text{cm}^{-1}$ which translates to $C_{\text{int}} < 1.175\,\text{pF}$ for babysensors.

The result of the strip scans before irradiation of all 2S and PS-s pre-production batches outside the US (measured at KIT) is given in table 7.3. The mean value is the mean over all strips of all sensors that have been measured during irradiation tests. The spread is estimated as the standard deviation of this set of strips. In total approximately 2500 and 500 strips have been measured of 2S and PS-s batches, respectively. In case of the bias resistance measurements the value is pretty accurate and similar for 2S and PS-s batches. The higher coupling capacitance of the PS-s wafers is due to the broader implant. The coupling capacitance of $C_{\text{ac}} > 62\,\text{pF}$ for 2S batches and $C_{\text{ac}} > 70.5\,\text{pF}$ for the PS-s batches is fulfilled as well. Both mean values exceed the lower limit of the specification by 20%. The PS-s sensor is expected to show a slightly higher single strip current because the strips are slightly broader. This is also reflected by the measurements. However, the leakage current is three orders of magnitude below the specification of $I_{\text{leak}} < 23.5\,\text{nA}$. The interstrip resistance R_{int} is orders of magnitude higher than the specified lower limit as well. However, this also leads to the issue that the interstrip current is not really resolvable anymore for the picoammeter. Therefore, the spread is comparably high. The interstrip capacitance on the other hand is much more precisely measurable. The limit of $C_{\text{int}} < 1.175\,\text{pF}$ is reached and the measurements show great accuracy. A small number of six pinholes has been identified during the measurement procedure. The relative number of pinholes per total number of tested strips is 0.2% which is acceptable, especially, when the history of the devices is considered for which already handling, dicing and measurement procedures have been applied.

7.2.2. Electrical Characterisation of Diodes after Irradiation

Diodes are used to determine the leakage current of the silicon substrate. In principle the diode leakage current should be comparable with the current per volume of the strip sensors.

However, the strip sensors are more prone to surface damage and, due to the segmentation, less comparable to other studies. Therefore, diodes are used to estimate the radiation tolerance of the base material. Usually, the *current-related damage rate* α is used as an indicator for the expected leakage current following the NIEL hypothesis. It can also serve as an indicator of the fluence since the current depends neither on the material nor the particle type but just on the equivalent fluence. The leakage current increase $\Delta I = I_{\text{after}} - I_{\text{pre}}$ per volume V scales linearly with the applied fluence Φ_{eq}

$$\frac{\Delta I}{V} = \alpha \cdot \Phi_{\text{eq}} \tag{7.1}$$

with α the proportionality factor. The volume of the diode is estimated with the outer edge of the guard implant that determines the edge of the active volume. Further correcting for the rounded corners, the volume is $V = 8.37\,\text{mm}^3$, considering an active thickness of 290 µm.

After irradiation, the leakage current increases to up to 500 µA for the PS fluence, which is around six orders of magnitude higher compared to the current pre irradiation of $I_{\text{pre}} \approx 0.1\,\text{nA}$. Therefore, the current pre irradiation can be neglected in good conscience.

The temperature dependence of the leakage current follows a proportionality independent of the irradiation state following [Chi13].

$$I(T) \propto T^2 \exp(-1.21\,\text{eV}/2k_{\text{B}}T). \tag{7.2}$$

with Boltzmann's constant k_{B} in $\text{eV}\,\text{K}^{-1}$ and temperature T in K. The relative current scaling r_{curr} from one temperature T_{from} to another temperature T_{to} can be calculated via

$$r_{\text{curr}}(T_{\text{to}}, T_{\text{from}}) = \left(\frac{T_{\text{to}}}{T_{\text{from}}}\right)^2 \cdot \exp\left[\frac{1.21\,\text{eV}}{2k_{\text{B}}} \cdot \left(\frac{1}{T_{\text{from}}} - \frac{1}{T_{\text{to}}}\right)\right]. \tag{7.3}$$

An example is the current scaling to 20 °C from a measurement at −20 °C that has been used in previous studies. In that case, the current is 59 times higher for the higher temperature. For simplicity, the diodes on CMS Phase-2 production wafers are measured at 20 °C. Such a leakage current measurement takes below five minutes. In case of cooling down, the time to dry the air and the cooling itself can take up to one hour, which is considerably longer. Additionally, the precision is worse since the temperature on the chuck is not homogeneous and the absolute value of the temperature of the diodes is erroneous (compare section 6.1.1). Moreover, at lower temperatures, the impact of a deviating temperature is more pronounced than at 20 °C. The relative current r_{curr} to the current at $T_{\text{from}} = -20\,°\text{C}$ that emerges when the temperature is actually the temperature plotted on the x-axis ($T_{\text{to}} = T_{\text{from}} \pm 5\,°\text{C}$) is shown in fig. 7.5a calculated with eq. (7.3). For example a temperature difference of 1 °C, thus −19 °C or −21 °C, results in a measured current that is 12.41% higher or 11.12% lower, respectively. The similar procedure but with the reference temperature of 20 °C is shown in fig. 7.5b. Here, a temperature difference of 1 °C, thus 19 °C or 21 °C results in a measured current that is 8.5% lower or 9.22% higher, respectively. Therefore, the error due to a 1 °C temperature deviation can be mitigated by three percent points by choosing a higher reference temperature. To extract the damage rate at a well defined annealing state, a higher temperature treatment is done on a pre-heated aluminium chuck (with a mass of 475 g) in an oven. An annealing at a temperature of 60 °C for 80 min, which refers to nearly two weeks at room temperature, is applied to all diodes after irradiation.

The resulting damage rate for all pre-production 2S and PS-s batches in Europe is shown in fig. 7.6. The error bars represent the propagated statistical uncertainty. It has been evaluated with a toy Monte Carlo simulation with varying equally distributed temperatures between 19 °C and 21 °C. This temperature range is a result of the measurement specifications. If the

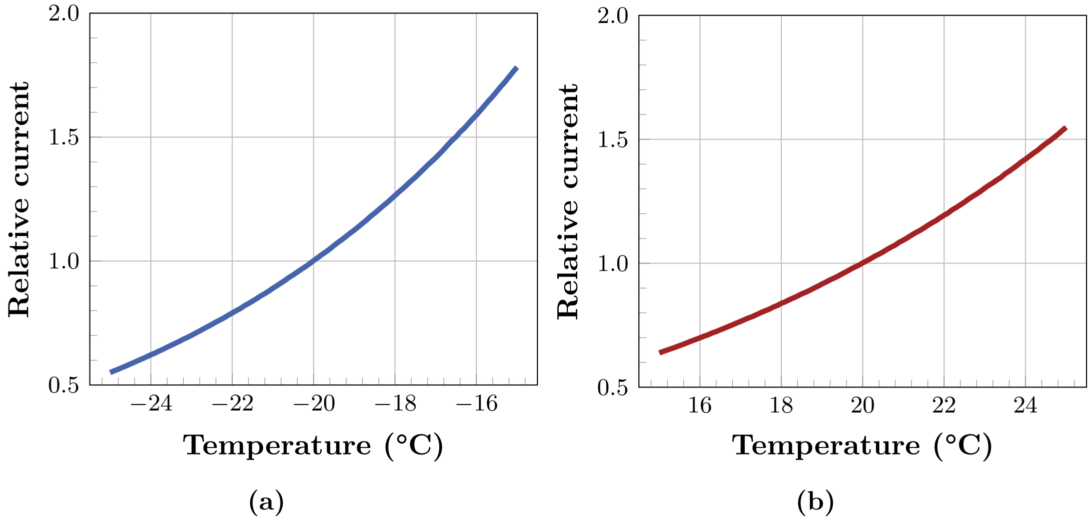

Figure 7.5.: Relative leakage current scaling for different temperatures around −20 °C (a) and 20 °C (b).

temperature is outside of a ±1 °C window around the set temperature the measurement is not conducted. On the other hand that means that the temperature can be up to ±1 °C off of the assumed 20 °C. In reality the temperature might not really be equally distributed. The most likely cases are the cases when the temperature is around the set temperature or when it enters the required range at around 19 °C and 21 °C. Nevertheless, for the error estimation an equal distribution has been assumed as a best guess. Additional to the temperature uncertainty, the fluence statistically varies by 10.3% because of spectroscopy and weight of the nickel foil that is used for the fluence determination after the irradiation. Hence, a Gaussian distribution with $\sigma = 10.3\%$ is assumed. The damage rate depends on these two parameters over

$$\alpha(T, \Phi) \propto I(T, \Phi) \propto T^2 \exp(-1.21\,\mathrm{eV}/2k_\mathrm{B}T) \times \Phi. \tag{7.4}$$

Varying the temperature and the fluence as explained leads to a standard deviation of the resulting $\alpha(T, \Phi)$ distribution of 11.52%. This is plotted as the error bars in fig. 7.6. The standard deviations for every wafer i lead to weighting factors w_i

$$w_i = \frac{1}{\sigma_i^2}. \tag{7.5}$$

The weighted mean of the estimated damage rate α is then given by

$$\overline{\alpha} = \frac{\sum w_i \cdot \alpha_i}{\sum w_i}. \tag{7.6}$$

Finally, the uncertainty on the mean value of α can be calculated via

$$\sigma_\alpha = \sqrt{\frac{1}{\sum w_i}}. \tag{7.7}$$

The final outcome $\alpha = (3.85 \pm 0.07) \times 10^{-17}\,\mathrm{A\,cm^{-1}}$ is indicated by the horizontal line in fig. 7.6. This value is 3.5% below the literature value of $\alpha_\mathrm{Moll} = (3.99 \pm 0.03) \times 10^{-17}\,\mathrm{A\,cm^{-1}}$ [Mol99]. It is expected that the two values do not match perfectly because of the difference in the procedures. Different to the investigations in [Mol99], the guard ring has not been connected during the measurements. This is to keep the preparation time as low as possible. The guard ring connection would help to establish a more defined active region. This is compensated by increasing the volume for the calculation by the guard region. The volume is fixed to $V = 8.37\,\mathrm{mm}^3$ for the calculations, since always a similar diode with the same geometry is used. In the procedure in [Mol99] the current has been extracted in saturation of the $I(V)$ characteristics. However, since no clear saturation occurs for the diodes of the Outer Tracker sensor production, the current is always extracted at 600 V bias. The bias of 600 V is the nominal operation voltage in Phase-2 and has been used in the previous R&D studies as well.

Despite the differences in the procedure, the two values of [Mol99] and of this work are quite close to each other. However, what is more relevant in terms of production and quality control is the spread of the measured values for the different wafers. The final spread, defined as the standard deviation of the damage rate data set, is $0.28 \times 10^{-17}\,\mathrm{A\,cm^{-1}}$. This is 7.3% of the mean and comparably small considering the pure statistical uncertainties of 11.5%. Therefore, the uncertainty might be slightly overestimated. The investigation of the diodes of the pre-production 2S and PS-s batches demonstrates a working procedure for continuous reliable leakage current and related damage rate estimations. These investigations serve as a reference for the following structures of the production. Although there is no specific limit for the damage rate that could trigger a deeper investigation, it is possible to monitor trends during the full mass production.

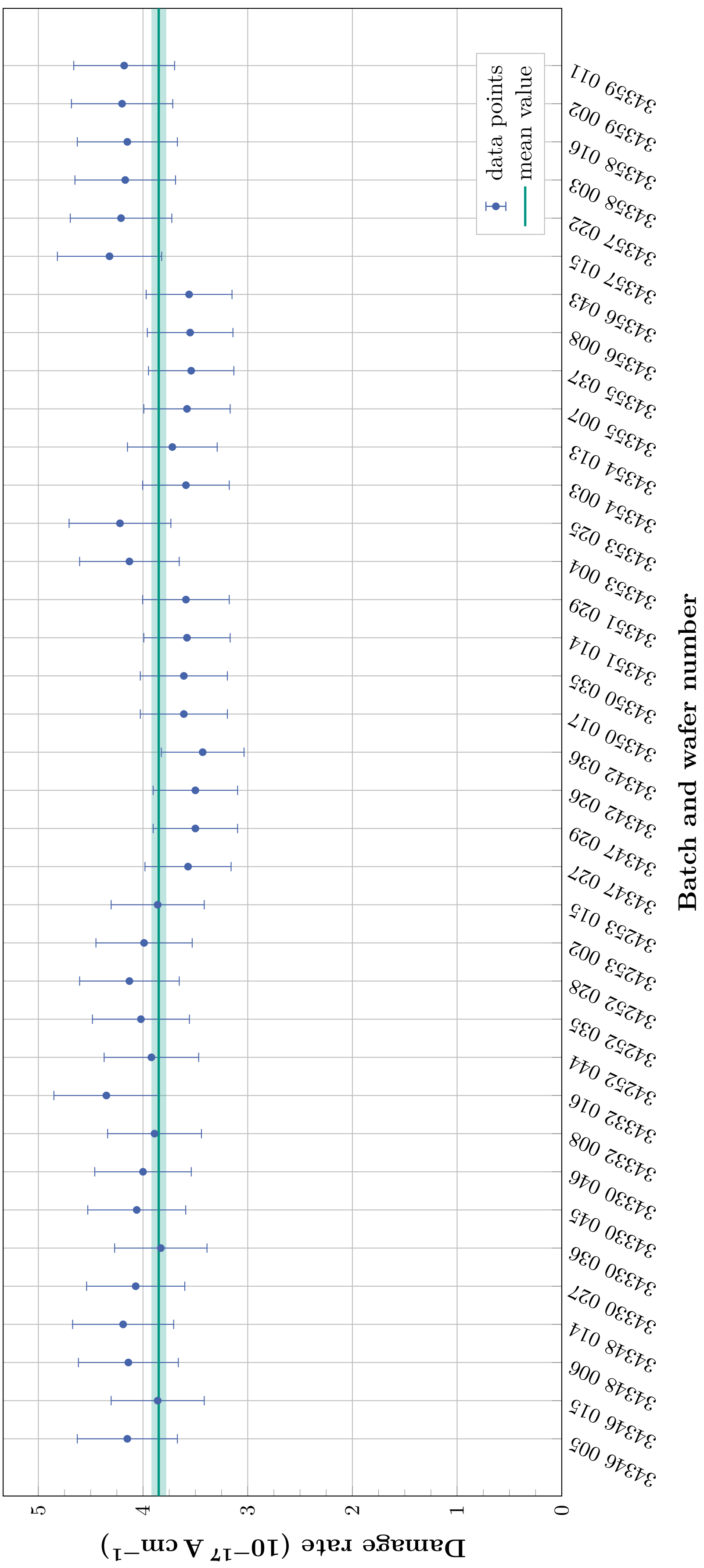

Figure 7.6.: Results of damage rate estimations for all 2S and PS-s batches from the pre-production outside of the US (KIT). The error bars represent the statistical uncertainty on the damage rate as explained in the text.

Table 7.4.: Settings of the leakage current and capacitance over applied bias measurements on sensors after irradiation.

Leakage current measurement		Capacitance measurement	
Backplane bias	0 V to −1000 V	Backplane bias	0 V to −1000 V
Step size	10 V	Step size	10 V
Compliance	300 µA	Compliance	300 µA
		AC amplitude	250 mV
		AC frequency	1 kHz
Temperature	−20 °C	Temperature	−20 °C

7.2.3. Electrical Characterisation of Strip Sensors after Irradiation

After the strip sensors have been irradiated and the radioactivity of the material is subsided, they are returned back to the IT centre and receive a reception annealing. In order to equalise effects from unintended annealing during shipment or handling, the hadron irradiated strip sensors undergo a high temperature treatment of 60 °C for 20 min. This is equivalent to 3.8 days at 21 °C which is usually referred to as room temperature (RT). Afterwards leakage current and capacitance characteristics are conducted according to the specifications in table 7.4. To cope with the high leakage current after irradiation, the sensors are cooled down to −20 °C. This is also close to the expected sensor temperature in the Phase-2 Outer Tracker. Although the leakage current is suppressed by a factor of 59 by the cooling, the current compliance limit has to be increased by an order of magnitude. The maximum applied bias voltage for the capacitance measurement is increased to 1000 V, since the full depletion voltage is increased by irradiation. However, the extraction of the depletion voltage is not trivial and also less reliable after irradiation. Therefore, these measurements are conducted in case they might be interesting later but not analysed on a regular basis. What is more important for the operation of the sensors in the assembled detector is the charge collection, which is presented in section 7.2.4.

Similar to the strip scans pre irradiation, strip scans after irradiation are performed. The constant bias voltage is again 600 V but the temperature is decreased to $T_{\text{meas}} = -20\,^{\circ}\text{C}$ in order to cope with the high defect-induced leakage current. The summary of the strip scans is shown in table 7.5. It can be seen that the measured value for the bias resistance is now considerably higher compared to the measurements prior to irradiation in table 7.3. However, this is not an effect of the irradiation but a side-effect due to the cooling. The polysilicon bias resistance R_{poly} is increased for lower temperatures and at a value that is expected for −20 °C as investigated in [Fis20]. The fact that the increase of the bias resistances cannot be a result of the irradiation is also reflected by the fact that the 2S and PS-s values are similar although the fluence is roughly tripled. The AC coupling capacitance C_{ac} has not changed after the irradiation as expected. Again, the value is slightly higher for the PS-s batches because of the wider implant. The strip leakage current I_{leak} is increased by several orders of magnitude compared to the case without radiation defects. The PS-s batches received a fluence of $\Phi_{\text{PS-s}} = 1.1 \times 10^{15}\,\text{n}_{\text{eq}}/\text{cm}^2$ that is 2.75 times higher than the 2S fluence of $\Phi_{2\text{S}} = 4 \times 10^{14}\,\text{n}_{\text{eq}}/\text{cm}^2$. Consequently, due to the proportionality of the leakage current to the fluence, the mean value of the strip leakage current scales up similarly. This is a result of the increased bulk leakage current that is distributed among the strips. It can be seen that the spread is comparably high for the strip leakage current measurements. This is due to the reduced reproducibility of the low temperatures well below the ambient temperature. The chuck is controlled following temperature readings by sensors at the outer edges of the chuck.

Table 7.5.: Results of the strip scans after irradiation.

	2S batches		**PS-s batches**	
Parameter	Mean	Spread	Mean	Spread
R_{poly}	$2.33\,\mathrm{M\Omega}$	$0.08\,\mathrm{M\Omega}$	$2.41\,\mathrm{M\Omega}$	$0.13\,\mathrm{M\Omega}$
C_{ac}	$76.5\,\mathrm{pF}$	$1.2\,\mathrm{pF}$	$85.4\,\mathrm{pF}$	$1.03\,\mathrm{pF}$
I_{leak}	$131\,\mathrm{nA}$	$45.6\,\mathrm{nA}$	$340\,\mathrm{nA}$	$163\,\mathrm{nA}$
R_{int}	$1.52\,\mathrm{G\Omega}$	$1.34\,\mathrm{G\Omega}$	$0.958\,\mathrm{G\Omega}$	$0.78\,\mathrm{G\Omega}$
C_{int}	$1.08\,\mathrm{pF}$	$0.07\,\mathrm{pF}$	$1.07\,\mathrm{pF}$	$0.03\,\mathrm{pF}$

However, in section 6.1 it has been shown that the temperature distribution is non-uniform. Hence, the actual temperature depends on the position on the chuck but also on the dry air flux and the chucks position in the station. Since the measurements were conducted by different operators who used different settings, the fluctuations are high. This can be mitigated by using the exact same conditions for every measurement. This will be done for the production but the measurements presented here cannot be repeated because the sensors underwent the full annealing procedure already. The interstrip resistance R_{int} is decreased drastically after irradiation. Again, for the PS-s batches it is even lower than for 2S batches because of the higher fluence. Intuitively this is expected because surface damage is applied by the ionising proton irradiation. This picture is sufficient to explain the observations in this case but the complex interplay of surface and bulk defects on the interstrip isolation is further evaluated in chapter 8. In fact, the interstrip resistance is lower because of the general increase of the number of free charge carriers in the substrate in case of the higher fluence and not because of the surface damage. The value is slightly below the specification for the sensors tested pre irradiation. However, it is still sufficiently high compared to the bias resistance. A very conservative estimation holds that the interstrip resistance should be 100 times higher than the bias resistance, which would be $0.2\,\mathrm{G\Omega}$, approximately. Additionally, the spread is comparably high, similar to the case of the strip leakage current. This is again a result of the fluctuations of the temperature between the different measurements with different configurations of dry air flux and chuck position. Since the interstrip resistance is determined by a current flow between the strips the impact of the temperature is similar. In addition, the high bulk leakage current that flows through the strips forces the ampere-meter to switch to a less sensitive range. This decreases the accuracy of the measurement itself for heavily irradiated sensors. The interstrip capacitance C_{int} is not affected by the radiation damage as long as the strips are isolated. Hence, the values after irradiation are virtually identical to the values prior to irradiation. Unexpectedly, the number of pinholes is slightly decreased to four of the 2S wafers and still zero for PS-s wafers. This is unlikely a physical behaviour of the devices because pinholes cannot be cured by radiation. However, in both cases, pre and after irradiation, the pinhole currents are sometimes close to the threshold of $I_{\text{diel}} = 10\,\mathrm{nA}$. Hence, two pinholes were not counted because they dropped slightly below the specification. This can also be due to the lower temperature that resulted in a current slightly below the limit. In any case, the most important outcome is that the number of pinholes has not increased by the irradiation.

7.2.4. Signal Measurements on Strip Sensors after Irradiation

After the reception annealing and electrical characterisation is done, signal measurements are performed. The sensors are placed on an ALiBaVa board that is used for charge collection measurements, as described in section 6.2. Wire bonds are placed connecting the sensors'

Table 7.6.: Annealing steps during sensor pre-production. The annealing steps alternate with leakage current and charge collection measurements. The RT equivalent annealing refers to the integrated annealing time at room temperature.

Unit	Annealing time min	Annealing temperature °C	RT equivalent annealing days	 weeks
Step 1	20	60	6.9	0.99
Step 2	40	60	13.3	1.9
Step 3	60	60	23.9	3.41
Step 4	60	60	37.0	5.29
Step 5	15	80	95.8	13.69
Step 6	15	80	160.7	22.96
Step 7	30	80	273.3	39.04
Step 8	30	80	378.6	54.09

AC aluminium pads to a pitch adapter that is further connected to the readout chip. The board is then placed inside the custom-made setup onto a copper bridge. The bridge is temperature controlled via Peltier elements so that the sensor temperature can reach −20 °C for measurements and up to 80 °C for high-temperature annealing. Within the ALiBaVa setup a sequence comprised of leakage current measurement, charge collection measurement and annealing is performed repeatedly. This includes an $I(V)$ curve from 0 V to 1000 V and charge collection measurements from 300 V to 900 V in 100 V steps. As described in section 6.2, a ^{90}Sr source is used to generate a MIP-like signal in the sensors. A charge collection measurement consists of a noise estimation run, a calibration run that unifies the channel response of the readout chip and the final signal run. All measurements are conducted at −20 °C to cope with the high leakage current and to be comparable to previous studies. The annealing procedure is summarised in table 7.6 for the extended procedure that has been used in the scope of this work during the pre-production. Before the first annealing step and after every subsequent step measurements are conducted. A more condensed annealing procedure is foreseen during the full mass production in order to reduce the measurement time: Two steps of table 7.6 are always merged so that the minimal procedure in table 7.7 is obtained. The expected annealing during Phase-2 with an operation of ten years can be estimated by the regular year-end technical stops (YETS). These usually take around two weeks so that after ten years 20 weeks annealing at room temperature (RT) is accumulated. In total, both accelerated annealing procedures end up at roughly a year (378.6 days) room temperature equivalent annealing time, which is clearly above the expected annealing time during Phase-2. Thus, the investigated annealing range yields a wide margin of 270% on the expected value. The calculation of the room temperature equivalent annealing time is based on the annealing of the current-related damage rate α according to the findings in [Mol99] and is calculated with the tool in [ETPa].

The charge collection annealing study has been performed for all of the pre-production 2S (14) and PS-s (3) batches in Europe with at least two sensors per batch. The important parameter for the operation in the real detector is the seed signal. As explained in more detail in section 6.2 the seed signal is the signal that one strip delivers. The specifications hold that the most probable value of the seed signal should exceed 12 times the noise. With a conservative estimation of the noise of the readout chip of 2S sensors, the CBC[3], and the readout chip of PS-s sensors, the SSA[4], limits of 12 000 e^- and 9600 e^- are obtained, respectively. Previous

---

[3] CBC: CMS Binary Chip

[4] SSA: Short Strip ASIC

Table 7.7.: Annealing steps during sensor production. Annealing steps alternate with leakage current and charge collection measurements. The RT equivalent annealing refers to the integrated annealing time at room temperature.

	Annealing time	Annealing temperature	RT equivalent annealing	
Unit	min	°C	days	weeks
Step 1	60	60	13.3	1.9
Step 2	120	60	37.0	5.29
Step 3	30	80	160.7	22.86
Step 4	60	80	378.6	54.09

investigations in a beam test have shown that these limits are indeed reasonable and the seed signal is sufficient to detect particles efficiently [CMSb]. In any case, the investigations aim to monitor a potential drift of the signal after irradiation over the production and cannot directly be compared to the situation in the real detector.

The most important result of the annealing study is shown in fig. 7.7. It shows the seed signal in dependence on the annealing for a constant bias of 600 V, which is the desired maximum operation voltage of the new CMS Outer Tracker. The two limits are indicated by the horizontal lines in red and green for 2S and PS-s batches, respectively. The data points represent the mean of all 2S (PS-s) batches that have been irradiated with protons to a fluence of $\Phi_{2S} = 4 \times 10^{14}\,\mathrm{n_{eq}/cm^2}$ ($\Phi_{PS} = 1.1 \times 10^{15}\,\mathrm{n_{eq}/cm^2}$). The transparent bands indicate the spread of the values that have been calculated as the standard deviation of the data set. Dashed lines indicate the maximum and minimum values of the whole pre-production sensors that have been measured for the respective annealing condition. It can be seen that these bands are quite narrow. Especially the full distance between the maximum and minimum value of the measurements on 2S samples is in the order of the specified uncertainty of the system of $1000\,\mathrm{e^-}$. For the PS-s wafers the band is similarly narrow but widens a bit when reverse annealing comes into play at annealing times higher than the expected time during Phase-2.

The data in fig. 7.7 includes wafers with a pre irradiation depletion voltage of 260 V to 340 V. From the maximum and minimum values it can be seen that there is no clear dependence on the bias voltage visible, although a slight difference might be expected. However, if there is an impact, it is below the resolution of $1000\,\mathrm{e^-}$. For the subsequent production of wafers it is expected that the charge collection measurements after irradiation with the respective fluence will be in the bands derived by this pre-production evaluation.

Impact of the Strip Pitch on the Charge Collection

A question that arises is how significant the impact of the different pitches of the 2S and PS-s strip sensors is. The smaller pitch of 90 µm of the 2S strip sensors is expected to result in a lower seed signal. This is due to the slightly smaller area in which the charge is collected per strip. In addition, the cluster size (number of strips in a signal cluster) should be slightly increased. In case of the PS-s pitch of 100 µm the cluster size should be smaller and the seed signal higher. Overall, the cluster signal should be independent of the pitch, since it reflects the charge collection of the full generated signal by the substrate. After irradiation, the cluster signal is decreased due to the trapping but should not depend on the pitch.

In order to investigate the pitch dependence of the signal, two 2S-like strip sensors have been irradiated to the PS fluence of $\Phi_{PS} = 1.1 \times 10^{15}\,\mathrm{n_{eq}/cm^2}$. The charge collection measurement compared to the measurements on PS-s type strip sensors is shown in fig. 7.8a. A small difference can be observed for half of the annealing time. However, the difference vanishes

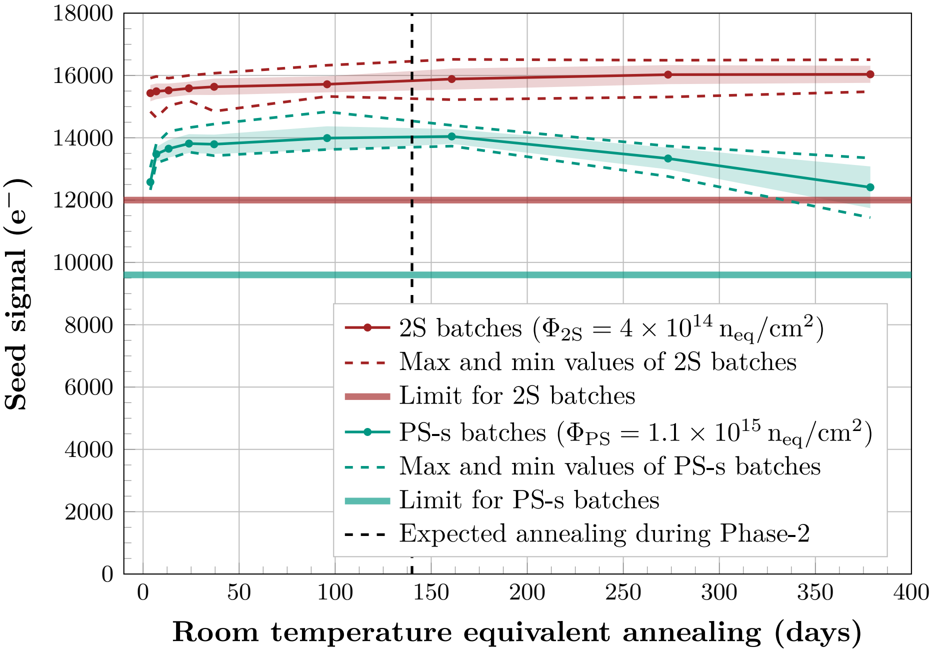

Figure 7.7.: Seed signal of pre-production 2S and PS-s batches at a bias voltage of 600 V dependent on the annealing time. The expected annealing during Phase-2 is indicated with the vertical dashed black line. If annealing exceeds this expected value reverse annealing starts in case of the higher fluence of $\Phi_{PS} = 1.1 \times 10^{15}$ n$_{eq}$/cm^2.

more and more towards the reverse annealing. The cluster signal is shown in fig. 7.8b. It scales similarly for all samples with the annealing time, which is a good consistency check.

When the cluster signal is equal but the seed signal is smaller, the cluster size has to be larger. This is reflected in fig. 7.9a for the 2S and PS-s type sensors at the PS fluence. It can be concluded that the cluster size is slightly increasing and therefore the seed signal slightly decreases. However, the effect is not that severe and more like a tendency than a significant finding. The cluster size of the 2S batches with the 2S fluence and the PS batches with the PS fluence are compared in fig. 7.9b. It can be seen that the cluster size is higher for the 2S sensors. From the previous investigation in fig. 7.9a it is clear that this is not only the result of the different strip pitch. More important than the pitch is that the general signal decreases for increasing fluence, thus there is less signal that can spread over several strips.

Comparison to Neutron Irradiation

In the frame of the hadron irradiation tests sensors have been irradiated with protons at KIT. In addition, two sensors have been irradiated and measured so far in the US with neutrons. The difference between the measurements is shown in fig. 7.10. A significantly stronger annealing characteristics is visible for the neutron irradiated samples for both fluences. This is expected because of the findings in [Gos18], where a clear difference of the seed signal's annealing behaviour after neutron and proton irradiation for Outer Tracker prototype sensors has been found. However, for the 2S fluence it is not expected that the signal strength exceeds the signal of purely proton irradiated sensors. This might be a hint that the neutron fluence was in fact slightly lower than expected. It can also be seen that for the PS fluence the neutron irradiated sample drops slightly below the specified limit of 9600 e$^-$ for very long annealing times beyond 250 d at room temperature. However, the particle composition in Phase-2 will be

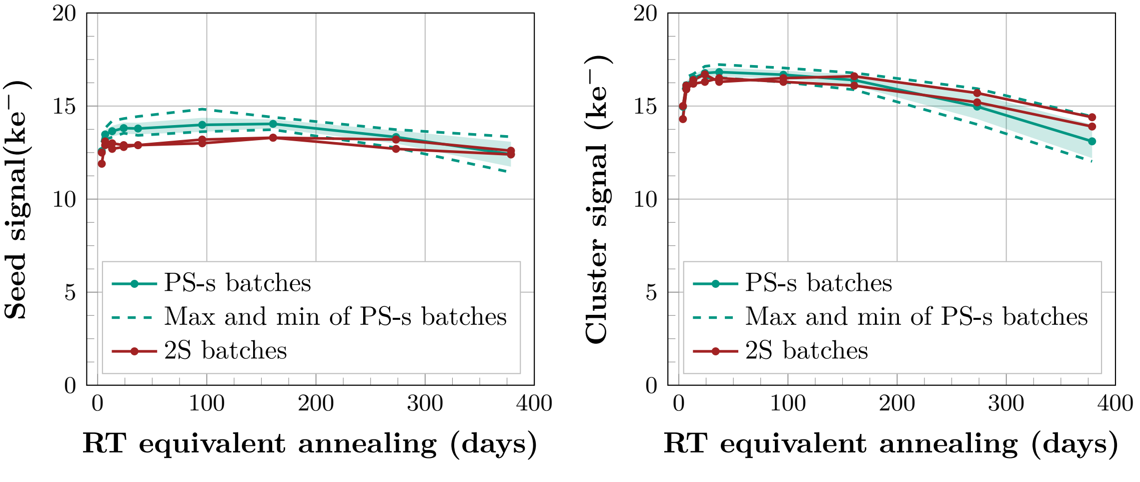

(a) (b)

Figure 7.8.: Seed signal (a) and cluster signal (b) comparison of strip sensors with different pitches from PS-s and 2S wafers at 600 V. All sensors have been irradiated to the fluence of $\Phi \approx 1.1 \times 10^{15}\,\mathrm{n_{eq}/cm^2}$.

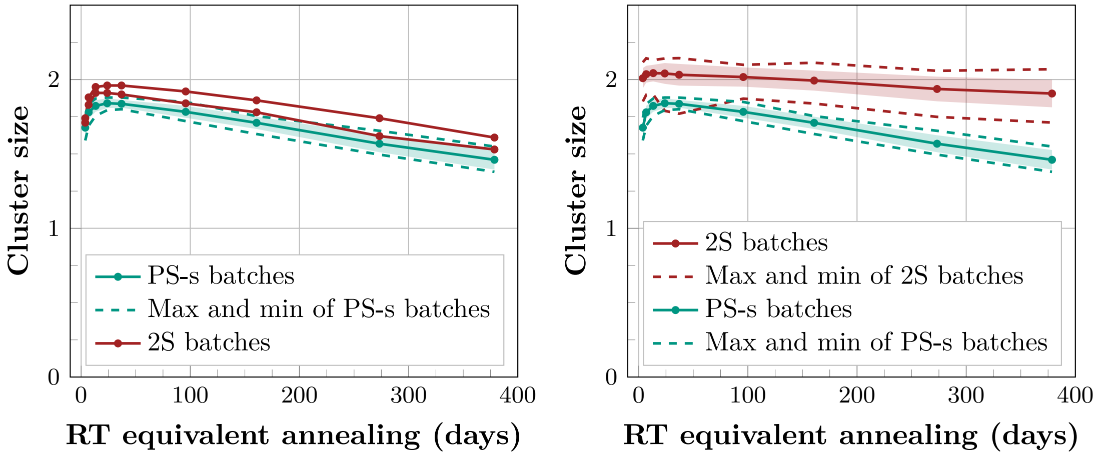

(a) (b)

Figure 7.9.: Cluster size comparison of sensors from PS-s and 2S wafers with a different pitch at a constant bias voltage of 600 V for the same fluence of $\Phi = 1.1 \times 10^{15}\,\mathrm{n_{eq}/cm^2}$ (a). Comparison of the cluster size of PS-s and 2S wafers with the respective expected fluence in Phase-2 at a constant bias of 600 V (b).

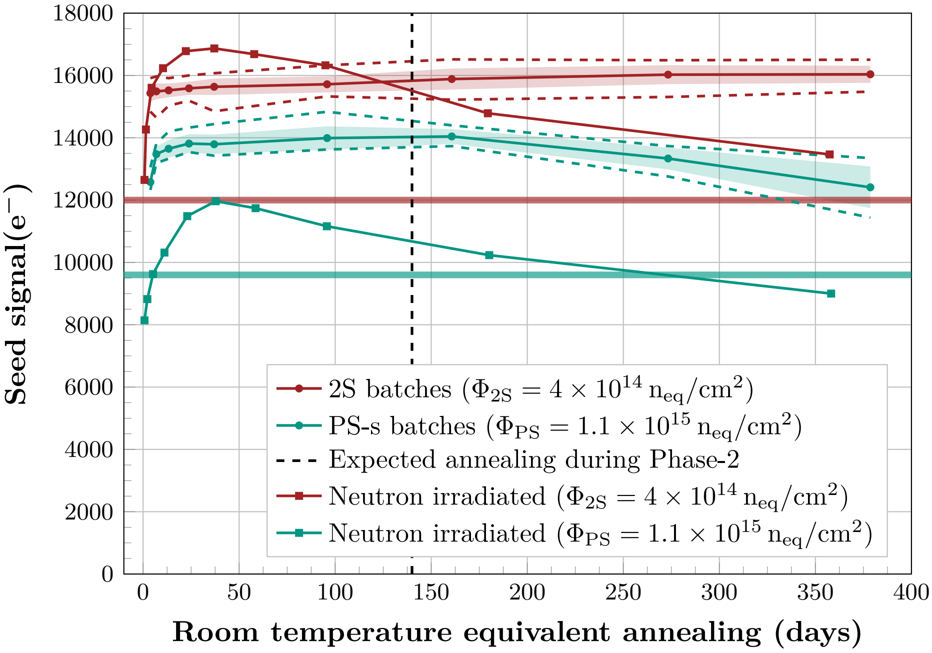

Figure 7.10.: Seed signal comparison of neutron irradiated samples, irradiated and measured in the US, to the sensors irradiated with protons and investigated at KIT with a constant bias voltage of 600 V.

a mixture (compare section 2.5.3). Therefore, the pure neutron irradiation overestimates the effect of expected reverse annealing in Phase-2. Nevertheless, around the expected annealing, the signal is still sufficiently high. In addition, the limits here indicate conservative estimations and efficient particle detection is still possible if the signal drops slightly below.

7.2.5. Electrical Characterisation after Annealing and Signal Measurements

After the full annealing procedure with charge collection measurements is conducted, the strip sensors are electrically characterised again. This is done under the premise of gaining as much information as reasonably possible in case they will be required. The strip scan results are displayed in table 7.8. Similar to the measurements pre annealing, the measurements are conducted at $T = -20\,^{\circ}\mathrm{C}$. All parameters that were not affected by the irradiation are also not affected by annealing of radiation-induced defects. These are the resistance of the polysilicon bias resistor R_{poly}, the AC coupling capacitance C_{ac} and the interstrip capacitance C_{int}.

The strip leakage current has decreased by at least 50% compared to the case after irradiation but with only 3.8 days RT annealing. However, again the spread is comparably high because the measurement is prone to temperature variations. The interstrip resistance has at least doubled compared to the situation after irradiation but without annealing. This is expected since the defects that lead to a higher charge carrier concentration partially recombined. Also here, as explained in section 7.2.3, the measurements are sensitive to temperature deviations. Additionally, the number of pinholes is increased to five for 2S and three for PS-s wafers. This is not expected since annealing should not harm the coupling oxide. However, the sensors have been handled a lot and especially the AC pads have been contacted with wire bonds that are pulled of again. The hypothesis is therefore that the pinholes might have emerged due to the handling. Nevertheless, the fraction of pinholes per tested strips is still very low, with 0.32%, approximately.

Table 7.8.: Results of the strip scans after annealing.

	2S batches		**PS-s batches**	
Parameter	Mean	Spread	Mean	Spread
R_{poly}	2.35 MΩ	0.09 MΩ	2.45 MΩ	0.14 MΩ
C_{ac}	75.4 pF	1.13 pF	84.8 pF	1.08 pF
I_{leak}	62.8 nA	21.1 nA	137 nA	45.9 nA
R_{int}	3.59 GΩ	1.8 GΩ	2.98 GΩ	1.73 GΩ
C_{int}	1.1 pF	0.07 pF	1.06 pF	0.15 pF

Table 7.9.: Stations that test structures in the frame of X-ray irradiation tests pass through in chronological order.

X-ray test structures	
Process	Location
Manufacturing	HPK
Shipment	to CERN
Shipment	to PQC centre
Shipment	to KIT (ETP)
Reception measurements	Probe station
Dicing (for 2S type)	KIT (IPE)
Irradiation	KIT (ETP)
Specific treatment	Oven and probe station
Electrical tests	Probe station
Storage	Freezer

7.3. Irradiation Tests with X-Ray Irradiation

The X-ray irradiation tests are performed to ensure a reliable oxide quality over the full sensor production. Without radiation damage, this is already covered by PQC. The procedure is extended for the situation with surface damage, by a specific irradiation testing procedure. Different to the hadron irradiation, X-ray irradiation is exclusively performed at KIT. The structures that are studied for these investigations are located on the right part of the irradiation test half-moon in fig. 7.4. This includes a MOS (metal-oxide-semiconductor) capacitor and a GCD (gate-controlled diode), whose basic functionalities are explained in detail in chapter 5. The stations that these structures pass through are summarised in chronological order in table 7.9. Since both are situated on the same piece of silicon, both pass through the same stations at the same time. A dicing procedure is only applied for 2S wafers. In case of PS-s and PS-p wafers the structures are already separated from the babysensor and the diode set so that no further cut is required. When the dicing is done, pre irradiation measurements are performed. In case of the MOS, the capacitance is measured in dependence on the backplane bias to extract the flat-band voltage. The diode part of the GCD is biased and the current is measured for varying gate voltages to extract the surface current with the corresponding surface generation velocity. Then, the structures are irradiated with X-rays to a dose that will be specified later. The irradiation is followed by a specific treatment that is also explained in greater detail in a subsequent section. Finally, the electrical measurements after irradiation are conducted and the samples are stored in the freezer to prevent annealing.

Table 7.10.: Settings of the measurements on the MOS and GCD structures pre irradiation.

MOS		GCD	
Backplane bias	−2 V to 5 V	Gate bias	−20 V to 5 V
Step size	0.1 V	Step size	0.1 V
AC amplitude	250 mV	Backplane bias	−5 V
AC frequency	10 kHz		
Compliance	300 µA	Compliance	30 µA
Temperature	20 °C	Temperature	20 °C

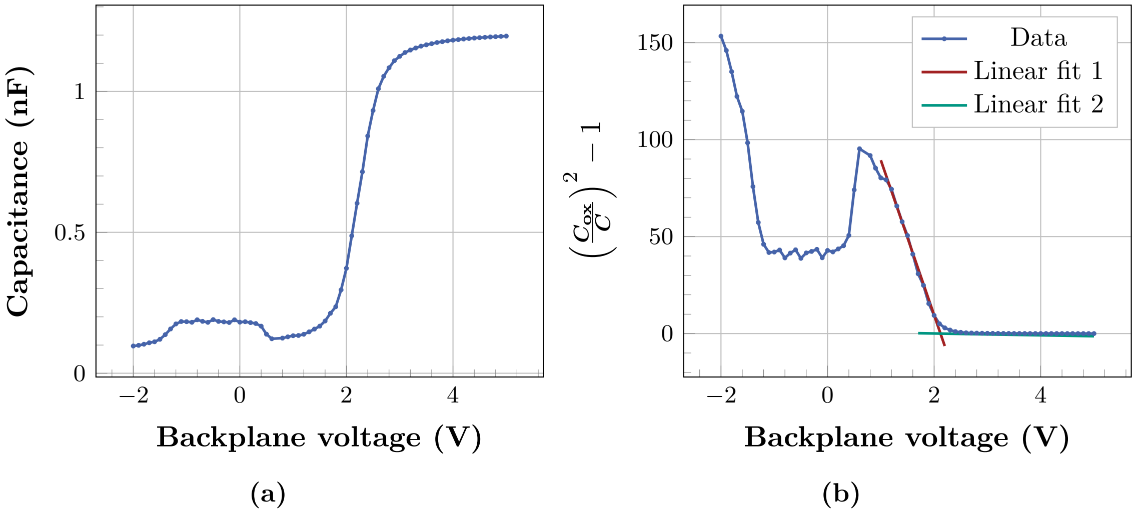

(a) (b)

Figure 7.11.: Measurement of the capacitance of a MOS dependent on the backplane bias (a) and method to extract the flat-band voltage (b).

7.3.1. Characterisation pre Irradiation

The X-ray irradiation tests are performed to ensure good quality of the oxide and interface regions of the sensors throughout the production. The MOS and GCD (shown in fig. 7.4 on the right side) are used to determine the flat-band voltage V_{fb} and the surface generation velocity s_0, respectively. Prior to any irradiation the applied voltage range is rather small since the flat-band voltage is only about a few volts. The measurement parameters are given in table 7.10. For the capacitance measurement on the MOS the frequency is set to 10 kHz instead of the 1 kHz of the measurements on diodes and sensors to stay comparable to other studies. Pre irradiation, no dependence of the flat-band voltage on the frequency has been observed in a reasonable frequency range.

For the pre-production of 2S and PS-s batches every batch outside of the US has been tested in the course of this work. Similar to the hadron irradiation, a minimum of two wafers per batch are tested for the sake of reliability. Additionally, test structures of two pre-production PS-p batches arrived in time so that they could be tested as well. The other PS-p batches will arrive later and will be tested then. The flat-band voltage can be extracted from a capacitance over bias potential measurement as explained in section 5.2.2. A reliable analysis procedure is required in order to establish a baseline for the extracted parameters. Therefore, it is not extracted as the inflection point of the curve but with a method that has been compared to other methods in [PP10] and is explained in the following.

A bare capacitance measurement on a MOS structure is shown in fig. 7.11a. The same measurement but transformed to $(C_{\mathrm{ox}}/C)^2 - 1$ is presented in fig. 7.11b. The oxide capacitance $C_{\mathrm{ox}} = 1.2\,\mathrm{nF}$ is similar for all devices, since it depends on the geometry. Two linear fits are performed to extract the flat-band voltage. One fit (red in the figure) represents the depletion regime of the device. Its intersection with the x-axis determines the flat-band voltage. The starting point of the fit is around the local maximum and adjusted manually first. A different approach to determine the starting point is explained in section 7.3.3. The stopping point where the curvature starts is not sharply defined. Therefore, a second linear fit to the accumulation regime defines the stopping point for the first fit so that both fits represent the data as well as possible. Technically, the fitting procedure is done by creating a section-wise defined function that consist of two linear functions for x values higher and lower than the intersection point i.

$$f(x) = \begin{cases} m_1 \cdot x + b_1 & \text{for } x \leq i \\ m_2 \cdot (x - i) + m_1 \cdot i + b_1 & \text{for } x > i \end{cases} \tag{7.8}$$

In general, for $x > i$ the second fit part would be $f(x) = m_2 \cdot (x - i) + b_2$. At the intersection point $x = i$ where the transition from one section to the other occurs with eq. (7.8) it gives

$$m_2 \cdot (i - i) + b_2 = m_1 \cdot i + b_1 \tag{7.9}$$

$$\Rightarrow b_2 = m_1 \cdot i + b_1 \tag{7.10}$$

Therefore, the free parameters can be condensed down to four with i, m_1, b_1, and m_2 since b_2 is substituted by a combination of m_1, b_1 and i. With the "curve_fit" method of the scipy optimisation package of python ([Pyt]), these four parameters are optimised so that $f(x)$ fits the measured curve as close as possible. The flat-band voltage is then calculated by

$$V_{\mathrm{fb}} = -\frac{b_1}{m_1} \tag{7.11}$$

The uncertainty of the fitting parameters is propagated to the uncertainty $\sigma_{V_{\mathrm{fb}}}$ on the flat-band voltage with

$$\sigma_{V_{\mathrm{fb}}} = \sqrt{\left(\frac{\sigma_{b_1}}{m_1}\right)^2 + \left(\frac{b_1 \cdot \sigma_{m_1}}{m_1}\right)^2}. \tag{7.12}$$

The result of the flat-band voltage determination of all pre-production measurements prior to irradiation is shown in fig. 7.12 with uncertainties according to eq. (7.12). For the wafers that have been processed in an AC process with a stronger focus on the coupling oxide, the flat-band voltage is considerably lower than the with the pure DC process. The flat-band voltage for the 2S and PS-s batches is $V_{\mathrm{fb,\,AC}} = (1.790 \pm 0.007)\,\mathrm{V}$ indicated with the cyan blue line in the figure. In case of the DC process for the PS-p batches, where there is no specific coupling oxide but just the standard oxide, the flat-band voltage is $V_{\mathrm{fb,\,DC}} = (3.56 \pm 0.07)\,\mathrm{V}$, which is twice as high.

The surface current I_{surf} is extracted from measurements on the GCDs, with the parameters of table 7.10, exactly as explained in section 5.3. With the elementary charge e, the gate area of $A_{\mathrm{gate}} = 0.095\,91\,\mathrm{cm}^2$ and the intrinsic charge carrier concentration of silicon at 20 °C $n_i = 5.42 \times 10^9\,\mathrm{cm}^{-3}$ (according to [MT93]), the surface generation velocity can be calculated with

$$s_0 = \frac{I_{\mathrm{surf}}}{e \cdot n_i \cdot A_{\mathrm{gate}}}. \tag{7.13}$$

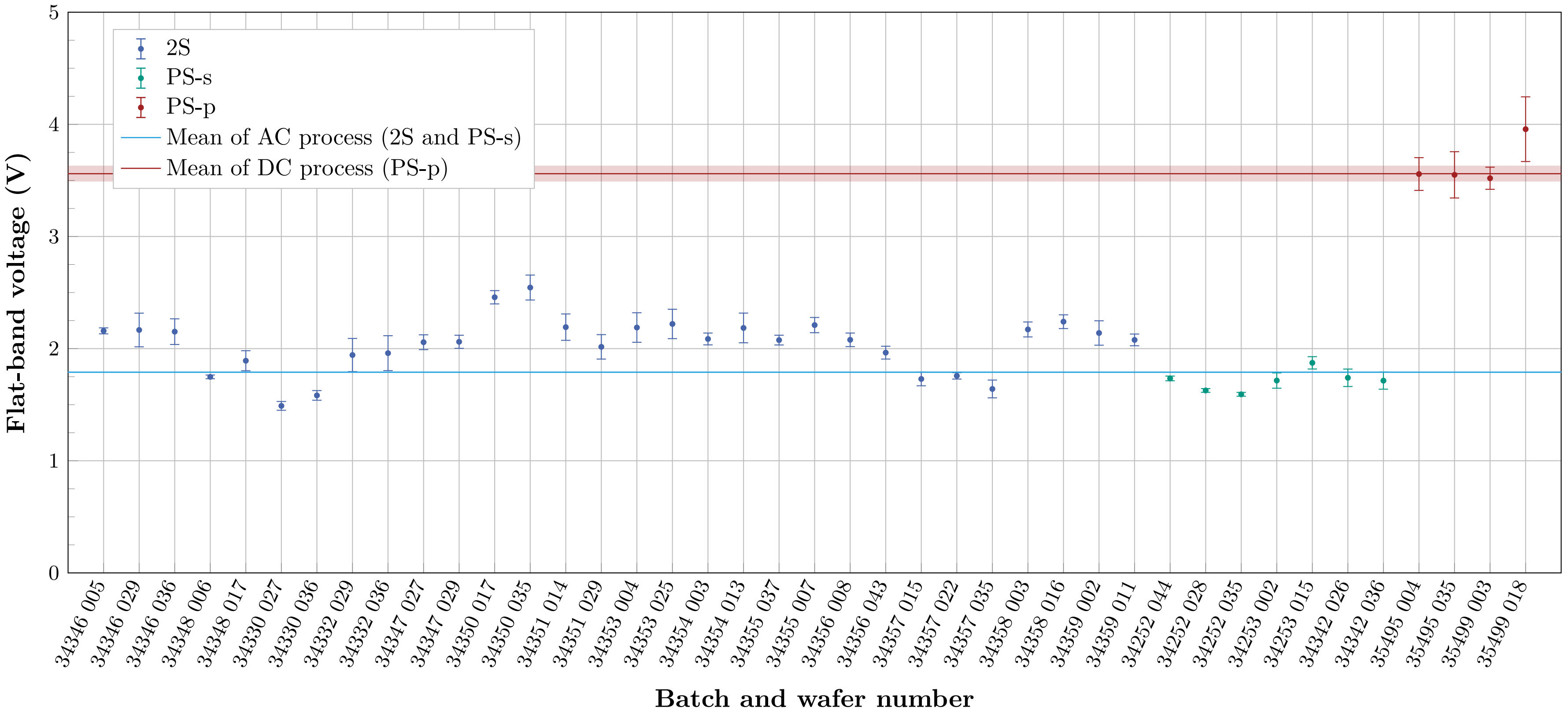

Figure 7.12.: Results of the flat-band voltage extraction from capacitance over backplane bias curves of MOS devices prior to irradiation. The error bars represent the fit uncertainty propagated to the flat-band voltage. The bands around the mean indicate the uncertainty of the mean value.

The result of the surface generation velocity of all the 2S and PS-s pre-production batches and the two PS-p batches are shown in fig. 7.13. Again, the values of the wafers with an AC process show a better oxide quality (lower s_0) than the DC process of the PS-p wafers. The extracted surface generation velocity for the AC processes is $s_{0,\,\mathrm{AC}} = (0.84 \pm 0.02)\,\mathrm{cm\,s^{-1}}$ and for the DC process $s_{0,\,\mathrm{DC}} = (1.70 \pm 0.13)\,\mathrm{cm\,s^{-1}}$, which is again doubled. Intuitively it makes sense that both parameters scale similarly with the oxide quality as it is the case here. However, in general it cannot be assumed that the parameters are fully correlated because they depend on different physical defects.

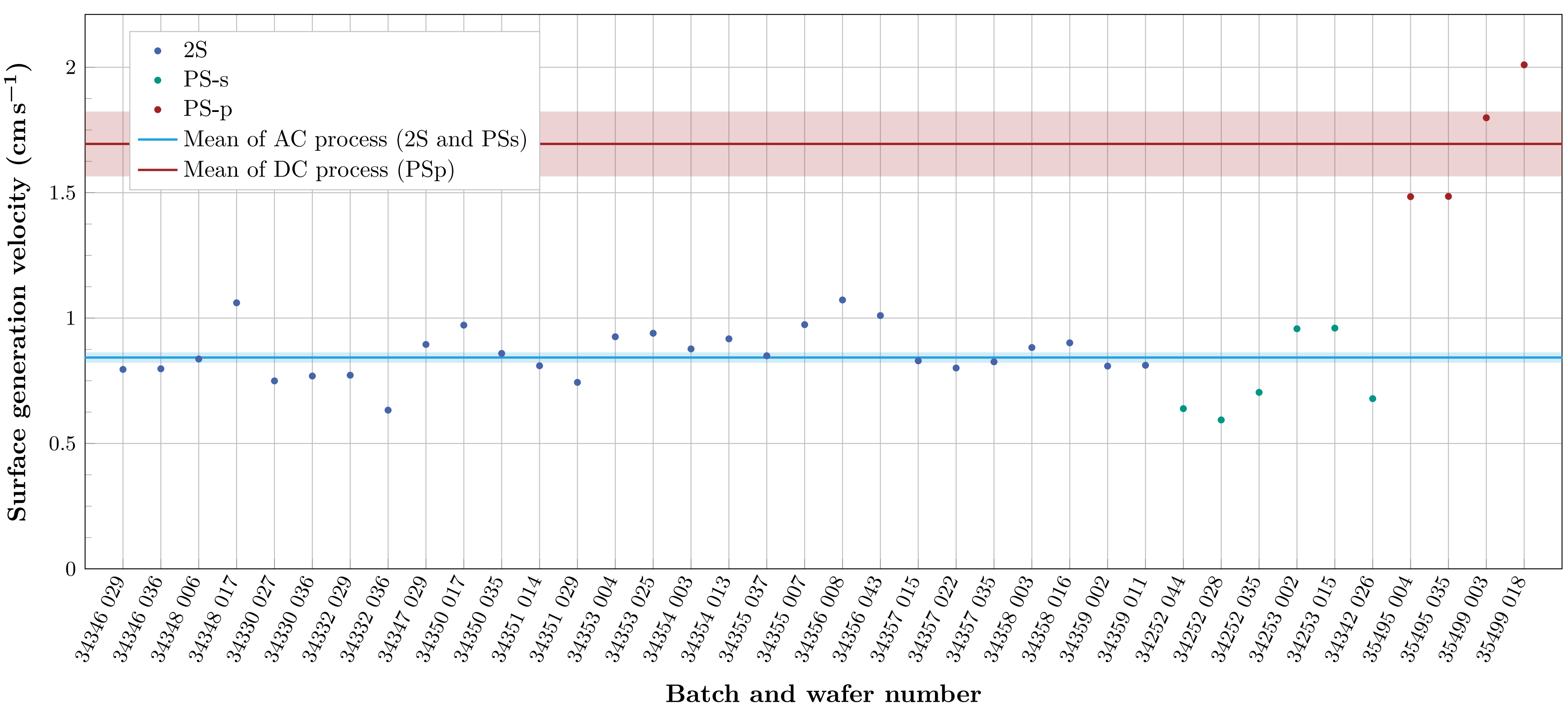

Figure 7.13.: Results of the surface generation velocity extracted from diode current measurement dependent on the gate voltage of GCDs. The bands around the mean indicate the uncertainty of the mean value.

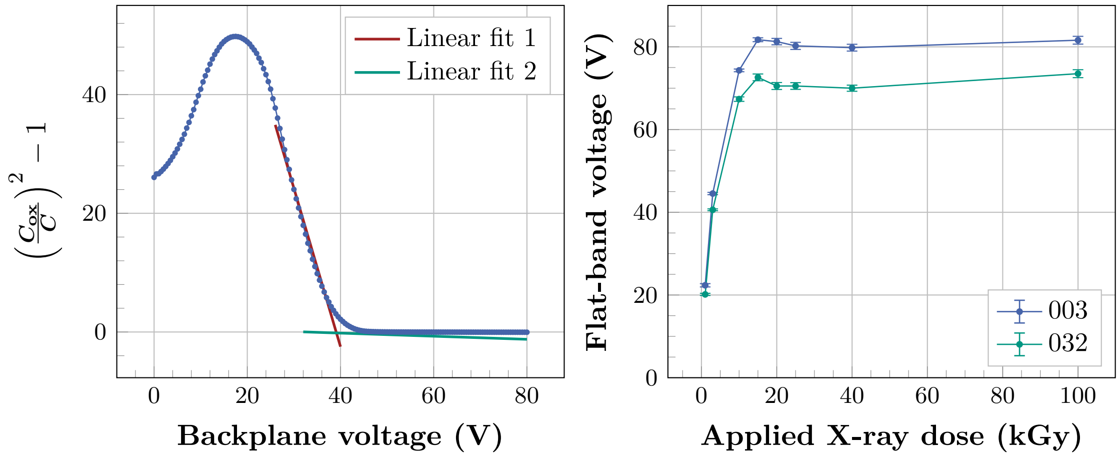

(a) (b)

Figure 7.14.: Exemplary measurement on a MOS after X-ray irradiation (a). The flat-band voltage is extracted with the help of two linear fits. X-ray dose dependence of the flat-band voltage (b) of two wafers from the same batch. Both curves saturate around 15 kGy but at slightly different values.

7.3.2. First Investigations after Irradiation

After irradiation, the flat-band voltage and surface generation velocity are expected to increase significantly. For the hadron irradiation tests, the fluences that are used to irradiate the test structures are determined from the maximum expected accumulated fluence during the operation. However, for the expected dose in the 2S region it would be $D_{2\mathrm{S}} = 100\,\mathrm{kGy}$ and in the PS region up to $D_{\mathrm{PS}} = 1\,\mathrm{MGy}$. The homogeneous X-ray irradiation procedure (explained in section 6.3.3) takes 0.68 h per 1 kGy for the MOS and GCD structure together. Therefore, irradiating for 68 h or even longer for only one wafer to reach $D_{2\mathrm{S}}$ is clearly too much. In addition, there is no specific limit for the surface related parameters that have to be fulfilled different to, for example, for the signal measurements. Therefore, the strategy is to keep track of the oxide degradation caused by X-rays over the production.

In previous studies it has been observed that the flat-band voltage saturates at around 10 to 20 kGy. In order to investigate the behaviour of the flat-band voltage and the surface generation velocity after irradiation, two wafers of one batch of the pre-production have been irradiated subsequently to 100 kGy. An exemplary $(C_{\mathrm{ox}}/C)^2 - 1$ over bias voltage curve after irradiation is shown in fig. 7.14a. Compared to the case pre irradiation, the curve is shifted considerably to higher bias voltages. Additionally, the transitions of inversion into depletion and from depletion into accumulation are less sharp. Nevertheless, it is still possible to apply the two linear fits and estimate the flat-band voltage. Similar to the case pre irradiation, the uncertainty on the flat-band voltage is estimated as the propagated uncertainties on the first fit with eq. (7.12).

The result of a subsequent irradiation alternating with measurements is shown in fig. 7.14b. The first and most important outcome is that the flat-band voltage saturates at around 15 kGy. This is consistent with previous internal investigations on n-type MOS capacitors but also with the findings in chapter 8 on strip sensors. Additionally, it can be seen that the two structures do not saturate at the same flat-band voltage value. This will be discussed further after the discussion of the results of measurements on GCDs.

An example of a measurement after irradiation on a GCD is given in fig. 7.15a. To be comparable to other studies, a higher fixed diode bias than before of $-10\,\mathrm{V}$ is used. Compared

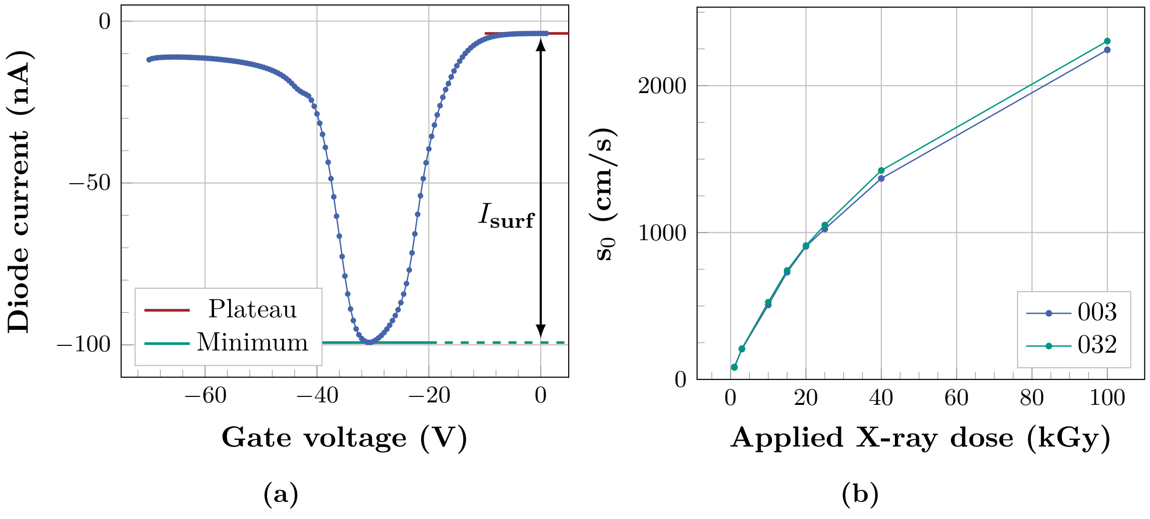

(a) (b)

Figure 7.15.: Exemplary measurement of a GCD after X-ray irradiation (a) and the resulting surface generation velocity (b) dependent on the applied X-ray dose.

to the case pre irradiation, the curve is shifted to the left, since the flat-band voltage is increased. Additionally, the minimum diode current is significantly higher as well. Because there is no clear plateau anymore in depletion, the minimum value is determined. Similar to the situation prior to any irradiation, the average value of the plateau in the inversion regime is taken as the baseline from which the difference to the minimum value is taken.

Measurements on the GCD have been performed alternating with X-ray irradiation similar to the MOS case. The results are illustrated in fig. 7.15b. Different to the flat-band voltage investigation, the surface generation velocity of the two structures scales similarly. This might be an indicator that the two wafers are actually similar in terms of oxide quality and that there was no error in the irradiation procedure. Instead, it can be concluded that a more reliable measurement procedure is required for the MOS structures. Contrary to the flat-band voltage extracted from MOS measurements in fig. 7.14b, the surface generation velocity s_0 does not saturate for doses below 100 kGy.

This leads to the question which dose should be considered for the irradiation tests in the course of the CMS Phase-2 Outer Tracker sensor production. In order to not spend too much effort on multiple irradiations which requires more time and is erroneous, the MOS and GCD structures should be irradiated to the same dose. Contrary to the seed signal investigations, there is no clear limit that could distinguish an acceptable s_0 and an unacceptable s_0. The main goal of the irradiation testing procedure in general, and the X-ray irradiation in particular, is to verify that the oxide degradation due to surface damage does not change over the production for several years. Hence, it is crucial that all structures are irradiated to the same dose and that the measurement and irradiation procedures are reliable. Therefore, the applied dose is set to 40 kGy for the GCD and the MOS for which at least the flat-band voltage is saturated.

The difference of the two MOS structures in fig. 7.14b could be due to a physical difference of the oxide. However, during the investigation of these and also other MOS structures after irradiation some inconsistencies have been observed. If the structures are measured directly after the irradiation procedure, a high flat-band voltage is the result. However, if the structures are measured after a short period of time, even if they are stored in a freezer, the flat-band voltage changes. Similar findings were also found by other teams in the community that deal with X-ray irradiated MOS capacitors at the same time. The matter is further explained with examples in the following.

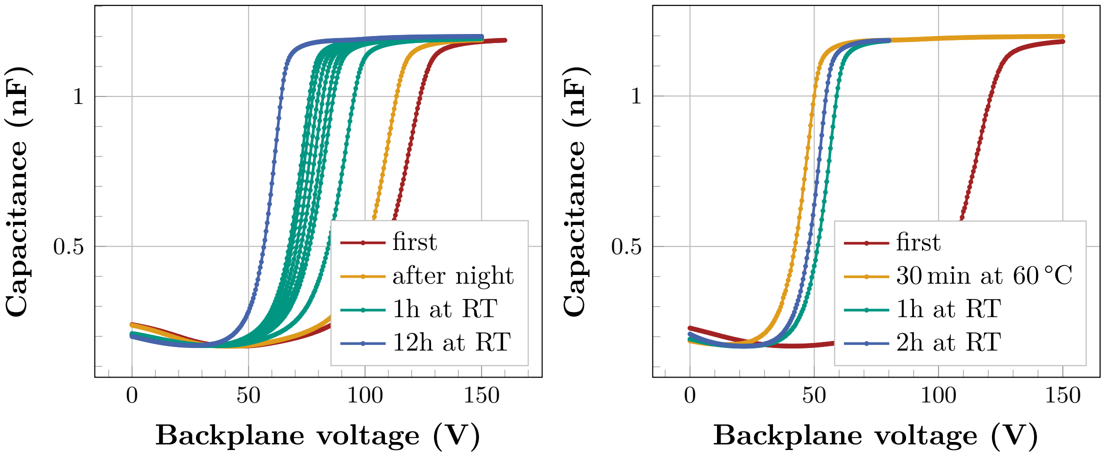

(a) (b)

Figure 7.16.: Change of capacitance measurements dependent on the backplane bias of two irradiated MOS capacitors. One is stored in the freezer over night first and then annealed at room temperature (RT) in (a). The other one received an accelerated annealing followed by relaxation at 20 °C.

In fig. 7.16a, measurements on a structure that has been irradiated well in saturation with X-rays are shown after irradiation. The first measurement is represented as the rightmost red line. The sample has then been stored in a freezer at −32 °C over night and remeasured afterwards. This measurement is represented by the orange line in the plot. Since the sample has been stored in the freezer in which annealing is expected to be effectively frozen out, this first shift is interpreted as a relaxation effect. During the irradiation, charge is generated in the oxide. The mobility of holes is about seven orders of magnitude lower in the silicon oxide than in silicon. Therefore, the discharging process is not as fast as in the substrate. The following green curves from right to left are taken after one hour at room temperature each. The curves are shifted subsequently to lower backplane voltages. It can be seen that the first green curve shows the most significant shift but already after 2 hours, the shift decreases considerably. Letting the structure anneal at 20 °C for 12 h, approximately, still shifts the curve. The interpretation is that somewhere after the night in the freezer and the first measurements a transition from relaxation to pure annealing effects occurs. In order to accelerate the relaxation, a higher temperature treatment can be applied. This is tested on another structure that has been irradiated to saturation with X-rays as well. The first measurement is shown in fig. 7.16b in red. Then, annealing of 30 min at 60 °C has been applied to speed up the relaxation. The following measurement is indeed shifted considerably to smaller backplane voltages. However, now waiting another hour at room temperature results in a shift back towards higher voltages (green). This is not an artefact and has been observed several times on different structures. It might be that due to the high temperature annealing charge carriers are injected in the surface from which they have to recombine again on an unknown time scale. Waiting for another two hours leads to a curve that is in between the one after annealing and the one after the first hour. Subsequent measurements after this procedure yield stable results. The two plots in fig. 7.16 are just examples that summarise the issue. The outcome of these and also other investigations is that a combination of higher temperature annealing, waiting time at room temperature and biasing of the devices is required in order to obtain reliable results.

Therefore, a specific treatment for X-ray irradiated MOS capacitors has been developed that is summarised in table 7.11. First, the devices are irradiated to a dose of 40 kGy independent

Table 7.11.: Specific treatment for X-ray irradiation tests of MOS capacitors.

Task	Details
Irradiation to 40 kGy	homogeneously and at $T = -20\,°\mathrm{C}$
Annealing for 30 min at 60 °C	directly on a hot jig
Relaxation for 2 h	at room temperature in the laboratory
Measurement×2	with the standard measurement procedure
Relaxation for 30 min	at room temperature in the laboratory
Measurement of the final curve	at $T = 20\,°\mathrm{C}$

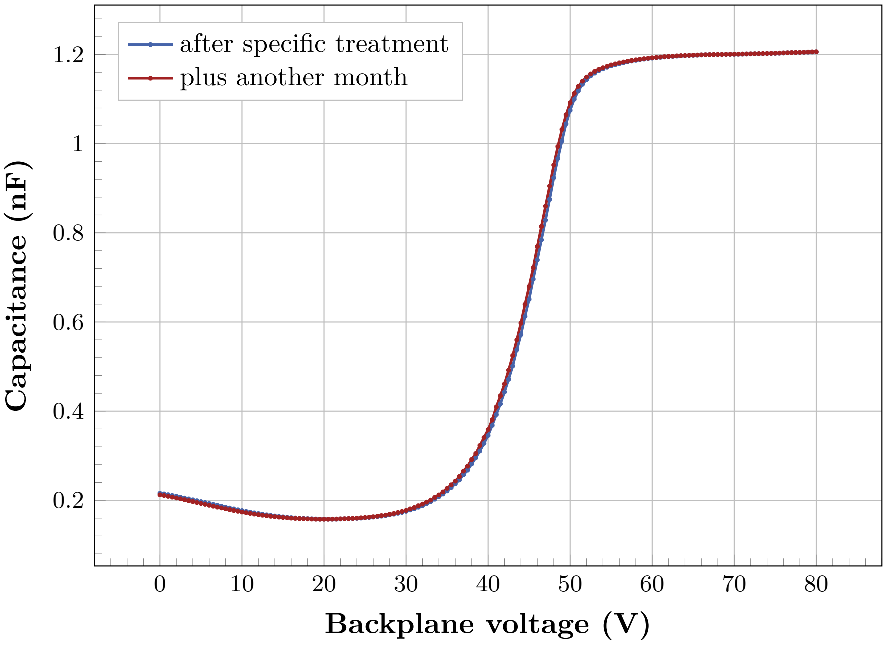

Figure 7.17.: Measurements after the specific treatment and another month later.

of the batch type. Then, the annealing of 30 min at 60 °C is applied, followed by a relaxation time of 2 h at room temperature. Afterwards, the sensor is measured twice, thus biased up to 80 V, to speed up the time that is required to reach the equilibrium at room temperature. This could also be done by specific biasing for a particular time period. However, it is more convenient for the personnel that handles the irradiation tests during the production to just perform measurements with the same settings. After the two measurements, another shorter relaxation time of 30 min follows. Finally, the resulting curve can be measured from which the flat-band voltage can be extracted. The GCDs are measured afterwards since they were not changing that much during all the investigated procedures. Nevertheless, they should be measured after the specific treatment which incorporates annealing procedures to obtain comparable results.

The fig. 7.17 shows that the specific treatment procedure actually results in reliable measurements. One measurement has been performed according to the procedure described in table 7.11. After one month during which the sample has been stored in the freezer, another measurement has been conducted. This outcome is similar to the first measurement so that stable conditions can be assumed. Therefore, the procedure is validated with which the initially severe uncertainties due to relaxation effects can be cancelled out.

Table 7.12.: Settings of the measurements on MOS and GCD structures after irradiation.

MOS		GCD	
Backplane bias	0 V to 80 V (100 V for PS-p)	Gate bias	−70 V to 5 V
Step size	0.5 V	Step size	0.5 V
AC amplitude	250 mV	Backplane bias	−10 V
AC frequency	10 kHz		
Compliance	300 µA	Compliance	300 µA
Temperature	20 °C	Temperature	20 °C

7.3.3. Pre-production Results after Irradiation

The irradiation with X-rays to 40 kGy has been performed for at least two wafers of each batch of the 2S and PS-s pre-production. Additionally, two PS-p batches, thus four wafers, have been irradiated as well. The specific treatment of table 7.11 has been performed on all of these structures. The measurement settings after irradiation are summarised in table 7.12 for MOS and GCD structures. Compared to the situation prior to irradiation, for the capacitance measurement of the MOS structure, the gate voltage is varied from 0 V up to 80 V in order to monitor the considerably increased flat-band condition after irradiation. The step size is enlarged to 0.5 V to reduce the measurement time. In case of the PS-p wafers an even higher bias voltage is required since the flat-band voltage is increased, as will be shown in the following. The gate voltage for the GCD measurement is increased to −70 V compared to the case pre irradiation and the constant backplane bias is increased to −10 V to be comparable to previous studies.

For the analysis of the flat-band voltage of MOS structures the question arises at which value the fit of the section-wise defined function should start. An example measurement with the flat-band voltage extraction method is shown in fig. 7.18a. In first instance, the x value of the starting point of the first fit should be higher than the maximum. However, it is not obvious where the transition from the more quadratic region into the linear region starts. In principle, it would be possible to insert the distance from the maximum x_{dist} as another free parameter in the optimisation procedure. However, the more free parameters the less stable becomes the fitting procedure. Therefore, the x_{dist} value should be fixed beforehand. In order to estimate a reasonable value, the standard deviation of the flat-band voltage is calculated for every measurement. The parameter x_{dist} is varied between 0 and 30, which covers a voltage range of up to 15 V away from the maximum (with a step size of 0.5 V). For every x_{dist} value the whole available pre-production measurements have been analysed and the uncertainty, propagated to the flat-band voltage, has been extracted according to eq. (7.12). The mean of the uncertainties on the flat-band voltage in dependence on x_{dist} is shown in fig. 7.18b. It can be seen that the uncertainties are first high if the maximum $x_{\mathrm{dist}} = 0$ is taken. This makes sense, because the linear region does not start at the maximum of the curve. The uncertainties decrease until a minimum is reached at $x_{\mathrm{dist,\ opt}} = 13$. For even higher x_{dist}, they are increasing again because the starting point cuts into the linear region of the depletion zone. Hence, the number of available data points is smaller, which decreases the reliability of the fit parameters. With this procedure the last free parameter of the analysis procedure is fixed to $x_{\mathrm{dist}} = 13$ for the pre-production and for the following production.

The result of flat-band voltage of all pre-production wafers that were available after irradiation is shown in fig. 7.19. Similar to the situation pre irradiation, the PS-p wafers that stem from the DC processed wafers of the vendor show a higher flat-band voltage. The flat-band voltage of the AC processed wafers from the 2S and PS-s batches is $V_{\mathrm{fb,\ AC}} = (43.37 \pm 0.09)\,\mathrm{V}$ and for

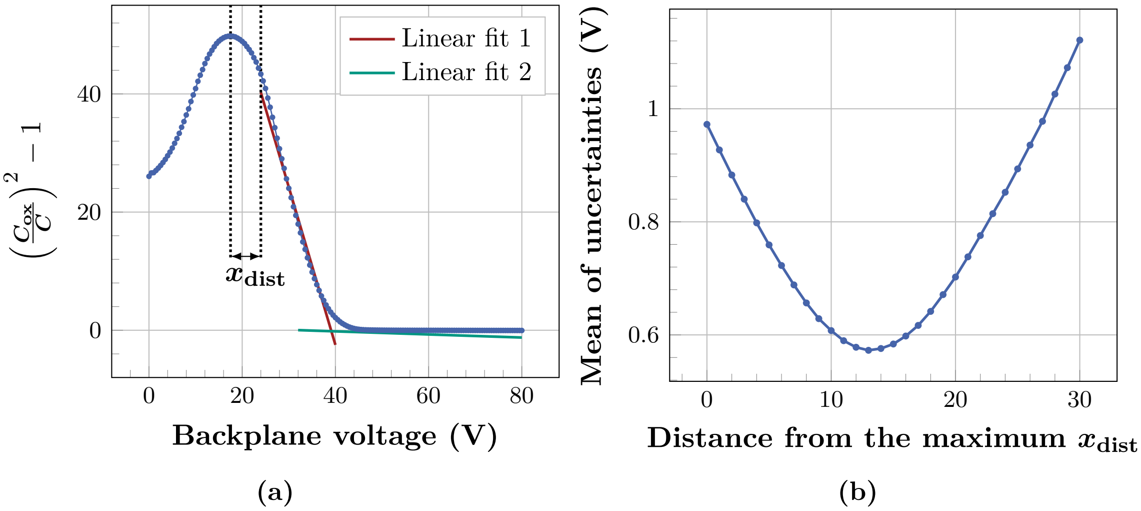

Figure 7.18.: Definition of the starting point for the first linear fit as the distance from the maximum (a). Mean of the uncertainties on the flat-band voltage due to the optimisation procedure of all available pre-production batches dependent on the x_{dist} values. A minimum is obtained at $x_{\mathrm{dist}} = 13$.

the PS-p wafers $V_{\mathrm{fb,\,DC}} = (60.70 \pm 0.39)\,\mathrm{V}$. This means a 1.4 times higher value for the DC processed wafers. For the DC process the uncertainty on the resulting mean is higher, since there were only four wafers available.

The result of the extraction of the surface generation velocity s_0 for all pre-production wafers is shown in fig. 7.20. Different to the case pre irradiation, the PS-p wafers do not show a considerably higher s_0 than the others. Hence, the mean value is calculated for all the investigated wafers, which gives $s_0 = (1147 \pm 15)\,\mathrm{cm\,s^{-1}}$.

In the following a closer look into correlations of the parameters, flat-band voltage and surface generation velocity, is taken. The correlation between the flat-band voltage of the MOS capacitors pre irradiation to the flat-band voltage after irradiation is shown in fig. 7.21. It can be seen that the higher the flat-band voltage pre irradiation the higher it is also after irradiation. However, it also becomes visible that without the PS-p wafers the outcome would not be so clear. This is due to the small variation of the flat-band voltage pre irradiation, which shows once more that the process quality is satisfying. The correlation might become even clearer with more batches during the production and especially with more structures from PS-p wafers.

The relation of the surface generation velocity to the flat-band voltage after irradiation is shown in fig. 7.22a. It can be seen immediately that there is a difference of the PS-p to 2S and PS-s batches in terms of the flat-band voltage. However, this does not seem to be correlated with the surface generation velocity since even wafers with high s_0 values show a lower flat-band voltage and vice versa. The reason why the two parameters are not correlated after irradiation becomes clearer by looking at fig. 7.22b. Here, the correlation of s_0 before to after irradiation is presented. Again, there is no clear connection visible. This has already been hinted at from the summary plot of the s_0 after irradiation in fig. 7.20 where no difference between the 2S and PS-s to the PS-p wafers is observed. Thus, if the flat-band voltage pre and after irradiation correlate, but the surface generation velocity pre and after irradiation do not, it is unlikely that the two parameters after irradiation correlate. Nevertheless, it might be that such a possible correlation will become clearer by increasing the number of data points in the

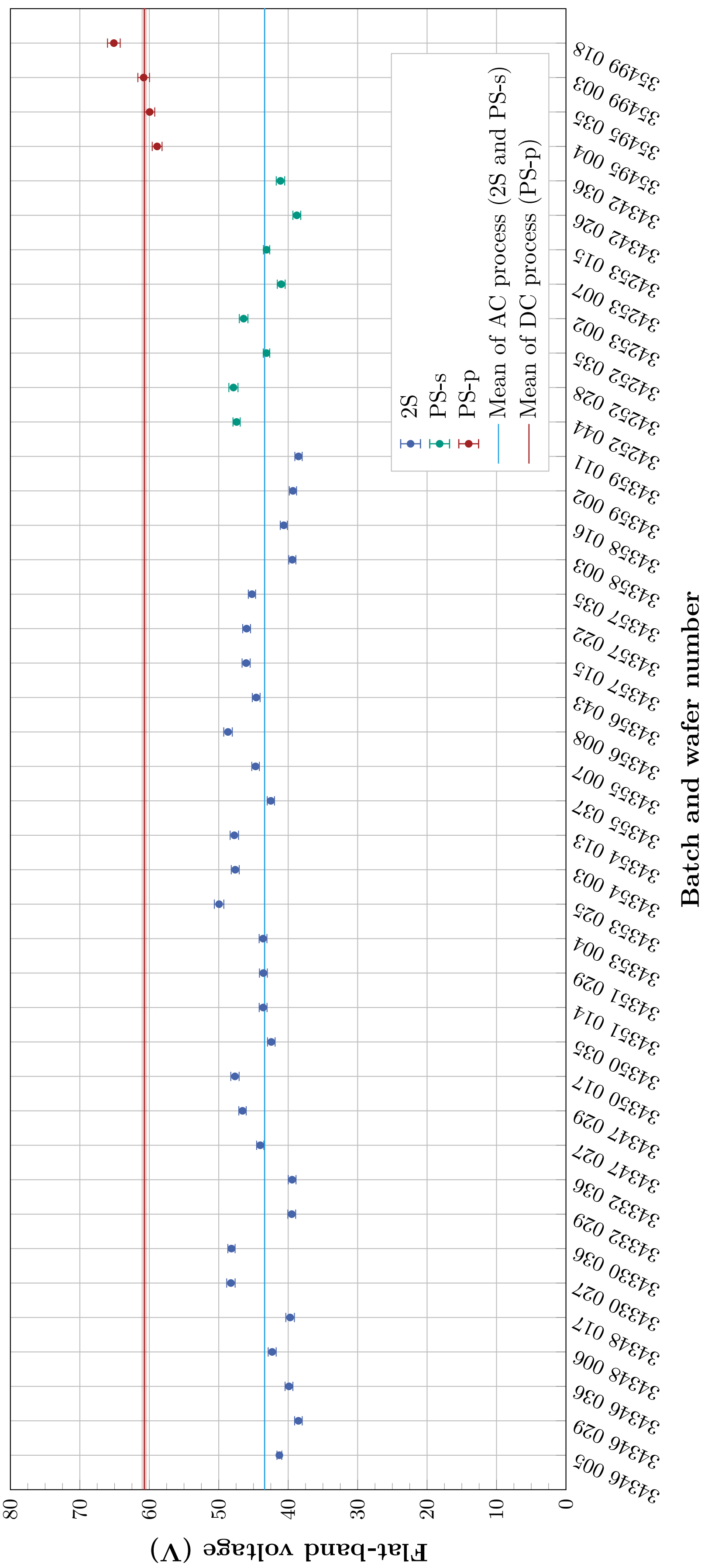

Figure 7.19.: Flat-band voltage after irradiation and specific treatment for all available pre-production batches. The error bars represent the fit uncertainty propagated to the flat-band voltage. The bands around the mean indicate the uncertainty of the mean value.

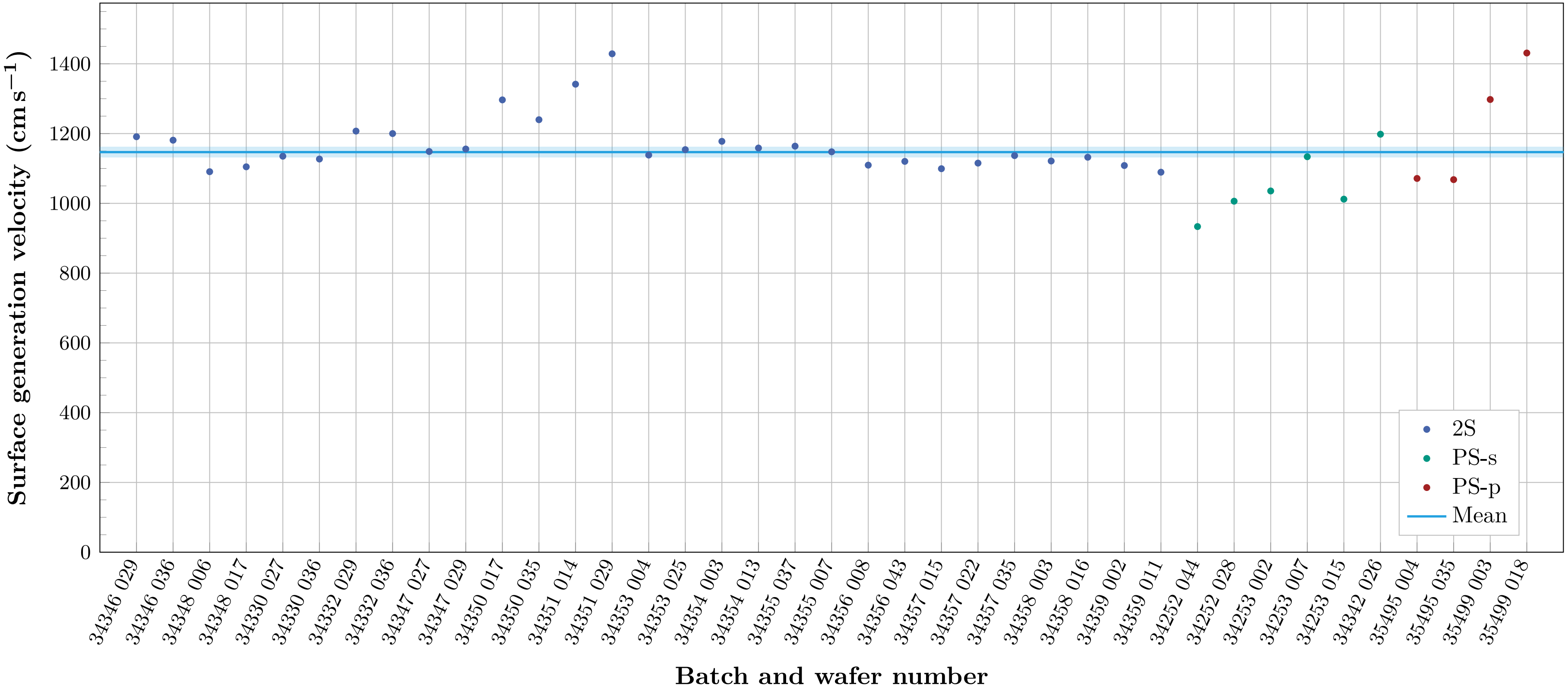

Figure 7.20.: Surface generation velocity after irradiation and specific treatment for all available pre-production batches. The bands around the mean indicate the uncertainty of the mean value.

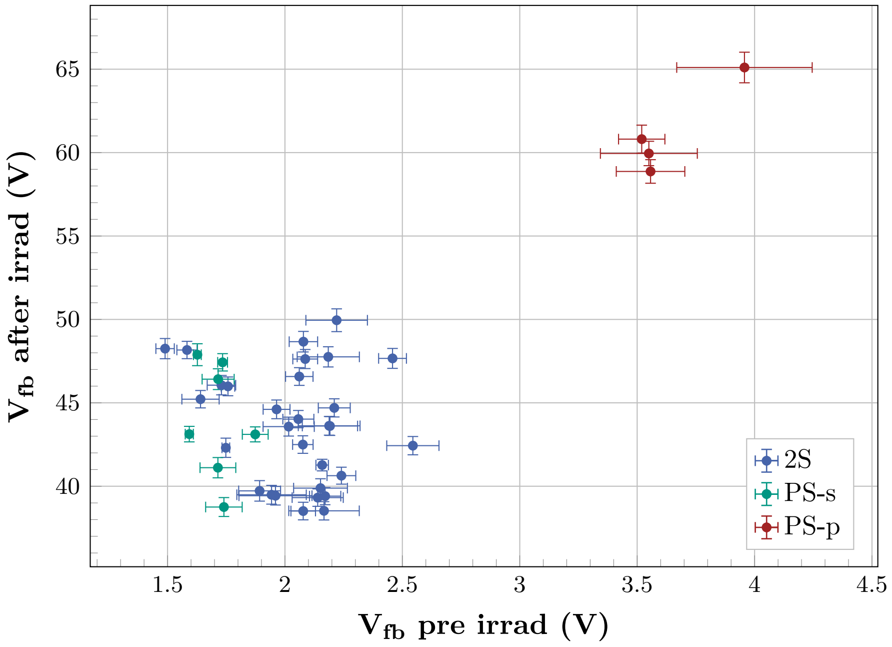

Figure 7.21.: Flat-band voltage dependence after irradiation on the value pre irradiation. Within the bulk of 2S and PS-s structures no clear correlation is visible. By taking the PS-p wafers into account it can be seen that if the flat-band voltage pre irradiation is higher, it is also likely higher after irradiation.

following years during the full mass production. At this point the data is not sufficient to make a clear statement.

These investigations yield a solid baseline for the flat-band voltage and the surface generation velocity with X-ray radiation-induced defects for the following production, on the one hand in terms of expected values and on the other hand in terms of an estimation of fluctuations that can be expected between the different batches. Also robust procedures were developed that will be used in the subsequent full production.

7.4. Escalation Strategy

The procedure of interpreting the parameters after irradiation for the production is discussed in this section. In general, there are no concrete limits for the measurements after irradiation except for the MPV of the seed signal. Therefore, the overall strategy is to obtain similar results over the full mass production. A concerning measurement would be an statistical outlier compared to the findings in the pre-production in this work. Hence, this work sets a baseline that should be matched during the following investigations over the next years. In case outliers will be spotted, a closer look into the details is required. Also, a drift over several batches might be observed over time. Of course not all the possible cases can be foreseen beforehand but two examples that could in principle arise are covered in the following.

The diode measurements and the extracted damage rate give insight in the pure bulk properties after irradiation. It is unlikely that the bulk doping or the base material itself is contaminated such that the damage rate differs severely from the findings here. Even if such a contamination occurs it should be spotted already during the SQC and PQC but can be complemented by the irradiation tests. Therefore, if outliers in the damage rates are found the

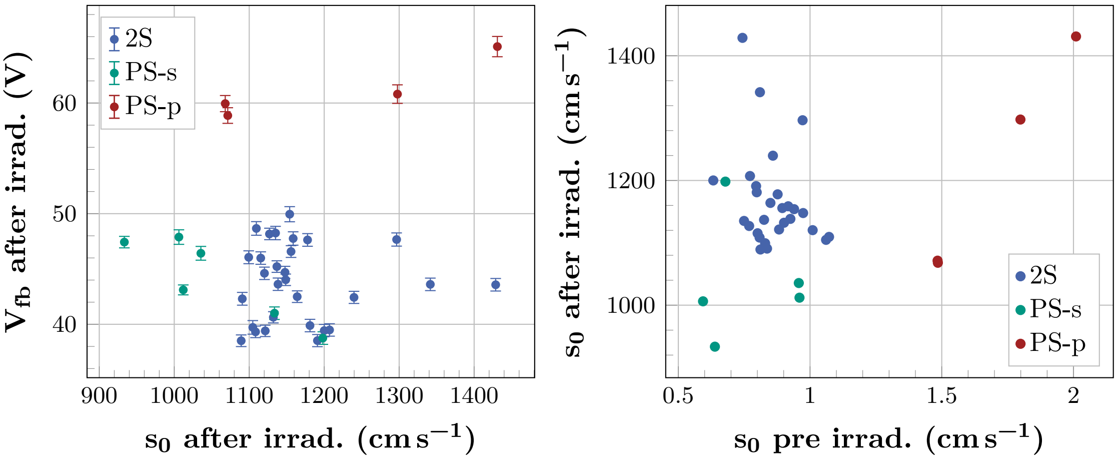

(a) (b)

Figure 7.22.: Correlation of the flat-band voltage after irradiation to the surface generation velocity pre irradiation (a). Surface generation velocity after irradiation in dependence on the value pre irradiation (b).

more likely reason is that the target fluence has not been reached or that the annealing time or temperature differ from the expectation.

In case there are problems with the oxide quality during the production this would be reflected by the PQC measurements. The X-ray irradiation tests would complement the picture and answer the question how severe these deviations are after irradiation. Additionally, the strip scans can show if the coupling capacitance and the interstrip resistance is still sufficient after irradiation to operate the sensor. Ultimately, the sensor always has to deliver the required signal to detect particles after irradiation. Only the full picture of measurements on full-sized sensors, dedicated process quality control structures and the irradiation tests makes it possible to decide which issues are critical and which might be acceptable.

In the end, it is not possible to cover every eventuality beforehand but by conducting all the quality assurance measurements it is possible to obtain a great overview with a lot of information. An Outer Tracker Sensor Expert Production Panel (OTSEPP) has been established that meets weekly. If issues of the quality of the wafers occur, they will be addressed there. The most likely case is that first of all deeper investigations will be discussed. Eventually a decision will be made to accept the quality or to reject the concerning batch. If slight drifts of parameters will be detected during the production of several batches, it might be possible to negotiate with the vendor so that the process can be adjusted.

8

Interstrip Isolation of p-type Strip Sensors

The majority of state of the art planar silicon sensors consist of n-type implants inside a p-type bulk substrate (n-on-p). One crucial benefit of this technology over p-type implants in an n-type bulk (p-on-n) is the improved radiation tolerance. Since the electron mobility in silicon is higher than the hole mobility, the charge collection is less degraded by trapping. Therefore, the signal is higher for p-type bulk material [Ada+17]. Additionally in case of heavily irradiated p-on-n sensors, because of the type inversion of the previous n-type bulk to p-type, the depletion zone grows from the backside. This results in a strong electric field on the backside but smaller field in the strip regions (shown in ref. [Ebe13]) where most of the signal is induced by the dense weighting field (compare section 3.6.2). Free charge carriers inside an undepleted bulk recombine rapidly. Hence, it is of major importance to operate these sensors fully depleted in order to collect enough charge in the electrodes. At fluences expected for the CMS tracker during the HL-LHC phase, it is not possible anymore to operate the sensors fully depleted. Since at fluences around $5 \times 10^{14}\,\mathrm{n_{eq}/cm^2}$ the full depletion voltage can exceed 1000 V already (shown in ref. [Ada+17]), n-on-p sensors are used for upcoming detectors, for example the new CMS tracker.

However a disadvantage of the n-on-p technology is that an additional isolation mechanism is required. In general, there is positive charge inside the oxide surface of the sensors due to impurities in the material but especially after irradiation as explained in section 4.3. This positive oxide charge attracts electrons from the bulk, forming an electron inversion layer just beneath the surface. Hence, the strips or pixels are short-circuited and eventually the spatial resolution is degraded severely. Common precautions are to introduce a small highly p-doped region between the strips or pixels (p-stop) or distributed along the surface (p-spray). These additional implants break the electron layer as illustrated in fig. 8.1, thus preserving the interstrip isolation. Previous studies have shown that p-type implant doping concentrations of $N_{\text{dop, pstop}} < 5 \times 10^{15}\,\mathrm{cm^{-3}}$ are sufficient to keep a reasonable interstrip isolation, before and after irradiation [Pri16; Har17]. However, after heavy irradiation with fluences above $\Phi = 10^{15}\,\mathrm{n_{eq}/cm^2}$ or with a higher p-stop doping concentration, very strong electric fields may occur, as illustrated in fig. 8.2. The figure shows the electric field strength in dependence of the p-stop doping concentration and the fluence. Increasing one of them leads to a higher electric field inside the p-stop. If the electric field strength exceeds the critical value of $3 \times 10^5\,\mathrm{V\,cm^{-1}}$, the sensor suffers from local breakdowns, which influences leakage currents, noise and may also lead to irreversible damage of the sensor.

In previous investigations, an unexpected high interstrip resistance has also been observed with moderate p-type implant concentrations or even without any precautions, after proton irradiation to high fluences [Unn+07]. There are attempts to understand this behaviour and replicate the interstrip isolation in simulations. Usually the radiation damage is divided into two parts, the surface and the bulk damage. However, the observed feature indicates that the interplay of surface and bulk defects has to be taken into account to describe the surface properties properly. It has been shown in [Gos18] as well that substrate defects seem to play a very crucial role regarding the strip isolation. Previous attempts to explain the situation were

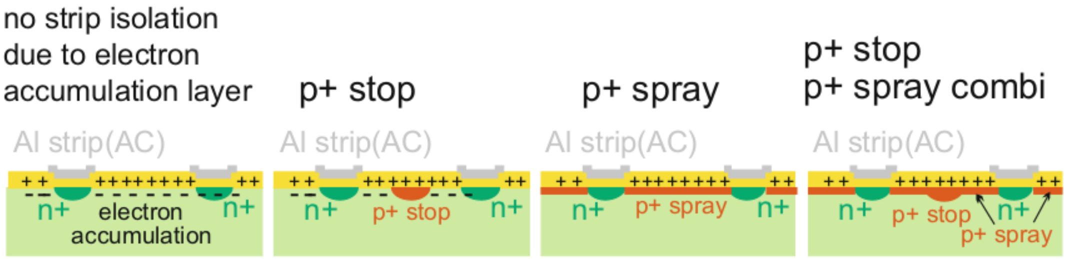
no strip isolation
due to electron
accumulation layer
p+ stop
p+ spray
p+ stop
p+ spray combi
Al strip(AC)
n+
electron
accumulation
p+ stop
p+ spray
p+ spray

Figure 8.1.: Scheme of a strip sensor without any precautions (left), a p-stop implant (second left), p-spray layer (second right) and combination of a p-stop implant and a p-spray layer (right) [Har17].

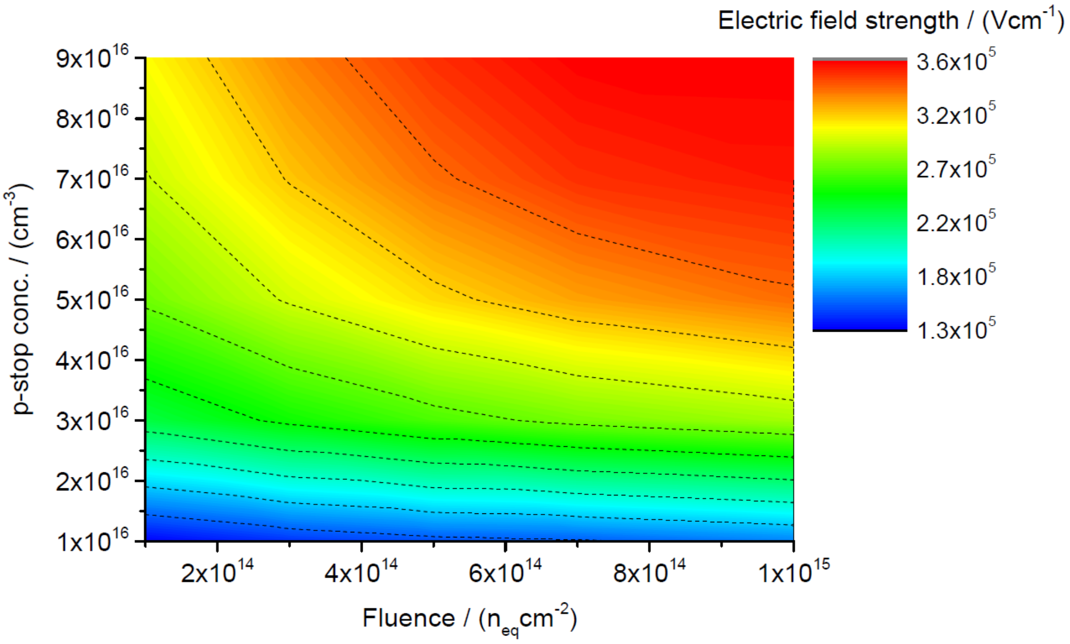

Figure 8.2.: Simulated electric field dependent on the p-stop doping concentration and proton fluence with a constant bias voltage of −600 V and at a temperature of −20 °C [Pri16]

for instance using an effective five-trap model for bulk defects which is tuned to reproduce the interstrip resistance after proton irradiation in [Dal+14] but did not implement pure surface damage properly. There were also ideas of splitting up the defect models between near-surface and pure bulk regions. However, this attempt is unsatisfying because the bulk is physically one unit and in reality not divided into two parts. The aim of this chapter is to develop a comprehensive understanding how the surface properties are influenced by surface and bulk defects. This will be demonstrated by several measurements and comparison to simulation approaches for sensors without any interstrip isolation implant. Finally, a simulation model that describes the strip isolation with the complex interplay of surface and bulk defects properly is derived so that measurements after irradiation can be replicated.

8.1. Measurement Procedure

The measurement procedure is described in the following. First, the reverse bias potential is applied on the sensor's backplane and the strips are grounded over the bias ring with the bias needle. For the interstrip resistance measurement, two adjacent DC pads are contacted with one needle each as illustrated in fig. 8.3a. Then, the bias potential on one needle is ramped up while the resulting current flow into the other strip is measured with the other needle and a picoamperemeter. The interstrip current increases linearly with the applied interstrip potential as shown in fig. 8.3b. Hence, a linear fit can be performed and the interstrip resistance is obtained by the inverse slope of the fitted line.

In general, during the measurement, the electric field of the sensor should be altered as little as possible. Therefore, a small interstrip voltage ramp is preferred. Prior to any irradiation, the interstrip potential's range is 0 to 1 V. However, after irradiation, especially with hadrons, the leakage current increases drastically. The measurement in fig. 8.3b is an example of a sensor without interstrip implant that has been irradiated with protons to a fluence of $\Phi = 6 \times 10^{14}\,\mathrm{n_{eq}/cm^2}$. Therefore, the total strip current is high compared to the current that has been added by the interstrip potential. The strip leakage current due to bulk defects is roughly two orders of magnitude higher than the interstrip current if only one volt interstrip potential is applied. Consequently, by increasing the low voltage ramp to 10 V the interstrip current's fraction of the total strip current can be increased from 0.5% to 5%, approximately. This noticeably improves the stability of the results. Therefore, in the following, if sensors are hadron irradiated, an interstrip potential ramp to 10 V is always used. Additionally, to obtain consistent results, the interstrip resistance measurements are performed on a set of at least five strips per sensor. The final interstrip resistance value that is plotted in the following is the mean of this set with the associated standard deviation. The standard deviation is a measure of the spread and consistency of the measurements on one sensor but should not be understood as an absolute uncertainty on the value.

8.2. Simulated Device

The simulated device should match the real device as close by as possible in order to obtain comparable results. However, it is not possible to simulate a full-sized sensor, since this would lead to unreasonable calculation times of the simulator. It is also not required to emulate the full number of strips, since they are behaving exactly the same. Since the region of interest is the interstrip region, one 2D cross section of the interstrip region with two half-strips is emulated. Using the continuity along the strips, the interstrip resistance can be normalised to the strip length which would be the third dimension in this case. Because the interstrip resistance is inversely proportional to the strip length, it is always multiplied

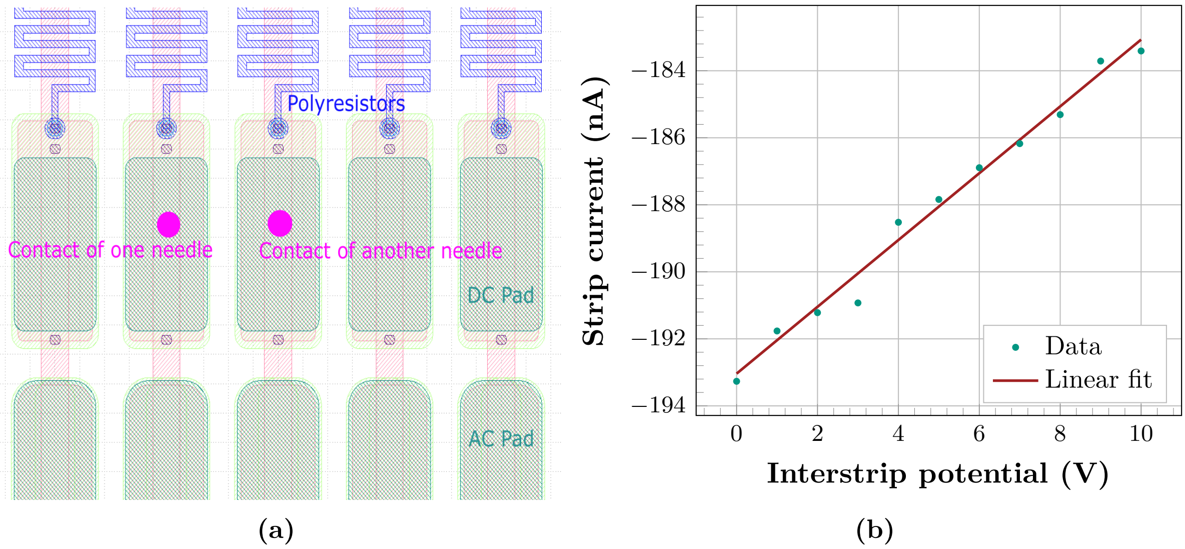

Figure 8.3.: Scheme of the interstrip resistance measurement. Two adjacent DC pads are contacted with two needles (a). A voltage ramp is applied on one needle while the current on the other strip is measured with the other needle. The interstrip resistance is determined by the inverse slope (b) which yields 1 GΩ here.

with the strip length for normalisation in the following. The constructed device with the finite-element simulation framework Synopsys Sentaurus TCAD (described in section 6.4) is shown in fig. 8.4. In the figure, the strip implants that are highly n-doped with a concentration of $N_{\text{dop, strip}} = 1 \times 10^{19}\,\text{cm}^{-3}$ are highlighted in red. The doping decreases with a Gaussian function towards a depth of 2 µm. Above the strips there is a 250 nm thin coupling oxide that couples the strip to the overlaying aluminium strip implant capacitively. On top of the aluminium strips, another aluminium strip deposition is implemented, which represents the metal overhang over the implant. Between the left and right strip with a pitch of 90 µm, there is a thicker silicon dioxide layer protecting the substrate in a real detector. The simulated sensor's bulk is p-doped with a concentration of $N_{\text{dop, bulk}} = 4.5 \times 10^{12}\,\text{cm}^{-3}$ and similarly thick as the sensor on which the comparable measurements are performed. Since the sensors used in this work stem from different prototype batches of CMS Outer Tracker radiation campaigns, the active thickness varies between 200 and 290 µm. On the backside of the sensor, a highly doped p-type implant is implemented above the aluminium metal contact (both not visible in the figure). The coordinate system is placed in the middle of the device in x-direction and in the oxide-bulk interface in y-direction. Positive y-direction means deeper in the bulk and negative y would be inside the oxide or the aluminium strips. The borders are treated with Neumann boundary conditions, which means that not the values are specified but the derivatives of the differential equations are set to a specific value, which is in this case zero. Therefore, there is no charge flow or current at the borders. Hence, no current can leave or enter the device except for the separately defined contacts at the strip and backside implants.

Finite elements that constitute a mesh in which the differential equations for the simulations are calculated have to be defined. This mesh can be seen in fig. 8.5 for the near-surface region of the left half-strip. It is determined by the variation of the doping concentrations. Deep in the bulk region, the mesh is several micrometers wide to keep the simulation time reasonable. Closer to the surface and interface regions, the mesh is considerably more dense to obtain precise results. Especially at the pn-junction's transition and the surface-bulk interface, the

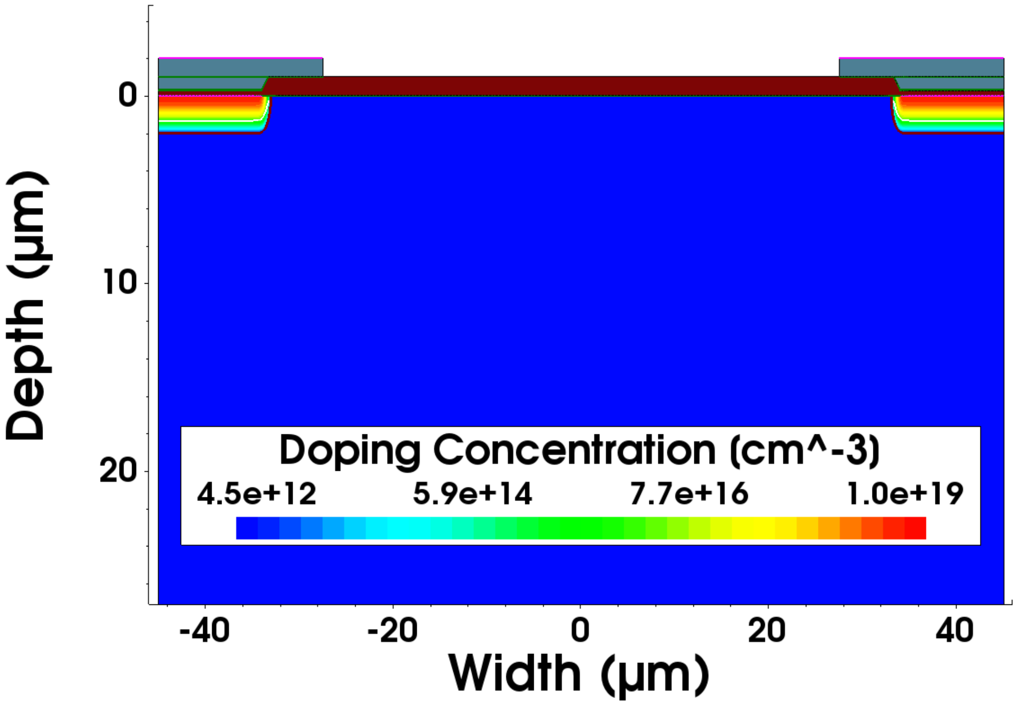

Figure 8.4.: Scheme of the simulated device with the corresponding doping concentrations

mesh's point distance is decreased to a few nanometers, because these are the regions of interest for this study.

8.3. Situation pre Irradiation

8.3.1. Experimental Results

Prior to irradiation, the measurement temperature is controlled to +20 °C. The interstrip resistance measurements on a sensor with and without a p-stop implant are shown in fig. 8.6. The p-stop peak doping concentration is $N_{\text{dop, pstop}} \approx 5 \times 10^{15}\,\text{cm}^{-3}$. In case of the sensor with a p-stop implant the interstrip resistance is high, independent of the applied bias voltage. This is because the fixed repulsive field of the p-stop implantation region repels electrons, thus breaks the electron accumulation at the surface. The interstrip resistance of the sensor without any isolation implant is indicated in red. It can be seen that the interstrip resistance is poor for low bias voltages as expected. The full depletion voltage of these sensors is around 300 V. However, at roughly 100 V already a steep rise in the interstrip resistance over bias potential curve starts. Further increasing the bias voltage leads to a very high interstrip resistance, similar to the case with a p-stop implant. A conservative estimation of a sufficient interstrip resistance value for the operation of a sensor as particle detector is indicated with the horizontal red line in the figure. It holds that the resistance should be two orders of magnitude above the resistance of the bias resistor, which is around $R_{\text{bias}} \approx 2\,\text{M}\Omega$ for sensors in this work. Therefore, the limit translates to $R_{\text{int}} \approx 1 \times 10^{8}\,\Omega\,\text{cm}$ as an approximation. This limit will always be indicated in the following when the interstrip resistance is plotted on the y-axis to guide the eye.

The considerably strong increase of the interstrip resistance at slightly above 100 V was replicated by simulations. In order to do so, a fixed positive charge with a concentration of

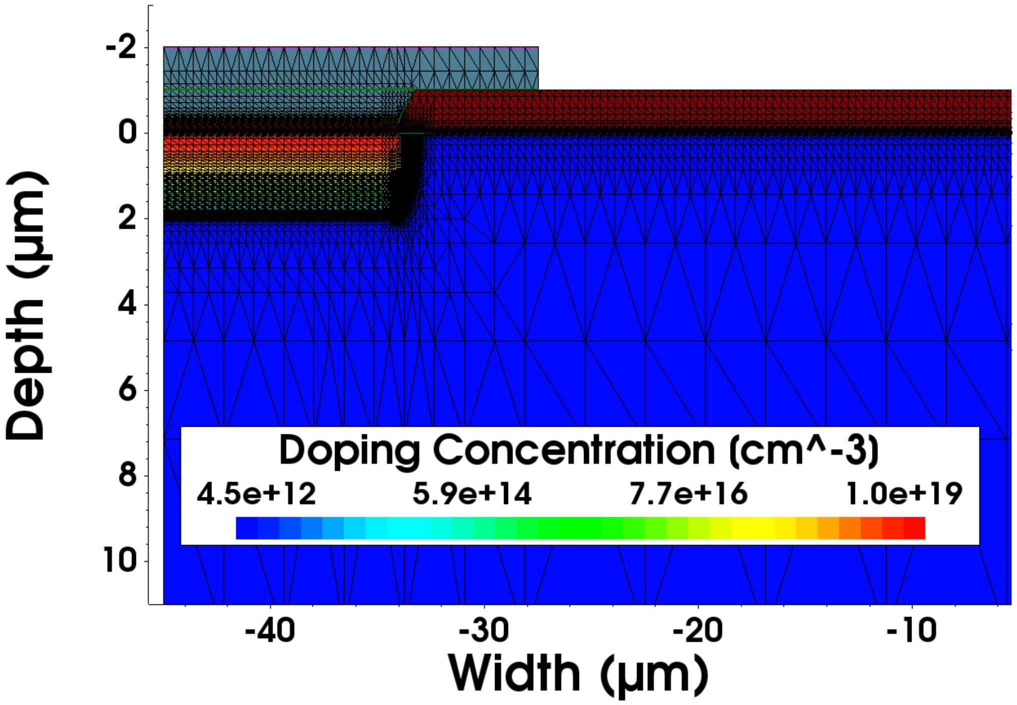

Figure 8.5.: Scheme of the simulated device zoomed into the surface region in order to see the mesh's density.

$N_{\mathrm{ox}} = 8 \times 10^{10}\,\mathrm{cm}^{-2}$ was introduced into the interface region. This reflects the net positive charge in the oxide together with the interface region itself. Here and in the following simulated curves are always represented in figures by lines without dots for data points. The deviation between simulated and measured behaviour at low bias voltages is the result of a protection circuit (with a resistance of $12\,\mathrm{k\Omega}$) protecting the amperemeter. At even lower bias voltages, thus lower interstrip resistance, the interstrip current reaches the maximum current limit. Hence, no values are obtained in this regime.

8.3.2. Destruction of the Electron Layer

Through simulations it is possible to gain deeper understanding of the ongoing effects inside the sensor. The bare interstrip resistance measurements do not indicate what is going on inside the detector but the macroscopic result. For the fixed charge concentration of $N_{\mathrm{ox}} = 8 \times 10^{10}\,\mathrm{cm}^{-2}$ a steep rise of the interstrip resistance occurs slightly above 100 V applied reverse bias. What happens there can be seen in the 2D simulations in fig. 8.7. The figure shows a zoom onto the surface region of the device and in the middle of the two half strips (around $y = 0$). In fig. 8.7a on the upper left, a dense electron layer is established beneath the surface for a bias voltage of 112 V. Applying only two volts more results in a considerably decreased electron layer in fig. 8.7b. Note the same colour code that indicates the electron density which has decreased from around $5 \times 10^{14}\,\mathrm{cm}^{-3}$ several orders of magnitude to $1 \times 10^{10}\,\mathrm{cm}^{-3}$, roughly. If again 2 V more are applied, the electron layer is almost fully destructed as shown in fig. 8.7c. For 118 V reverse bias the electron layer is totally removed and the electron density is nine orders of magnitude below the density at 112 V. Thus no charge can flow between the strips and the interstrip resistance is high.

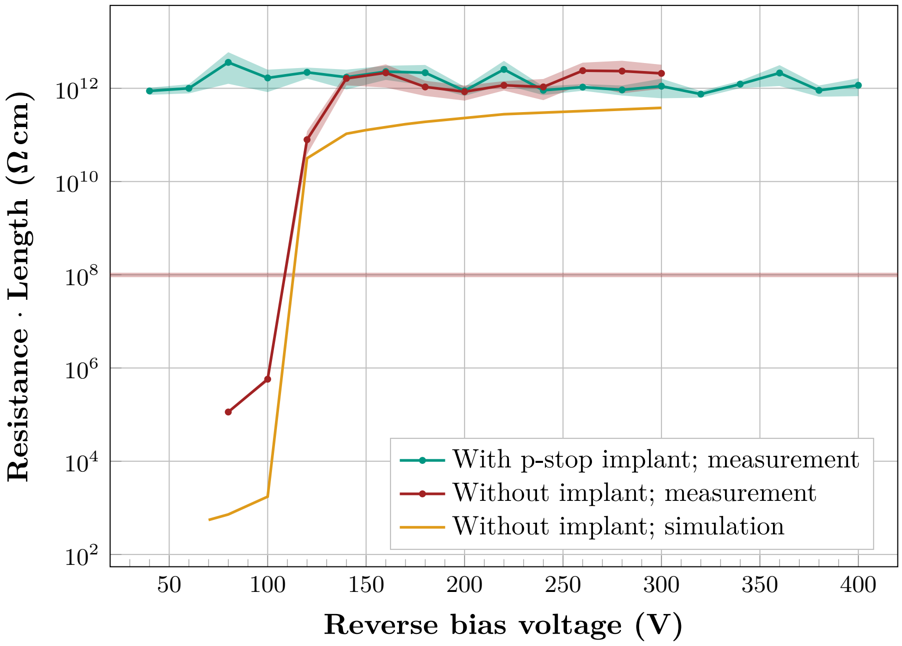

Figure 8.6.: Measured interstrip resistance in dependence of the applied bias voltage before irradiation. A sensor without interstrip isolation implant is indicated in red and another sensor with a p-stop implant in green. The simulated behaviour without isolation implant is represented by the orange line without dots.

8.3.3. Impact of the Doping Concentration

The effects that influence the interstrip isolation become clearer when a closer look at the bulk doping concentration's impact is taken. Sensors in the scope of this work have a bulk doping concentration of around $N_{\mathrm{dop}} \approx 4.5 \times 10^{12}\,\mathrm{cm}^{-3}$. The simulated interstrip resistance in dependence on the reverse bias voltage for different doping concentrations is displayed in fig. 8.8. In addition, a constant fixed positive oxide charge of $N_{\mathrm{ox}} = 3 \times 10^{11}\,\mathrm{cm}^{-2}$ has been used in all cases. This is an arbitrary but realistic value after irradiation. The figure shows that a higher doping concentration leads to a shift of the whole curve towards lower bias voltages Hence, a sufficiently high interstrip resistance is achieved already with a smaller bias potential.

The outcome of an increased strip isolation for higher doping concentrations might be counterintuitive, because it leads to stronger attractions of electrons towards the surface at a similar bias potential. This can be seen in fig. 8.9a. The y-component of the electric field inside the sensor 0.5 µm below the surface is shown in dependence on the x-position. With a constant reverse bias potential of 100 V, the electric field of the higher doping concentration is higher. This means that electrons are accelerated more strongly towards the surface which would support the build-up of an electron layer. The electric field increases for higher doping concentrations because the width of the depletion zone is smaller. Therefore, the reverse potential is attenuated in a smaller region and its gradient is higher. Since the electric field is defined by the potential's gradient, it increases for increasing doping concentrations. Nevertheless, as can be seen by comparison to fig. 8.8 the resulting interstrip resistance is higher in case of a higher field that points away from the surface, thus attracts electrons towards it.

However, so far only the electric field's y-component has been considered. In order to obtain a complete picture the x-component has to be included as well and is presented in fig. 8.9b. The figure shows a zoom on the left strip with the highest peaks at the corner of the strip implants. The second spike is due to the metal overhang of the device. Similar to the y-component, the

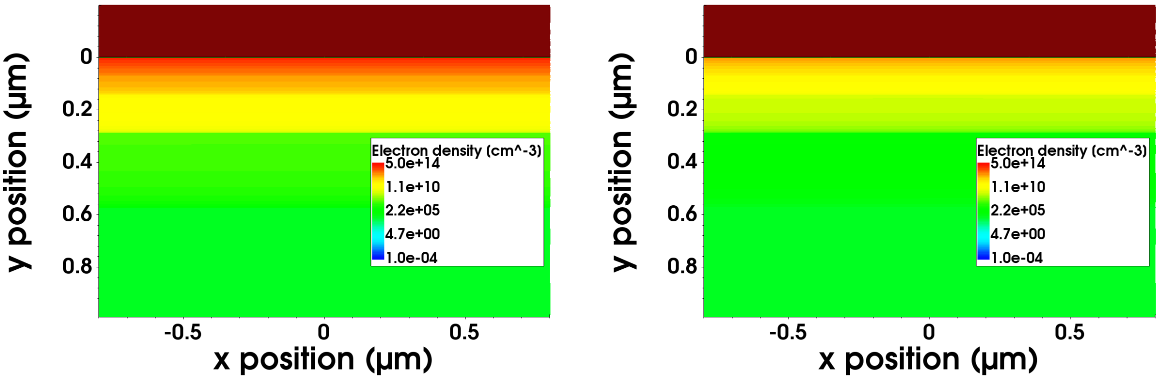

(a) 112 V

(b) 114 V

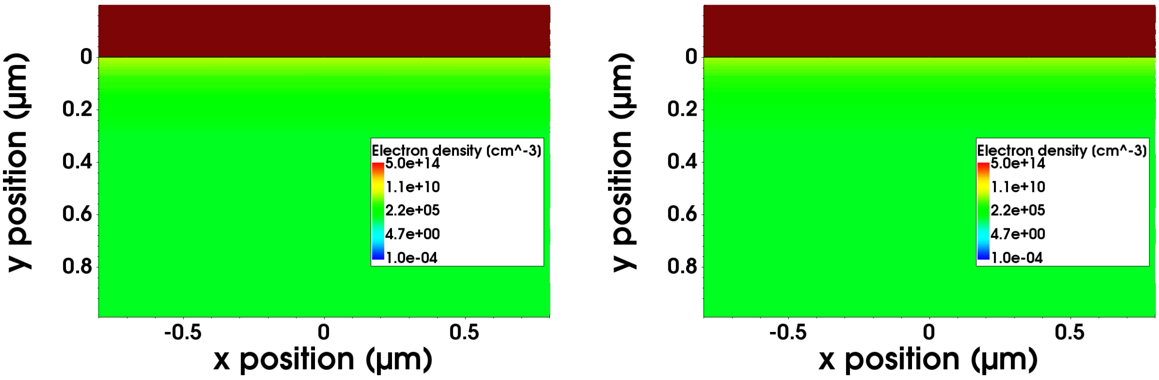

(c) 116 V

(d) 118 V

Figure 8.7.: Simulated electron density close to the surface of the device. The reverse bias voltage ranges from 112 V (upper left) to 118 V (lower right). It can be seen that the electron layer is destructed considerably although the bias voltage differs only by a few volts.

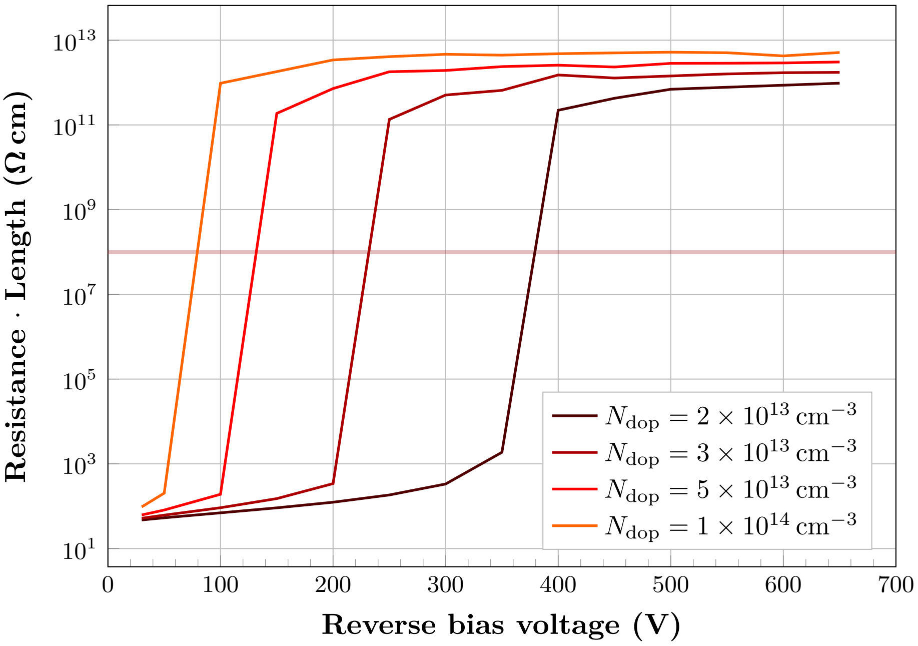

Figure 8.8.: Interstrip resistance in dependence of the reverse bias voltage and different doping concentrations. A positive charge concentration of $N_{\mathrm{ox}} = 3 \times 10^{11}\,\mathrm{cm}^{-2}$ is inserted in the oxide-bulk interface.

x-component is higher in case of the higher doping concentration. Especially in the region between the strips it is greater than zero everywhere. This means that electrons are attracted towards the strip implants, thus the build-up of a homogeneous electron layer at the interface is inhibited. It can be concluded that through an increased doping concentration electrons are stronger attracted to the surface but also towards the strips. Therefore, the strip isolation benefits from a higher doping concentration.

8.4. Pure Surface Damage

The main focus of this study is to understand and quantify the impact of bulk damage on the strip isolation. However, in practice, bulk defects cannot be introduced without introducing surface defects. Therefore, the starting point is to understand pure surface damage first so that the model can later be complemented with bulk defects. Pure surface damage can be applied by X-ray irradiation, since the energy of 60 keV is not sufficiently high to create bulk defects. The incident photons generate electron-hole pairs that react somewhere in the oxide if they do not recombine. A prominent example is the E' centre that is positively charged when occupied and constitutes the main fraction of the fixed positive charge in the oxide (compare section 4.3).

8.4.1. Experimental Results

A sensor without any strip isolation implant was irradiated until saturation of the interstrip resistance measurement occurred around 15 kGy. Then, two further steps to 20 kGy and 25 kGy have been performed to ensure saturation. The saturation dose is also comparable to the findings in chapter 7 on MOS capacitors. The irradiations were always performed below $T < -10\,°\mathrm{C}$ to suppress annealing. Because measurements after hadron irradiation are performed at $T = -20\,°\mathrm{C}$, the measurements after X-ray irradiation are also performed at $T = -20\,°\mathrm{C}$ to stay comparable. The interstrip resistance's dependence on the bias voltage

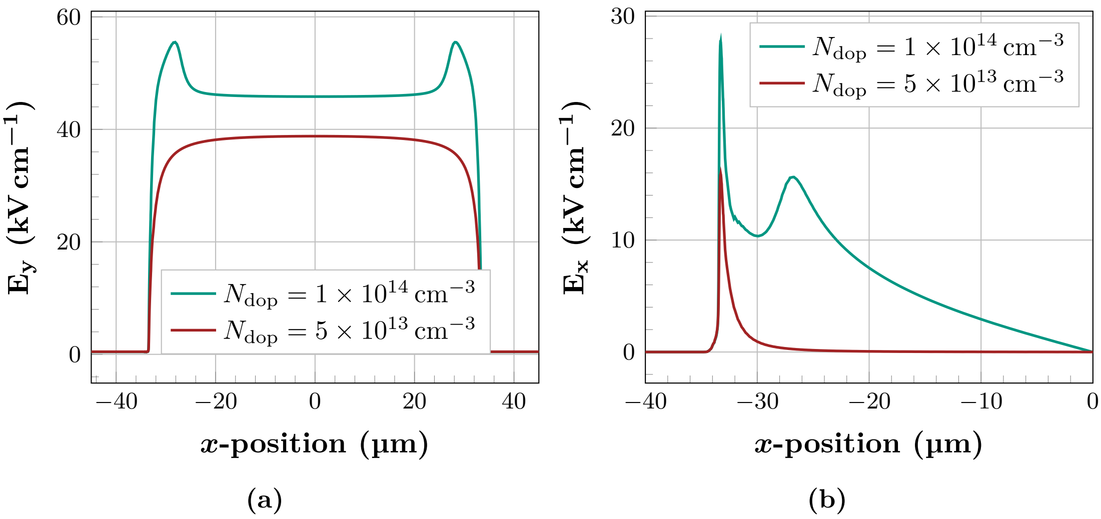

Figure 8.9.: Simulated electric field cut through $y = 0.5\,\mu m$ below the surface of the y (a) and x-component (b) for two different doping concentrations at a bias voltage of 100 V. The green curve refers to a high and the red curve to a low interstrip resistance according to fig. 8.8.

and the applied dose are illustrated in fig. 8.10. At high bias voltages the interstrip resistance is decreasing for increasing dose (increasing to brighter colours). However, it can also be seen that at low bias voltages, the interstrip resistance increases with the applied dose. This is a first hint that an augmentation of the defect model, which currently exclusively features a fixed positive charge, is necessary.

The impact of increasing charge concentration is illustrated in fig. 8.11. If only the fixed charge concentration is increased, the curve is shifted to higher bias voltages because stronger electric fields are required to destruct the electron layer. This finally shows that it is not possible to replicate the measurements from fig. 8.10 solely by inserting a fixed charge in the simulation, because the shape of the curve does not change.

8.4.2. Surface Defect Simulations

The current simulation model with only a certain fixed positive charge in the oxide-bulk interface has to be augmented. To obtain a behaviour as shown in fig. 8.10 defects that help to establish a high strip isolation are required. These could be occupied acceptor states that are negatively charged. On the other hand, donor states might be required to add to the fixed charge in certain circumstances. This dynamic behaviour can be achieved by implementing interface traps into the interface. Additionally, the presence of interface traps in the material is known for a long time already, as described in section 4.3.1. It is also known that the defects are amphoteric. Hence, the motivation for inserting them as acceptors and donors is not just to add whatever is required but their actual physical presence.

Three effective interface states are considered in order to augment the defect model similar to the model described in [Mos+17]. The energy levels are Gaussian distributed around the peak value and all capture cross sections are set to $1 \times 10^{-15}\,cm^2$, following [Mos+17]. A summary of the most important trap parameters is given in table 8.1. Both trap types (donor and acceptor) are introduced with an interface trap concentration N_{it} (cm^{-2}) each. However, since there are two acceptor trap types, the acceptor concentration is shared between them. The acceptor states at the higher energy of 0.6 eV are inserted with 60% and at 0.4 eV with

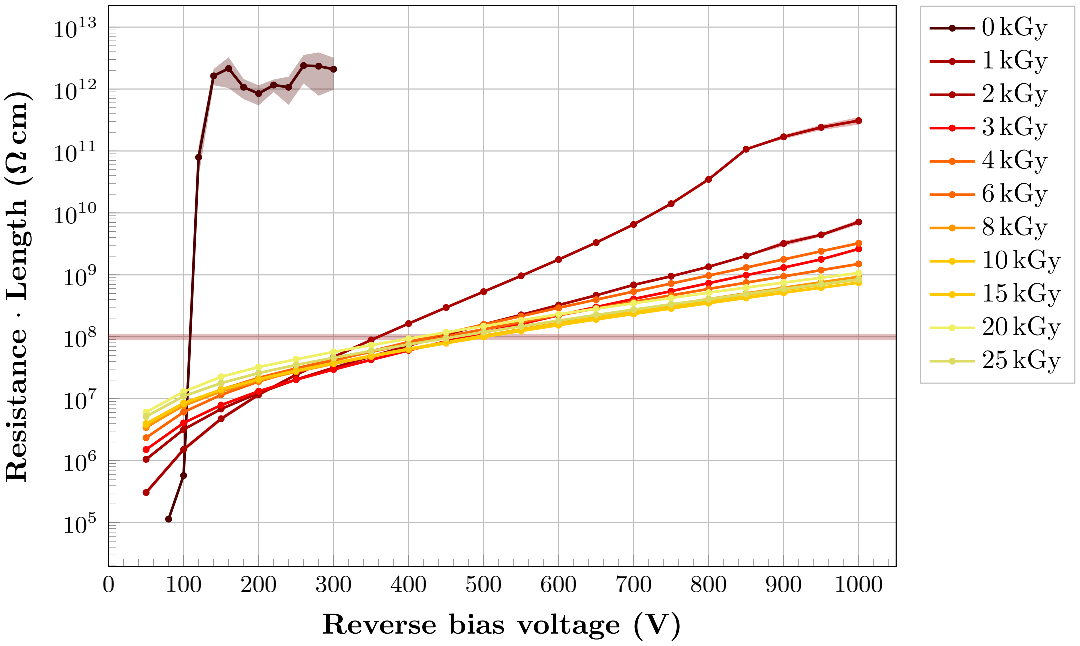

Figure 8.10.: Interstrip resistance in dependence of the reverse bias voltage and X-ray dose. At high bias voltages the interstrip resistance decreases as expected. However, at low bias voltages it increases with the applied dose.

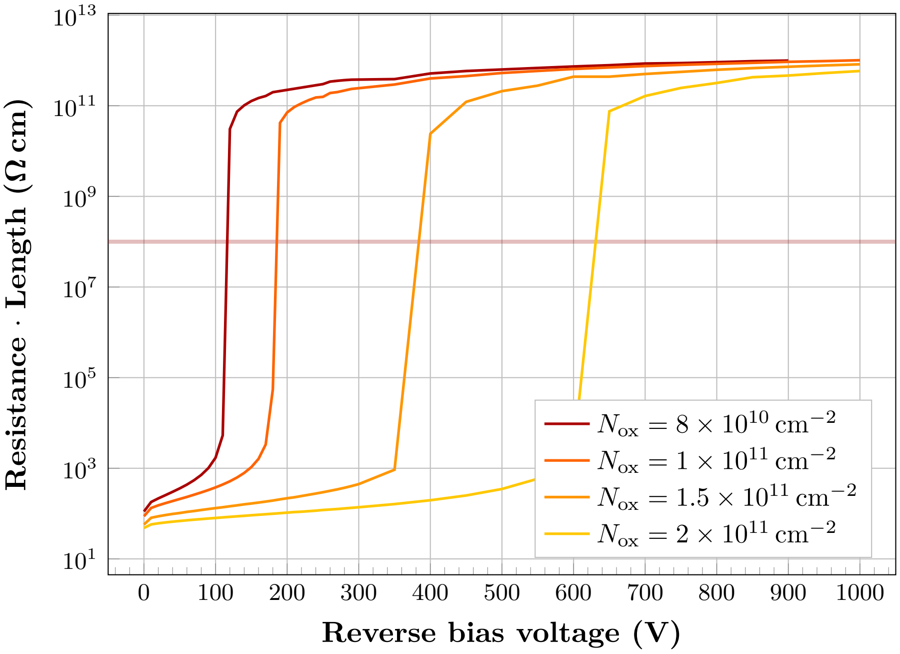

Figure 8.11.: Impact of inserting a positive fixed charge in the oxide-bulk interface on the interstrip resistance over bias voltage characteristics derived from simulations. The whole curve is shifted to higher bias voltages when the charge is increased.

Table 8.1.: Interface traps according to the surface defect model in [Mos+17].

Trap type	Peak energy (eV)	σ (eV)	Capture cross section (cm^2)	Fraction of $\mathrm{N_{it}}$
Donor	$E_\mathrm{v} + 0.70$	0.07	1×10^{-15}	100%
Acceptor	$E_\mathrm{c} - 0.40$	0.07	1×10^{-15}	40%
Acceptor	$E_\mathrm{c} - 0.60$	0.07	1×10^{-15}	60%

40% of N_it following [Mos+17]. Different to the procedure in [Mos+17] and other works that use the defect model, no dose independent ratio between the fixed charge concentration (N_ox) and the interface trap concentration (N_it) is assumed. Instead, they are treated separately.

How the distribution of traps in the band gap is done in the simulation tool for different distribution types is explained in section 6.4. Often, the interface trap density is given as a state density D_it ($\mathrm{cm}^{-2}\,\mathrm{eV}^{-1}$). Following Sentaurus's syntax [Syn18] the interface trap number $N(E)$ per energy level E of Gaussian distributed traps is given by

$$N(E) = N_0 \cdot \exp\left(-\frac{(E - E_0)^2}{2E_S^2}\right) \tag{8.1}$$

where N_0 is the interface state density D_it, E_0 the peak energy and E_S the Gaussian width. Integration over all energies up to the band gap E_g yields the total interface trap concentration N_it

$$N_\mathrm{it} = D_\mathrm{it} \cdot \int_0^{E_\mathrm{g}} \exp\left(-\frac{(E - E_0)^2}{2E_S^2}\right) dE. \tag{8.2}$$

The definite Gaussian integral

$$\int_{-\infty}^{\infty} \exp(-a(x+b)^2)dx = \sqrt{\frac{\pi}{a}} \tag{8.3}$$

can be used as a valid approximation, because the traps are sharply located within the band gap. Therefore, with $E_S = 0.07\,\mathrm{eV}$ and eq. (8.3), eq. (8.2) yields

$$N_\mathrm{it} = 0.175\,\mathrm{eV} \cdot D_\mathrm{it}. \tag{8.4}$$

In the following, N_it is always declared because its meaning is more intuitive but it can be translated to D_it at any time by dividing by $0.175\,\mathrm{eV}$.

8.4.3. Impact of Interface Traps on the Interstrip Resistance

Before the replication of measurements is discussed, it is investigated whether and how interface traps affect the strip isolation. In order to do so, four different configurations have been simulated. The same arbitrary but, after irradiation, realistic value for the fixed charge of $N_\mathrm{ox} = 3.15 \times 10^{11}\,\mathrm{cm}^{-2}$ is used in all cases. Then, pure interface donors, pure interface acceptors and both together have been inserted according to an again arbitrary but realistic value of $N_\mathrm{it} = 4 \times 10^{11}\,\mathrm{cm}^{-2}$. The outcome is illustrated in fig. 8.12. If donor interface states are introduced together with the positive fixed charge, no helpful effect can be observed. The interstrip resistance scales similarly to the case with pure fixed charge that is indicated exceptionally with data points and dashed lines although it is a simulated curve. It makes sense that the donors do not lead to an improvement of the strip isolation, because they are either uncharged or positively charged if unoccupied or occupied, respectively. Hence, the two

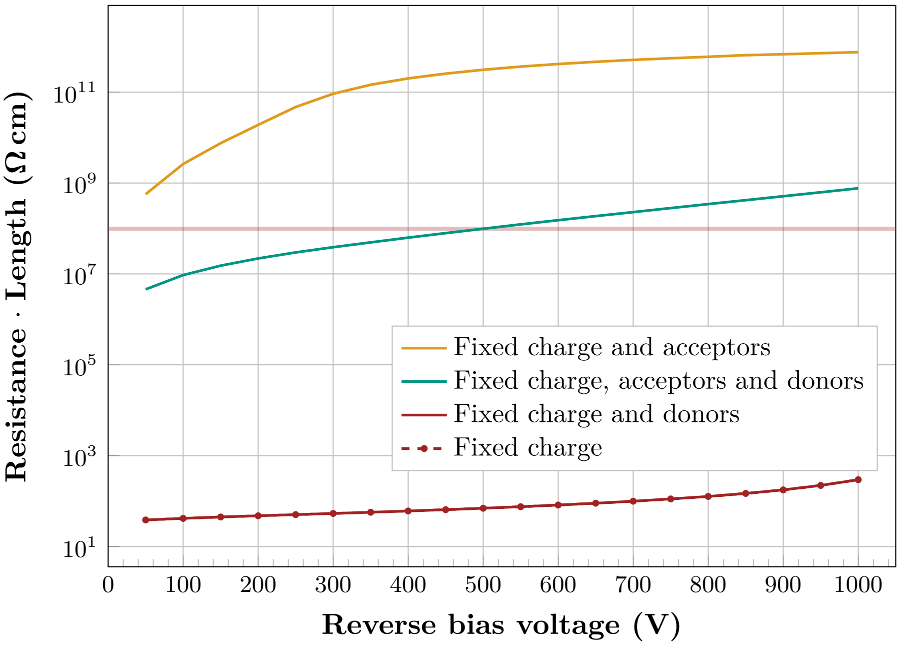

Figure 8.12.: Simulated impact of donor and acceptor interface states on the interstrip resistance. The acceptor states help to establish a sufficient strip isolation.

curves are actually indistinguishable in the figure. However, if only acceptors are introduced without donors the interstrip resistance is very high for all bias voltages. With the full defect model of fixed charge, donor and acceptor states, the interstrip resistance is around the limit, thus at reasonable values.

8.4.4. Replication of Measurements

How the defect concentrations scale with the applied X-ray radiation dose is unknown a priori. The "Optimizer" tool of the Sentaurus TCAD software has been utilised to adjust both defect concentrations (N_{ox} and N_{it}) so that the measurements are replicated as close by as possible. Since the interstrip resistance values are spread over a wide range of several orders of magnitude, the data points are weighted. The weights are estimated by simply dividing the highest value of a curve by the respective measured point. If for example one data point is around $1 \times 10^{6}\,\Omega\,\text{cm}$ but the highest point of the curve at $1 \times 10^{8}\,\Omega\,\text{cm}$, the weight of the point at $1 \times 10^{6}\,\Omega\,\text{cm}$ is 100. Without this weighting procedure low values would be effectively neglected, because the tool takes the absolute deviation from the target value which is significantly smaller if the data point itself is orders of magnitude lower. An example of the input for the optimisation of the defect concentrations for the measurement after 8 kGy is given in appendix D.2. The measurement at 8 kGy and the respective simulations are shown in fig. 8.13. The simulated curve (orange) matches the measured curve (blue) very accurately. This shows that the defect model is able to replicate the measurements. Dashed lines in the figure indicate the impact of defect concentrations deviating from the optimum. If the interface trap concentration increases (green), the whole interstrip resistance curves is increased. On the other hand, if the interface trap concentration is decreased (purple), the resulting curve falls below the measured curve. A similar effect can be observed if the fixed charge concentration is higher than the optimal concentration. However, an increase of the fixed charge still leads to a shift of the complete curve as shown in fig. 8.11. Variations of the interface trap density changes the slope of the

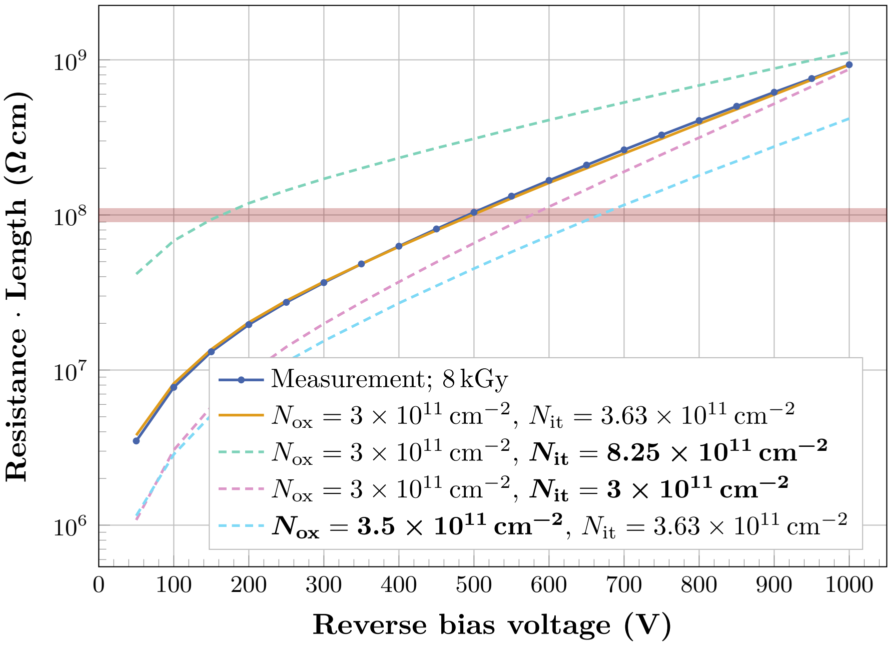

Figure 8.13.: Example of a comparison of the interstrip resistance dependent on the applied bias voltage between measurements (orange) and simulation (blue). The impact of deviating defect concentrations (marked with bold font) are indicated with dashed lines.

curves. Hence, it can be assumed that the optimum is stable because the fixed charge and the interface traps are not interchangeable.

The optimal defect concentrations are determined for every measured curve shown in fig. 8.10. The results are displayed in fig. 8.14. It can be seen that both, the interface trap concentration N_{it} and the fixed oxide charge concentration N_{ox}, are in a similar range and also scale similarly with the applied dose. At roughly 10 kGy both start to saturate at slightly different values. Since no unphysical outliers occur, it can be concluded again that the results obtained with this procedure are stable and reasonable. In this section, an effective defect model has been found that describes the strip isolation properly when pure surface damage is applied dependent on the dose in the silicon dioxide. The next step is therefore to augment the model with bulk defects that are generated by hadron irradiation.

8.5. Hadron Irradiation

A set of sensors without strip isolation features was irradiated to fluences ranging from $3 \times 10^{14}\,\mathrm{n_{eq}/cm^2}$ to $6 \times 10^{14}\,\mathrm{n_{eq}/cm^2}$ with protons and $1 \times 10^{10}\,\mathrm{n_{eq}/cm^2}$ to $6 \times 10^{14}\,\mathrm{n_{eq}/cm^2}$ with neutrons. Another sensor with a p-stop implant has been irradiated with protons to a fluence of $6 \times 10^{14}\,\mathrm{n_{eq}/cm^2}$ for comparison. Both, protons and neutrons introduce similar bulk damage according to the NIEL hypothesis (compare section 4.1.1) in the sensors. Additionally, for protons a high dose is deposited in the sensors' surface because of their charge. The irradiation facilities and the dose estimations are described in chapter 6. The estimated dose is 145 kGy per $1 \times 10^{14}\,\mathrm{n_{eq}/cm^2}$ for proton irradiation. Neutrons cannot ionise the silicon oxide, since they are uncharged. However, due to photon contamination inside the spallation reactor, the estimated dose is still 1 kGy per $1 \times 10^{14}\,\mathrm{n_{eq}/cm^2}$. As the bulk damage from proton and

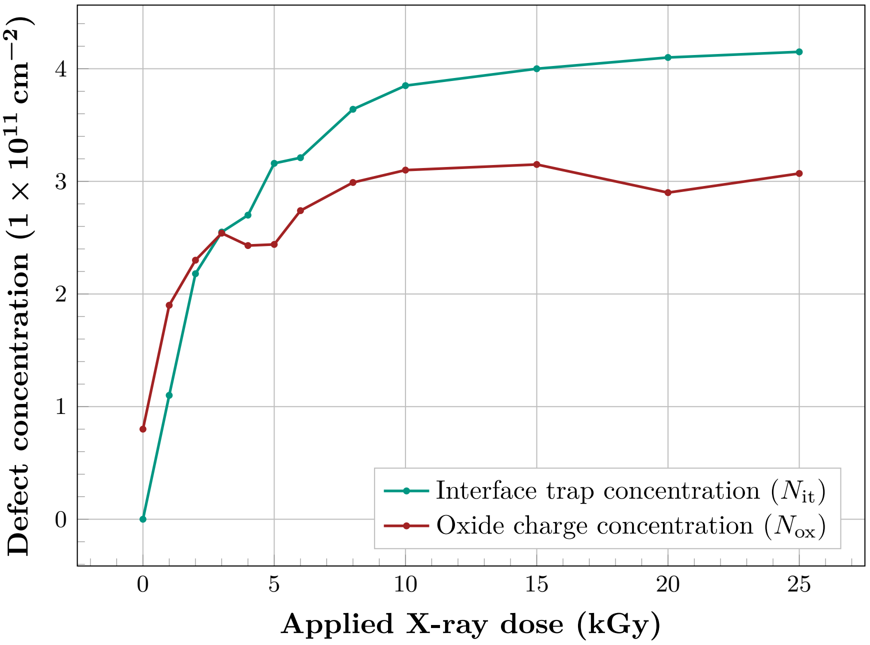

Figure 8.14.: Result of the optimised fixed charge and interface trap concentrations dependent on the applied dose. Both increase rapidly at the beginning but start to saturate around 10 kGy to 15 kGy.

neutron irradiation scales similarly with the fluence, but the surface damage is much lower for neutron irradiation, the impact of bulk and surface damage can be disentangled.

8.5.1. Experimental Results

A comparison of the interstrip resistance of sensors that have been irradiated to different fluences is shown in fig. 8.15. The significance of the bulk defects is visible from several viewpoints. First, by comparing the sensors which were irradiated with hadrons to the sensor which was solely irradiated with only 3 kGy X-rays (orange), it can be seen that the interstrip resistance is considerably higher for sensors with bulk defects. This is true even for the sensors that were irradiated with a proton fluence of $\Phi = 6 \times 10^{14}\,\mathrm{n_{eq}/cm^2}$, which refers to an applied dose in the SiO_2 of 870 kGy. If the neutron irradiated sensors (two blue lines) are compared to each other, it can be seen that more bulk defects also lead to a better strip isolation. Both represent a sensor without any interstrip implant and the darker line represents the higher fluence. Although the surface dose is doubled, the interstrip resistance is higher over the full bias voltage range. Finally, by comparing the two red lines to each other, it gets visible that also the p-stop becomes irrelevant to the strip isolation with these high defect concentrations. Both sensors were irradiated to the same fluence of $\Phi = 6 \times 10^{14}\,\mathrm{n_{eq}/cm^2}$ with protons and the dashed line refers to a sensor with a p-stop. Hence, the conclusion is that bulk defects are of major importance and cannot be neglected for the strip isolation.

The interesting and technologically important question arises at which fluence the bulk defects become relevant regarding the strip isolation. This question can be answered with fig. 8.16. A set of sensors without isolation implants has been irradiated with neutrons to fluences ranging from $1 \times 10^{10}\,\mathrm{n_{eq}/cm^2}$ to $1 \times 10^{14}\,\mathrm{n_{eq}/cm^2}$. A clear benefit of the interstrip resistance curves to the measurements with pure X-ray irradiation has only been observed at $1 \times 10^{14}\,\mathrm{n_{eq}/cm^2}$. As can be seen in the figure, the interstrip resistance is higher for neutron irradiation (blue) than for pure X-ray irradiation (orange) with the same equivalent dose of 1 kGy. However, with

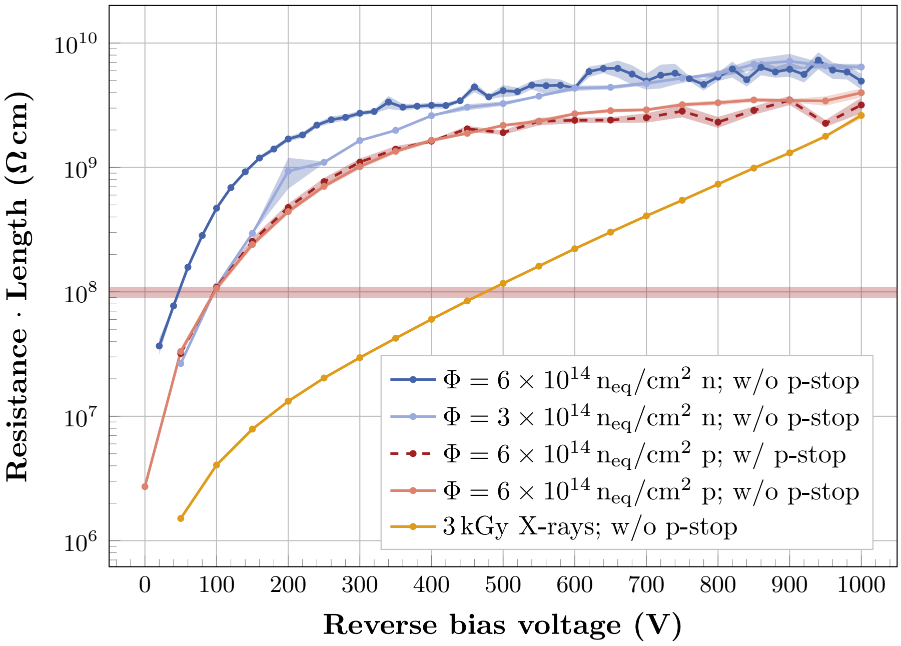

Figure 8.15.: Interstrip resistance dependent on the fluence and particle type. The beneficial effect of the bulk defects on the interstrip resistance is reflected by the fact that all hadron irradiated sensors show a higher interstrip resistance than the sensors irradiation with X-rays to a low dose of 3 kGy.

a bias voltage of over 700 V the X-ray irradiated sensor shows a higher interstrip resistance again. Why this is the case is explained in the next section. It can be concluded that, at least for fluences above $1 \times 10^{14}\,\mathrm{n_{eq}/cm^2}$, the bulk defects affect the interstrip isolation noticeably and should be considered in addition to pure surface damage.

8.5.2. Simulation of Bulk Defects

Bulk damage is responsible for manifold effects of typical bulk properties like leakage current, full depletion voltage and charge collection efficiency as explained in section 4.2. Defects in the middle of the band gap mainly generate leakage current since they can act like stepping stones for electrons in the valence band or holes in the conduction band. The increase of full depletion voltage is caused by an increase of the effective doping concentration after irradiation. Defects contribute to the effective doping concentration if they are acceptors or donors which are occupied by an electron or hole, respectively. The occupation probability of such a state increases towards the band edges. On the other hand, these traps degrade the collected charge if they are unoccupied at the operation temperature. This is more likely the case for acceptor states close to the conduction band and donor states close to the valence band. A charge carrier of the generated signal can get captured by the trap state. After a short period of time ($\mathcal{O}(\mu s)$), it is released again but this happens typically after the main pulse of the signal formation is over ($\mathcal{O}(ns)$). Afterwards, the defect can trap an electron or hole again.

There are different approaches to describe all these effects with an effective bulk defect model. In general, as less as possible defects are preferred in order to keep the model simple and understandable. On the other hand, it might intuitively be easier to implement one defect for each macroscopic effect. At least one donor and one acceptor state is required in order to be able to describe the electric field distribution in the sensor properly. In irradiation studies a

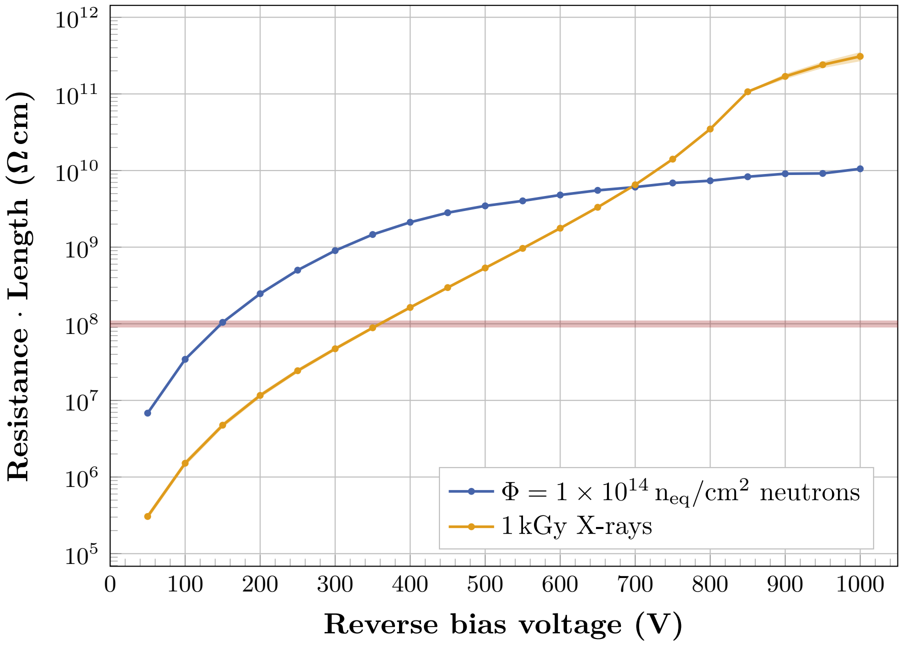

Figure 8.16.: Comparison of the interstrip resistance after irradiation with neutrons to a fluence of $1 \times 10^{14}\,\mathrm{n_{eq}/cm^2}$ and 1 kGy X-ray irradiation. The resistance of the neutron irradiated sensor is considerably higher for bias voltages below 700 V.

so-called double junction of the electric field has been observed by TCT[1] measurements which cannot be described by only one defect [Ebe13]. The model of choice for this work has been developed during an intense irradiation campaign of the CMS community on a similar base material [Ebe13]. In the reference, the defect concentrations and the capture cross sections have been determined so that a valid description of leakage currents, depletion voltages, electric field distributions and charge collection was possible. The defects are located close enough to the middle of the band gap so that leakage current is effectively generated. On the other hand, they are situated close enough to the band edges, so that a fraction is ionised which affects the effective doping concentration. A summary of the defect parameters for proton irradiation is shown in table 8.2. The model is valid for fluences above $1 \times 10^{14}\,\mathrm{n_{eq}/cm^2}$ and has been tested to fluences of $1 \times 10^{15}\,\mathrm{n_{eq}/cm^2}$. The respective parameters for neutron irradiation are indicated in table 8.3. The main difference between the proton and neutron defect model is the scaling of defect concentrations with the fluence. Additionally, the capture cross sections are 20% higher in case of neutron-induced defects. It can be seen from table 8.2 and table 8.3 that for proton irradiation the donor concentration is higher than the acceptor concentration above $1.042 \times 10^{14}\,\mathrm{n_{eq}/cm^2}$ (essentially everywhere in the valid range). For neutron irradiation, the acceptor concentration is higher than the donor concentration for all fluences.

8.5.3. Impact of Bulk Defects on the Interstrip Resistance

Before comparisons of simulations to measurements are shown, it is illustrated that the defect model is able to emulate a beneficial effect on the strip isolation. It makes sense to try to understand the most important effects qualitatively first. The idea before the investigations of this work started, for example in [Dal+14; Pri16], was that the bulk defects lead to a negative

---

[1] TCT: **T**ransient **C**urrent **T**echnique

Table 8.2.: Bulk defect model for proton irradiation, validated at $T = -20\,^{\circ}\mathrm{C}$ and fluences ranging from $\Phi = 1 \times 10^{14}\,\mathrm{n_{eq}/cm^2}$ to $\Phi = 1 \times 10^{15}\,\mathrm{n_{eq}/cm^2}$ [Ebe13]. The energy level of the valence is denoted by E_v and of the conduction band by E_c.

Trap type	Energy level (eV)	Defect concentration ($\mathrm{cm^{-3}}$)	Capture cross section ($\mathrm{cm^2}$)
Donor	$E_\mathrm{v} + 0.48$	$\Phi \cdot 5.598 - 3.949 \times 10^{14}$	1×10^{-14}
Acceptor	$E_\mathrm{c} - 0.525$	$\Phi \cdot 1.189 + 6.454 \times 10^{13}$	1×10^{-14}

Table 8.3.: Bulk defect model for neutron irradiation, validated at $T = -20\,^{\circ}\mathrm{C}$ and fluences ranging from $\Phi = 1 \times 10^{14}\,\mathrm{n_{eq}/cm^2}$ to $\Phi = 1 \times 10^{15}\,\mathrm{n_{eq}/cm^2}$ [Ebe13]. The energy level of the valence is denoted by E_v and of the conduction band by E_c.

Trap type	Energy level (eV)	Defect concentration ($\mathrm{cm^{-3}}$)	Capture cross section ($\mathrm{cm^2}$)
Donor	$E_\mathrm{v} + 0.48$	$\Phi \cdot 1.395$	1.2×10^{-14}
Acceptor	$E_\mathrm{c} - 0.525$	$\Phi \cdot 1.55$	1.2×10^{-14}

space charge in the surface region that should repel electrons from the surface, thus prevent the electron accumulation.

First, a varying proton fluence, thus varying bulk defects, is considered and the impact on the intertrip resistance curves is illustrated in fig. 8.17. In order to avoid distraction by other defects, interface traps are fully excluded for the moment and a sensor without any strip implant is considered. A certain fixed oxide charge concentration has to be inserted, since otherwise the interstrip resistance would be too high. Hence, the value of $3 \times 10^{11}\,\mathrm{cm^{-2}}$ is considered similarly to the investigations in section 8.3.3. Brighter colours represent increasing fluence, which leads to a shift of the whole curve to lower bias voltages. This effect is similar to the effect of an increasing doping concentration in section 8.3.3. The similarity is because the bulk defects increase the effective doping concentration of the bulk as explained in section 4.2.

Similar to the investigation procedure with a varying doping concentration, the electric field's x and y-components are considered. The proton bulk defect concentrations according to fluences of $6 \times 10^{14}\,\mathrm{n_{eq}/cm^2}$ and $9 \times 10^{14}\,\mathrm{n_{eq}/cm^2}$ are used with a fixed charge of $3 \times 10^{11}\,\mathrm{cm^{-2}}$ in fig. 8.18. The interstrip resistance at 300 V is low in case of $6 \times 10^{14}\,\mathrm{n_{eq}/cm^2}$ and well above the limit for $9 \times 10^{14}\,\mathrm{n_{eq}/cm^2}$. Because of the increased bulk defect concentration, the electric field components increase. In fig. 8.18a it can be seen that the y-component 0.5 µm below the interface is higher in case of the higher fluence. This means that electrons are attracted more strongly towards the surface. However, similar to the case with varying doping concentrations, the x-component of the electric field is also higher in the interstrip region as illustrated in fig. 8.18b. Therefore, the electrons cannot build up a homogeneous layer between the strips and the strip isolation is preserved with the higher fluence.

Another effect of an increased fluence is that the maximal achievable interstrip resistance is decreased compared to the cases before irradiation, for example in fig. 8.8. This is because the bulk defects cause a general increased free charge carrier concentration, different to the increased doping concentration. Hence, the current flow from one strip to the other is increased, even if no electron layer is formed between the strips. This explains why the bulk defects in fig. 8.16 lead to a considerably higher interstrip resistance for low bias voltages, but less interstrip resistance for higher bias voltages. The achievable upper limit of the interstrip resistance is determined by the current that is generated between the strips due to the bulk

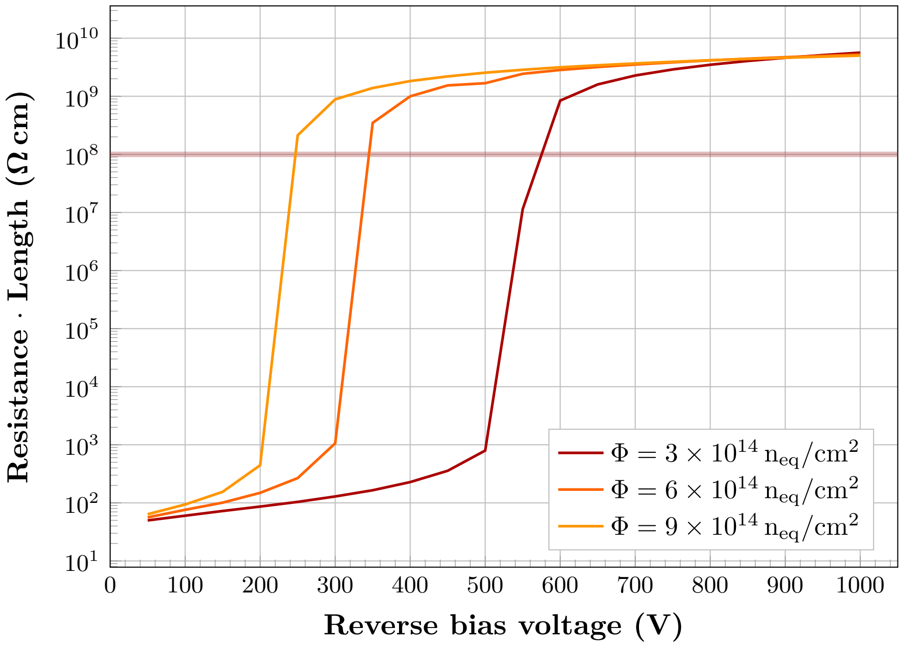

Figure 8.17.: Impact of bulk defects on the interstrip resistance's dependence on the bias voltage derived from simulations. A constant fixed oxide charge of $3 \times 10^{11}\,\mathrm{cm^{-2}}$ is used and interface traps are excluded for simplicity.

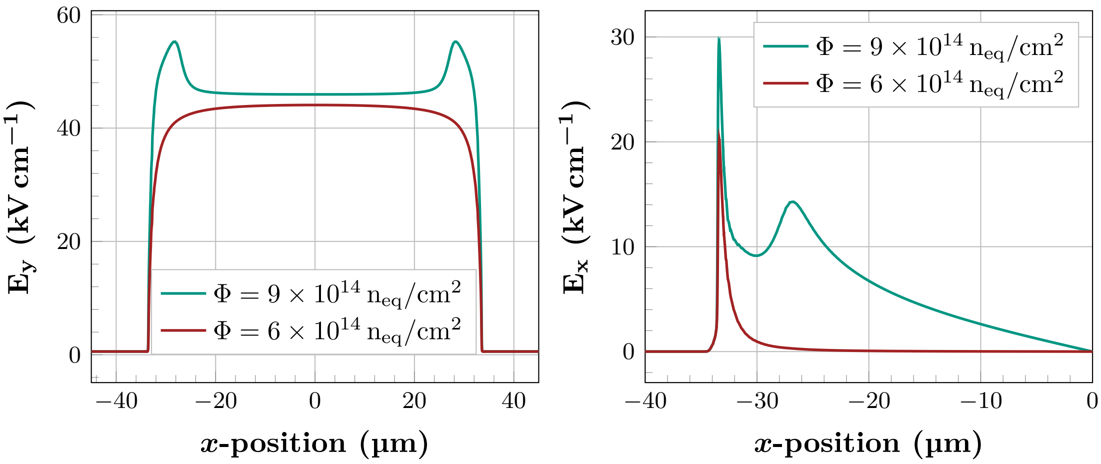

(a) **(b)**

Figure 8.18.: Simulated electric field's y (a) and x-component (b) 0.5 µm below the surface at a bias voltage of 300 V. The y-axis points perpendicular to the surface into the substrate and the x-axis points towards the middle of the device. The second peak of the green curve in (b) is due to the metal overhang. A two-dimensional representation of the device can be found in fig. 8.4.

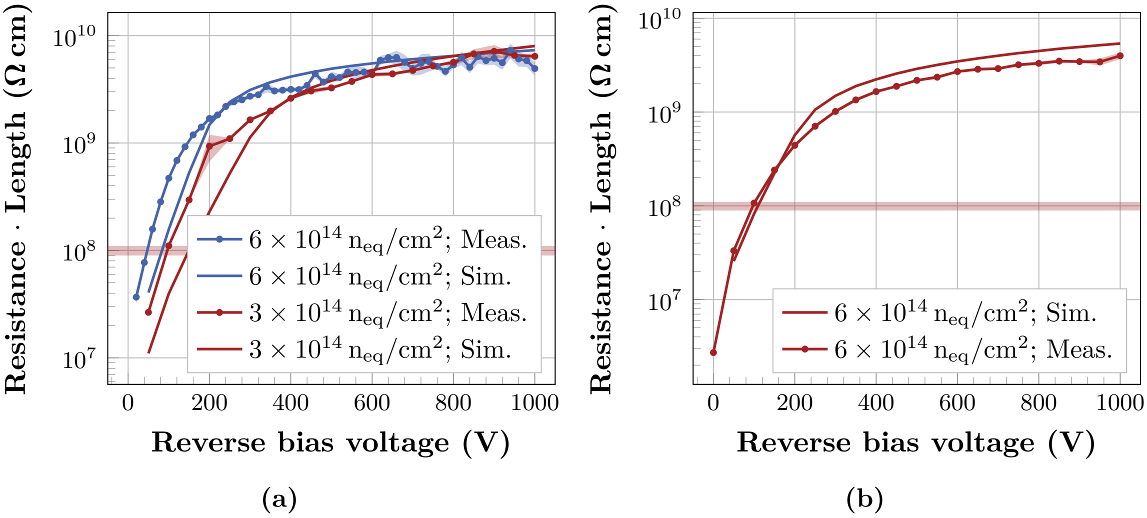

Figure 8.19.: Replication of measurements by simulations after neutron irradiation with different fluences (a) and with proton irradiation to a fluence of $\Phi = 6 \times 10^{14}\,\mathrm{n_{eq}/cm^2}$ (b). Curves that should match each other are indicated with the same colour.

defects. This is also the reason why the p-stop loses its impact at these high fluences, as has been concluded from fig. 8.15.

8.5.4. Comparison of Simulations to Measurements

After the impact of bulk defects on the strip isolation is understood, the replication of the measurements of fig. 8.15 can be attempted. In section 8.4.4, a model describing the pure surface damage induced by X-rays has been validated. Estimations of the defect concentrations (N_{ox} and N_{it}) have been done on the basis of simulations and measurements for the sensor types used in the scope of this work. Therefore, any applied dose can be converted into defect concentrations of the surface defect model. In case of neutron irradiation the applied dose is 1 kGy per $1 \times 10^{14}\,\mathrm{n_{eq}/cm^2}$. Thus, the neutron fluence of $3 \times 10^{14}\,\mathrm{n_{eq}/cm^2}$ corresponds to a dose of 3 kGy and $6 \times 10^{14}\,\mathrm{n_{eq}/cm^2}$ to 6 kGy. The respective defect concentrations from section 8.4.4 of $N_{\mathrm{ox}} = 2.54 \times 10^{11}\,\mathrm{cm^{-2}}$ and $N_{\mathrm{it}} = 2.55 \times 10^{11}\,\mathrm{cm^{-2}}$ are inserted to emulate the surface damage part of the neutron irradiation with a fluence of $\Phi = 3 \times 10^{14}\,\mathrm{n_{eq}/cm^2}$. Similarly, $N_{\mathrm{ox}} = 2.74 \times 10^{11}\,\mathrm{cm^{-2}}$ and $N_{\mathrm{it}} = 3.21 \times 10^{11}\,\mathrm{cm^{-2}}$ have been used in case of a fluence of $\Phi = 6 \times 10^{14}\,\mathrm{n_{eq}/cm^2}$. The bulk defects from the neutron irradiation are introduced according to table 8.3. A comparison of the resulting interstrip resistance curves to the measurement is shown in fig. 8.19a. Measurements are indicated with lines and data points and the respective simulations are indicated with continuous lines without data points but with the same colour. The agreement is accurate, especially if the various measurement uncertainties are taken into account like unintended annealing during shipment and general uncertainty of around 15% on the fluence.

The same procedure has been applied for the proton irradiated sensor without any strip isolation implant and visualised in fig. 8.19b. Here, the saturation concentrations (corresponding to 15 kGy) of $N_{\mathrm{ox}} = 3.15 \times 10^{11}\,\mathrm{cm^{-2}}$ and $N_{\mathrm{it}} = 4 \times 10^{11}\,\mathrm{cm^{-2}}$ have been used. Again, the simulated characteristics matches the measured one accurately.

After the measurements had been conducted, the two neutron irradiated sensors were further irradiated with X-rays to a dose of 20 kGy, which is well in saturation. The measured curves after additional X-ray irradiation are indicated in fig. 8.20a. In order to ensure saturation, the

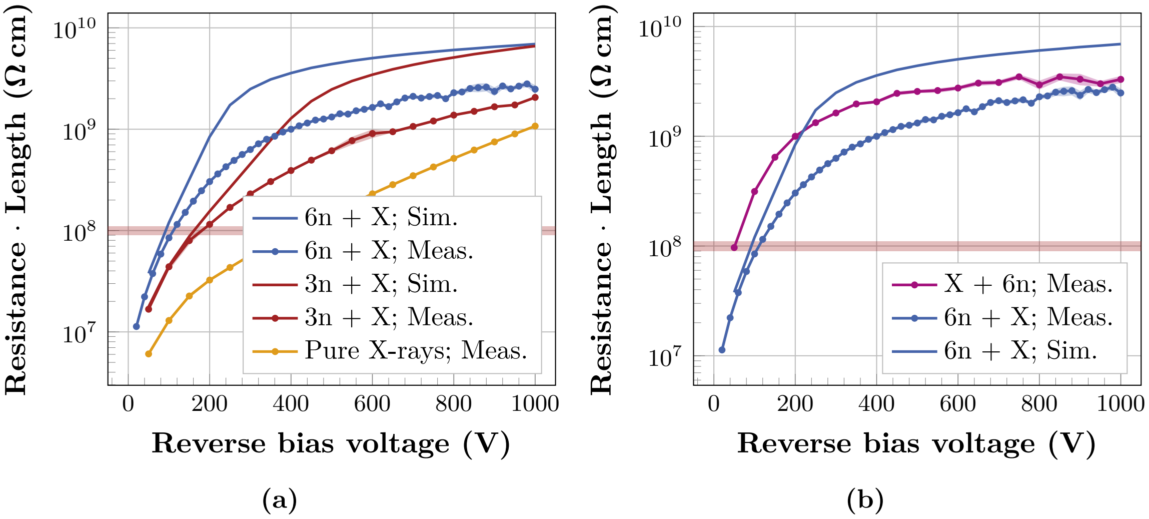

(a) (b)

Figure 8.20.: Interstrip resistance in dependence of the irradiation sequence neutrons first, followed by X-ray irradiation (a) and X-ray irradiation followed by neutron irradiation (b). The abbreviations 6n and 3n stand for a neutron fluence of $3 \times 10^{14}\,\mathrm{n_{eq}/cm^2}$ and $6 \times 10^{14}\,\mathrm{n_{eq}/cm^2}$, respectively. The X-ray irradiation with a dose of 20 kGy is denoted by the X.

sensors were also irradiated further to even higher doses. However, since they were in fact saturated already, these curves at higher doses are not shown, because they are similar and would degrade the clarity in the plot. In first instance, the plot shows the beneficial effect of the bulk defects once again, since the interstrip resistance is considerably higher compared to the case with pure X-ray irradiation of the same dose (orange line). If the surface defect concentrations are increased to the corresponding concentrations from section 8.4.4, the lines without data points in the figure are obtained. It can be seen that the simulated curves overestimate the interstrip resistance in both cases. A hypothesis would be that the saturation of the surface related defect concentrations is influenced by the neutron irradiation. It might be that the neutrons induce different defects inside the oxide which are not considered yet. These could be uncharged first but react further to charged defects by the following X-ray irradiation. Until now, only bulk defects due to neutron irradiation are considered and the surface defects are estimated solely on the basis of photon contamination inside the reactor. There is no reason why neutrons should not generate relevant defects in the oxide in addition to the bulk.

To get deeper insight into the matter, another sensor has been irradiated with 20 kGy X-rays first (in saturation) and irradiated with neutrons to a fluence of $6 \times 10^{14}\,\mathrm{n_{eq}/cm^2}$ afterwards. Indeed, a difference can be observed, as illustrated in fig. 8.20b where the purple curve represents the irradiation sequence with X-rays first. In that case, the simulation would fit better but still not perfect. However, the fact that there is indeed a difference in the irradiation sequence, is a hint that there might be some influence of the neutron irradiation on the oxide or interface region.

Some follow-up studies have been performed. Since they are not fully conclusive or deal with aspects that are not directly linked for the investigations presented here, they can be found in appendix D.3.

In this chapter, the understanding and mechanisms of strip isolation have been evaluated in depth. Several unsolved questions that occurred previously concerning the strip isolation of n-on-p sensors have been successfully addressed. Most importantly, the impact of bulk defects on the interstrip resistance is understood and could even be replicated by TCAD simulations. The findings of these investigations can give input to new radiation-hard sensor designs with critical strip or pixel isolation. In addition, the general necessity of a p-stop is put into perspective. The main outcome of these investigations has also been summarised and published in [Mül+21].

Part IV.

Summary and Outlook

9

Summary and Outlook

The LHC will undergo a major upgrade towards the HL-LHC in the time period between 2025 and 2027, which results in an increased instantaneous luminosity by a factor of five to seven. That implies a considerably higher interaction rate. The projected integrated luminosity will be at least $3000\,\mathrm{fb}^{-1}$, which is ten times higher than before. Because probabilistic processes are studied, the potential of discovering new physics grows with the number of events. However, for the detectors both, the higher instantaneous luminosity and also the integrated luminosity, imply new challenges.

The pile-up (number of simultaneous collisions per bunch crossing) increases drastically. The efficiency of the Level-1 trigger therefore needs to be improved to keep the trigger rate at an acceptable level. An important novelty is that the Outer Tracker contributes to the first level of the trigger system with information about tracks of particles with high transverse momentum p_T. This is achieved by a new module concept referred to as p_T-modules. The Outer Tracker houses two types of these modules that are comprised of two similarly aligned sensors per module. PS modules are placed in the inner region, which incorporate a strip and a macro-pixel sensor (PS-s and PS-p). The outer region is instrumented by 2S modules that house two strip sensors with longer strips.

A crucial requirement for the new tracker is that it has to withstand the significantly increased radiation damage that comes with the integrated luminosity. If the sensors are not able to cope with the radiation damage, the detector is not operable anymore. Therefore, radiation hardness is a crucial property of the new sensors. In order to find the best-suited substrate material and sensor design, over several years intense R&D irradiation campaigns have been performed. After the Outer Tracker community agreed on design specifications, the production of these sensors has started. A pre-production of wafers with the sensors mentioned above (PS-s, PS-p and 2S) has been accomplished to ensure that the vendor is able to deliver the required quality and production rate. The quality assurance testing scheme consist of three tasks: sensor quality control (SQC), process quality control (PQC) and irradiation tests (IT). These tasks are performed by several institutes worldwide. The ETP contributes to SQC and IT and this work in particular dealt with the irradiation tests in the course of the pre-production.

Radiation damage in silicon sensors can be divided into two parts: bulk and surface damage. Bulk defects are generated by non-ionising energy loss (NIEL) of heavy particles, for example hadrons. The expected maximum fluences of the Outer Tracker are $\Phi_{\mathrm{2S}} = 4 \times 10^{14}\,\mathrm{n_{eq}/cm^2}$ and $\Phi_{\mathrm{PS}} = 1.1 \times 10^{15}\,\mathrm{n_{eq}/cm^2}$ for 2S and PS modules, respectively. Bulk damage is investigated in this work by irradiating with protons and with neutrons. The second part, surface damage, is induced by ionisation of the oxide. Hence, surface damage is also applied by proton irradiation, since protons are charged particle. In case of neutron irradiation inside a spallation reactor, a small amount of surface damage is applied by the photon background radiation. Pure surface damage is applied in this work by X-ray irradiation. To investigate the complex interplay of the bulk and surface damage on the strip isolation of the p-type silicon strip sensors, a dedicated study has been performed and discussed in this work.

Irradiation Tests for the CMS Outer Tracker Sensor Production

The first part of this work is dedicated to the development of routines for the irradiation tests and the execution of these on pre-production batches. All foreseen pre-production irradiation tests at KIT have been finished for the 2S and PS-s batches. In total 14 batches of 2S sensors and 3 PS-s sensor batches have been investigated.

Diodes and miniature strip sensors of 2S and PS-s wafers have been irradiated to the corresponding expected fluence in Phase-2 with protons of an energy of 23 MeV. This is done for at least two wafers (two structures) per batch. This number of two per batch is also foreseen for the full mass production, but not every batch will be tested. Prior to irradiation, all global sensor and strip parameters show very small variations and meet the specified limits.

After irradiation, leakage current measurements on the diodes have been performed to extract the current-related damage rate. The spread of the measured damage rate of the different batches is 7.3%. Therefore, the procedure is reliable and the substrate quality is constant over the batches. In addition, the mean value is close to the value of previous investigations although the procedures differ slightly. The damage rate will be monitored during the subsequent batches of the full production to spot a potential drift of the quality of the substrate.

Strip parameters have been extracted from the miniature strip sensors on the irradiation test half-moons. After irradiation, all strip parameters changed as expected. Besides the strip parameters, the charge collection of the sensors has been investigated. A rule of thumb holds that the most probable value of the seed signal should be higher than three times the acceptance threshold for a binary readout mode. This translates to limits of $12\,000\,\mathrm{e}^-$ and $9600\,\mathrm{e}^-$ for the 2S and PS-s sensors, respectively. It has been shown in this work that this requirement is met at the target operation voltage of 600 V after proton irradiation, independent of the annealing. The seed signal is around $16\,000\,\mathrm{e}^-$ for the sensors from 2S batches irradiated with the corresponding target fluence of $\Phi_{2S} = 4 \times 10^{14}\,\mathrm{n_{eq}/cm^2}$ and around $14\,000\,\mathrm{e}^-$ for PS-s batches with the fluence of $\Phi_{PS} = 1.1 \times 10^{15}\,\mathrm{n_{eq}/cm^2}$. Also, the spread of the values at similar fluences is small, which reflects the homogeneous substrate quality again.

To monitor the radiation hardness of the oxide X-ray irradiations have been performed. The corresponding test structures MOS and GCD are used to extract the flat-band voltage and the surface generation velocity, respectively. There are no previously defined ranges of acceptable values as for the seed signal. Therefore, the aim of this work was to establish reasonable estimations of which range of values can be expected during the production. The expected doses during Phase-2 are too high to perform such irradiations on a regular basis. However, in some first investigations of irradiated MOS and GCD structures it has been found that the flat-band voltage of MOS capacitors does not change anymore for a dose in SiO_2 above 15 kGy. Therefore, with a sufficient margin, a dose of 40 kGy has been specified for all subsequent X-ray irradiation tests. For the surface generation velocity no saturation effect was observed.

For the extraction of the flat-band voltage from a high-frequency capacitance measurement after irradiation some severe instabilities have been observed. To ensure the reliability of the MOS capacitor measurements, a specific treatment has been developed during this work. It is composed of an annealing step at 60 °C, relaxation at room temperature and biasing. The specific treatment is of major importance to the X-ray irradiation tests, since the key aspect of the irradiation test procedure is that the results are comparable.

The irradiation to a dose of 40 kGy and the specific treatment have been performed on two wafers of the 14 2S batches and 3 PS-s batches each. In addition, two batches of PS-p wafers have been investigated. Since the PS-p sensors are DC coupled, the requirement on the oxide quality is less strict. This is also reflected by the flat-band voltage and surface generation velocity prior to irradiation. Both values are approximately doubled compared to the 2S and PS-s wafers. After irradiation, the flat-band voltage values of the 2S and PS-s wafers are in a similar range around 43 V. The flat-band voltage of the PS-p wafers stays considerably higher, at 60 V. Unexpectedly, the surface generation velocity after irradiation turned out to be similar around $1150\,\mathrm{cm\,s^{-1}}$ for all three wafer types.

To conclude, an optimised irradiation testing procedure that will apply for the whole Outer Tracker sensor production of the next years, has been established in this work based on the investigation of pre-production batches. In addition, baselines in terms of measurement, extraction procedures and results has been set with this work on which the production can be built upon.

Interstrip Isolation of Silicon Strip Sensors

The second main topic of this thesis is the understanding of the strip isolation of n-on-p silicon strip sensors. During the prototyping phase of the Outer Tracker sensors, sensors without any strip isolation structures have been produced. These have been used in this work to generate a deeper understanding of the strip isolation mechanism, especially considering radiation-induced damage. Using sensors without any isolation structures had the advantage that there is no implant between the strips, like for example a p-stop, that could disguise the underlying mechanism.

The starting point of these investigations was that in previous studies after hadron irradiation some unexpectedly high interstrip resistances have been observed on sensors with a very low p-stop doping concentration or without any p-stop doping. The expectation, on the other hand, was that the radiation damage harms the detector by introducing positive charge in the oxide. Therefore, the build-up of an electron layer that short-circuits the strips should be promoted. However, this did not seem to be the case. Since in these previous investigations the samples were irradiated with hadrons, the working hypothesis for this work is that the generated bulk damage helped to set up the strip isolation.

The main parameter that provides information about the strip isolation is the interstrip resistance between to adjacent strips. The interstrip resistance measurements conducted in this work showed that it is indeed low for small bias voltages when there is no specific isolation implant between the strips, prior to irradiation. However, already for a reverse bias voltage of around 100 V usually an interstrip resistance level similar to the resistance of the sensors with the standard design, which comprise a p-stop implant, has been reached. To support the outcome of the measurements, TCAD finite-element simulations have been conducted. In the simulated device it has been seen that the voltage that is required to remove the short-circuiting electron layer depends on the positive oxide charge density, thus on the process quality.

In the next step, radiation damage has been applied to the sensors by X-ray irradiation to study the impact of pure surface damage. As expected, the measured interstrip resistance decreased considerably after irradiation for bias voltages above 100 V. Saturation was observed for a dose around 15 kGy, which is similar to the findings of the flat-band voltage of the MOS structures for the irradiation tests of the CMS Outer Tracker sensor pre-production. The measurements were used to validate a defect model that replicates the observed behaviour. This model expands the pure fixed oxide charge used previously by three interface trap states introduced at the interface between oxide and silicon bulk. The oxide charge and the defect concentrations for every dose step have been tuned so that the measured behaviour is successfully replicated by the simulation.

In order to investigate the impact of additional bulk defects, neutron and proton irradiations have been performed. Since a significantly different dose is applied in proton and neutron irradiations, the irradiation with different particles generated a comprehensive understanding of how strongly the bulk defects affect the strip isolation. For all fluences that range from $\Phi = 3 \times 10^{14}\,\mathrm{n_{eq}/cm^2}$ to $\Phi = 6 \times 10^{14}\,\mathrm{n_{eq}/cm^2}$ a considerably higher interstrip resistance was observed compared to the purely X-ray irradiated case. The highest interstrip resistance has been seen on a sensor that was irradiated with neutrons, thus small dose but high bulk defect concentration. Hence, it has been concluded that bulk defects are beneficial for the strip isolation.

An explanation of the beneficial influence of bulk defects has been found with the help of simulations. A bulk defect model that was developed during the intense CMS radiation campaigns on similar material has been validated by comparing the simulated curves to the measurements. With the composite defect model of positive charge in the oxide, three trap types at the interface and two bulk defects, it was possible to replicate most of the measurements. The electric properties of the simulated device revealed the underlying mechanism. The simulations show a higher electric field in the near-surface bulk region for higher bulk defect concentrations. By comparing the impact of different doping concentrations without bulk defects, it has been verified that a higher doping concentration or bulk defect concentration is indeed changing the electric configurations similarly such that the strip isolation is promoted. Although electrons are accelerated more strongly towards the interface perpendicular to the surface, they are also attracted to the strips parallel to the surface. Therefore, the build-up of a homogeneous electron layer that would short-circuit the strips is inhibited. This is how a higher hadron fluence can promote the strip isolation.

Outlook

This work has shown that the new CMS Outer Tracker sensors will be able to cope with the expected radiation damage if the vendor is able to keep the same quality as during the pre-production. To ensure this, several testing routines have been developed. They have been executed on pre-production batches, which gave tightly confined reference values for the various parameters after irradiation. These routines will accompany the whole production phase during the next years. In addition, an escalation strategy was demonstrated on two made-up examples, that showed how to deal with issues that might arise.

Although being mostly academic, the results of the second part of this work can give valuable input to new sensor designs, in case no p-stop implant can be implemented. The composite TCAD model can be used to estimate the strip or pixel isolation of future sensors that are embedded in a harsh radiation environment. A concrete case could be the design scheme of pixel sensors with high spatial resolution, thus small pixel distance. If the distance between the pixels becomes limited by the isolation implants between them, it might be worth evaluating whether such an implant is required. The study has not only shown that it might be possible to leave out the p-stop and the sensor will still be functional but in particular for a proton fluence of $\Phi = 6 \times 10^{14}\,\mathrm{n_{eq}/cm^2}$ the p-stop was in fact not relevant anymore in terms of interstrip resistance. By the findings of this study, it turned out that the p-stop is mostly helpful prior to irradiation or at low fluences. In addition, it is known that a high p-stop doping concentration can also lead to local breakdowns and it should be chosen with care. Therefore, the general usage of a p-stop is put into perspective by the outcome of this work and it is worth evaluating whether such an implant is required for the design of future silicon sensors.

Part V.

Appendix

A

Appendix to Chapter 5

Fig. A.1 shows the states of a MOS device with an n-type substrate dependent on the gate voltage.

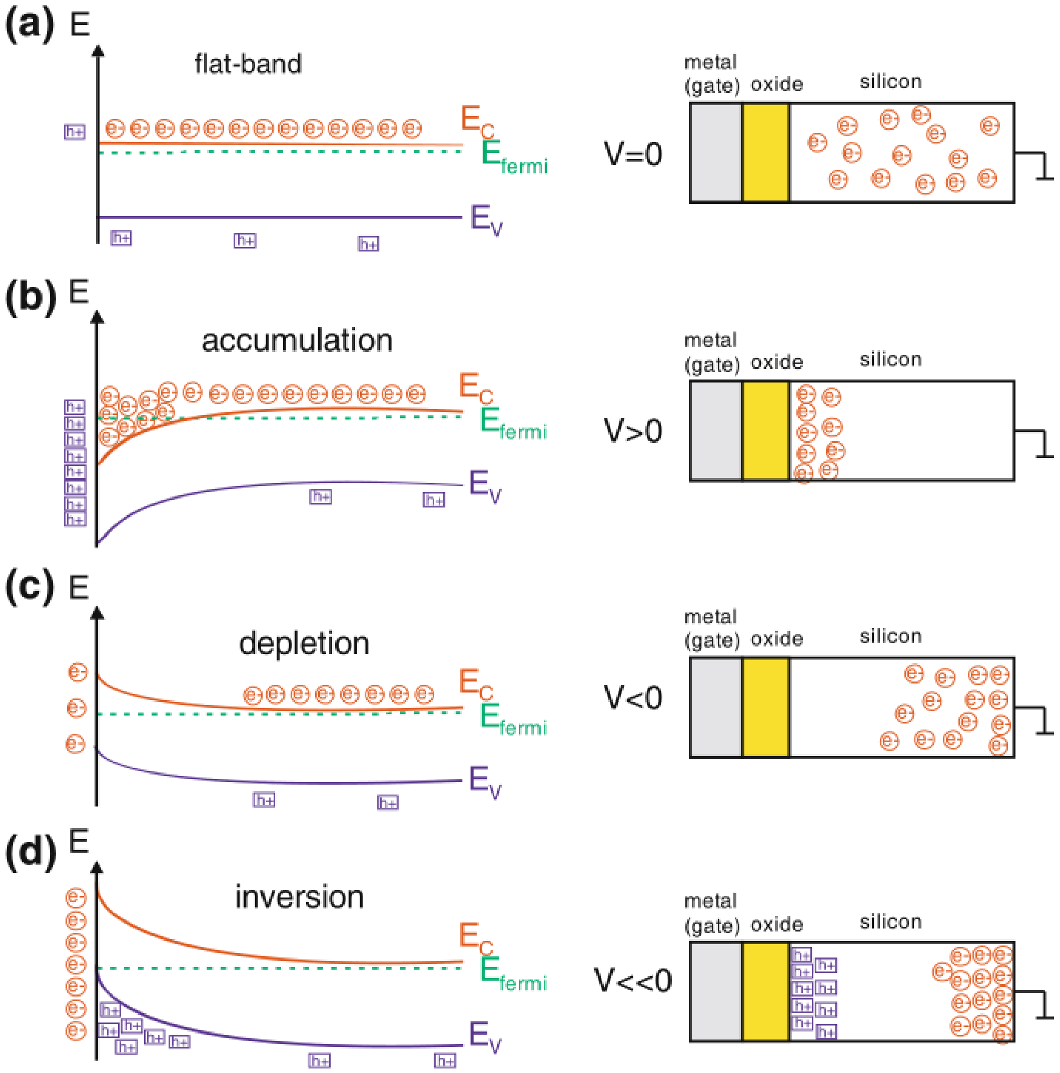
(a)
E
flat-band
h+
e-
E_C
E_fermi
E_V
V=0
metal (gate)
oxide
silicon
(b)
E
accumulation
V>0
(c)
E
depletion
V<0
(d)
E
inversion
V<<0

Figure A.1.: Explanation of the different conditions of a MOS capacitor dependent on the gate voltage. The band model scheme is shown on the left side and a sketch of the corresponding device on the right side [Har17].

B

Appendix to Chapter 6

Fig. B.1 shows the exterior of the probe station with a PC on the left and the measurement devices on the right of the aluminium housing.

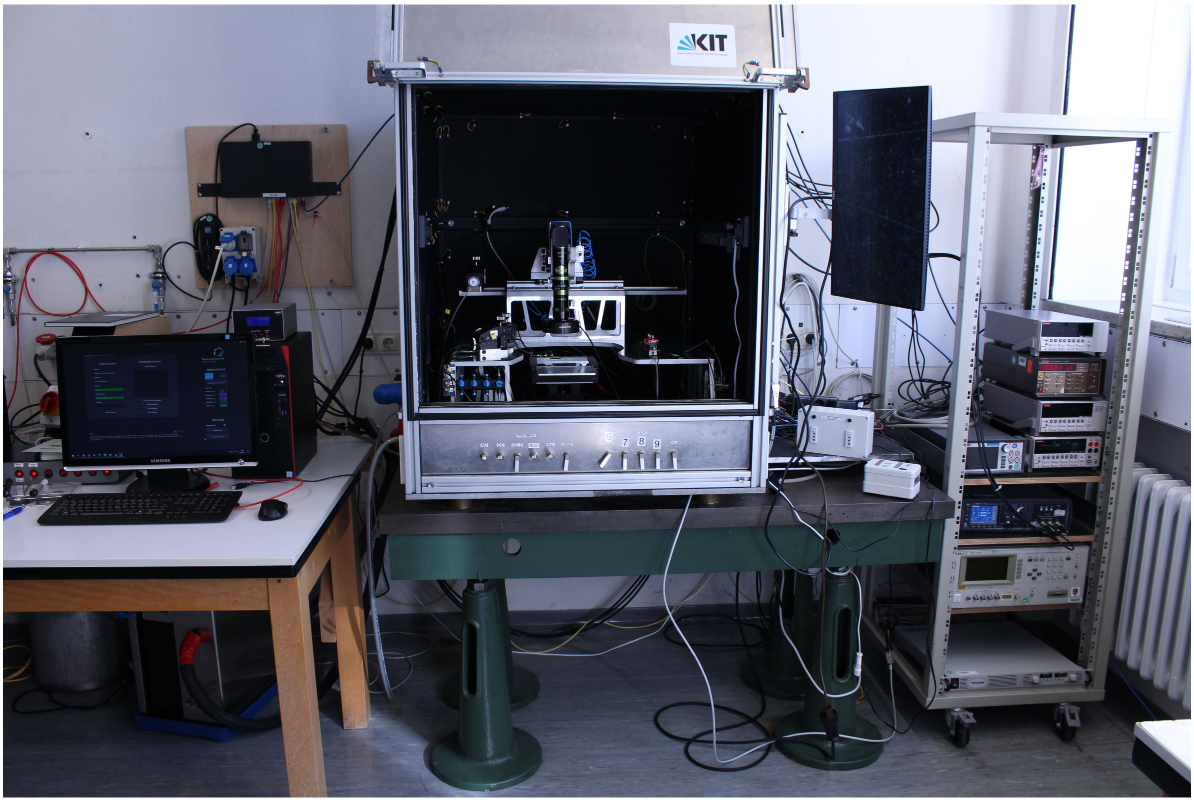

Figure B.1.: Exterior of one of the two probe stations that are available at ETP. This station has been used for most of the measurements, especially after irradiation.

C

Appendix to Chapter 7

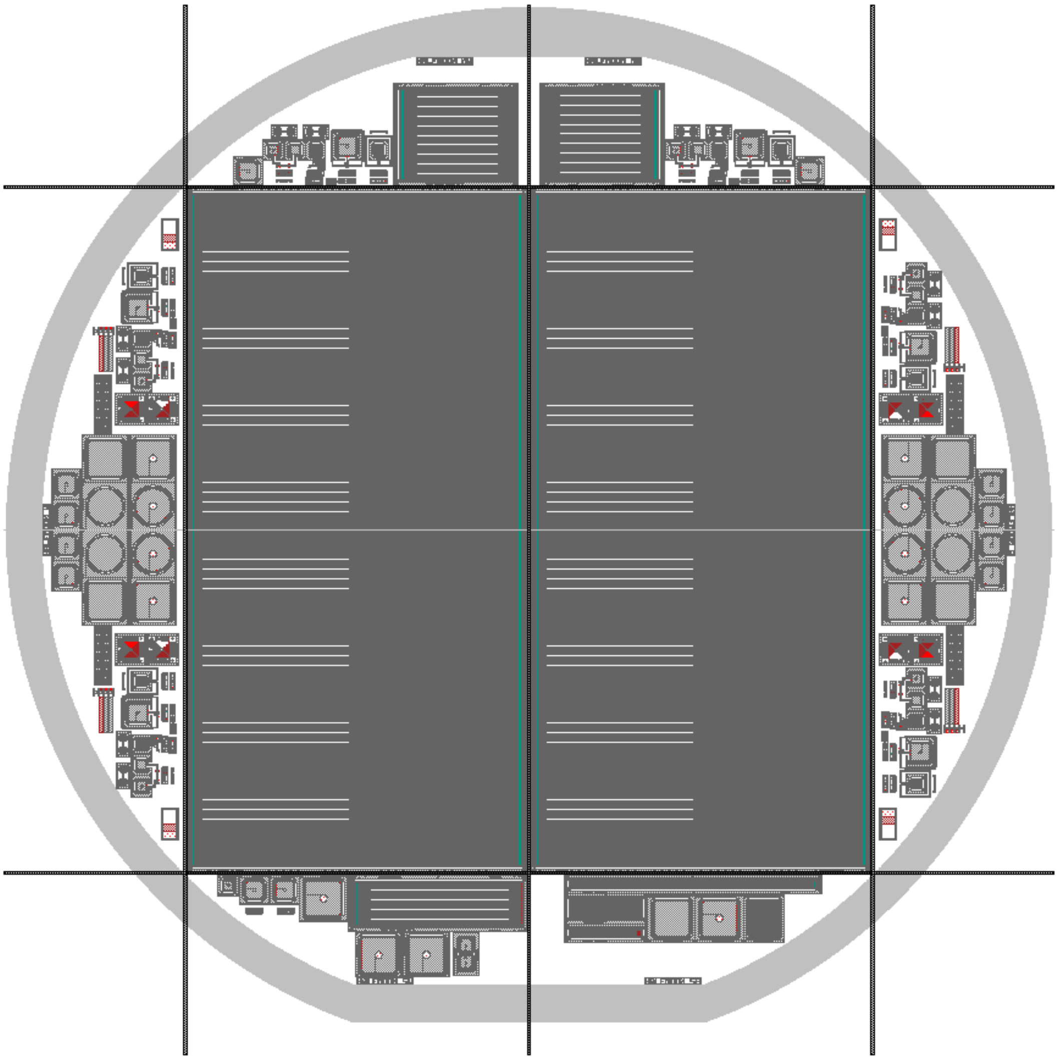

Figure C.1.: Design file of the PS-s wafer with dicing lines.

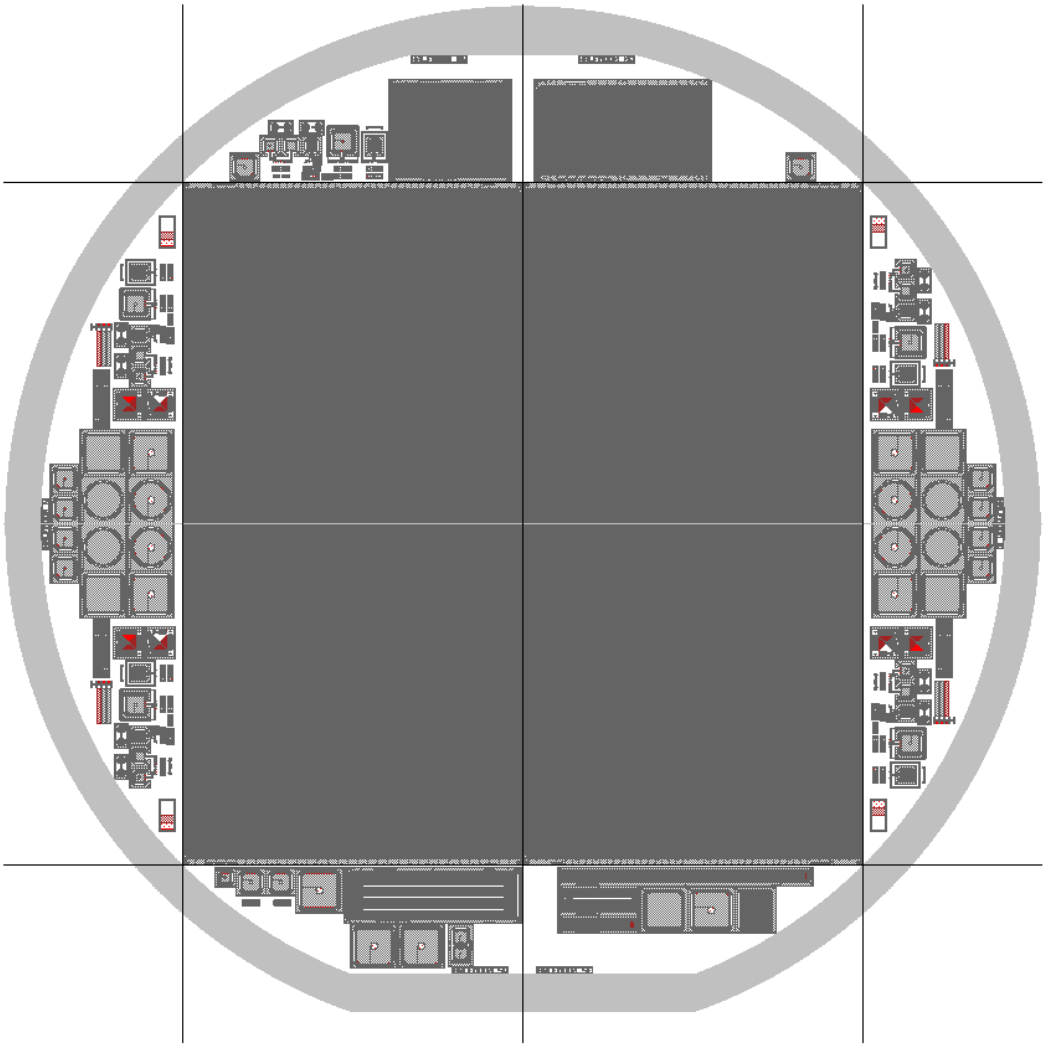

Figure C.2.: Design file of the PS-p wafer with dicing lines. Besides the layout of the full-sized sensors in the middle the processes do not feature a specific coupling oxide nor polysilicon structures. Therefore, punch-through biasing schemes are applied that substitute the bias resistor for the small test sensors. In addition, a small test sensor with macro-pixels instead of strips is placed on the top right.

D

Appendix to Chapter 8

D.1. Example Sentaurus Device File

The following code refers to an exemplary Sentaurus device configuration file. Here, the physics and the solve methods are defined. Pure interface traps are defined if fluence $\Phi = 0$, thus without bulk defects. If the fluence is $\Phi > 0$, proton bulk defects according to table 8.2 are added. The avalanche parts can be activated to include charge multiplication effects, as described in appendix D.3.4. In the solve section the bias voltage is ramped to the specified value and one simulated interstrip resistance measurement is performed.

```
Device raw{
    Electrode
    {
        {Name=”c_back” Voltage=0.0}
        {Name=”c_acL” Voltage=0.0}
        {Name=”c_acR” Voltage=0.0}
        {Name=”c_dcL” Voltage=0.0}
        {Name=”c_dcR” Voltage=0.0}
    }

    File
    {
        Grid    = ”@tdr@”
        Current = ”@plot@”
        Plot    = ”@dat@”
        * # Parameter = ”@parameter@”
        TrappedCarPlotFile = ”trapped_car”
    }

    Physics
    {
        areafactor = 14500
        Temperature = @temp@
        Fermi
        Mobility
        (
            * #     DopingDep
            eHighFieldSaturation
            hHighFieldSaturation
            PhuMob( Phosphorus Klaassen )
            * #     Enormal
            * #     CarrierCarrierScattering (ConwellWeisskopf)
        )
        Recombination
        (
            SRH
            (
                DopingDependence
                TempDependence
                ElectricField(Lifetime=Hurkx DensityCorrection=None)
            )
            Auger
            #eAvalanche (vanOverstraeten Eparallel)
            #hAvalanche (vanOverstraeten Eparallel)
        )
        EffectiveIntrinsicDensity(Slotboom)
    }

    #if ”@Fluence@” == 0
    Physics (MaterialInterface = ”Silicon/SiO2”)
    {
        Recombination( SurfaceSRH )
        Traps(
            (FixedCharge Conc=@Nox_fixed@)
            (Donor Gaussian fromValBand Conc=!(puts [expr @N_it@ / 0.175])! EnergyMid=0.7   EnergySig=0.07  eXsection=1.0e-15   hXsection=1.0e-15)
            (Acceptor Gaussian fromCondBand Conc=!(puts [expr @N_it@ * 0.4 / 0.175])!   EnergyMid=0.4   EnergySig=0.07  eXsection=1.0e-15   hXsection=1.0e-15)
            (Acceptor Gaussian fromCondBand Conc=!(puts [expr @N_it@ * 0.6 / 0.175])!   EnergyMid=0.6   EnergySig=0.07  eXsection=1.0e-15   hXsection=1.0e-15)
        )
    }
    #endif

    #if ”@Fluence@” > 0
    Physics ( material = ”Silicon” )
    {
        * # Eber protons
        Traps
        (
            * # Deep Donor
            (
                Donor Level
                fromValBand
                Conc=!(puts [expr [expr @Fluence@ * 5.598] - 3.949e14])!
                EnergyMid= 0.48
                eXsection=1e-14
                hXsection=1e-14
            )
            * # Deep Acceptor
            (
                Acceptor Level
                fromCondBand
                Conc=!(puts [expr [expr @Fluence@ * 1.189] + 6.454e13])!
                EnergyMid= 0.525
                eXsection= 1e-14
                hXsection= 1e-14
            )
        )
    }

    Physics (MaterialInterface = "Silicon/SiO2")
    {
        Recombination( SurfaceSRH )
        Traps(
            (FixedCharge Conc=@Nox_fixed@)
            (Donor Gaussian fromValBand Conc=!(puts [expr @N_it@ / 0.175])! EnergyMid=0.7  EnergySig=0.07  eXsection=1.0e-15  hXsection=1.0e-15)
            (Acceptor Gaussian fromCondBand Conc=!(puts [expr @N_it@ * 0.4 / 0.175])!  EnergyMid=0.4  EnergySig=0.07  eXsection=1.0e-15  hXsection=1.0e-15)
            (Acceptor Gaussian fromCondBand Conc=!(puts [expr @N_it@ * 0.6 / 0.175])!  EnergyMid=0.6  EnergySig=0.07  eXsection=1.0e-15  hXsection=1.0e-15)
            )
    }
    #endif
}

System
{
    raw "sensor" ("c_back"=bg "c_acL"=acL "c_acR"=acR "c_dcL"=dcL "c_dcR"=dcR)
    Vsource_pset v (bg 0) {dc = 0}
    Vsource_pset vint (dcL dcR) {dc = 0}
    * Resistor_pset rA (A 0) {resistance = 0.1}
    * Resistor_pset rB (B 0) {resistance = 0.1}
    Resistor_pset r1 (dcL 0) {resistance = 1.5e6}
    Resistor_pset r5 (dcR 0) {resistance = 1.5e6}
    Resistor_pset r6 (acL 0) {resistance = 50}
    Resistor_pset r10 (acR 0) {resistance = 50}
}

Plot{
    eCurrent/Vector hCurrent/Vector Current/vector
    eDensity hDensity
    ElectricField ElectricField/Vector
    eEparallel hEparallel
    Potential SpaceCharge
    Doping DonorConcentration AcceptorConcentration
    Auger #eAvalanche hAvalanche AvalancheGeneration
    eMobility hMobility
    SRHRecombination
    EffectiveBandGap
    eTrappedCharge hTrappedCharge
    eInterfaceTrappedCharge hInterfaceTrappedCharge
    DeepLevels
    NegInterfaceCharge PosInterfaceCharge
    SurfaceRecombination
}

Math
{
    Method = blocked
    SubMethod = pardiso
    Number_of_Threads = 8
    Extrapolate
    Derivatives
    RelErrControl
    Digits=5
    Notdamped=50
    Iterations=20
    RecBoxIntegr (1e-2 10 1000)
    CheckTransientError
    BreakCriteria {Current(Contact=”c_dcR” Absval=1e-2)}
}

Solve
{
    Coupled (iterations=50 Notdamped=55) {Poisson}
    Coupled (iterations=50 Notdamped=55)
    {
        Poisson
        Electron
        Hole
    }

    NewCurrentPrefix = ”Ramp_”
    QuasiStationary
    (
        InitialStep=1e-5
        Minstep   = 1e-12
        MaxStep   = 1e-1
        Increment = 1.5
        Decrement = 2
        Goal
        {
            Parameter = v.dc
            Voltage=!(puts [expr @Voltage@ * -1])!
        }
    )
    {
        Coupled (iterations=50, Notdamped=55)
        {
            Poisson
            Electron
            Hole
            Contact
            Circuit
        }
        Plot (FilePrefix = ”@tdrdat@” Time=(1.0) NoOverwrite)
    }

    NewCurrentPrefix = ”Rint_”
    QuasiStationary
    (
        InitialStep=1e-5
        Minstep   = 1e-12
        MaxStep   = 1e-1
        Increment = 1.5
        Decrement = 2
        Goal
        {
            Parameter = vint.dc
            Voltage=1
        }
    )
    {
        Coupled (iterations=50, Notdamped=55)
        {
            Poisson
            Electron
            Hole
            Contact
            Circuit
        }
        Plot (FilePrefix = ”@tdrdat@_Rint_” Time=(1.0) NoOverwrite)
    }
}
```

D.2. Optimisation GUI

The usage of the optimisation tool to find the best suited N_{ox} and N_{it} to replicate an interstrip resistance measurement is explained here. Technically, the backplane voltage of the sensor is ramped to 1000 V in 50 V and measurements are performed iteratively in the simulation. This is similar to the actual measurements on the physical device. Then, for every step, the interstrip resistance is saved with the name *Rint$V$* with the bias voltage V. In fig. D.1 the interstrip resistance values are inserted in the column *Target* and weights in the column *Weights*. These weights are estimated by dividing the respective interstrip resistance value by the maximum value of the curve (usually at 1000 V). This ensures that values which are orders of magnitude below the maximum value do not get neglected but instead the relative deviation to the target value is taken.

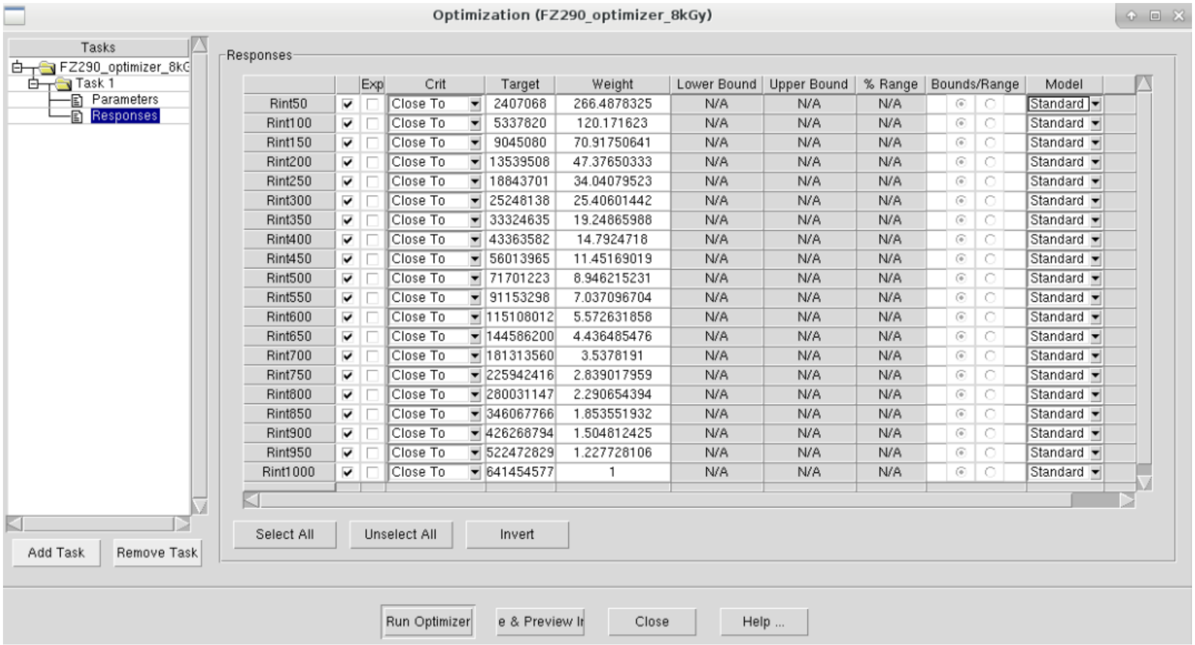

Responses

		Exp	Crit	Target	Weight	Lower Bound	Upper Bound	% Range	Bounds/Range		Model
Rint50	☑	☐	Close To	2407068	266.4878325	N/A	N/A	N/A	●	○	Standard
Rint100	☑	☐	Close To	5337820	120.171623	N/A	N/A	N/A	●	○	Standard
Rint150	☑	☐	Close To	9045080	70.91750641	N/A	N/A	N/A	●	○	Standard
Rint200	☑	☐	Close To	13539508	47.37650333	N/A	N/A	N/A	●	○	Standard
Rint250	☑	☐	Close To	18843701	34.04079523	N/A	N/A	N/A	●	○	Standard
Rint300	☑	☐	Close To	25248138	25.40601442	N/A	N/A	N/A	●	○	Standard
Rint350	☑	☐	Close To	33324635	19.24865988	N/A	N/A	N/A	●	○	Standard
Rint400	☑	☐	Close To	43363582	14.7924718	N/A	N/A	N/A	●	○	Standard
Rint450	☑	☐	Close To	56013965	11.45169019	N/A	N/A	N/A	●	○	Standard
Rint500	☑	☐	Close To	71701223	8.946215231	N/A	N/A	N/A	●	○	Standard
Rint550	☑	☐	Close To	91153298	7.037096704	N/A	N/A	N/A	●	○	Standard
Rint600	☑	☐	Close To	115108012	5.572631858	N/A	N/A	N/A	●	○	Standard
Rint650	☑	☐	Close To	144586200	4.436485476	N/A	N/A	N/A	●	○	Standard
Rint700	☑	☐	Close To	181313560	3.5378191	N/A	N/A	N/A	●	○	Standard
Rint750	☑	☐	Close To	225942416	2.839017959	N/A	N/A	N/A	●	○	Standard
Rint800	☑	☐	Close To	280031147	2.290654394	N/A	N/A	N/A	●	○	Standard
Rint850	☑	☐	Close To	346067766	1.853551932	N/A	N/A	N/A	●	○	Standard
Rint900	☑	☐	Close To	426268794	1.504812425	N/A	N/A	N/A	●	○	Standard
Rint950	☑	☐	Close To	522472829	1.227728106	N/A	N/A	N/A	●	○	Standard
Rint1000	☑	☐	Close To	641454577	1	N/A	N/A	N/A	●	○	Standard

Figure D.1.: Example of an optimisation configuration.

D.3. Follow-Up Studies to Chapter 8

This section introduces follow-up studies that have been performed with the aim to shed light on some further questions related to the strip isolation of n-on-p silicon sensors. Since these investigations are not fully conclusive or not immediately relevant for the understanding of the findings in chapter 8 they are placed in the appendix. They are presented here for the sake of completeness and yield results which could be built upon in the future.

D.3.1. Biased X-Ray Irradiation

All silicon sensors are biased during their operation. This bias can be applied over specific bias-bonds as for example in the case of the 2S and PS-s sensors in the 2S and PS module. The readout chip, which is not necessarily on the same potential as the ground over the bias-bonds, is then connected to the AC pad with wire-bonds. In addition, after irradiation when the strip leakage current is high, the voltage drop at the bias resistor increases. In case of the PS-s sensors with a fluence of $1.1 \times 10^{15}\,\mathrm{n_{eq}/cm^2}$, the strip leakage current will increase to around $I_{\mathrm{strip}} > 100\,\mathrm{nA}$ following the findings in section 7.2.5 (dependent on the concrete fluence and annealing state). Thus, the voltage drop at the bias resistor, which can be up to $R_{\mathrm{bias}} = 2\,\mathrm{M\Omega}$ according to the specifications, would be $V_{\mathrm{drop,\ bias}} = I_{\mathrm{strip}} \cdot R_{\mathrm{bias}} = 0.2\,\mathrm{V}$. Therefore, during operation, an electric field can build up in the oxide.

The question arises how much this bias affects the defect generation in the oxide and especially in the interface by ionising radiation. When electron-hole pairs are generated inside the oxide, the fraction of unrecombined electrons and holes depends on the incident particle type but also on the electric field in the oxide as explained in section 4.4. It depends on the electric field, since the oppositely charged free charge carriers are separated faster from each other. Hence, more surface charge is expected to aggregate when the oxide is biased during the irradiation.

This results in a higher flat-band voltage of MOS capacitors for increased oxide bias during X-ray irradiation, as has been determined previously in Ref. [Wei08]. How the impact translates to a strip sensor is investigated in this section. In order to do so, a specific board has been designed that enables the biasing of the oxide during the irradiation on the one hand. On the other hand, the sensor should be measurable without replacing the bonds several times. The principle is illustrated in fig. D.2 and fig. D.3. All AC pads are connected with wire-bonds to a copper line that is grounded over a plug. For the irradiation, a potential on the DC pads can be applied, as usual, over the bias ring with a bias bond. The backside is floating, thus the substrate is unbiased. A picture of the board inside the X-ray irradiation setup is shown in fig. D.3a. Similar to the unbiased case, the sensor's annealing is suppressed by cooling down the chuck.

For the measurements, the board can be placed in the probe station on the chuck as shown in fig. D.3b. In this case, the DC pads and the AC pads are both grounded over the plug. The chucks potential is forwarded to the backside of the sensor with a copper band that turns over from the frontside of the board and the backside of the sensor to the backside of the PCB. With such a configuration, the biasing of the sensor can be done without any additional needle. The interstrip resistance and capacitance measurements can then be performed as usual by contacting two adjacent DC pads.

The switch that can be seen in fig. D.3a and fig. D.3b was an idea of coupling out ten strips in the middle during the measurements, to evaluate if the measurements are influenced by the short-circuited AC pads. However, apparently it coupled too much noise into the measurements so that a reliable interstrip resistance estimation was not possible anymore. Therefore, in the following, the switch is not considered any further.

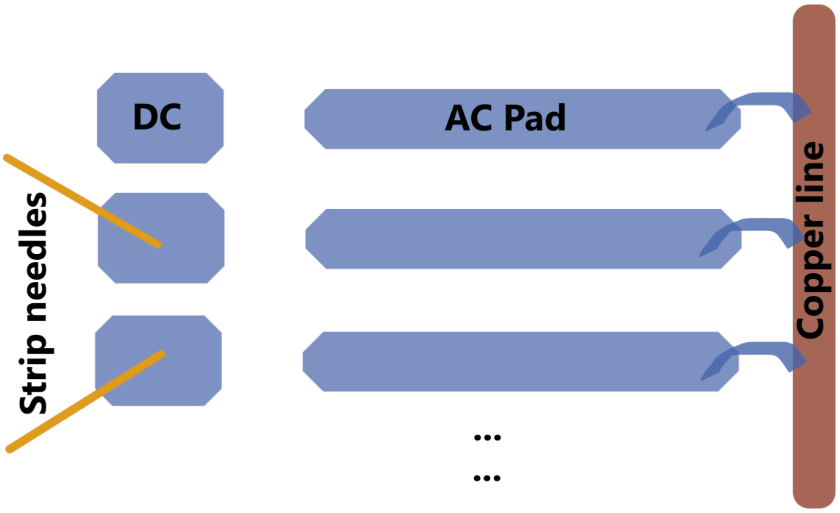

Figure D.2.: Scheme of the sensor on the PCB designed for biased X-ray irradiation with bias-bonds from the AC pads to a copper line for the irradiation and standard strip needle testing on the DC pads in the probe station setup.

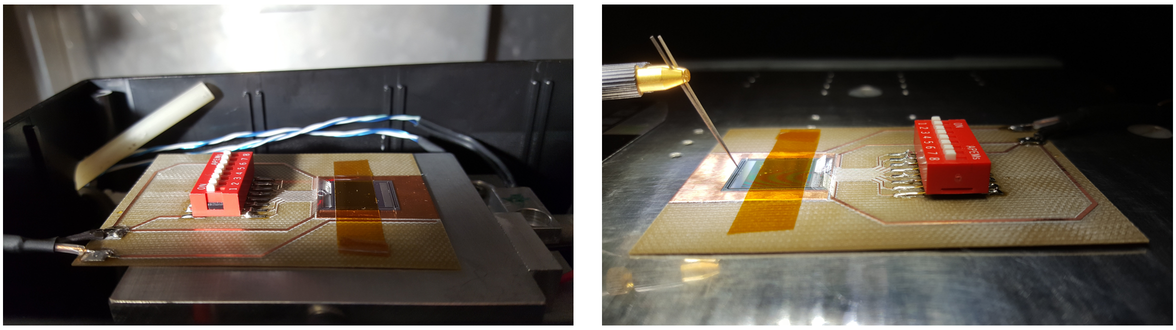

(a)

(b)

Figure D.3.: Biased X-ray irradiation board during irradiation (a) and measurements in the probe station (b).

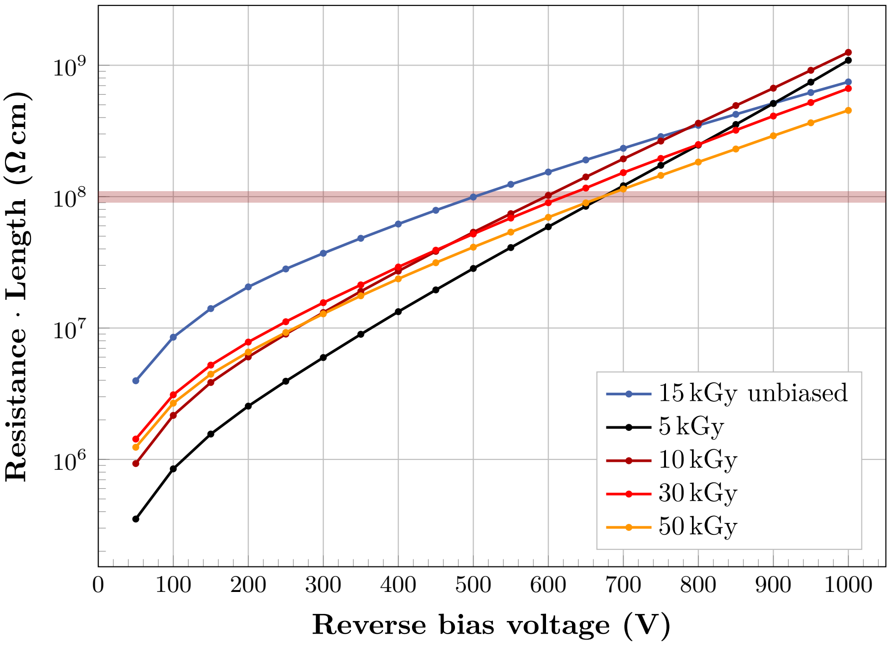

Figure D.4.: Interstrip resistance in dependence on the substrate bias voltage for different doses. A constant oxide bias of 5 V has been applied during the irradiation except for one that is shown for comparison.

A test sensor without any specific strip isolation implant has been irradiated subsequently with X-rays and an applied bias between the AC and DC pad of 5 V. This is a large margin compared to the estimation of the voltage drop at the bias resistor of 0.2 V. The polarity is chosen such that the negative potential is applied on the n^+-implant. This is the worst case, since the positive charge inside the oxide is accelerated towards the interface. Similar to the situation before, the chuck of the X-ray irradiation setup is cooled down. Because the PCB has a low thermal conductivity, the temperature of the sensor is expected to be higher than the temperature of the chuck. However, it should still be cold enough (with a chuck temperature of −20 °C) to suppress annealing during the irradiation. The outcome of the measurements that have been conducted alternating with irradiations with a bias of 5 V during the irradiation is shown in fig. D.4. The blue curve refers to a sensor from the previous study without any biasing during the irradiation. A difference of the interstrip isolation over reverse bias can be seen. However, the difference is, for example at 600 V comparing the 15 kGy unbiased curve to the others, roughly a factor of 2. This could be a temperature effect because the sensor on the PCB is warmer than a silicon chip directly on the chuck. In any case, the conclusion is that no severe decrease of the interstrip resistance was observed even for a comparably high bias of 5 V.

Why such a weak dependence on the bias is observed in the measurements can be explained by taking a deeper look into the simulated device. The electric field distribution in the sensor with a bias between the AC and DC contact is presented in fig. D.5. In fig. D.5a the 2D device is shown with its electric field distribution. The electric field strength in the coupling oxide is very high because of its small thickness. Also, a smaller electric field below the metal overhang emerges. However, in the major part of the surface, the electric field is not affected by the biasing. How rapidly the electric field decreases towards the middle of the surface is shown in fig. D.5b. This is in contrast to the bias of a MOS structure where the gate covers the whole surface of the device. Therefore, the outcome of irradiation with an oxide bias of MOS

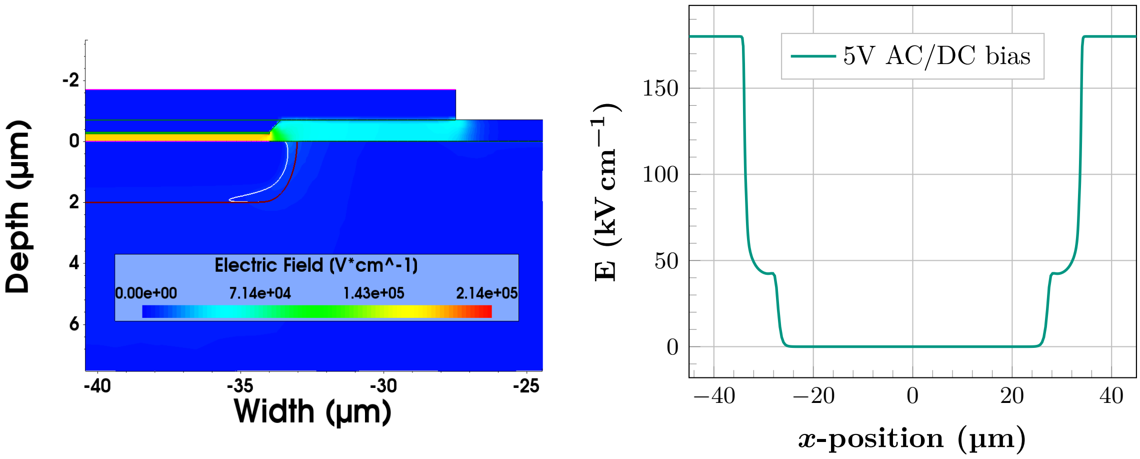

(a) (b)

Figure D.5.: Simulated electric field in the 2D representation of the device with a bias of 5V (a) and a cut 100 nm above the oxide parallel to the surface (b).

devices is not directly translatable to the behaviour of strip sensors. For a strip sensor, the most important region between the strips is in fact not biased during the operation.

D.3.2. Simulated Impact of Bulk Defects during X-Ray Irradiation

In section 8.5.4 it is hypothesised that neutron (and potentially proton) irradiation results in defects in the oxide similar to the bulk defects. These might then be charged up by a following X-ray irradiation. However, it might also be that an electric field in the oxide can enhance the defect generation. The hypothesis is that in case of the neutron irradiation that was followed by the X-ray irradiation, the recombination of radiation-induced electron-hole pairs is suppressed by an electric field that emerges from the bulk defects at the interface. Such a hypothesis is not accessible by measurements that are performed in the scope of this thesis. However, at least the plausibility can be evaluated with the help of simulations.

A strip sensor with different bulk defect concentrations and fixed surface defect concentrations is simulated with floating strip contacts as during standard hadron irradiations. Then, the electric field's y-component E_y is extracted for a cut parallel to the surface, 100 nm below the interface. A comparison of E_y between the different defect configurations is given in fig. D.6. First, the case with pure X-ray related defects according to a dose of 15 kGy (from section 8.4.4) sets the baseline. A small electric field builds up because of the acceptor and donor states in the interface that lead to a space charge, thus electric field. The dashed lines in the plot represent additional neutron and proton defects according to a fluence of $\Phi = 3 \times 10^{14}\,\mathrm{n_{eq}/cm^2}$ in blue and red, respectively. It can be seen that indeed the electric field strength is increased considerably, in case of a higher defect density in the bulk. For an even higher fluence of $\Phi = 6 \times 10^{14}\,\mathrm{n_{eq}/cm^2}$, the electric field increases further for both, neutron and proton defect models. In addition, it can be seen that the electric field with neutron defects is higher. This makes sense because the defect model according to table 8.3 introduces more acceptor states than the proton model (table 8.2). Therefore, the space charge is expected to be slightly higher which increases the electric field.

However, the question arises whether this electric field is able to increase the positive charge concentration at the interface so that the surface charge is enhanced. Although a high electric field in the case of bulk defects seems consistent, it points in the wrong direction. The y-component is positive, which means that positive charge is accelerated in positive direction,

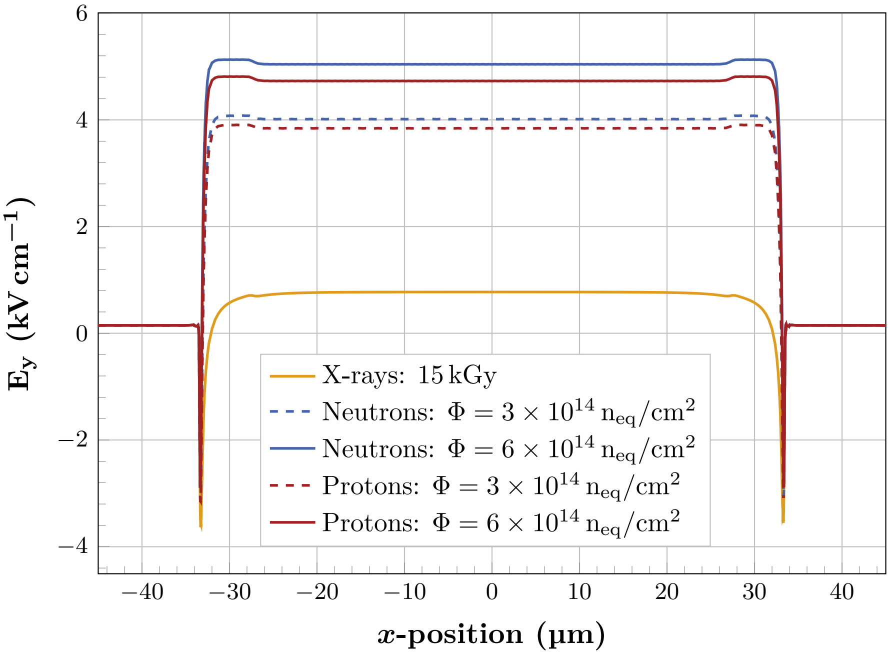

Figure D.6.: Simulated electric field's y component 100 nm below the interface with different defects. Same colours indicate the same particle type with dashed lines for the lower fluence of $\Phi = 3 \times 10^{14}\,n_{eq}/cm^2$ and continuous lines for the higher fluence of $\Phi = 6 \times 10^{14}\,n_{eq}/cm^2$.

thus away from the surface. This cannot explain how a stronger positive charge should be accumulated in the interface region. On the other side of the interface, in the oxide, the electric field is zero because there is no charge gradient and the surface is floating. Since the simulation shows the case of ideal materials, the situation might be different for a real silicon device. Therefore, it might be possible that the presence of bulk defects inside the bulk enhances the defect generation during a subsequent irradiation. However, if this is the case and to what extend is not clear.

D.3.3. Different Oxide Variants for the CMS HGCAL

For the new CMS detector, besides the replacement of the tracker, the calorimetry system will be upgraded. Both, the electromagnetic calorimeter (ECAL) and hadron calorimeter (HCAL) end-caps are replaced with a High Granularity Calorimeter (HGCAL) [CMS17]. Different to the current ECAL and HCAL, the HGCAL will feature silicon sensors in the regions where high fluences are expected to cope with the harsh radiation environment and to obtain a high granularity. These sensors are pad sensors in a hexagonal shape and placed on a wafer with a diameter of 8 inch. The standard size of wafers for the Outer Tracker is 6 inch. Since the pads of the HGCAL sensors are connected in DC mode to the readout chip, initially the standard DC process of the vendor (HPK) was used. Similar to the Outer Tracker, the HGCAL wafers feature some test structures like MOS and GCD but also miniature sensors whose design is close to the PS-p babysensor. A comparison of the interstrip resistance of the different oxide variants is shown in fig. D.7. All sensors have been irradiated with X-rays to a dose of 15 kGy to compare the surface radiation tolerance. Then, the interstrip resistance and capacitance has been measured similarly to the investigations in chapter 8 at $T = -20\,°C$. After a first delivery of the HGCAL wafers, the flat-band voltage extracted from MOS devices was higher

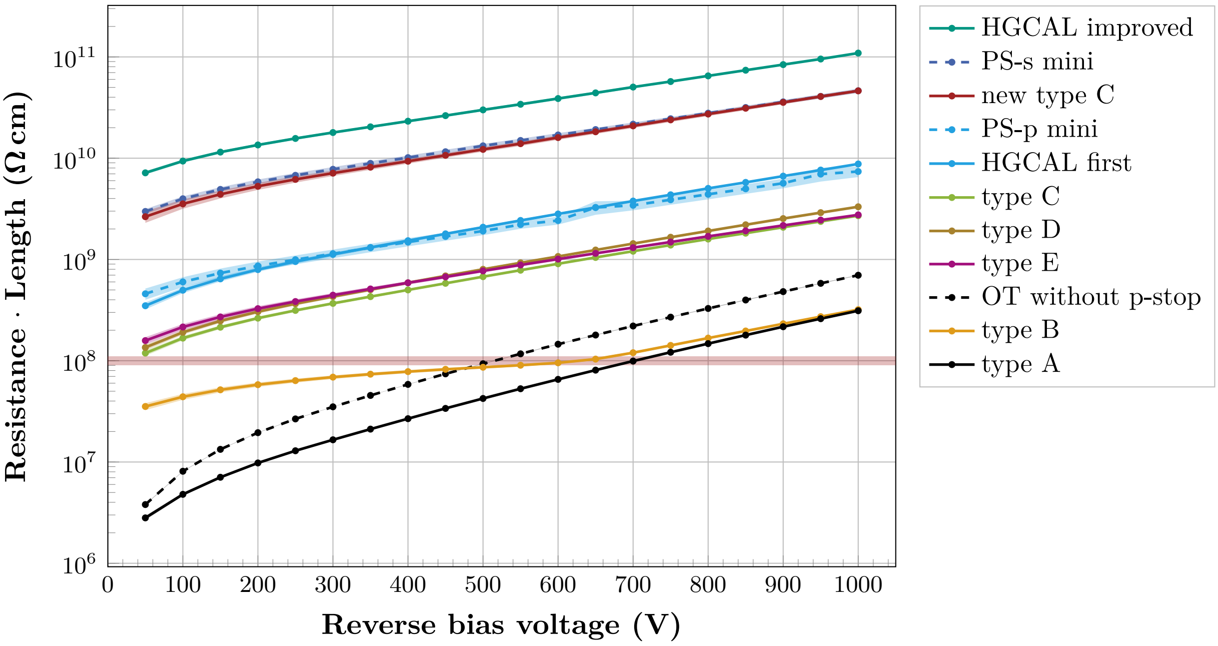

Figure D.7.: Interstrip resistance in dependence on the reverse bias voltage for different oxide types after X-ray irradiation to a dose of 15 kGy. Samples related to HGCAL test wafers are represented by continuous lines and CMS Outer Tracker wafers with dashed lines.

compared to typical values of the Outer Tracker wafers. It can be seen that the measurement of the sensor of the DC processed 8 inch wafer is close to the measurement of the PS-p test sensor that is the same process but on a 6 inch wafer. There is no clear limit for the interstrip resistance in case of the HGCAL but the generic limit from chapter 8 is indicated to guide the eye. Since there is no clear specification, the goal is to achieve the best-possible oxide quality, similar to what has been achieved for the Outer Tracker wafers with an AC process. Therefore, a better oxide quality has been requested to the vendor. Then, the vendor set up a process, similar to the 6 inch AC process of the Outer Tracker wafers. This already improved the oxide quality a lot and results in the highest interstrip resistance in the plot. Additionally, the vendor took the opportunity to try out different procedures where the final oxide variants are then simply labelled A to E. Unfortunately, the details of the difference between these variants are not known, because they belong to the vendors trade secrets. From the plot it can be seen that there is no noticeably difference between the variants C, D and E. However, a significantly lower interstrip resistance is observed for the types A and B. As a comparison, a measurement of an Outer Tracker sensor without a p-stop is inserted in the figure. It shows a higher interstrip resistance than A and at least from 500 V onwards than B. Therefore, these two oxide processes can be excluded. Finally, the vendor tried to improve the type C variant to a new type C variant that results in an interstrip resistance which is similar to the PS-s babysensor.

The interstrip capacitance has been measured as well. The results are presented in fig. D.8. The capacitance is normalised to the strip length but the slight differences in the geometry and the fact that some sensors are AC and some DC coupled cannot be cancelled out. Therefore, the outcome should be interpreted qualitatively in terms of shape and offsets should be neglected. The usual shape is that the capacitance increases for bias voltages below the depletion voltage but than stays constant. In some cases like for the A and B type the shape is not as expected,

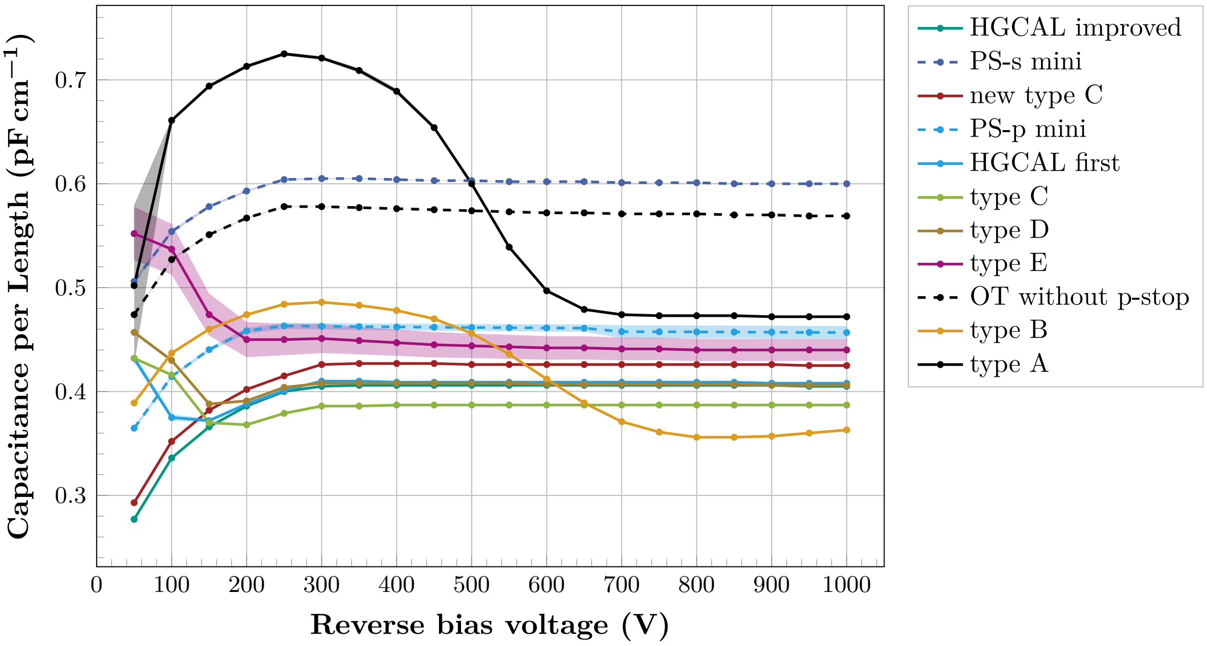

Figure D.8.: Interstrip capacitance in dependence on the reverse bias voltage for different oxide types after X-ray irradiation to a dose of 15 kGy. Samples related to HGCAL test wafers are represented by continuous lines and CMS wafers with dashed lines.

since it increases a lot first but then stays nearly constant around 700 V. Also the type C, D and E show an unexpected behaviour where the capacitance decreases first but reaches a constant region at around 300 V as well.

The conclusion of these investigation of the interstrip resistance and capacitance is that the oxide variants A and B should not be considered further. Type C, D and E are slightly better but still less convincing than the standard material of the Outer Tracker. The best-suited oxide processes in terms of interstrip parameters is the oxide process after the first improvement and the new type C from the HGCAL 8 inch wafers.

D.3.4. Impact of Charge Multiplication on the Interstrip Resistance

When an ionising particle traverses the silicon sensor, electron-hole pairs are generated. If these enter a high electric field region, they might get a sufficiently high kinetic energy to generate new electron-holes pairs themselves. Such avalanche or charge multiplication (CM) effects can be observed for heavily irradiated silicon sensors under certain circumstances [Cas10] However, many details are yet to be found. These avalanche effects can be problematic for the sensors, because they can induce local breakdowns, which might harm the sensor irreversible. It is also possible to make use of such effects, for example in case of avalanche photodiodes (APDs) or low gain avalanche detectors (LGADs). Here, the working principle is that the initial signal strength is very small. Thus, it is possible to multiply the number of electron-hole pairs, therefore signal strength, in specific high field regions to detect particles.

For the previous investigation in chapter 8 charge multiplication effects were not considered in the simulations. This is because even after long annealing times and with higher bias voltages than 1000 V no decreasing interstrip resistance, which could be an indicator of avalanche effects, has been observed up to $6 \times 10^{14}\,\mathrm{n_{eq}/cm^2}$. Also during the irradiation tests in chapter 7, no hint of charge multiplication effects has been found for the investigated fluences of up

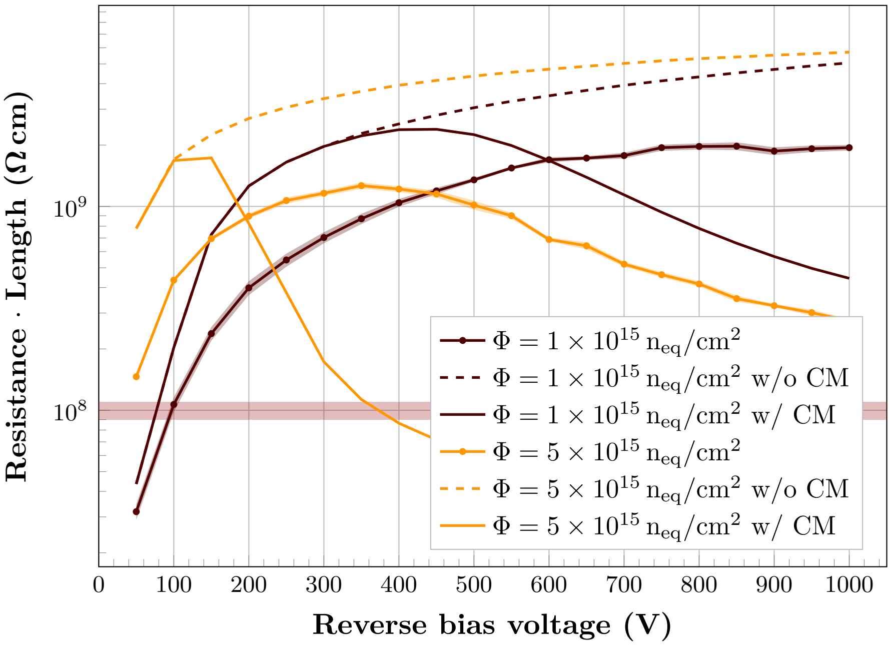

Figure D.9.: Interstrip resistance curves for high proton fluences where charge multiplication might become relevant. This is reflected by a decreasing interstrip resistance for increasing bias voltage which cannot be explained differently. The simulated curves (indicated by lines without data points) where charge multiplication is activated are labelled with CM.

to $1.1 \times 10^{15}\,\mathrm{n_{eq}/cm^2}$. To investigate the behaviour of the strip isolation of strip sensors without interstrip isolation implant at higher fluences than the ones in chapter 8, two sensors were irradiated with protons to fluences of $1 \times 10^{15}\,\mathrm{n_{eq}/cm^2}$ and $5 \times 10^{15}\,\mathrm{n_{eq}/cm^2}$. Respective measurements and the comparison to simulated curves are shown in fig. D.9. First of all, the measurements show that some effect that reduces the interstrip resistance for high fluences occurs at least for $5 \times 10^{15}\,\mathrm{n_{eq}/cm^2}$. The fluence of $5 \times 10^{15}\,\mathrm{n_{eq}/cm^2}$ is higher than the validated fluence range for the proton defect model [Ebe13]. Nevertheless, it is used as a best guess and the results are indicated with the dashed lines. In addition, the model according to [VD70] is used to emulate charge multiplication effects. Qualitatively, as can be seen in fig. D.9, the charge multiplication effects indeed decrease the interstrip resistance in the simulation. However, the effect seems to be overestimated for both fluences but even stronger for the higher fluence of $5 \times 10^{15}\,\mathrm{n_{eq}/cm^2}$.

Avalanche effects are closely connected to the details of the electric field in the surface region. Therefore, even small differences in the simulations and the physical device can result in more significant differences of the simulated and measured macroscopic interstrip resistance. Following the explanations in section 8.3.3 and section 8.5.3, a stronger electric field in the surface region results in a higher interstrip resistance. Therefore, the hypothesis that the avalanche effect is overestimated because the electric field in the simulations is higher than in the physical device is consistent with the fact that the interstrip resistance is overestimated if charge multiplication is not activated. However, further investigations would be required in order to resolve the matter.

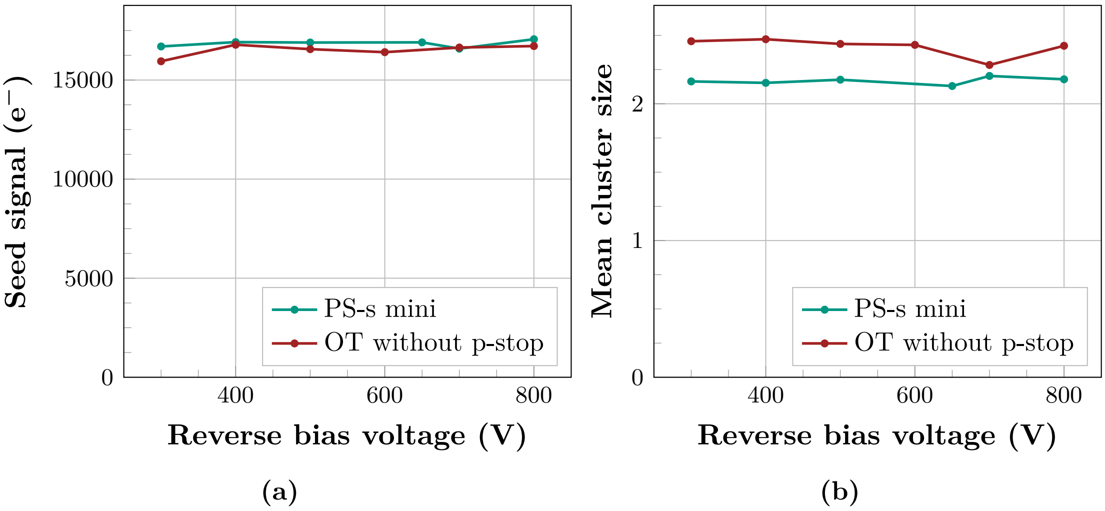

Figure D.10.: Seed signal (a) and cluster size (b) of two sensors with different strip isolation measures. One features a p-stop implant and the other one does not have any specific implant.

D.3.5. Sufficient Interstrip Resistance in Terms of Charge Collection

The studies about the interstrip resistance are a qualitative investigation of the surface properties and the influence of surface and especially bulk defects. The conservative limit of $1 \times 10^8\,\Omega\,\mathrm{cm}$ for a sufficient interstrip resistance is just a rough estimation based on the bias resistance. To validate that this limit holds, charge collection measurements have been performed on the PS-s babysensor and the sensor without p-stop, whose interstrip resistances after X-ray irradiation are shown in fig. D.7. For these two, the interstrip resistance spreads over a wide range from below $1 \times 10^7\,\Omega\,\mathrm{cm}$ up to $1 \times 10^{11}\,\Omega\,\mathrm{cm}$ depend on the sensor and the bias potential. The seed signal of these two sensors is presented in fig. D.10a. The minimum reverse bias voltage is chosen such that the sensors are depleted (around 300 V) to obtain reliable and realistic charge collection results. It can be seen that although for both sensor the interstrip resistance in fig. D.7 changes severely, this does not seem to have an impact on the charge collection. The seed signal of the sensors without a p-stop implant is partly slightly lower but below the resolution of around $1000\,\mathrm{e}^-$. The cluster signal, that is not plotted here, is also similar for both sensors independent on the bias voltage. A comparison of the mean cluster size that determines how much the signal spreads among the strips, is given in fig. D.10b. It can be seen that the cluster size of the sensor without a p-stop with the lower interstrip resistance shows broader clusters. This is consistent with the expectation due to the worse strip isolation and the slightly lower seed signal in fig. D.10a. However, this does not seem to affect the signal strength severely so that a particle detection is still be possible without any issues.

On the one hand, an estimation of a lower limit for the interstrip isolation was not successful. On the other hand, this is a result of the excellent oxide quality which leads to a relatively high interstrip resistance even without any strip isolation implant and after X-ray irradiation for reasonable bias voltages. Nevertheless, it is shown that the conservative approximation holds. Even with an interstrip resistance value of $3 \times 10^7\,\Omega\,\mathrm{cm}$, as for the sensor without p-stop implant at 300 V, the sensor is fully functional.

List of Figures

2.1. The CERN accelerator complex 6
2.2. Illustration of an Higgs-like event 6
2.3. Illustration of the Compact Muon Solenoid (CMS) detector 7
2.4. Slice of the CMS detector 9
2.5. New Phase-2 tracker design 11
2.6. Outer Tracker modules in Phase-2 12
2.7. Stub finding mechanism of p_T-modules 13
2.8. Expected fluence distribution of the tracker in Phase-2 14
2.9. TID distribution of the tracker in Phase-2 14
2.10. Particle fraction during Phase-2 in the CMS tracker 15

3.1. Band scheme of different materials 18
3.2. Illustration of doping 19
3.3. Float zone and Czochralski growth method 21
3.4. Example of lithography 21
3.5. The pn-Junction 22
3.6. Plot of the Bethe equation 25
3.7. Interactions of electrons in lead 26
3.8. Realistic energy loss in thin silicon layers 27
3.9. Working principle of a silicon strip sensor 28
3.10. Silicon sensor design for Phase-2 of CMS 29
3.11. Weighting field of a strip sensor 29

4.1. Radiation-induced defects in the crystal lattice 32
4.2. Simulated damage of neutrons and protons 32
4.3. Displacement damage function dependent on the energy 33
4.4. Defect locations in the band scheme 35
4.5. Macroscopic impact of defects 36
4.6. Leakage current increase with increasing fluence 37
4.7. Type inversion of n-doped substrates due to radiation damage 38
4.8. Signal of n-type and p-type sensors after irradiation 39
4.9. Annealing of the leakage current 40
4.10. Annealing impact on the effective doping concentration 41
4.11. Schematic illustration of surface defects 42
4.12. Example of interface traps 43
4.13. Example of an E' centre 44
4.14. Surface defect generation mechanism 45
4.15. Fraction of unrecombined holes in the oxide by ionising radiation 46

5.1. $I(V)$ and $C(V)$ characteristics of a diode 50
5.2. Working principle of a MOS capacitor 52
5.3. $C(V)$ characteristics of a p-type and an n-type MOS capacitor 54
5.4. Working principle of a GCD structure 55
5.5. Extraction of the surface current from a GCD 55

6.1. Interior of the probe station 58
6.2. Temperature on the probe station chuck 59

6.3. ALiBaVa setup at ETP 60
6.4. Noise and gain per strip 62
6.5. Timing of cluster signal 63
6.6. Seed signal distribution 64
6.7. Proton irradiation setup at KAZ 65
6.8. Beam spot profile of the X-ray tube 66
6.9. X-ray setup at ETP 67
6.10. Workflow of the Sentaurus device simulation 68
6.11. Trap implementation in sentaurus 69

7.1. Structures of the 2S wafer 75
7.2. Quality assurance strategy for the CMS Outer Tracker sensor production . . . 76
7.3. Fluence distribution of Phase-2 Outer Tracker modules 77
7.4. Irradiation test structure half-moon 78
7.5. Temperature dependence of the leakage current 83
7.6. Damage rate over batch and wafer numbers 85
7.7. Seed signal at 600 V 90
7.8. Seed and cluster signal of sensors with different pitch 91
7.9. Cluster size of signal measurements 91
7.10. Seed signal at 600 V for neutron and proton irradiation 92
7.11. Method to extract the flat-band voltage during the pre-production and production 94
7.12. Flat-band voltage of MOS capacitors prior to irradiation 96
7.13. Surface generation velocity prior to irradiation 98
7.14. Flat-band voltage after X-ray irradiation 99
7.15. Surface generation velocity after X-ray irradiation 100
7.16. Change of MOS measurements after irradiation 101
7.17. Measurements after the specific MOS treatment 102
7.18. Determination of the best suited x_{dist} value 104
7.19. Flat-band voltage after irradiation and specific treatment for the pre-production 105
7.20. Surface generation velocity after irradiation and annealing for the pre-production 106
7.21. Correlation plot of the flat-band voltage pre and after irradiation 107
7.22. Correlation plots of flat-band voltage pre and after irradiation 108

8.1. P-stop and p-spray implementations 110
8.2. Electric field dependent on the p-stop doping concentration and proton fluence 110
8.3. Interstrip resistance measurement procedure 112
8.4. Simulated device 113
8.5. Simulated device with mesh 114
8.6. Interstrip resistance before irradiation 115
8.7. Electric field's x and y-components with different bias potential 116
8.8. Impact of the doping concentration on the interstrip resistance derived from simulations. 117
8.9. Simulated electric field's x and y-components with different doping concentrations 118
8.10. Interstrip resistance after X-ray irradiation 119
8.11. Impact of fixed positive charge on the Interstrip Resistance 119
8.12. Impact of interface trap types on the interstrip resistance 121
8.13. Comparison of measurements and simulations after X-ray irradiation 122
8.14. Optimised defect concentrations after X-ray irradiation 123
8.15. Interstrip resistance after hadron irradiation 124

8.16. Comparison of neutron to X-ray irradiation with $\Phi = 1 \times 10^{14}\,\mathrm{n_{eq}/cm^2}$ and 1 kGy applied dose 125
8.17. Impact of bulk defects on the interstrip resistance 127
8.18. Comparison of electric fields with bulk and surface defects derived from simulations 127
8.19. Replication of interstrip resistance measurements after neutron and proton irradiation 128
8.20. Interstrip resistance in dependence of the irradiation sequence 129

A.1. Working principle of an n-type MOS capacitor 139

B.1. Exterior of the probe station 141

C.1. Design file of the PS-s wafer 143
C.2. Design file of the PS-p wafer 144

D.1. Example of an optimisation configuration 150
D.2. Scheme of the X-ray irradiation board during measurements 152
D.3. Board for a biased oxide during X-ray irradiations 152
D.4. Interstrip resistance after irradiation with a biased oxide 153
D.5. Electric field in a surface biased configuration 154
D.6. Simulated electric field's y-component close to the surface with bulk defects . 155
D.7. Interstrip resistance for different oxide processes after X-ray irradiation 156
D.8. Interstrip capacitance for different oxide processes after X-ray irradiation . . . 157
D.9. Simulated and measured interstrip resistance with higher proton fluences . . . 158
D.10. Charge collection measurements on two sensors with different interstrip resistance 159

List of Tables

7.1. Stations that test structures for hadron irradiation tests pass through 79
7.2. Measurement settings of the $I(V)$ and $C(V)$ characteristics of diodes pre irradiation. 80
7.3. Results of the strip scans pre irradiation 81
7.4. Measurement settings of the leakage current and capacitance measurements on sensors after irradiation 86
7.5. Results of the strip scans after irradiation 87
7.6. Annealing steps during pre production 88
7.7. Annealing steps during production 89
7.8. Results of the strip scans after annealing 93
7.9. Stations that test structures for X-ray irradiation tests pass through 93
7.10. Measurement settings of the MOS and GCD structure pre irradiation 94
7.11. Specific treament for X-ray irradiated MOS capacitors 102
7.12. Measurement settings of the MOS and GCD structure after irradiation 103

8.1. Interface trap defect model 120
8.2. Bulk defect model for proton irradiation 126
8.3. Bulk defect model for neutron irradiation 126

Bibliography

[Ada+17] W. Adam et al. *P-Type Silicon Strip Sensors for the new CMS Tracker at HL-LHC.* In: Journal of Instrumentation 12.06 (2017), P06018–P06018. DOI: `10.1088/1748-0221/12/06/p06018` (cited on pp. 39, 109).

[Ada+20] W. Adam et al. *Beam test performance of prototype silicon detectors for the Outer Tracker for the Phase-2 Upgrade of CMS.* In: Journal of Instrumentation 15.03 (Mar. 2020), P03014–P03014. DOI: `10.1088/1748-0221/15/03/p03014` (cited on p. 13).

[ASI07] ASIC Labor Heidelberg. *Beetle - a readout chip for LHCb.* 2007. URL: `http://www.kip.uni-heidelberg.de/lhcb/index.html` (visited on 07/28/2021) (cited on p. 59).

[ATL12] ATLAS Collaboration. *Observation of a new particle in the search for the Standard Model Higgs boson with the ATLAS detector at the LHC.* In: Physics Letters B 716.1 (Sept. 2012), pp. 1–29. DOI: `10.1016/j.physletb.2012.08.020` (cited on p. 3).

[Bar+94] E. Barberis et al. *Capacitances in silicon microstrip detectors.* In: Nucl. Instrument. Meth. A 342.1 (1994), pp. 90–95. ISSN: 0168-9002. DOI: `https://doi.org/10.1016/0168-9002(94)91414-1` (cited on p. 50).

[Bar09] A. R. Barron. *Composition and Photochemical Mechanisms of Photoresists.* In: OpenStax CNX (2009). URL: `http://cnx.org/contents/2997481b-ecd7-4e38-9465-677d8adbe0ad@2` (cited on p. 21).

[Böh+14] T. Böhlen et al. *The FLUKA Code: Developments and Challenges for High Energy and Medical Applications.* In: Nuclear Data Sheets 120 (2014), pp. 211–214. ISSN: 0090-3752. DOI: `https://doi.org/10.1016/j.nds.2014.07.049` (cited on p. 13).

[Bra+00] S. Braibant et al. *Investigation of design parameters and choice of substrate resistivity and crystal orientation for the CMS silicon microstrip detector.* Feb. 2000. URL: `http://cds.cern.ch/record/687211` (cited on p. 50).

[Cas10] G. Casse. *Charge multiplication in highly irradiated planar silicon sensors.* In: PoS (Vertex 2010) (Jan. 2010). DOI: `10.22323/1.113.0020` (cited on p. 157).

[CERa] CERN. *Detecting Muons.* URL: `http://cms.cern/detector/detecting-muons` (visited on 03/17/2020) (cited on p. 8).

[CERb] CERN. *Energy of Electrons and Photons (ECAL).* URL: `http://cms.cern/detector/measuring-energy/energy-electrons-and-photons-ecal` (visited on 03/17/2020) (cited on p. 8).

[CERc] CERN. *Energy of Hadrons (HCAL).* URL: `https://cms.cern/detector/measuring-energy/energy-hadrons-hcal` (visited on 03/17/2020) (cited on p. 8).

[CERd] CERN. *LHC Report: Another run is over and LS2 has just begun...* URL: `https://home.cern/news/news/accelerators/lhc-report-another-run-over-and-ls2-has-just-begun` (visited on 04/08/2021) (cited on p. 10).

[CERe] CERN. *The High Luminosity LHC Project.* URL: `https://hilumilhc.web.cern.ch/` (visited on 03/17/2020) (cited on p. 10).

[CERf] CERN. *Tracking.* URL: `http://cms.cern/detector/identifying-tracks` (visited on 03/17/2020) (cited on p. 8).

[Chi13] A. Chilingarov. *Generation current temperature scaling.* Tech. rep. Lancaster University, UK, Jan. 30, 2013. URL: `https://cds.cern.ch/record/1511886` (cited on pp. 37, 82).

[CMSa] CMS Collaboration. *Process Quality Control Specifications.* Tech. rep. (CMS intern). Geneva. URL: `https://edms.cern.ch/ui/#!master/navigator/document?D:100558268:100558268:subDocs` (cited on p. 76).

[CMSb] CMS Collaboration. *Selection of the silicon sensor thickness for the Phase-2 upgrade of the CMS Outer Tracker.* (CERN intern). URL: `https://cms.cern.ch/iCMS/user/noteinfo?cmsnoteid=CMS%20NOTE-2021/008` (visited on 10/01/2021) (cited on pp. 77, 89).

[CMSc] CMS Collaboration. *Sensor Quality Control Specifications.* Tech. rep. (CMS intern). Geneva. URL: `https://edms.cern.ch/ui/#!master/navigator/document?D:100557701:100557701:subDocs` (cited on pp. 74, 76).

[CMS12] CMS Collaboration. *Observation of a new boson at a mass of 125 GeV with the CMS experiment at the LHC.* In: Physics Letters B 716.1 (2012), pp. 30–61. DOI: `10.1016/j.physletb.2012.08.021` (cited on p. 3).

[CMS17] CMS Collaboration. *The Phase-2 Upgrade of the CMS Endcap Calorimeter.* Tech. rep. Geneva: CERN, Nov. 2017. URL: `https://cds.cern.ch/record/2293646` (cited on p. 155).

[CMS18] CMS Collaboration. *The Phase-2 Upgrade of the CMS Tracker.* Tech. rep. CERN-LHCC-2017-009. CMS-TDR-014. CERN, Apr. 16, 2018. URL: `https://cds.cern.ch/record/2272264` (cited on pp. 10–12, 14).

[Dal+14] R. Dalal et al. *Combined effect of bulk and surface damage on strip insulation properties of proton irradiated n^+-p silicon strip sensors.* In: Journal of Instrumentation 9.04 (Apr. 2014), P04007–P04007. DOI: `10.1088/1748-0221/9/04/p04007` (cited on pp. 111, 125).

[Dav16] S. R. Davis. *Interactive Slice of the CMS detector.* 2016. URL: `https://cds.cern.ch/record/2205172` (cited on p. 9).

[Dea80] B. E. Deal. *Standardized terminology for oxide charges associated with thermally oxidized silicon.* In: IEEE Transactions on Electron Devices 27.3 (Mar. 1980), pp. 606–608. ISSN: 1557-9646. DOI: `10.1109/T-ED.1980.19908` (cited on p. 43).

[Die13] A. Dierlamm. *Planar sensors for future Vertex and Tracking Detectors.* In: PoS Vertex (2013), p. 027. DOI: `10.22323/1.198.0027` (cited on p. 39).

[Ebe13] R. Eber. *Investigations of new Sensor Designs and Development of an effective Radiation Damage Model for the Simulation of highly irradiated Silicon Particle Detectors.* PhD thesis. Karlsruher Institut für Technologie (KIT), Nov. 29, 2013. DOI: `10.5445/IR/1000038403` (cited on pp. 109, 125, 126, 158).

[ETPa] ETP. *Calculation of current-related equivalent annealing time of irradiated silicon sensors.* URL: `https://annealing.cms-ka.fzk.de/` (visited on 10/02/2021) (cited on p. 88).

[ETPb] ETP. *ETP Proton Irradiation.* URL: `https://www.etp.kit.edu/english/264.php` (visited on 07/26/2021) (cited on pp. 64, 65).

[Fer+05] A. Ferrari et al. *FLUKA: A multi-particle transport code (Program version 2005).* Tech. rep. Oct. 2005. DOI: `10.2172/877507` (cited on p. 13).

[Fis20] R. Fischer. *Bestrahlungstests an Siliziumstreifensensoren für das Phase-2-Upgrade des CMS-Spurdetektors.* Bachelor Thesis. 2020. URL: `https://publish.etp.kit.edu/record/22036` (cited on p. 86).

[Fle92] D. M. Fleetwood. *'Border traps' in MOS devices.* In: IEEE Transactions on Nuclear Science 39.2 (Apr. 1992), pp. 269–271. ISSN: 1558-1578. DOI: `10.1109/23.277495` (cited on p. 44).

[Fre+02] E. Fretwurst et al. *Radiation damage in silicon detectors caused by hadronic and electromagnetic irradiation.* In: *Radiation effects on semiconductor materials, detectors and devices. Proceedings, 4th International Conference, RESMDD'02, Florence, Italy, July 10-12, 2002.* 2002. arXiv: `physics/0211118 [physics]` (cited on pp. 33, 38).

[Fur06] A. Furgeri. *Quality Assurance and Irradiation studies on CMS silicon strip sensors.* PhD Thesis. Universität Karlsruhe (TH), 2006. URL: `https://publish.etp.kit.edu/record/21628` (cited on p. 64).

[Gos18] J.-O. Gosewisch. *Irradiation Studies of Charge Collection and Interstrip Resistance of Silicon Strip Sensors in the Course of the CMS Phase-2 Upgrade.* Master Thesis. Karlsruhe Institute of Technology (KIT), 2018. URL: `https://publish.etp.kit.edu/record/21516` (cited on pp. 66, 73, 90, 109).

[Gut+12] M. Guthoff et al. *Geant4 simulation of a filtered X-ray source for radiation damage studies.* In: Nucl. Instrument. Meth. A 675 (2012), pp. 118–122. ISSN: 0168-9002. DOI: `10.1016/j.nima.2012.01.029` (cited on p. 66).

[Gut15] M. Guthoff. *1-D plot of FLUKA simulated 1MeV neutron equivalent in Silicon at the Tracker.* June 29, 2015. URL: `https://twiki.cern.ch/twiki/bin/view/CMSPublic/BRILRS1D1MeVneqAtTracker` (cited on p. 15).

[Har17] F. Hartmann. *Evolution of Silicon Sensor Technology in Particle Physics.* 2nd ed. Springer, Nov. 3, 2017. ISBN: 978-3-319-64434-9. DOI: `10.1007/978-3-319-64436-3` (cited on pp. 21, 23, 26, 28–30, 32, 36, 40, 52, 109, 110, 139).

[Hen06a] M. A. Henning. *Dotierung im zweidimensionalen Siliziumkristallgitter mit Aluminium.* Jan. 2006. URL: `https://upload.wikimedia.org/wikipedia/commons/0/0d/Schema_-_p-dotiertes_Silicium.svg` (visited on 10/03/2021) (cited on p. 19).

[Hen06b] M. A. Henning. *Dotierung im zweidimensionalen Siliziumkristallgitter mit Phosphor.* Jan. 2006. URL: `https://upload.wikimedia.org/wikipedia/commons/2/22/Schema_-_n-dotiertes_Silicium.svg` (visited on 10/03/2021) (cited on p. 19).

[HP94] C. R. Helms and E. H. Poindexter. *The silicon-silicon dioxide system: Its microstructure and imperfections.* In: Reports on Progress in Physics 57.8 (Aug. 1994), pp. 791–852. DOI: `10.1088/0034-4885/57/8/002` (cited on p. 43).

[Huh02] M. Huhtinen. *Simulation of non-ionising energy loss and defect formation in silicon.* In: Nucl. Instrument. Meth. A 491.1 (2002), pp. 194–215. ISSN: 0168-9002. DOI: `https://doi.org/10.1016/S0168-9002(02)01227-5` (cited on p. 32).

[Kit13] C. Kittel. *Einführung in die Festkörperphysik.* De Gruyter Oldenbourg, 2013. 776 pp. ISBN: 3486597558 (cited on p. 17).

[KS84] K. Kölbig and B. Schorr. *A program package for the Landau distribution.* In: Computer Physics Communications 31.1 (1984), pp. 97–111. ISSN: 0010-4655. DOI: `https://doi.org/10.1016/0010-4655(84)90085-7` (cited on p. 63).

[LC98] P. Lenahan and J. Conley. *What can electron paramagnetic resonance tell us about the Si/SiO2 system?* English (US). In: Journal of Vacuum Science and Technology B: Microelectronics and Nanometer Structures 16.4 (July 1998), pp. 2134–2153. ISSN: 1071-1023. DOI: `10.1116/1.590301` (cited on p. 43).

[Len07] P. Lenahan. *Deep level defects involved in MOS device instabilities.* In: Microelectronics Reliability 47 (June 2007), pp. 890–898. DOI: `10.1016/j.microrel.2006.10.016` (cited on pp. 43, 44).

[Lin+01] G. Lindström et al. *Radiation hard silicon detectors—developments by the RD48 (ROSE) collaboration.* In: Nucl. Instrument. Meth. A 466.2 (2001). 4th Int. Symp. on Development and Application of Semiconductor Tracking Detectors, pp. 308–326. ISSN: 0168-9002. DOI: `https://doi.org/10.1016/S0168-9002(01)00560-5` (cited on p. 33).

[Löc06] S. Löchner. *Development, Optimisation and Characterisation of a Radiation Hard Mixed-Signal Readout Chip for LHCb.* PhD thesis. Universität Heidelberg, 2006. URL: `http://www.kip.uni-heidelberg.de/lhcb/Publications/diss_loechner.pdf` (cited on p. 63).

[Man+04] I. Mandić et al. *Bulk damage in DMILL npn bipolar transistors caused by thermal neutrons versus protons and fast neutrons.* In: IEEE Trans. Nucl. Sci. 51 (2004). Ed. by J. Dufey, pp. 1752–1758. DOI: `10.1109/TNS.2004.832927` (cited on p. 65).

[Met20] M. Metzler. *Irradiation studies on n-in-p silicon strip sensors in the course of the CMS Phase-2 Outer Tracker Upgrade.* PhD thesis. Karlsruhe Institute of Technology (KIT), 2020. DOI: `10.5445/IR/1000105663` (cited on pp. 63, 73).

[Mob19] E. Mobs. *The CERN accelerator complex - 2019. Complexe des accélérateurs du CERN - 2019.* In: (July 2019). General Photo. URL: `https://cds.cern.ch/record/2684277` (cited on p. 6).

[Mol99] M. Moll. *Radiation Damage in Silicon Particle Detectors.* PhD thesis. University of Hamburg, 1999. URL: `https://mmoll.web.cern.ch/mmoll/thesis/` (cited on pp. 35, 37, 40, 41, 83, 84, 88).

[Mos+17] F. Moscatelli et al. *Effects of Interface Donor Trap States on Isolation Properties of Detectors Operating at High Luminosity LHC (HL-LHC).* In: IEEE Transactions on Nuclear Science PP (May 2017), pp. 1–1. DOI: `10.1109/TNS.2017.2709815` (cited on pp. 118, 120).

[MT12] T. Mc Cauley and L. Taylor. *CMS Higgs Search in 2011 and 2012 data: candidate ZZ event (8 TeV) with two electrons and two muons: 3D perspective, r-phi and r-z views.* CMS Collection. July 2012. URL: `https://cds.cern.ch/record/1606502` (cited on p. 6).

[MT93] K. Misiakos and D. Tsamakis. *Accurate measurements of the silicon intrinsic carrier density from 78 to 340 K.* In: Journal of Applied Physics 74 (Jan. 1993), p. 3293. ISSN: 00218979. DOI: `10.1063/1.354551` (cited on p. 95).

[Mül+21] J.-O. Müller-Gosewisch et al. *Influence of surface damage and bulk defects on the interstrip isolation of p-type silicon strip sensors.* In: Journal of Instrumentation 16.07 (July 2021), P07004. DOI: `10.1088/1748-0221/16/07/p07004` (cited on p. 130).

[Nic+02] C. J. Nicklaw et al. *The structure, properties, and dynamics of oxygen vacancies in amorphous SiO_2.* In: IEEE Transactions on Nuclear Science 49.6 (Dec. 2002), pp. 2667–2673. ISSN: 1558-1578. DOI: `10.1109/TNS.2002.805408` (cited on p. 43).

[NIS] NIST. *stopping-power and range tables for protons.* URL: `https://physics.nist.gov/PhysRefData/Star/Text/PSTAR.html` (visited on 10/03/2021) (cited on p. 64).

[Nis71] Y. Nishi. *Study of Silicon-Silicon Dioxide Structure by Electron Spin Resonance I.* In: Japanese Journal of Applied Physics 10.1 (Jan. 1971), pp. 52–62. DOI: `10.1143/jjap.10.52` (cited on p. 42).

[Oli+14] K. Olive et al. *Review of Particle Physics.* In: Chinese Physics C 38.9 (2014), p. 090001. URL: `http://stacks.iop.org/1674-1137/38/i=9/a=090001` (cited on p. 26).

[Per11] H. Perrey. *Jets at Low Q2 at HERA and Radiation Damage Studies for Silicon Sensors for the XFEL.* en. PhD thesis. DESY, 2011. URL: `http://www-library.desy.de/cgi-bin/showprep.pl?desy-thesis-11-021` (cited on p. 55).

[PGP14] H. Przewlocki, T. Gutt, and K. Piskorski. *The inflection point of the capacitance-voltage, C(VG), characteristic and the flat-band voltage of metal-oxide-semiconductor structures.* In: Journal of Applied Physics 115 (May 2014), p. 204510. DOI: `10.1063/1.4880399` (cited on p. 53).

[Poi+81] E. H. Poindexter et al. *Interface states and electron spin resonance centers in thermally oxidized (111) and (100) silicon wafers.* In: Journal of Applied Physics 52.2 (1981), pp. 879–884. DOI: `10.1063/1.328771`. eprint: `https://doi.org/10.1063/1.328771` (cited on p. 42).

[Poi+84] E. H. Poindexter et al. *Electronic traps and Pb centers at the Si/SiO2 interface: Band-gap energy distribution.* In: Journal of Applied Physics 56.10 (1984), pp. 2844–2849. DOI: `10.1063/1.333819` (cited on p. 42).

[PP10] K. Piskorski and H. Przewlocki. *The methods to determine flat-band voltage VFB in semiconductor of a MOS structure.* In: The 33rd International Convention MIPRO (Jan. 2010), pp. 37–42 (cited on p. 94).

[Pri16] M. Printz. *Development of radiation-hard n-in-p type silicon detectors and studies on modules with transverse momentum discrimination for the CMS detector at the LHC.* PhD thesis. Karlsruher Institut für Technologie (KIT), 2016. DOI: `10.5445/IR/1000052766` (cited on pp. 109, 110, 125).

[Pyt] Python Software Foundation. *Official Python website.* URL: `https://www.python.org/` (visited on 09/03/2021) (cited on pp. 57, 95).

[Rad20] V. Radeka. *Signal Processing for Particle Detectors.* Sept. 2020, pp. 439–484. ISBN: 978-3-030-35317-9. DOI: `10.1007/978-3-030-35318-6_10` (cited on p. 29).

[Ram39] S. Ramo. *Currents Induced by Electron Motion.* In: Proceedings of the IRE 27.9 (1939), pp. 584–585. DOI: `10.1109/jrproc.1939.228757` (cited on p. 28).

[Ras21] Raspberry Pi Foundation. *Raspberry Pi Website.* 2021. URL: `https://www.raspberrypi.org/` (visited on 07/28/2021) (cited on p. 57).

[Rho21] Rhode Island Nuclear Science Center. *The Rhode Island Nuclear Science Center.* Sept. 3, 2021. URL: `http://www.rinsc.ri.gov/` (cited on p. 78).

[Rut11] E. Rutherford. *The scattering of α and β particles by matter and the structure of the atom.* In: The London, Edinburgh, and Dublin Philosophical Magazine and Journal of Science 21.125 (1911), pp. 669–688. DOI: `10.1080/14786440508637080` (cited on p. 3).

[Rya+10] J. Ryan et al. *Recovery-Free Electron Spin Resonance Observations of NBTI Degradation*. In: IEEE International Reliability Physics Symposium Proceedings (June 2010), pp. 43–49. DOI: `10.1109/IRPS.2010.5488854` (cited on p. 43).

[Sak19] T. Sakuma. *Cutaway diagrams of CMS detector*. May 2019. URL: `https://cds.cern.ch/record/2665537` (cited on p. 7).

[Sch+08] J. Schwank et al. *Radiation effects in MOS oxides*. In: Nuclear Science, IEEE Transactions on 55 (Sept. 2008), pp. 1833–1853. DOI: `10.1109/TNS.2008.2001040` (cited on pp. 45, 46).

[Sch19] D. Schell. *Development of a Macro-Pixel sensor for the Phase-2 Upgrade of the CMS experiment*. PhD thesis. Karlsruhe Institute of Technology (KIT), 2019. DOI: `10.5445/IR/1000094129` (cited on p. 74).

[Sho38] W. Shockley. *Currents to Conductors Induced by a Moving Point Charge*. In: Journal of Applied Physics 9.10 (1938), pp. 635–636. DOI: `10.1063/1.1710367` (cited on p. 28).

[Spi05] H. Spieler. *Semiconductor Detector Systems*. OXFORD UNIV PR, Oct. 11, 2005. 489 pp. ISBN: 9780198527848. URL: `http://www.ebook.de/de/product/4443566/helmuth_spieler_semiconductor_detector_systems.html` (cited on pp. 23, 28).

[SR52] W. Shockley and W. T. Read. *Statistics of the Recombinations of Holes and Electrons*. In: Phys. Rev. 87 (5 Sept. 1952), pp. 835–842. DOI: `10.1103/PhysRev.87.835` (cited on p. 35).

[Syn18] Synopsys. *Sentaurus Device User Guide*. 2018 (cited on pp. 66–68, 120).

[Syn21] Synopsys. *TCAD*. 2021. URL: `https://www.synopsys.com/silicon/tcad.html` (visited on 07/26/2021) (cited on pp. 35, 66).

[SŽT12] L. Snoj, G. Žerovnik, and A. Trkov. *Computational analysis of irradiation facilities at the JSI TRIGA reactor*. In: Applied Radiation and Isotopes 70.3 (2012), pp. 483–488. ISSN: 0969-8043. DOI: `https://doi.org/10.1016/j.apradiso.2011.11.042` (cited on p. 65).

[Tan+18] M. Tanabashi et al. *Passage of particles through matter*. 2018. URL: `http://pdg.lbl.gov/2018/mobile/reviews/pdf/rpp2018-rev-passage-particles-matter-m.pdf` (cited on pp. 25, 27).

[The07] U. TheNoise. *A p-n junction in thermal equilibrium*. Aug. 2007. URL: `https://upload.wikimedia.org/wikipedia/commons/d/d6/Pn-junction-equilibrium.png` (cited on p. 22).

[Unn+07] Y. Unno et al. *p-Bulk silicon microstrip sensors and irradiation*. In: Nucl. Instrument. Meth. A 579.2 (2007). Proceedings of the 6th Hiroshima Symposium on the Development and Application of Semiconductor Detectors, pp. 614–622. ISSN: 0168-9002. DOI: `https://doi.org/10.1016/j.nima.2007.05.256` (cited on p. 109).

[VD70] R. Van Overstraten and H. De Man. *Measurement of the ionization rates in diffused silicon p-n junctions*. In: Solid State Electronics 13 (1970), pp. 583–608. ISSN: 0038-1101. DOI: `https://doi.org/10.1016/0038-1101(70)90139-5` (cited on p. 158).

[Wei08] Q. Wei. *Studies of Radiation Hardness of MOS Devices for Application in a Linear Collider Vertex Detector*. PhD Thesis. Technische Universität München, 2008. URL: `https://mediatum.ub.tum.de/doc/668264/668264.pdf` (cited on p. 151).

[Žon+99] D. Žontar et al. *Time development and flux dependence of neutron-irradiation induced defects in silicon pad detectors*. In: Nucl. Instrum. Meth. A 426 (1999). Ed. by E. Borchi and M. Bruzzi, pp. 51–55. DOI: `10.1016/S0168-9002(98)01468-5` (cited on p. 65).

Acknowledgments – Danksagung

Abschließend möchte ich allen danken, die mich bei der Promotion unterstützt haben.

Zuerst möchte ich Herrn Prof. Dr. Thomas Müller danken, für die Ermöglichung, sowie für die Betreuung der Promotion am Institut für Experimentelle Teilchenphysik. Ebenso danke ich Herrn Prof. Dr. Ulrich Husemann für die Übernahme des Korreferats und die Unterstützung in jeglichen Belangen.

Dr. Alexander Dierlamm danke ich für die herausragende Betreuung, interessanten Fragestellungen und stets hilfreichen Gesprächen.

Dr. Andreas Nürnberg danke ich für die Begleitung während der Promotion und die erfolgreichen Diskussionen.

Tobias Barvich, Felix Bögelspacher, Marius Neufeld, Dr. Hans Jürgen Simonis, Julian Stanulla, Pia Steck und Anita Weddigen danke ich für die Beratung in technischen und elektrotechnischen Fragestellungen. Ebenso danke ich für die zuverlässige Durchführung von Bestrahlungen, das Bonden, und die Konstruktion und Wartung von Komponenten für die zahlreichen Testsysteme.

Meinen Kollegen, die mich über die Zeit der Promotion begleitet haben, Alexander Droll, Roland Koppenhöfer, Stefan Maier, Marius Metzler und Florian Wittig danke ich dafür, dass sie den Arbeitsplatz zu einem Ort gemacht haben, an dem man sich immer gerne aufhält.

Der Landesgraduiertenförderung des Landes Baden-Württemberg und der Karlsruhe School of Elementary Particle and Astroparticle Physics: Science and Technology (KSETA) möchte ich für die Unterstützung während der Promotion danken.

This project has received funding from the European Union's Horizon 2020 Research and Innovation programme under Grant Agreement no. 654168.

Declaration

I declare that the work in this dissertation was carried out in accordance with the requirements of the University's Regulations and that it has not been submitted for any other academic award. Except where indicated by specific reference in the text, the work is the candidate's own work. Work done in collaboration with, or with the assistance of, others is indicated as such.

Karlsruhe, October 2021

Jan-Ole Müller-Gosewisch